Final Report

Project DE- EE0002761

THMC MODELING OF EGS RESERVOIRS – CONTINUUM THROUGH DISCONTINUUM REPRESENTATIONS: CAPTURING RESERVOIR STIMULATION, EVOLUTION AND INDUCED SEISMICITY

Derek Elsworth, Ghazal Izadi, Quan Gan, Yi Fang
Energy and Mineral Engineering
EMS Energy Institute
and
Center for Geomechanics, Geofluids and Geohazards
Pennsylvania State University

Josh Taron[1] and Eric Sonnenthal[2]
[1] USGS, Menlo Park
[2]Lawrence Berkeley National Laboratory

July 28, 2015

THMC Modeling of EGS Reservoirs – Continuum through Discontinuum Representations: Capturing Reservoir Stimulation, Evolution and Induced Seismicity

Derek Elsworth, Ghazal Izadi, Quan Gan, Yi Fang

Josh Taron and Eric Sonnenthal

Table of Contents

EXECUTIVE SUMMARY

This work has investigated the roles of effective stress induced by changes in fluid pressure, temperature and chemistry in contributing to the evolution of permeability and induced seismicity in geothermal reservoirs. This work has developed continuum models [1] to represent the progress or seismicity during both stimulation [2] and production [3]. These methods have been used to resolve anomalous observations of induced seismicity at the Newberry Volcano demonstration project [4] through the application of modeling and experimentation. Later work then focuses on the occurrence of late stage seismicity induced by thermal stresses [5] including the codifying of the timing and severity of such responses [6]. Furthermore, mechanistic linkages between observed seismicity and the evolution of permeability have been developed using data from the Newberry project [7] and benchmarked against field injection experiments. Finally, discontinuum models [8] incorporating the roles of discrete fracture networks have been applied to represent stimulation and then thermal recovery for new arrangements of geothermal wells incorporating the development of flow manifolds [9] in order to increase thermal output and longevity in EGS systems.

[1**]** We use a continuum model of reservoir evolution to explore the interaction of coupled thermal, hydraulic and chemical processes that influence the evolution of seismicity within a fractured reservoir from stimulation through production. Events occur from energy release on seeded fractures enabling moment magnitude, frequency and spatial distribution to be determined with time. Event magnitudes vary in the range -2 to +2 with the largest event size (~2) corresponding to the largest fracture size (~500m) and a prescribed stress drop of 9MPa. Modeled b-values (~0.6 to 0.7) also correspond to observations (~0.7 to 0.8) for response in the Cooper Basin (Australia). We track the hydrodynamic and thermal fronts to define causality in the triggering of seismicity. The hydrodynamic front moves twice as fast as the thermal front and envelops the triggered seismicity at early time (days to month) – with higher flow rates correlating with larger magnitude events. For later time (months to years) thermal drawdown and potentially chemical influences principally trigger the seismicity but result in a reduction in both the number of events and their magnitudes.

[2] We utilize this continuum model of reservoir behavior subject to coupled THMC (thermal, hydraulic, mechanical and chemical) processes to explore the evolution of stimulation-induced seismicity and related permeability in EGS reservoirs. Our continuum model is capable of accommodating changes in effective stresses that result due to the evolving spatial variations in fluid pressure as well as thermal stress and chemical effects. Discrete penny-shaped fractures (~10-1200m) are seeded within the reservoir volume at both prescribed (large faults) and random (small fractures) orientations and with a Gaussian distribution of lengths and location. Failure is calculated from a continuum model using a Coulomb

criterion for friction. Energy release magnitude is utilized to obtain the magnitude-moment relation for induced seismicity by location and with time. This model is applied to a single injector (stimulation) to the proposed Newberry EGS field (USA). Reservoir stimulation is assumed to be completed in four zones at depths of 2000, 2500, 2750 and 3000 m. The same network of large fractures (density of 0.003 m^{-1} and spacing 300 m) is applied in all zones and supplemented by more closely spaced fractures with densities from 0.26 m^{-1} (deepest zone) through 0.5 m-1 (shallow zone) to 0.9 m^{-1} (intermediate depth zone). We show that permeability enhancement is modulated by hydraulic, thermal, and chemical (THMC) processes and that permeability increases by an order of magnitude during stimulation at each depth. For the low density fracture networks, the increase in permeability reaches a smaller radius from the injection point and permeability evolution is slower with time compared to the behavior of the higher density fracture network. For seismic events that develop with the stimulation, event magnitude (MS) varies from -2 to +1.9 and the largest event size (~1.9) corresponds to the largest fractures (~1200m) within the reservoir. We illustrate that the model with the highest fracture density generates both the most and the largest seismic events (MS =1.9) within the 21 day stimulation. Rate of hydraulic and thermal transport has a considerable influence on the frequency, location and time of failure and ultimately event rate. Thus the event rate is highest when the fracture network has the largest density ($0.9m^{-1}$) and is located at depth where the initial stresses are also highest. Also apparent from these data is that the closely spaced fracture network with the higher stress regime (at the deeper level) has the largest b-value ~0.74.

[3] This coupled continuum model representing thermo-hydro-mechanical behaviors is then applied to follow the evolution of induced seismicity within a prototypical enhanced geothermal system (EGS) reservoir. The model is applied to the potential Newberry EGS field (USA) by assuming fracture sizes of 10 to 1200 m. Models are classified by their conceptualization of the fractured reservoir geometry as networks of discrete fractures and with equivalent fractured media as fill-in. The THMC model is applied to a doublet injector-producer to explore the spatial and temporal triggering of seismicity for varied fracture network geometries both shallow (2000m) and at depth (2750m). The magnitude of the resulting seismic events is in the range -2 to +1.9. The largest event size (~1.9) corresponds to the largest fracture size (~1200m) within the reservoir. The rate of hydraulic and thermal transport has a considerable influence on the amount, location, and timing of failure, and ultimately, on the event rate. The event rate is highest when the fracture density is highest ($0.9m^{-1}$) and the initial stresses highest (at depth). In all cases, the *a*-value decreases and the *b*-value increases with time. The *b*-value is largest (~1.34) for the highest fracture density and the highest stress regime. Thermal energy recovered during production is also greatest at depth and for the highest density of fractures.

[4] Stimulation of enhanced geothermal system (EGS) reservoirs by fluid injection can enhance the reservoir permeability but may also result in undesired microearthquakes (MEQs). A bimodal depth distribution of fluid-injection-induced MEQs was observed in the 2012 stimulation phase of the Newberry Volcano EGS Demonstration project in Oregon, US. During 7 weeks of hydraulic stimulation of well NWG 55-29, 90% of MEQs occurred in the shallow reservoir (~ 500 m to ~1800 m), only a few occurred adjacent to the bottom of the open borehole (~ 2500 to ~3000 m) while almost no seismicity was observed in the intervening interval (~1800 m to ~2500 m). Our analysis of frictional stability using spatial models for fluid pressure diffusion of injected fluids show that the distribution of MEQs is consistent with observed casing damage, and a possible leak at ~700 m, and is inconsistent with migration of fluids from the casing shoe. The role of fluid injection through the ruptured casing is further supported by the analyses of shear failure and pore-pressure diffusion. Finally, the absence of seismicity at intermediate depths is consistent with our laboratory determinations of frictional stability, showing velocity strengthening frictional behavior for samples from intermediate depths, bracketed by velocity neutral and weakening behavior for samples from shallower and greater depths.

[5] We explore the issue of fault reactivation induced in Enhanced Geothermal Systems (EGS) by fluid injection. Specifically we investigate the role of late stage activation by thermal drawdown. A THM (Thermal-Hydrological-Mechanical) simulator incorporating a ubiquitous joint constitutive model is used to investigate the elastic-plastic behavior of an embedded fault. We apply this new THM model to systematically simulate the seismic slip of a critically-stressed strike-slip fault embedded within the reservoir. We examine the effects of both pore pressure perturbation and thermal shrinkage stress on the magnitude of the resulting events and their timing. We analyze the sensitivity of event magnitude and timing to changes in the permeability of the fault and fractured host, fracture spacing, injection temperature, and fault stress obliquity. From this we determine that: (1) the fault permeability does not affect the timing of the events nor their size, since fluid transmission and cooling rate is controlled by the permeability of the host formation. (2) When the fractured medium permeability is reduced (e.g. 10^{-13} to 10^{-16} m^2), the timing of the event is proportionately delayed (by a corresponding three orders of magnitude), although the magnitude of the seismic event is not impacted by the change in permeability. (3) Injection temperature has little influence on either the timing or size of the early hydro-mechanically induced events, but it does influence the magnitude but not the timing of the secondary thermal event. The larger the temperature differences between that of the injected fluid and the ambient rock, the larger the magnitude of the secondary slip event. (4) For equivalent permeabilities, changing the fracture spacing (*10m-50m-100m*) primarily influences the rate of heat energy transfer and thermal drawdown within the reservoir. Smaller spacing between fractures results in more rapid thermal recovery but does not significantly influence the timing of the secondary thermal rupture.

[6] Late-stage seismic-slip in geothermal reservoirs has been shown as a potential mechanism for inducing seismic events of magnitudes to ~2.6 as late as two decades into production. We investigate the propagation of fluid pressures and thermal stresses in a prototypical geothermal reservoir containing a centrally-located critically-stressed fault from a doublet injector and withdrawal well to define the likelihood, timing and magnitude of events triggered by both fluid pressures and thermal stresses. We define two bounding modes of fluid production from the reservoir. For injection at a given temperature, these bounding modes relate to either low- or high-relative flow rates. At low relative dimensionless flow rates the pressure pulse travels slowly, the pressure-driven changes in effective stress are muted, but thermal drawdown propagates through the reservoir as a distinct front. This results in the lowest likelihood of pressure-triggered events but the largest likelihood of late-stage thermally-triggered events. Conversely, at high relative non-dimensional flow rates the propagating pressure pulse is larger and migrates more quickly through the reservoir but the thermal drawdown is uniform across the reservoir and without the presence of a distinct thermal front, and less capable of triggering late-stage seismicity. We evaluate the uniformity of thermal drawdown as a function of a dimensionless flow rate Q_D that scales with fracture spacing s (m), injection rate q (kg/s), and the distance between the injector and the target point L^* ($Q_D \propto qs^2 / L^*$). This parameter enables the reservoir characteristics to be connected with the thermal drawdown response around the fault and from that the corresponding magnitude and timing of seismicity to be determined. These results illustrate that the dimensionless temperature gradient adjacent to the fault dT_D / dx_D is exclusively controlled by the factor Q_D. More significantly, this temperature gradient correlates directly with both the likelihood and severity of triggered events, enabling the direct scaling of likely magnitudes and timing to be determined a priori and directly related to the characteristics of the reservoir. This dimensionless scaling facilitates design for an optimum Q_D value to yield both significant heat recovery and longevity of geothermal reservoirs while minimizing associated induced seismicity.

[7] In the stimulation of fractured geothermal reservoirs, injection wellhead pressure, flow rate and microearthquake (MEQ) data are crucial feedbacks recorded in order to characterize the evolution of subsurface fluid flow. However, one of the hurdles to successful EGS development and operation is the lack of reliable evaluation for the initial and evolving hydraulic properties of the fractured reservoir. Specific spatial conditions (e.g., location and direction) of fracture permeability in the field are vital in defining reservoir response during stimulation and then production. To constrain the evolving permeability, we propose a model that maps the in-situ permeability based onto the *Oda* crack tensor using the moment magnitude of individual MEQs, assuming that the induced seismicity is controlled by the Mohr-Coulomb shear criterion. The MEQ catalog of locations, fault plane solutions, and moment

magnitudes are used to estimate fracture apertures of individual events/fractures that are a dynamic function of in-situ stress, fluid pressure, shear displacement and fracture size. The corresponding in-situ 2D permeability tensors are computed and mapped at various scales within the reservoir. Results suggest that the permeability magnitude largely depends on MEQ moment magnitude and fracture frictional properties while permeability direction is dominantly controlled by fracture orientation. However, uncertainty remains within the results, which need improvements in constraint from laboratory and in-situ fracture characterization, the quality of seismic monitoring and reliability of appropriate assumptions.

[8] We present a model coupling stress and fluid flow in a discontinuous fractured mass represented as a continuum by coupling the continuum simulator TF_FLAC^{3D} with cell-by-cell discontinuum laws for deformation and flow. Both equivalent medium crack stiffness and permeability tensor approaches are employed to characterize pre-existing discrete fractures. The advantage of this approach is that it allows the creation of fracture networks within the reservoir without any dependence on fracture geometry or gridding. The model is validated against thermal depletion around a single stressed fracture embedded within an infinite porous medium that cuts multiple grid blocks. Comparison of the evolution of aperture against the results from other simulators confirms the veracity of the incorporated constitutive model, accommodating stress-dependent aperture under different stress states, including normal closure, shear dilation, and for fracture walls out of contact under tensile loading. An induced thermal unloading effect is apparent under cold injection that yields a larger aperture and permeability than during conditions of isothermal injection. The model is applied to a discrete fracture network to follow the evolution of fracture permeability due to the influence of stress state (mean and deviatoric) and fracture orientation. Normal closure of the fracture system is the dominant mechanism where the mean stress is augmented at constant stress obliquity ratio of 0.65 – resulting in a reduction in permeability. Conversely, for varied stress obliquity (0.65 – 2) shear deformation is the principal mechanism resulting in an increase in permeability. Fractures aligned sub-parallel to the major principal stress are near-critically stressed and have the greatest propensity to slip, dilate and increase permeability. Those normal to direction of the principal stress are compacted and reduce the permeability. These mechanisms increase the anisotropy of permeability in the rock mass. Furthermore, as the network becomes progressively more sparse, the loss of connectivity results in a reduction in permeability with zones of elevated pressure locked close to the injector – with the potential for elevated pressures and elevated levels of induced seismicity.

[9] In this work, a stimulation then heat production optimization strategy is presented for prototypical EGS geothermal reservoirs by comparing conventional stimulation-then-production scenarios against revised stimulation schedules. A generic reservoir is selected with an initial permeability in the range of 10^{-17} to 10^{-16} m^2, fracture density of ~0.09 m^{-1} and fractures oriented such that either none, one, or both

sets of fractures are critically stressed. For a given reservoir with a pre-existing fracture network, two parallel manifolds are stimulated that are analogous to horizontal wells that allow a uniform sweep of fluids between the zones. The enhanced connectivity that develops between the injection zone and the production zone significantly enhances the heat sweep efficiency, while simultaneously increasing the fluid flux rate at the production well. For a 10m deep section of reservoir the resulting electric power production reaches a maximum of 14.5 MWe and is maintained over 10 years yielding cumulative energy recoveries that are a factor of 1.9 higher than for standard stimulation. Sensitivity analyses for varied fracture orientations and stimulation directions reveal that the direction of such manifolds used in the stimulation should be aligned closely with the orientation of the major principal stress, in order to create the maximum connectivity. When the fractures are less prone to fail, the output electric power is reduced by a decrease in the fluid flux rate to the production well. The short circuiting response during heat extraction is significant for the low fracture density condition, which can result early thermal breakthrough in the production well.

References

1. Izadi, G., Elsworth, D. (2013) The effects of thermal stress and fluid pressures on induced seismicity during stimulation to production within fractured reservoirs. Terra Nova. Vol. 25. pp. 774-380.
2. Izadi, G., Elsworth, D. (2014) Reservoir stimulation and induced seismicity: role of fluid pressure and thermal transients on reactivated fracture networks. Geothermics. Vol. 51. pp. 368-379.
3. Izadi, G., Elsworth, D. (2015) The influence of thermal-hydraulic-mechanical-and chemical effects on the evolution of permeability, seismicity and heat production in geothermal reservoirs. Geothermics. Vol 53. pp. 385-395.
4. Fang, Y., den Hartog, S.A.M., Elsworth, D., Marone, C., Cladouhos, T. (2015) Anomalous distribution of microearthquakes in the Newberry geothermal reservoir: mechanisms and implications. In press. Geothermics. 40 pp.
5. Gan, Q., Elsworth, D. (2014) Analysis of fluid injection-induced fault reactivation and seismic slip in geothermal reservoirs. J. Geophys. Res. Vol. 119, No. 4, pp. 3340-3353.
6. Gan, Q. and Elsworth, D. (2014) Thermal drawdown and late-stage seismic-slip fault-reactivation in enhanced geothermal reservoirs. J. Geophys. Res. Vol. 119, pp. 8936-8949.
7. Fang, Y., Elsworth, D., & Cladouhos, T. T. (2015). Mapping permeability tensors in fractured geothermal reservoirs using MEQ data. Proc. 49th U.S. Symposium on Rock Mechanics. ARMA. June
8. Gan, Q. and Elsworth, D. (2015) An equivalent continuum model for coupled stress and fluid flow in discrete fractures in geothermal reservoirs. Prepared for submission.
9. Gan, Q. and Elsworth, D. (2015) Production optimization in geothermal reservoirs using a coupled discrete fracture network model. Prepared for submission.

1 CHAPTER 1: THE EFFECTS OF THERMAL STRESS AND FLUID PRESSURE ON INDUCED SEISMICITY DURING STIMULATION TO PRODUCTION WITHIN FRACTURED RESERVOIRS

Abstract

We use a continuum model of reservoir evolution to explore the interaction of coupled thermal, hydraulic and chemical processes that influence the evolution of seismicity within a fractured reservoir from stimulation through production. Events occur from energy release on seeded fractures enabling moment magnitude, frequency and spatial distribution to be determined with time. Event magnitudes vary in the range -2 to +2 with the largest event size (~2) corresponding to the largest fracture size (~500m) and a prescribed stress drop of 9MPa. Modeled *b*-values (~0.6 to 0.7) also correspond to observations (~0.7 to 0.8) for response in the Cooper Basin (Australia). We track the hydrodynamic and thermal fronts to define causality in the triggering of seismicity. The hydrodynamic front moves twice as fast as the thermal front and envelops the triggered seismicity at early time (days to month) – with higher flow rates correlating with larger magnitude events. For later time (month to years) thermal drawdown and potentially chemical influences principally trigger the seismicity but result in a reduction in both the number of events and their magnitudes.

1.1 Introduction

Fluid injection at pressures intermediate between the minimum principal stress and the Coulomb stress will induce shear failure within enhanced geothermal reservoirs (EGS) [Hubbert and Rubey, 1959; Majer and Peterson, 2007; Majer et al., 2007; Segall, 1989] and may trigger seismicity [Grasso and Wittlinger, 1990; Yerkes and Castle, 1976]. Influence of fluid pressures on failure is exacerbated by the significant changes in total stress that may result from thermal drawdown and potentially from chemical effects within the reservoir. Shear failure may occur aseismically but is also manifest as microseismic activity in many cases.

In these cases the induced seismicity results from fluid injection and is expected to migrate within the reservoir with time as driven by the various interactions of thermal, hydraulic, mechanical and chemical processes which also migrate through the reservoir on different length-scales and timescales [Barton et al., 1985; Elsworth and Yasuhara, 2010; Goodman, 1976; Taron and Elsworth, 2009; Walsh, 1965]. Defining the potential causes of induced seismic activity due to production from engineered geothermal systems is a significant concern – both to understand mechanisms and to mitigate damaging consequences. The size of the resulting seismic event is defined by the total energy release that in turn relates to the stress drop and how fast it fails [Brune and Thatcher, 2002.].

In the following we use a continuum model of reservoir evolution subject to coupled THMC processes [Taron and Elsworth, 2009a] to explore the evolution of production-induced seismicity in a prototypical EGS reservoir. In this study we define the relationship between the magnitudes of induced seismic events and the applied fluid injection rates as well as the evolution of thermal stress. Our focus is to determine dominant behaviors controlling the triggering of induced seismicity that is unique in comparison to previous studies. We show that induced seismicity is modulated by hydraulic, thermal, and chemical processes which also migrate through the reservoir [Elsworth and Yasuhara, 2010b; Taron and Elsworth, 2009b]. We then explore how pore-pressure and thermal stress can be linked to the seismic frequency–magnitude distribution, which is described by its slope, the b-value.

1.2 Model dimension and description

1.2.1 Reservoir and fracture network characterization

We assume a doublet geometry (500m spacing) and the dimension of the reservoir volume in the model is 2000×1000×100 m3 for the half-symmetry. Figure 1 representative of the Cooper Basin geothermal field. The THMC model evaluates the evolution of flow rate, pressure and temperature distribution during stimulation. The applied injection pressure and temperature are assumed to be equal to 39.8MPa and 70°C. Reservoir pressure and temperature are assumed to be 29.8MPa and 250°C. Boundary stresses and the values of the solid medium properties utilized in the simulation for this case are defined in Table 1. Reactive composition of the host reservoir rock is presented in Table 2.

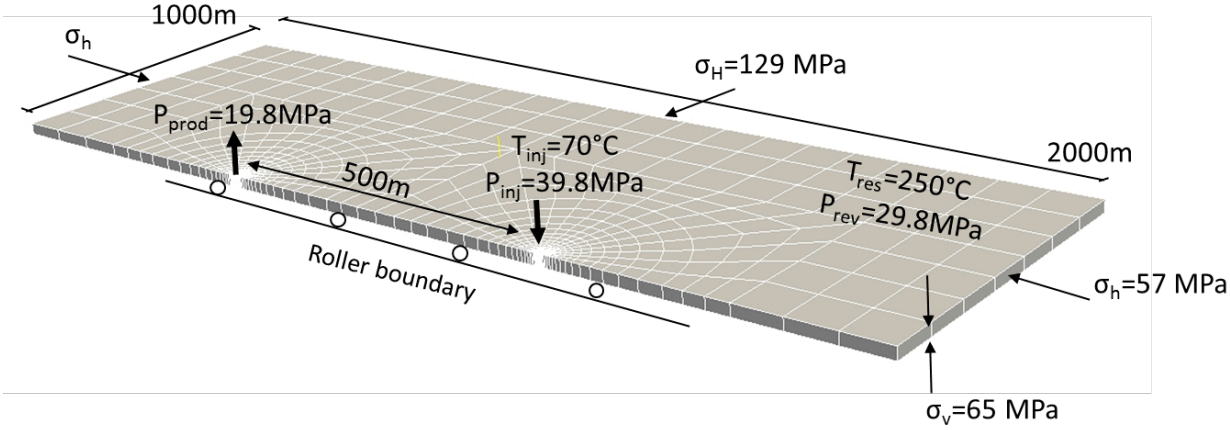

Figure 1: Geometric layout and boundary conditions of EGS reservoir as used in the simulation.

Calcite and amorphous silica are expected to be the minerals primarily responsible for permeability change due to precipitation and dissolution. Other likely minerals are also followed, as listed in Table 2. Rate constants for precipitation/dissolution and mineral reactive surface areas of these common minerals

are available in the literature [Kovac et al., 2006.; Xu and Pruess, 2001], and were utilized as in [Xu and Pruess, 2004].

Table 1: Parameters utilized in the simulation.

Parameter	**Unit**	**Cooper Basin**
S_{zz}	MPa	65
S_{yy}	MPa	57
S_{xx}	MPa	129
Fluid pressure(P_{inj})	MPa	39.8
Injection temperature	°C	70
Reservoir temperature	°C	250
Bulk modulus of intact rock(K_m)	GPa	17
Cohesion	MPA	10
Poisson's ratio(υ)	-	0.27
Bulk modulus of fluid(k_f)	GPa	8
Bulk modulus of solid grain(K_s)	GPa	54.5
Internal friction angle(φ)	°	35
Residual friction angel(β)	°	11
Coefficient of thermal expansion(α_T)	1/°C	1.2×10^{-5}
Thermal conductivity(λ)	W/mK	2.9
Heat capacity(c_p)	J/kgK	918
Porosity within fractures(ϕ)	-	0.3

Table 2: Initial volume fraction of reactive minerals in host reservoir

Mineral	**Volume fraction of solid rock**	
	Granodiorite	**Fractured vein**
Anorthite	0.33	--
Calcite	0.02	0.31
Chlorite	--	0.23
K-Feldspar	0.17	--
Quartz	0.34	0.17
Amorphous Silica	--	--

1.2.2 THMC Model

Here we focus on the complex interaction of coupled thermal, hydraulic, mechanical and chemical (THMC) processes that influence the evolution of EGS reservoirs and describe the dominant behaviors that progress with the evolution of the reservoir. We apply a coupled THMC model [*Taron et al.*, 2009] with static-dynamic frictional strength-drop to determine energy release for fractures of different size embedded within an elastic medium.

Change of stress state is calculated from the pore pressures, thermal drawdown and chemical effects within FLAC^{3D}-TOUGHREACT [*Taron and Elsworth*, 2009a]. Shear failure calculations are handled with FLAC^{3D} utilizing a Mohr-Coulomb failure (fracture propagation is not considered). The friction angle on fractures is assumed constant (35^{o}) and during failure the maximum shear stress drop (~9.0 MPa) is prescribed to represent the residual strength. This model calculates the flow rate, pressure and temperature distribution during stimulation. The changes in pressure and temperature induce displacements that consequently lead to a new change in pressure distribution.

These include short-term response where effective stresses and thermal quenching are expected to dominate the behavior of the reservoir and are influenced by the local structure in the rock and orientation of pre-existing fractures. Typical behaviors include the reduction of local mean stresses and the development of shear fracturing principally on pre-existing fractures. The very short-term response (days to month) **Figure 2** is controlled by fluid pressure and effective stress effects (HM).

Throughout the evolution of the reservoir, these coupled effects control the development of permeability, of heat-transfer area, and thereby thermal output of the reservoir, together with the evolution of induced seismicity. We applied different models to illustrate the timing of THMC effects separately (**Figure 2)**. Thus we note the sequencing of fluid pressure effects as fastest-acting followed by thermal stresses then chemical effects influence the timing and migration of changes in effective stress within reservoirs as illustrated in **Figure 2**. Since seismicity is indexed to changes in effective stresses then these rates of change will influence triggering within the reservoir.

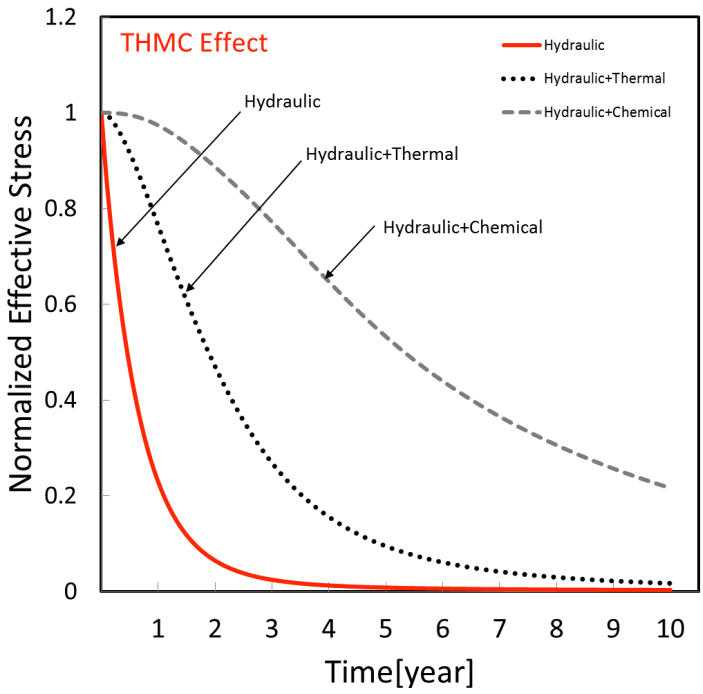

Figure 2: Normalized effective stress vs. time at 50m far from injection point. Hydraulic, thermal and chemical effect is separately illustrated during 10 year production and their influence on triggering seismicity. Red solid line, injection pressure assumed 39.8MPa and reservoir pressure is 29.8MPa and temperature of injection is assumed the same as rock temperature (250°C) and no chemical reaction occurs. Black dash line, both pressure and temperature changed; injection pressure is 39.8MPa and reservoir pressure is 29.8MPa, injection temperature is 70°C and reservoir temperature is 250°C, again no chemical reaction. Gray dash line, injection pressure is 39.8MPa and reservoir pressure is 29.8MPa, injection temperature is the same as reservoir temperature (250°C), chemical reaction is considered [injection fluid component illustrated table2].

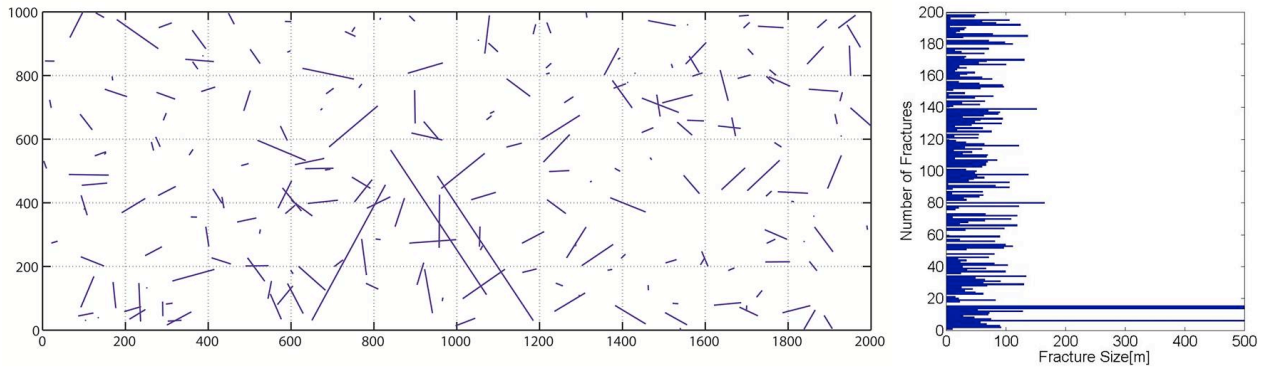

Figure 3: Fracture data utilized in the simulation. Fracture density of 0.1 m^{-1} and these vary in length from 1 to 500m. (Left) Fracture distribution by location and (right) fracture distribution by size.

1.3 Observation and calibration

We examine the performance of our models against the observed response of the Cooper Basin geothermal field (Australia) and specifically the progress of seismicity as the reservoir is developed in terms of rates, magnitudes and locations [*Baisch et al.*, 2006].

1.3.1 Evolution of moment magnitude

The potential energy released within reservoirs for different fracture spacing is defined based on the evaluation of the elastic energy released from the failure of large penny-shaped fractures. Shear stress drop is calculated in FLAC^{3D} as a function of normal stress and pore pressure for a variety of uniform fracture spacings at different locations within the reservoir.

Shear stress builds in the early time (<1month) and reaches a maximum magnitudes in the range ~28MPa as defined by prescribed peak strengths. This peak strength is defined by a cohesion of 10 MPa, peak friction angle of 35 and during failure the maximum shear stress drop (~9.0 MPa) is prescribed to represent the residual strength. Then we calculate the potential energy release, E_p, from failure of a penny-shaped fractures due to a stress drop $\Delta\tau$ at different location within reservoir. This relation is defined as $E_p = \frac{2\Delta\tau^2 a^3}{3G}$, where a is the radius of the fracture in the plane and G is a shear modulus.

Energy release from fractures is most conveniently represented as a moment magnitude [*Aki*, 1967; *Kanamori*, 1977; *Keylis-Borok*, 1959]. The moment magnitude relation is defined as [*Purcaru and Berckemer*, 1978]: $\log M_0 = 1.5M_s + 9.1$, where M_0 is seismic moment and M_S is moment magnitude. In this model M_0 is seismic energy which is derived from the elastic energy released by shear on pre-existing fractures. This relation allows us to determine both the spatial and temporal evolution of moment magnitude in EGS reservoirs and such moment magnitude (M_s) varies from -2 to +2 for the largest fracture size (~500m).

We then use a stress-strain fracture criterion to determine the total strain energy available for release – this energy is assumed to be shed seismically. During the rupture process the shear stress drops an amount $\Delta\tau$ from an initial value of τ_i to final value τ_f, then we can define an expression for total energy $E_T = \int \Delta\tau^T \Delta\varepsilon dV$, where strain changes from an initial value of ε_i to a final value ε_f where V is volume of the matrix. Here we introduce a relation to determine the number of events which occur during the failure process based on potential and total energy as $N_{event} = \frac{E_T}{E_p}$, where N_{event} is the number of seismic events, E_T is the total energy of matrix block and E_p is the potential energy released of fractures.

Here the energy release of fractures within the reservoir determines the evolution of seismic event magnitude. The release of seismic energy (stress drop=9MPa) which is generated in the Cooper Basin EGS reservoir due to thermal, mechanical and chemical effects when seeded with fractures (1-500m) is illustrated in **Figure 4**. This outcome indicates that during simulation the potential energy within the reservoir containing fracture networks is released gradually and extends far from injection. The characteristic event magnitude distribution that occurs has a stress drop of ~9 MPa which implies the occurrence of larger magnitude events (~1-2) near injection at early times (days to month) during the stimulation. This process is controlled by the population of fracture sizes and the stress drop.

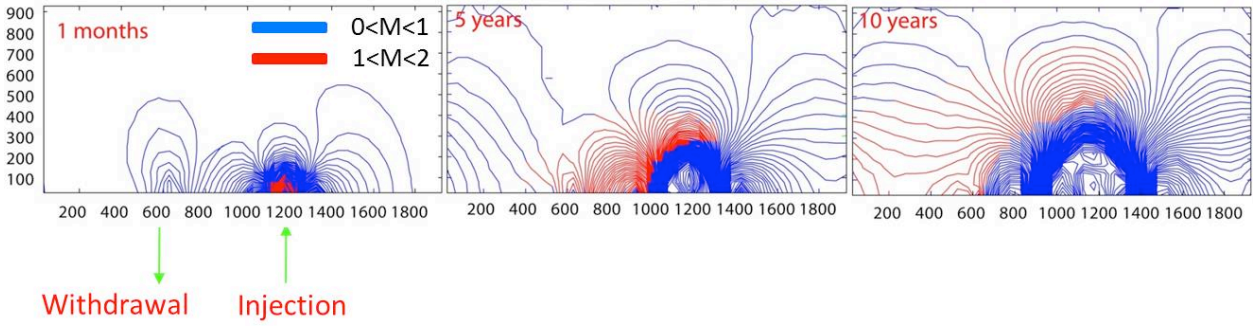

Figure 4: The evolution of moment magnitude in the Cooper Basin EGS reservoir over 10 years of simulation. Solid lines illustrate the failure in each location of reservoir. Blue region illustrates smallest event magnitude and red region illustrates the largest potential energy that is released in different locations due to combined thermal, mechanical and chemical effects.

1.3.2 Empirical relation for triggering seismicity

The b-value recovered from the analysis is used to calibrate the model against field data. The b-value is an observable parameter from accumulated seismic observations and may be used to calibrate models – as is attempted here.[Aki, 1981] speculated that the b-value relates to the fractal geometry of the fault plane assemblage and argued that the log N-M relation for earthquakes is equivalent to a fractal distribution. The b-value is an important parameter for the estimation of earthquake hazard. The b-value is related to the rock type and the state of stress and increases with the ductility of the rock [Scholz, 1986].

The modeled b-value represents the cumulative number of seismic events at each location within the reservoir with the local magnitude evaluated from its seismic moment. Gutenberg & Richter (1944) expressed the magnitude distribution in the form log Nevent = a - bM, where Nevent is the number of seismic events within a magnitude interval M±ΔM. Here we discuss the scaling of the frequency of events Nevent as a function of fluid pressure and temperature. The magnitude-frequency relation evaluated at early time (first month) is illustrated in Figure 5- left. The approximate b-value is ~0.7 and this is constrained only by an assumed fracture density. The shape of the resulting frequency–magnitude

distribution is similar to that reported for the Cooper Basin [Baisch et al., 2009; Shapiro and Dinske, 2009b] and the evaluated b-value in particular matches the Habanero-1 well data. The histogram of event magnitudes which was determined for the 2005 data catalog indicates a b-value of 0.8 in the magnitude range -0.8 to +1.5 [Baisch et al., 2009] and the approximate b-value from Shapiro and Dinske [2009b] is +0.75. Events migrate during the simulated evolution due to the progress of fluid pressure diffusion. For this particular reservoir the microseismicity begins at the injector and migrates upwards with time. From the Gutenberg-Richter relation, from Aki's [1981] supposition and from our observations we conclude that the b-value describes fracturing processes in the seismic region and is related to the size, location, distribution and spacing of fractures.

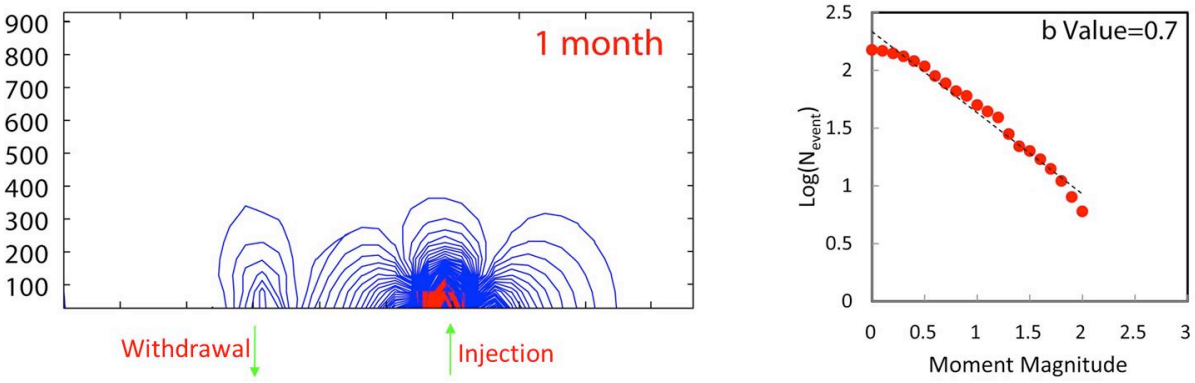

Figure 5: (Left) Evolution of moment magnitude in the Cooper Basin EGS reservoir after 1 month stimulation. (right) number of events as a function of magnitude indicating b value of 0.7 and moment magnitude range 0-2.

1.3.3 Effect of hydrodynamic and thermal front on triggered seismicity

The numerical model is used to follow the hydrodynamic and thermal fronts as it propagates through the reservoir. The data used in this simulation are related to the Cooper Basin EGS which is also discussed elsewhere [*Shapiro and Dinske*, 2009a].

The location of these fronts is defined by the propagation of the fluid flow rate at any given time within TOUGHREACT module [*Xu et al.*, 2006]. The evolution of seismicity for 10 years reservoir production is shown in a radius-time plot relative to the propagation of these fluid and thermal fronts in **Figure 6-a** (injection flow rate is set at 15 *l/s* in the simulation). This shows the progress of the fluid and thermal fronts in the reservoir together with the progress of induced seismicity. We observe that the rate of propagation of the hydrodynamic front is approximately twice as rapid as the thermal front.

This illustrates that most of the seismic activity is triggered by hydraulic effects at early times (days to month) relative to the initiation of stimulation. At later time (month to years), thermal effects specifically,

or chemical effects possibly, may contribute to the seismicity when the seismicity front lags behind the hydrodynamic front due to small changes in pressure. By following the propagation of fluid pressure, thermal fronts through the reservoir with time we associate large early-time events with the fluid front and the lower seismic magnitude later-time events with the transit of the thermal/chemical front.

Then we confirm the form of observations in our model against those reported in [*Shapiro and Dinske*, 2009a] which in turn has been calibrated against field data. We observe good agreement between our model observations and those in the Cooper Basin [*Shapiro and Dinske*, 2009a; *Shapiro and Dinske*, 2009b]. We then compare the magnitude-frequency relations evaluated for the Cooper Basin stimulation at three different times **Figure 4-a** (first month followed by after 5 and 10 years). We considered a 14 days window at each time frame to normalize the number and magnitude of events at any location within the reservoir **Figure 4-b, c, d**. The number of events as a function of time is controlled only by the cumulative mass of fluid injected which then results in failure and energy release. The larger this energy release the larger number of seismic events induced at a given location and time.

Also we characterize the induced seismicity by the *b*-value for these different time periods. The approximate *b*-value is illustrated in **Figure 4-e, f, g** and corresponds closely with observations. The plot of event magnitudes determined here indicate a *b*-value of 0.72 in the magnitude range 0 to +2 at early time, +0.7 after five years and +0.68 after ten years. This behavior shows that the *b*-value is highest at early time and means that the larger events occur earliest (days to month) and due to the passage of the fluid pressure front. At later times (month to years) the principal factor triggering the seismicity is thermal effects. Finally in **Figure 4-h** we illustrate the number of event at each time. It shows that the largest number of seismic events exist for $0<Ms<2$ induced near injection and decrease away from the point of injection.

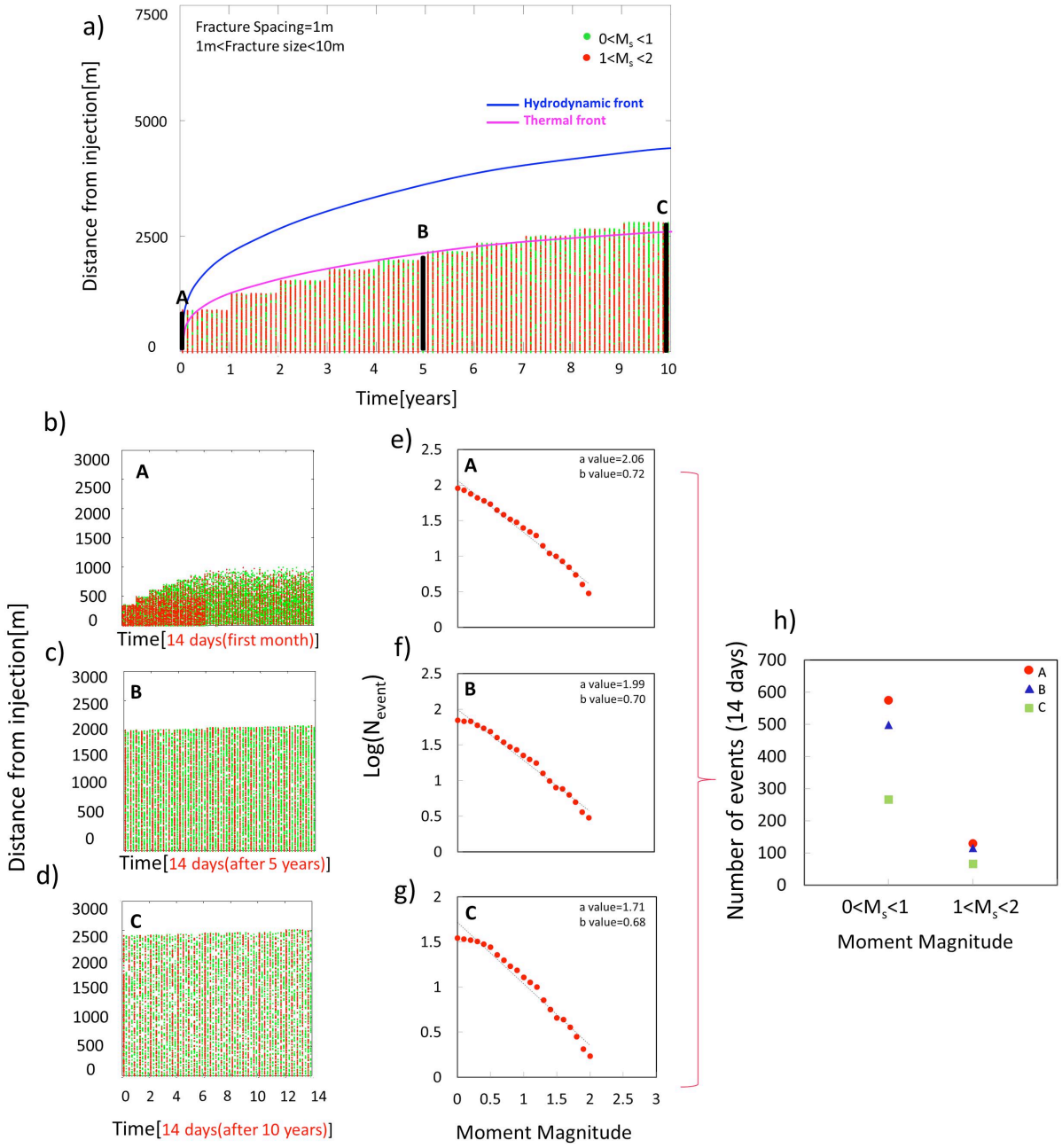

Figure 6: a) Radius versus time plot for short term of the progress of fluid and thermal fronts in the reservoir and of induced seismicity after 10 years production (Injection flow rate is 15 l/s). Seismic moment of individual events shown green(smaller event): $0<M_s<1$ and red(larger event): $1<M_s<2$. The hydrodynamic front illustrated with blue and thermal front with pink solid line. Fracture density is ~$0.1m^{-1}$ (fractures are in the ranges of 1m-500m, fracture spacings are in the ranges of 10m-500m). We separately zoom in 3 windows (considering 2 weeks period at each window) A, B and C at three different times (14 days after stimulation, after 5 years and after 10 years). b) Seismic activity at early time

[2weeks period]. c) Seismic activity after 5 years stimulation [2weeks period]. d) Seismic activity after 10 years stimulation [2weeks period]. e, f, g) number of events as a function of magnitude indicating *b*-value of 0.72 at early time, 0.7 after 5 years and 0.68 after 10 years stimulation [moment magnitude range 0-2]. i) Number of events as a function of moment magnitude for three different times [first month, 5 and 10 years]. The number of events with small ($0<M_s<1$) and large ($1<M_s<2$) magnitude shows in three different colors; red, blue and green. Red; Number of events at the stimulation period, blue; Number of events after 5 years production, green; Number of events after 10 years production.

1.4 Conclusions

We explore the coupling between Thermal- Hydraulic- Mechanical- Chemical behaviors on fractured reservoirs to understand the critical processes during thermal recovery from EGS reservoirs. Large fractures (faults) with infill fractures (small-large) of various spacing, orientation and fracture placement represent the distributed fracture network within the reservoir. We use this distribution for a fractured geothermal reservoir in the Cooper Basin to understand the significant behaviors of THMC effects on fractured reservoirs. The activated fractures due to pore pressure propagation and induced thermal and chemical strains can generate different failure regimes in the reservoir and the incremental development of energy release of fractures can induce seismic events with varying ranges of magnitude (-3 to 5) at short and long time scales.

We capture the energy release of fractures and then the magnitude is utilized to obtain the magnitude-moment relation and to compare our model with the measured b-value that observed at early-time reservoir stimulation (2 weeks) to understand the induced seismicity at the Cooper Basin. This is then extended to explore the evolution of seismicity expected over an extended period of production (10 years).

Events occur from energy release on seeded fractures enabling moment magnitude, frequency and spatial distribution to be determined with time. We evaluated the magnitude of events and it varies from -2 to +2 and the largest event size (~2) corresponds to the largest fracture size (~500m) which represents the weakest planes within reservoir and a prescribed stress drop of 9MPa.

We separately examine the impact of thermal stresses, pore pressure and chemical effects on the evolution of seismicity during this long term production. The most important mechanism which triggers slip and promotes seismic events along the weak planes and also may change the moment is the augmentation of fluid pressure at early time. However, with migration of fluid in the fractures at later time thermal quenching can cause a reduction in effective stress and additionally contribute to triggered seismicity.

Modeled *b*-values (~0.6 to 0.7) also correspond to observations (~0.7 to 0.8) and this approach is verified using data for the Cooper Basin (Australia) geothermal field. We tracked the hydrodynamic and thermal fronts to define causality in the triggering of seismicity.

To describe the reservoir from valid data we tried to find a good correlation between spacing, length, orientation and placement of fractures in the model and then calibrate the model by replicating observed *b*-values during reservoir production. The *b*-value describes the fracture process within reservoirs and is related to size, location, distribution and spacing of fractures.

Finally we illustrate the penetration of Hydrodynamic and thermal fronts through the reservoir with time. The hydrodynamic front moves twice as fast as the thermal front and envelops the triggered seismicity at early time (days to month) – with higher flow rates correlating with larger magnitude events. For later time (>1year) thermal drawdown and potentially chemical influences principally trigger the seismicity but result in a reduction in both the number of events and their magnitude.

Acknowledgements: This work is the partial result of support from the Department of Energy Office of Energy Efficiency and Renewable Energy and Geothermal Technology Program under contract EE-10EE0002761. This support is gratefully acknowledged.

1.5 References

1 Aki, K. (1967), Scaling law of seismic spectrums, J. Geo-phys. Res., 72, 1217-1231.
2 Aki, K. (1981), A probabilistic synthesis of precursory phenomena. In: Simpson D.W. and Richards, P.G.(Eds), Earthquake prediction, Am. Geophys. Union, Washington D.C. pp. 566-574.
3 Baisch, R. Vörös, R. Weidler, and D. Wyborn (2009), Investigation of Fault Mechanisms during Geothermal Reservoir Stimulation Experiments in the Cooper Basin, Australia, Bulletin of the Seismological Society of America, Vol. 99, No. 1, pp. 148–158, doi: 10.1785/0120080055.
4 Baisch, R. Weidler, Vo¨ro¨s, D. Wyborn, and L. Graaf (2006), Induced seismicity during the stimulation of a geothermal HFR reservoir in the Cooper Basin, Australia. Bulletin Seismological Society of America 96, 2242–2256.
5 Barton, N., S. Bandis, and K. Bakhtar (1985), Strength, deformation, and conductivity coupling of rock joints. Int J Rock Mech Min Sci ;22(3):121-140.
6 Brune, J., and W. Thatcher (2002.), International Handbook of Earthquake and Engineering Seismology, vol. 81A. International Association of Seismology and Physics of Earth's Interior, Committee on Education, pp. 569-588.
7 Elsworth, D., and H. Yasuhara (2010), Mechanical and transport constitutive models for fractures subject to dissolution and precipitation. In press. Int. J. Num. Meth. Geomechs. Vol. 34, pp. 533-549. Doi:10.1002/nag.831.
8 Goodman, R. E. (1976), Methods of Geological Engineering in Discontinuous Rocks, 472 pp., West Publishing, New York.
9 Grasso, J. R., and G. Wittlinger (1990), 10 years of seismic monitoring over a gas field area. Bull. Seismol. Soc. Am. 80, 450–473.
10 Hubbert, M. K., and W. W. Rubey (1959), Role of fluid pressure in mechanics of overthrust faulting 1. Mechanics of fluid-filled porous solids and its application to overthrust faulting, Geological Society of America Bulletin, 70(2), 115-166.
11 Kanamori, H. (1977), The energy release in great earthquakes, d. Geophys.Res., 82, 2981-2987.

12 Keylis-Borok, V. I. (1959), On estimation of the displace-ment in an earthquake source and of source dimensions, Ann. Geofisic. 12, 205-214.
13 Majer, E. L., and J. E. Peterson (2007), The impact of injection on seismicity at The Geysers, California Geothermal Field, *Int J Rock Mech Min*, *44*(8), 1079-1090.
14 Majer, E. L., R. Baria, M. Stark, S. Oates, J. Bommer, B. Smith, and H. Asanuma (2007), Induced seismicity associated with enhanced geothermal systems, Geothermics, 36(3), 185-222.
15 Purcaru, G., and H. Berckemer (1978), A magnitude scale for very large earthquakes.tectonophys.49:189-198.
16 Scholz, C. H. (1986), The frequency-magnitude relation of microfracturing in rock and its relation to earthquakes. Bull, Seism. Soc. Am. 58, 399-415.
17 Segall, P. (1989), Earthquakes triggered by fluid extraction. Geology 17, 942–946.
18 Shapiro, S. A., and C. Dinske (2009a), Fluid-induced seismicity: Pressure diffusion and hydraulic fracturing, Geophys. Prospect., 57, 301– 310.
19 Shapiro, S. A., and C. Dinske (2009b), Scaling of seismicity induced by nonlinear fluid-rock interaction, Journal of Geophysical Research, Vol. 114, B09307, doi:10.1029/2008JB006145.
20 Taron, J., and D. Elsworth (2009), Thermal-hydrologic-mechanical-chemical processes in the evolution of engineered geothermal reservoirs. Int J Rock Mech Min Sci, doi:10.1016/j.ijrmms.2009.01.007.
21 Taron, J., D. Elsworth, and K. B. Min (2009), Numerical simulation of thermal-hydrologic-mechanical-chemical processes in deformable, fractured porous media, International Journal of Rock Mechanics and Mining Sciences, *46*(5), 842-854.
22 Walsh, J. B. (1965), Effect of cracks on uniaxial elastic compression of rocks. J Geophys Res :399-411.
23 Yerkes, R. F., and R. O. Castle (1976), Seismicity and faulting attributable to fluid extraction. Eng. Geol. 10, 151-167.

2 CHAPTER 2: RESERVOIR STIMULATION AND INDUCED SEISMICITY: ROLES OF FLUID PRESSURE AND THERMAL TRANSIENTS ON REACTIVATED FRACTURED NETWORKS

Abstract

We utilize a continuum model of reservoir behavior subject to coupled THMC (thermal, hydraulic, mechanical and chemical) processes to explore the evolution of stimulation-induced seismicity and related permeability in EGS reservoirs. Our continuum model is capable of accommodating changes in effective stresses that result due to the evolving spatial variations in fluid pressure as well as thermal stress and chemical effects. Discrete penny-shaped fractures (~10-1200m) are seeded within the reservoir volume at both prescribed (large faults) and random (small fractures) orientations and with a Gaussian distribution of lengths and location. Failure is calculated from a continuum model using a Coulomb criterion for friction. Energy release magnitude is utilized to obtain the magnitude-moment relation for induced seismicity by location and with time. This model is applied to a single injector (stimulation) to the proposed Newberry EGS field (USA). Reservoir stimulation is assumed to be completed in four zones at depths of 2000, 2500, 2750 and 3000 m.. The same network of large fractures (density of 0.003 m^{-1} and spacing 300 m) is applied in all zones and supplemented by more closely spaced fractures with densities from 0.26 m^{-1} (deepest zone) through 0.5 m^{-1} (shallow zone) to 0.9 m^{-1} (intermediate depth zone). We show that permeability enhancement is modulated by hydraulic, thermal, and chemical (THMC) processes and that permeability increases by an order of magnitude during stimulation at each depth. For the low density fracture networks, the increase in permeability reaches a smaller radius from the injection point and permeability evolution is slower with time compared to the behavior of the higher density fracture network. For seismic events that develop with the stimulation, event magnitude (M_S) varies from -2 to +1.9 and the largest event size (~1.9) corresponds to the largest fractures (~1200m) within the reservoir. We illustrate that the model with the highest fracture density generates both the most and the largest seismic events (M_S=1.9) within the 21 day stimulation. Rate of hydraulic and thermal transport has a considerable influence on the frequency, location and time of failure and ultimately event rate. Thus the event rate is highest when the fracture network has the largest density ($0.9m^{-1}$) and is located at depth where the initial stresses are also highest. Also apparent from these data is that the closely spaced fracture network with the higher stress regime (at the deeper level) has the largest *b*-value ~0.74.

2.1 Introduction

Stimulation of natural fractures provides a method to increase production in conventional geothermal wells and low permeability regions of otherwise productive geothermal systems. Effective stimulation is

provided by circulating fluid through fractures and produces a permeable reservoir volume to extract heat energy from the rock mass. Injection induced pore pressure as well as thermal stresses may enhance the fracture networks and create conductive pathways [*Elsworth*, 1989a; *Murphy*, 1982; *Nemat-Nasser*, 1982; *Pine and Cundall*, 1985; *Purcaru and Berckemer*, 1978]. For stimulation at stresses below the minimum principal stress, induced seismicity results by hydro-shearing of fracture zones through the reservoir for a variety of stress, temperature and geochemical regimes [*Baisch et al.*; *Bruce et al.*, 2009; *Shapiro and Dinske*, 2009a; *Shapiro and Dinske*, 2009b].

Early practice in this area has shown that the interaction of fluid pressures on fracture networks within a geothermal reservoir is one of the key technical challenges in reservoir stimulation [*Renshaw*, 1995; *Shapiro et al.*, 1998 ; *Zoback and Harjes*, 1997]. Seismic activity is a function of the fluid conductivity of the fracture distribution and the injection rate [*Rutqvist et al.*, 2001; *Shapiro and Dinske*, 2007]. For a given distribution of conductive fractures a limit for event magnitude can be determined as a function of flow rate and reservoir volume [*Dinske et al.*, 2010; *Evans et al.*, 2005; *Shapiro et al.*, 1998]. Models are typically classified by their conceptualization of the fractured reservoir geometry as either networks of discrete fractures or as equivalent porous media. In the following we use a continuum model of reservoir evolution subject to coupled THMC processes to explore the evolution of stimulation-induced seismicity and evolution of permeability in a prototypical EGS reservoir. We use the resulting fluid pressure and thermal stresses on rate, location and magnitude of seismic events in the short term.

In particular we define the relationship between the magnitudes of these induced seismic events and the applied fluid injection rates as well as the evolution of thermal stress. During stimulation of the single injection or production well we observe the enhancement of fracture permeability as a result of circulating fluid through these fracture networks under geothermal conditions. Together, hydraulic and thermal effects contribute to the reactivation of the natural fracture network and this may enhance the permeability. Both these effects may reactivate natural fractures and induce seismicity during stimulation. Our focus is to determine dominant behaviors controlling the enhancement of permeability and the triggering of induced seismicity that is unique in comparison to previous studies.

We then explore how pore-pressure and thermal stress can be linked to the seismic frequency–magnitude distribution, which is described by its slope, the *b-value*. We evaluate this response for the proposed stimulation of the Newberry EGS site and illustrate the modeled event-size distribution and evolution of related event-sizes due to fluid and thermal effects during a short-term (~21 day) proposed stimulation. We show that permeability enhancement is modulated by hydraulic, thermal, and chemical (THMC) [*Taron and Elsworth*, 2009a] processes which also migrate through the reservoir on different length-

scales and timescales [*Elsworth and Yasuhara*, 2010; *Taron and Elsworth*, 2009b] and may also trigger seismicity.

2.2 Model description

Our objective is to determine the effect of hydraulic- and thermal-mechanical stimulation in the evolution of induced seismicity and of permeability during short term reservoir stimulation. Fracture networks provide a path for fluid transmission in a prototypical EGS reservoir. As fluid is circulated, changes in total stress result due to the penetration of fluid, the accompanying migration of fluid pressures, and as a result of thermal and chemical strains. These changes in the stress regime may drive portions of the reservoir towards failure with this failure accompanied by a seismic release of energy.

The THMC simulator [*Taron et al.*, 2009], links FLAC^{3D} and TOUGHREACT by a separate code, referred to as the "interpolation module", capable of parsing data outputs from each primary simulator as input to the companion. In addition to data interpolation, the module executes constitutive relationships including permeability evolution response to stress, and thermodynamically controlled fluid compressibility. All flow and transport equations are derived from the principles of mass (or energy) conservation. The models for fluid have been discussed in detail by Pruess (1987 and 1991) and Pruess et al. (1999). FLAC^{3D} is used for mechanical deformation, where undrained fluid allows calculation of the short-time build-up in fluid pressures that results from an instantaneous change in stress. The complex thermodynamics of phase equilibria of multiphase water mixtures can be tracked in the pre-existing framework of TOUGHREACT. The modeling structure calculates permeability change from the combined action of, thermo-mechanical, hydro-mechanical deformation, with each depending on temperature, effective stress, and chemical potential.

Chemical reactions are assumed to represent the geochemical systems. Component or primary species are defined and mass action equation is used for the rate of dessolution and participation of components. Kinetic rates are calculated within TOUGHREACT based on activation energy, rate constants at 25°C, gas constant and absolute temperature.

We apply a coupled THMC model [*Taron et al.*, 2009] with static-dynamic frictional strength-drop to determine energy release for fractures of small (10m) to large (1200m) diameter embedded within an elastic medium. The change of stress state is calculated from the pore pressures, thermal drawdown and chemical effects within FLAC^{3D}-TOUGHREACT [*Taron and Elsworth*, 2009a]. The model incorporates the effects of fractured reservoirs involving fracture networks of variable densities and connectivities and for various reservoir conditions of initial stress, temperature, and permeability – as these may exert significant influence on the evolution of permeability and seismicity.

We represent brittle failure on a pre-existing fracture as a prescribed stress drop (~3 MPa). For a prescribed frictional strength the model calculates the shear resistance from the change of normal stress and pore pressure. Stress builds and reaches a peak strength followed by a rapid decline to a residual strength [*Goodman*, 1976; *Jaeger et al.*, 2007]. This model is used to follow the evolution of seismic rupture within the system.

This model has been previously applied to two EGS reservoir fields [*Izadi and Elsworth*, 2012] and verified against these field data. This model is now applied to the doublet geometry (700m spacing) within a larger reservoir geometry with half-symmetry (2000m×1000m×300m) (**Figure 1**) representative of the Newberry geothermal field. The Newberry demonstration EGS project is located southeast of Bend, Oregon. Data from well NWG 55-29 are used to build a reservoir model used in the subsequent simulation [*Cladouhos et al.*, 2011]. This presumed half-symmetry is only approximate but represents the essence of important behaviors that act in the reservoir.

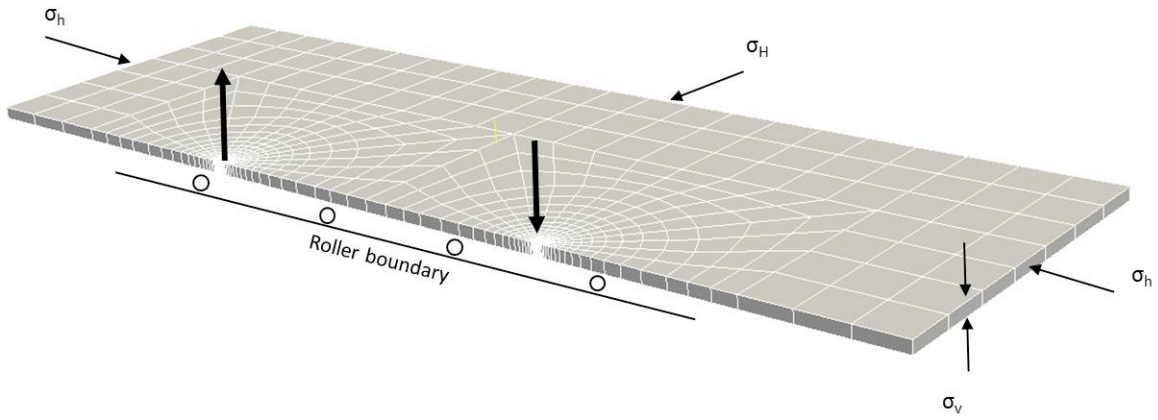

Figure 7: Geometric layout of EGS reservoir as used in the simulation. Reservoir geometry with half-symmetry (2000m×1000m×300m). The spacing between injection and production well is assumed 700m. A vertical and two horizontal stresses are indicated.

The present model applies the vertical stress as the lithostat and two horizontal principal stresses, which are designated as the maximum and minimum principal stresses. During stimulation, fluid pressure is increased within the near-wellbore rock volume with low permeability, causing shear displacement of some of the existing fractures. This model calculates the flow rate, pressure and temperature distribution during stimulation. The changes in pressure and temperature induce displacements that consequently lead to a new change in pressure distribution.

In this study the modeling is considered for the reservoir defined as four different zones (shallow to deep) and at four different depths of 2000, 2500, 2750 and 3000 m. The four zones are defined from fracture structures (as zones B, C, D, and E) and with horizontal stresses increasing with depth as identified in **Table 3**. Boundary stresses, in both horizontal and vertical directions, pore pressure and temperatures corresponding to depths of 2000, 2500, 2750 and 3000m are applied to the four different realizations of this geometry (**Table 3**) applied for this geothermal field. The characteristics and the values of the parameters utilized in simulation for the *in-situ* reservoir are defined in **Table 1**. Each of these zones requires different inputs for fracture orientations and density as defined in **Table 4**. Reactive composition of the host reservoir rock is presented in **Table 5**. Calcite and amorphous silica are expected to be the minerals primarily responsible for permeability change due to precipitation and dissolution. Other likely minerals are also followed, as listed in **Table 5**. Rate constants for precipitation/dissolution and mineral reactive surface areas of these common minerals are available in the literature [*Kovac et al.*, 2006.; *Xu and Pruess*, 2001], and were utilized as in [*Xu and Pruess*, 2004].

Table 3: Solid medium properties as used in simulations.

Parameter	**Unit**	**Newberry**
Bulk modulus of intact rock(K_m)	GPa	17
Cohesion	MPa	10
Poisson's ratio(υ)	-	0.27
Bulk modulus of fluid(k_f)	GPa	8
Bulk modulus of solid grain(K_s)	GPa	54.5
Internal friction angle(φ)	°	35
Residual friction angel(β)	°	11
Coefficient of thermal expansion(α_T)	1/°C	1.2E-5
Thermal conductivity(λ)	W/mK	2.9
Heat capacity(c_p)	J/kgK	918
Initial Permeability(k)	m^2	1.10E-17
Porosity within fractures(ϕ)	-	1.0

Table 4: Summary of zones based on parameters observed in NWG 55-29.

Zone	Depth Range [m]	Thickness [m]	Fracture Count	Fracture Density/Meter	Lithology
A	1966-2000	34	5	0.06	Primary: welded lithic tuff Secondary: other tuff
B	2000-2440	440	173	0.4	Primary: tuffs Secondary: basalt, andesite
C	2440-2633	193	157	0.8	Primary: basalt, basaltic andesite
D	2633-2908	275	16	0.06	Primary: microcrystalline granodiorite Secondary: basalt, one large
E	2908-3066	158	No Data	No Data	Primary: basalt

Table 5: Parameters utilized in the simulation.

Parameters	Unit	Depth[m]			
		2000	2500	2750	3000
		Zone B	Zone C	Zone D	Zone E
S_{hmin}	MPa	36	45	50	54
SH_{max}	MPa	48	58	64	70
S_v	MPa	48	60	66	72
$P_{injection}$	MPa	29	33	35	37
$P_{reservoir}$	MPa	24	28	30	32
$P_{production}$	MPa	19	23	25	27
Peak Strength	MPa	25	30	35	38
T_{rock}	°c	230	280	290	310
$T_{injection}$	°c	20	20	20	20

Table 6: Fracture data that utilized in the simulation.

Fracture Characterization	**Unit**	**Depth[m]**			
		2000	**2500**	**2750**	**3000**
		Zone B	**Zone C**	**Zone D**	**Zone E**
Density of small Fractures	m^{-1}	0.5	0.9	0.9	0.26
Density of large Fractures	m^{-1}	0.003	0.003	0.003	0.003
Number of seeded fractures	-	1000	1800	1800	600
Initial Permeability	m^2	1.6×10^{-17}	3×10^{-17}	3×10^{-17}	10^{-17}
Fracture size	m	10-1200	10-1200	10-1200	10-1200
Fracture Azimuth	°	0-360	0-360	0-360	0-360
Fracture spacing	m	1-300	1-300	1-300	1-300
Standard deviation($\bar{\sigma}$)	-	19	19	19	19
Mean($\bar{\mu}$)	-	360	360	360	360

Table 5: Initial volume fraction of reactive minerals in host reservoir.

Mineral	**Volume fraction of solid rock**	
	Granodiorite	**Fractured vein**
Anorthite	0.33	--
Calcite	0.02	0.31
Chlorite	--	0.23
K-Feldspar	0.17	--
Quartz	0.34	0.17
Amorphous Silica	--	--

2.2.1 Model dimensions and zones

The reservoir volume that is utilized in all models is the same for zones B, C, D and E (**Figure 1**). For the Newberry EGS reservoir model the open hole is divided into five zones (A, B, C, D and E) from BHTV (Borehole televiewr) fracture density and lithology. Based on observation from the BHTV data, four zones (B, C, D and E) may be the best targets for stimulation. The characteristics of these zones are summarized in **Table 2**.

The moderate fracture density in zone B allows for significantly more stimulated volume in zone B than zone A (shallowest zone). A wide range of fracture orientations and high fracture density make zone C and zone D the most favorable zones for stimulation (intermediate zones). The BHTV did not reach the depth of zone E, however, zone E has a lower fracture density when compared to zones B, C and D. Thus, in this study we choose zone B as the shallowest zone, zones C and D as an intermediate zone and zone E as the deepest zone. Boundary stresses that are utilized in the simulation for these four depths are defined in **Table 3**. The other difference between these zones is related to the fracture density and orientation. In the following section we explain how the fracture spacing, density and orientation for the shallow to deep reservoir are defined.

In our experiments a load is applied at the top of the longer forcing block, producing shear relative to the static side block (Figs. 1 and 2). Pore fluid is supplied along a line source at the top and base of the static load platen (Fig. 2), allowing either uniform or differential fluid pressures to be applied along the shear surface. This fluid input is controlled by upstream and downstream reservoirs (Fig. 1). The jacketing system has been configured to guarantee a seal on the sample during the large relative displacements sustained during these shear experiments. It comprises two layers of latex tubing (diameter: 7 cm and length: 15 cm) surrounding the sample, sealed by two rubber o-rings constricted by two aluminum collars (54.5×70 mm and 54.5×90 mm). Between the latex layer and the surfaces of the sample another rubber layer, which is 3-mm thick, is used to protect the jackets from puncturing when a confining pressure is applied (Fig. 2).

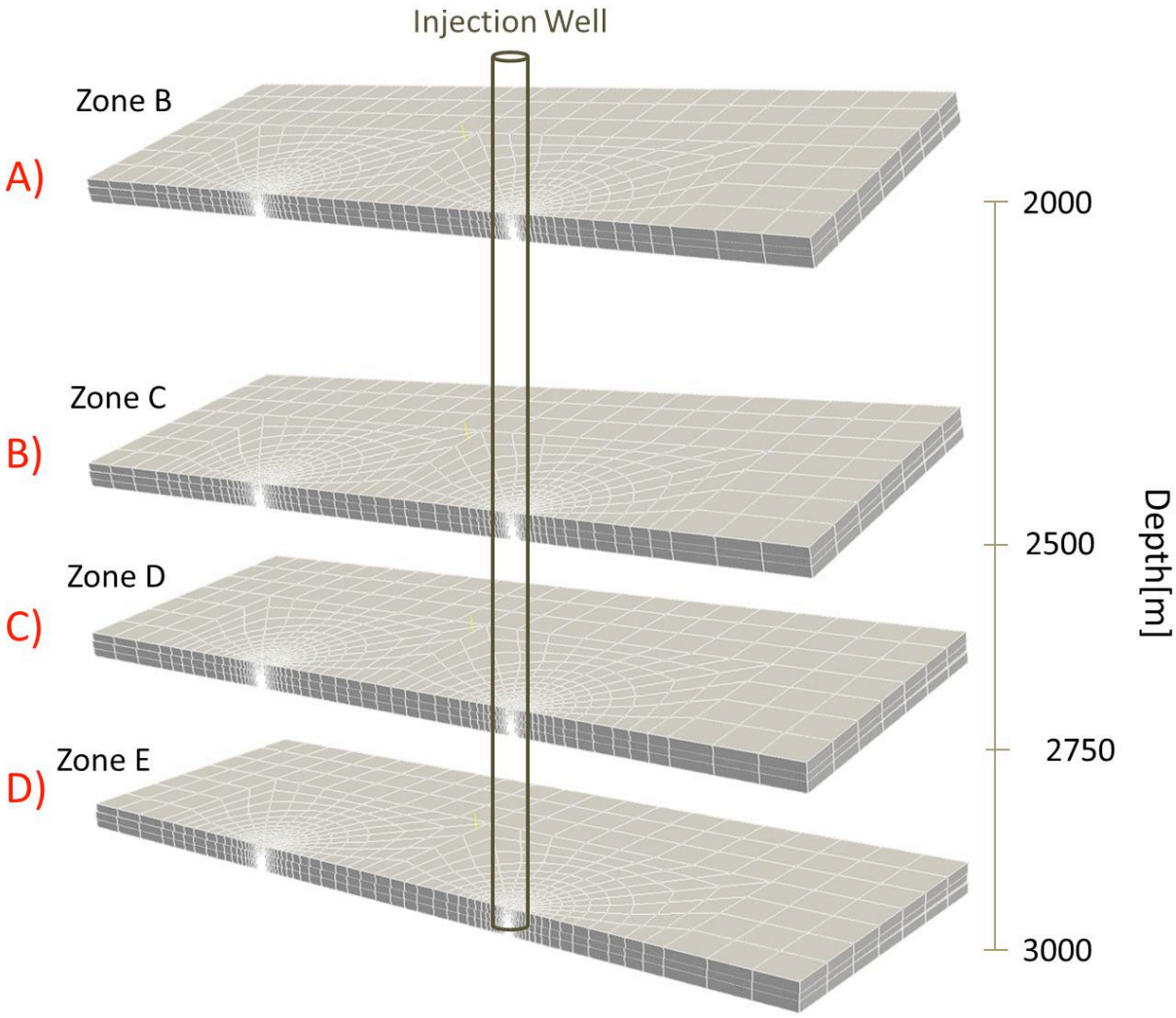

Figure 8: Geometric layout of EGS reservoir for Newberry defined as four different zones (shallow to deep) and at four different depths of 2000, 2500, 2750 and 3000 m. A) Reservoir is located at shallow zone B (2000m depth). B) Reservoir is located at intermediate zone C (2500m depth). C) Reservoir is located at intermediate zone D (2750m depth). D) Reservoir is located at deepest zone E (3000m depth).

2.2.2 Fracture networks model

Our numerical experiments are conducted for different zones (B, C, D and E). We use BHTV data to determine the frequency and orientation of natural fractures that are representative of the reservoir. These are then used to build the fracture network models used in the analysis. Fracture permeability changes can be approximated by change in the hydraulic aperture. The hydraulic aperture is calculated from the

fracture spacing and initial permeability by a cubic law relation. The flow regime is evaluated from:

$$Q = \frac{A}{\mu} k \frac{dp}{dx} = \frac{dp}{dx} \frac{A}{\mu} \left(\frac{b_0^3}{12 s_1} + \frac{b_0^3}{12 s_2} + \ldots + \frac{b_0^3}{12 s_n} \right) \frac{dp}{dx}$$

where Q is fluid flow, k is permeability, A is cross-sectional area to flow and the dp/dx is pressure drop along fractures and μ is viscosity. b_0 is an initial hydraulic aperture and b_0 is calculated from: $b_0 = \sqrt[3]{12 k_0 s}$, where k_0 is initial permeability and s is spacing between fractures.

This shows when the fracture spacing is larger the hydraulic aperture is larger. Shear dilation during hydraulic and thermal process change the hydraulic aperture and ultimately enhance the permeability.

The reservoir is assumed filled with various fracture sizes: Fracture lengths are in the range 10-1200m and are also distributed with a Gaussian distribution [Bryc, 1995]. This is defined as

$$f(\bar{x}, \bar{\mu}, \bar{\sigma}) = \frac{1}{\bar{\sigma}\sqrt{2\pi}} e^{-\frac{1}{2}\left(\frac{\bar{x}-\bar{\mu}}{\bar{\sigma}}\right)^2} \qquad (1)$$

where *e* is Euler's number, $\bar{x}$ is a normal random variable, $\bar{\sigma}$ is the standard deviation and $\bar{\mu}$ is the mean. Small fractures (10-200m) are distributed randomly within the volume both vertically and horizontally and with multiple azimuthal orientations (π to 2π). Large fractures (200-1200m) are rotated relative to the orientations of the principal stresses. For all fractures, failure is calculated from the evolution of shear and normal stresses recovered from the finite difference model FLAC^{3D}.

We distinguish a set of long and widely spaced fractures with infilling from a set of short and closely spaced fractures. Our best estimate for the network is given in **Figure 3**. The shallow (B), intermediate (C and D) and deepest (E) zones have different densities of the closely spaced fractures (more closely spaced in the deeper zones C and D) but the same network of large fractures (density of 0.003 m^{-1} and spacing 300 m) (**Figure 3**) is present. The more closely spaced fractures have densities of 0.5 m^{-1} in the shallow zone B, 0.9 m^{-1} in the intermediate zones C and D and 0.26 m^{-1} in the deepest zone E (**Figure 3**). The fracture structure is defined based on orientation, size and number of fractures to determine the induced seismicity during stimulation.

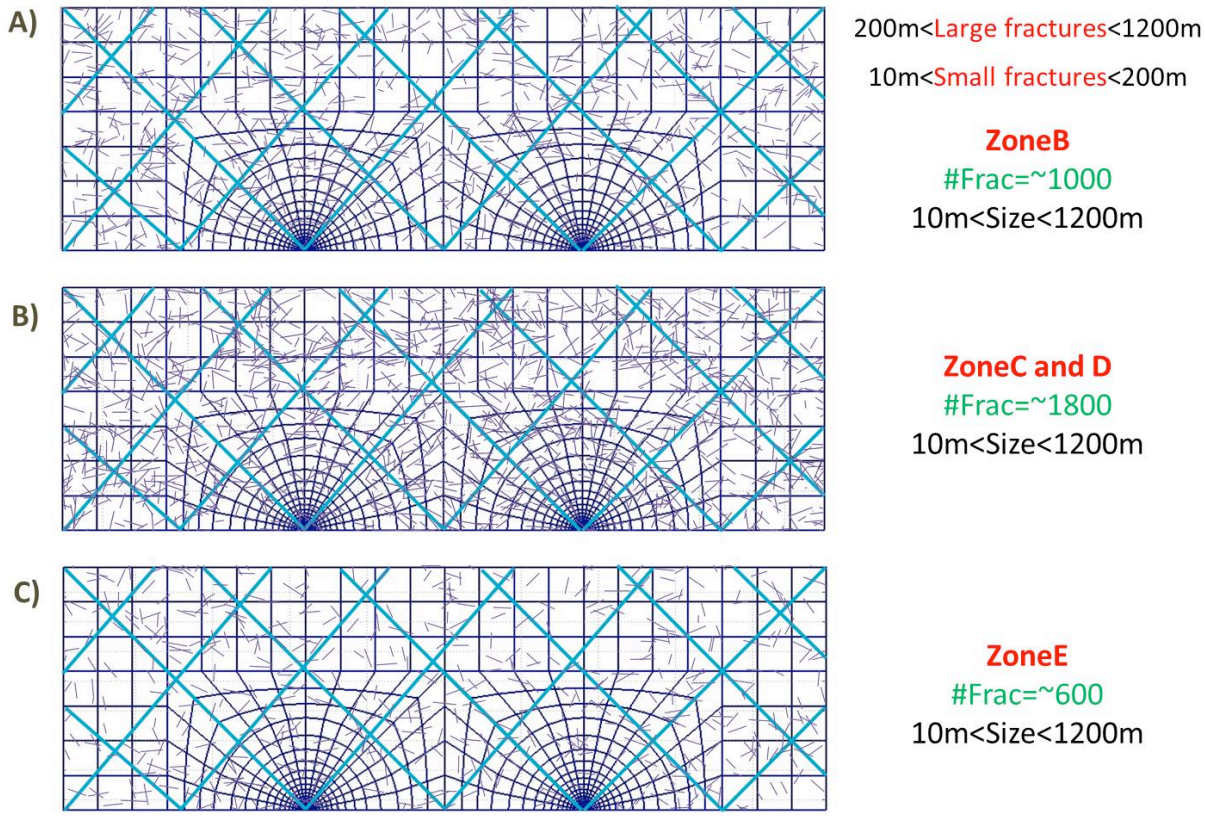

Figure 9: Fracture network structure for the Newberry EGS reservoir, fracture size varies between 10m to 1200m. The same network of large fractures (density of 0.003 m-1 and spacing 300 m) defined for zone B, C, D and E. A). The more closely spaced fractures have densities of 0.5 m^{-1} in the shallow zone B. B) Fracture density of 0.9 m^{-1} applied in the intermediate zones C and D. C) fracture density of 0.26 m^{-1} applied in the deepest zone E.

2.3 Stress drop distribution during reservoir stimulation

We represent a model for evolution of strength and brittle failure on a pre-existing fracture as a stress drop. Shear failure calculations are handled with FLAC^{3D} utilizing a Mohr-Coulomb failure (fracture propagation is not considered). The friction angle on fractures is assumed constant (35^{o}) and during failure the maximum shear stress drop (~3.0 MPa) is prescribed to represent the residual strength.

Stress drops resulting from the anticipated fracture networks are shown in **Figure 4** (mean spacing 300m). **Figure 10-B, C** shows the denser networks (zones C and D), **Figure 4-A** illustrates the shallowest zone (B) and **Figure 4-D** illustrates the deepest zone (E) with the lowest fracture density. In all simulations we considered a single injector and observe that the stress drop along the large fractures is capped at the

prescribed stress drop, τ. However for all the models with various fracture densities the mean stress drop is limited to be smaller than the maximum prescribed stress drop.

We observe during the short term stimulation that the development of stress drop begins earlier, reaches further from injection in a given time (~21 days) and is completed fastest for zones C and D with the largest fracture density ($0.9m^{-1}$). This results because the more closely spaced fractures allow the more rapid removal of heat from the matrix blocks and the thermal migration occurs more rapidly and progresses more quickly. This allows failure to occur with smaller stress drops, rather than for the sharper thermal front migrating in the system with larger fracture spacing.

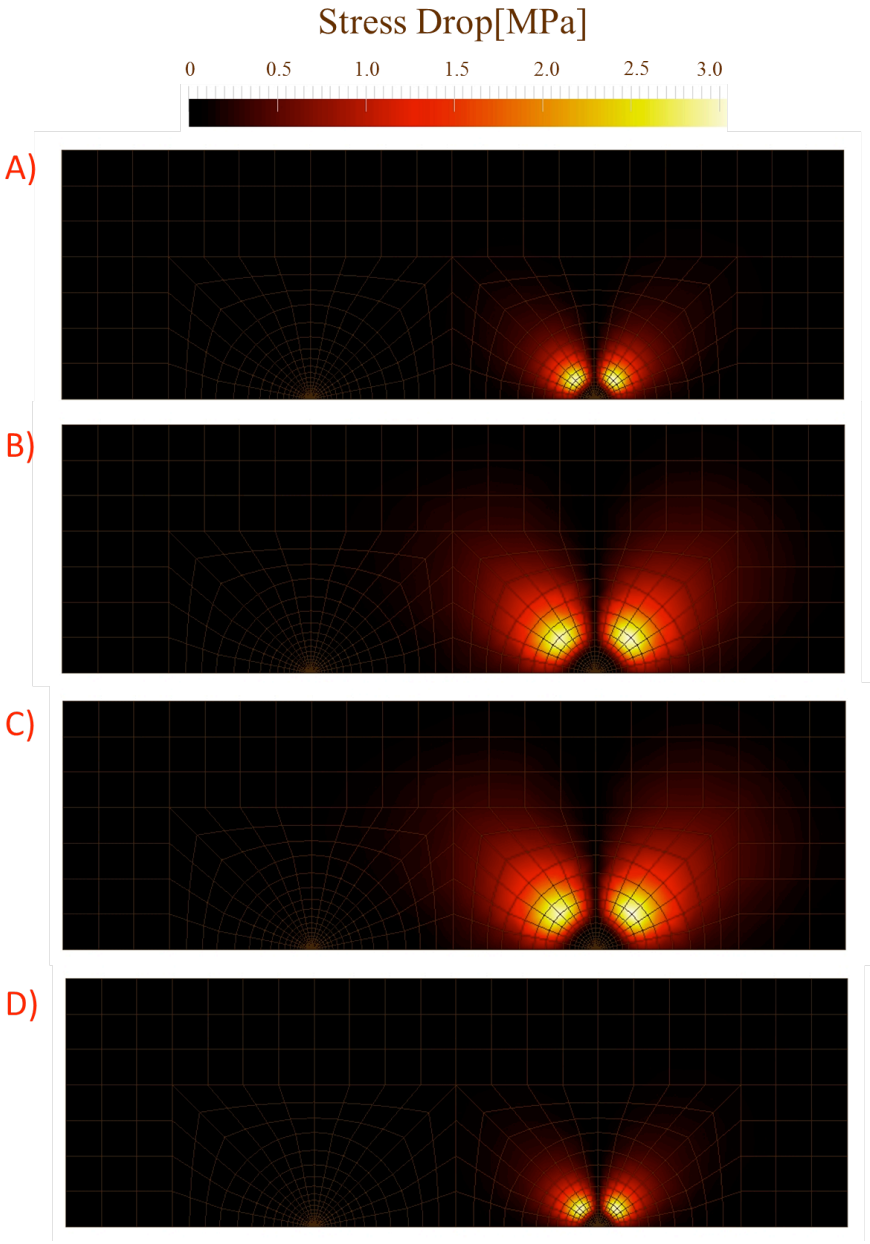

Figure 10: Development of stress drop at four different zones (shallow to deep) and at four different depths of 2000, 2500, 2750 and 3000 m after 21 day stimulation. The same network of large fractures (density of 0.003 m^{-1} and spacing 300 m) applied in each zone. A) The more closely spaced fractures have densities of 0.5 m^{-1} in the shallow zone B. B) Intermediate zone C with 0.9 m^{-1} fracture density. C) Intermediate zone D with 0.9 m^{-1} fracture density. D) Deepest zone E with 0.26m^{-1} fracture density.

This larger reactivated domain within the reservoir may trigger seismicity and enhance the permeability during stimulation. We conclude that a significant factor in predicting the evolution of seismic events and permeability with time and location is related to the location, time and magnitude of such a stress drop.

2.4 Permeability evolution during short term stimulation

It is of interest to evaluate the evolution of hydraulic, thermal and mechanical effects and to deconvolve the dominant mechanisms with time and location. The THMC model is capable of linking the alteration of fluid transport and thermal transfer subject to the injection of a cold fluid. The hydraulic presurization may have a near immediate effect and thermal transfer rate is then much slower than the hydraulic effect. Permeability evolution is related to the change of such hydraulic, thermal and mechanical effects in EGS reservoirs.

Figure 5 is a comparison of how average radial matrix permeability changes at different depths (shallow to deep) and for different fracture structures (low to high density) by the end of stimulation. The contours of permeability (**Figure 5-A, C)** at each depth define the spatial distribution of reservoir permeability enhancement due to the contribution of the thermo-hydraulic mechanism. The permeability enhancement is concentrated along the direction of the large fractures that intersect the well and grows with time. Mechanical shearing on these major fractures (dilation angle is 10°) occurs due to the change in effective stress driven by fluid and thermal effects and their influence on reservoir shear failure. Since the fluid pressure distribution is anticipated to reach a steady state rapidly upon application, the migration with time represents a significant thermoelastic effect.

It is clear that for the widely spaced fracture network (shallow zone B and deepest zone E) **(Figure 5-A and D)**, the increase in permeability reaches a smaller radius from the injection point and permeability evolution is slower with time compared to the behavior of the closely spaced fracture network **(Figure 5-B and C)**. **Figure 5-E** shows reservoir permeability change at a cross section from the injection well after 21 days of stimulation in the shallow and deep zones. **Figure 5-E** shows clearly how this penetration corresponds to the population of small fractures around the injection well with permeability increased by one order of magnitude even after this short-term stimulation.

This behavior occurs because for the closely spaced fractures (zones C and D), transport of fluid pressure and thermal drawdown in individual blocks is much faster than for the network of widely spaced fractures (zones B and E). As a result the fluid propagates faster with distance for the closely spaced fractures as observed for zones C and D in a given time. Thus the permeability enhancement for the closely spaced network (zones C and D) is both larger and reaches further from the injection well when compared to the wider-spaced network (zones B and E). Permeability improvement in all zones is not radially symmetric as it is related to the shear-induced permeability along the population of large fractures that intersect the injection borehole.

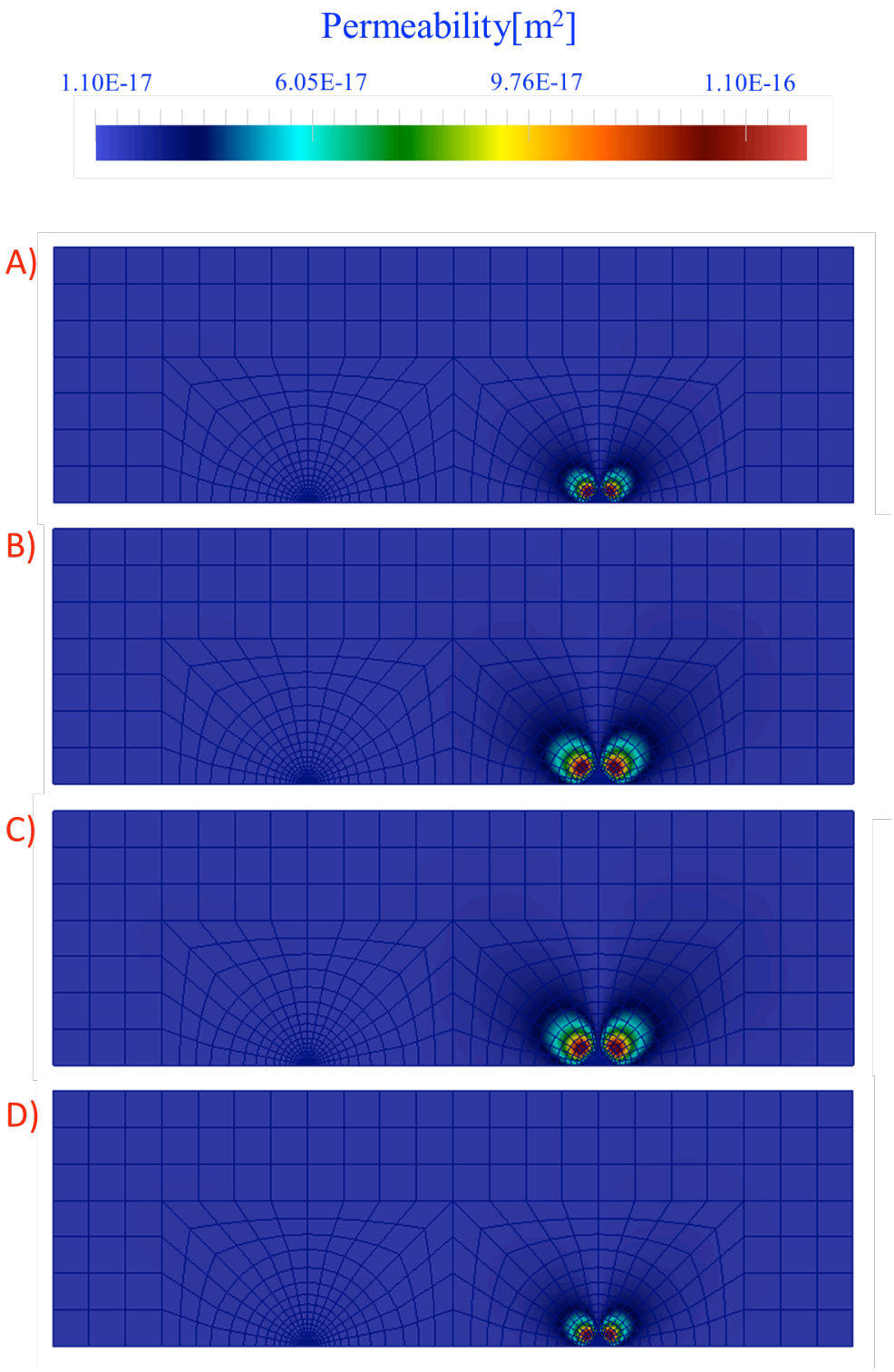
Permeability[m²]
1.10E-17
6.05E-17
9.76E-17
1.10E-16
A)
B)
C)
D)

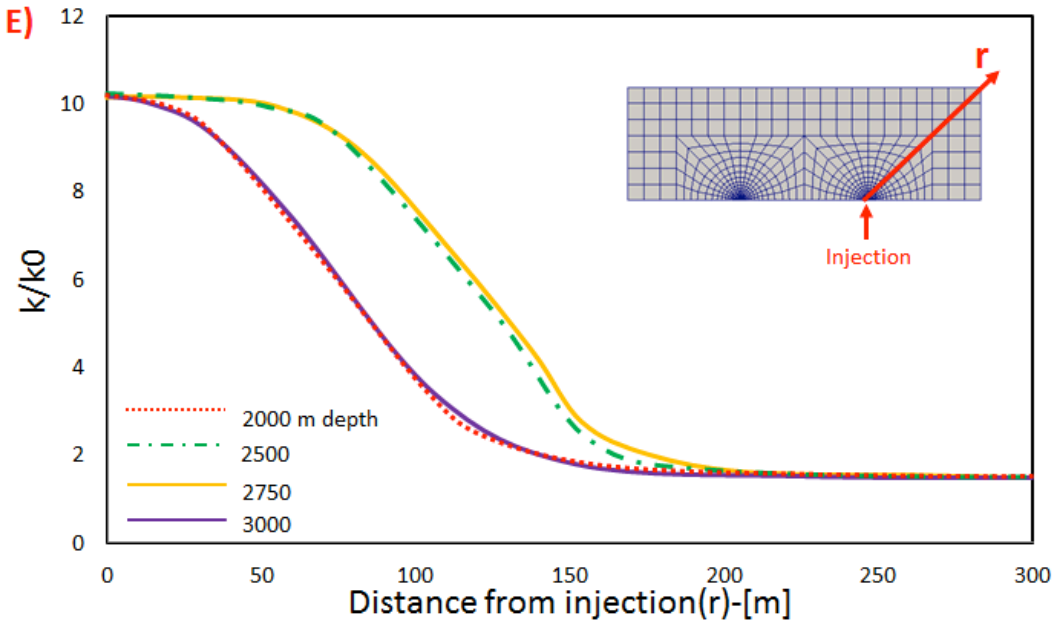

Figure 11: Evolution of permeability in four different zones (shallow to deep) and at four different depths of 2000, 2500, 2750 and 3000 m after 21 day stimulation. The same network of large fractures (density of 0.003 m^{-1} and spacing 300 m) applied at each zone. A) The more closely spaced fractures have densities of 0.5 m^{-1} in the shallow zone B. B) Intermediate zone C with 0.9 m^{-1} fracture density. C) Intermediate zone D with 0.9 m^{-1} fracture density. D) Deepest zone E with 0.26m^{-1} fracture density. E) Permeability change along the radius(r) where long fracture is located in the shallow and deep zones.

We show the evolution of reservoir permeability with time for the widely-spaced (zone B) and closely-spaced fracture (zone D) networks in **Figure 6**, to compare the rate of permeability enhancement for shallow and deep zones with low (0.5m^{-1}) and high (0.9m^{-1}) fracture densities. **Figure 6-A** shows the response of the shallow reservoir (zone B) with a fracture density of 0.5 m^{-1} and compares this with the response of the deeper reservoir (zone D) with a higher fracture density (0.9 m^{-1}) (**Figure 6-C).** We observe that by increasing the fracture density from 0.5 to 0.9 m^{-1}, the evolution of permeability occurs approximately twice as rapidly as for the 0.5m^{-1} density fracture network (**Figure 6-C)** and reaches further into the reservoir at any given time. **Figure 6-B** and **D** shows how this barrier corresponds to the fracture spacing around the injection well. We observe that the widely spaced fracture network at shallow zone B experiences less enhancement with radius at any given time (21 days stimulation) compared to the closely spaced fracture network in the deeper zone D. This relates to the faster thermal drawdown reaching to a larger radial distance from the injection point due to development of a larger connective path at intermediate depth (zone C and D).

Such changes in permeability may stimulate the fracture networks especially near the injection point and produce large and early seismic events. The following section explains the relation between permeability evolution and induced seismicity to examine how permeability enhancement during short-term stimulation influences the magnitude of seismic events for different characteristics of the fracture networks and stress regimes at different locations within the reservoir.

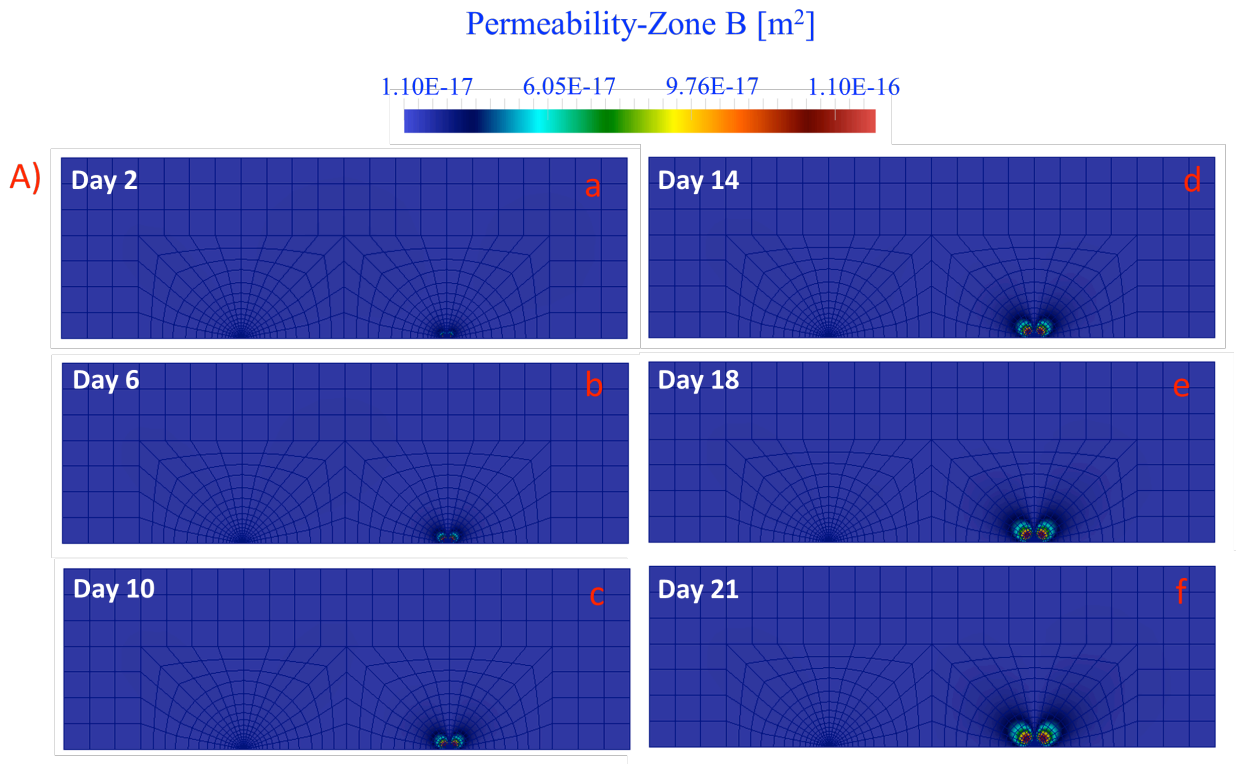

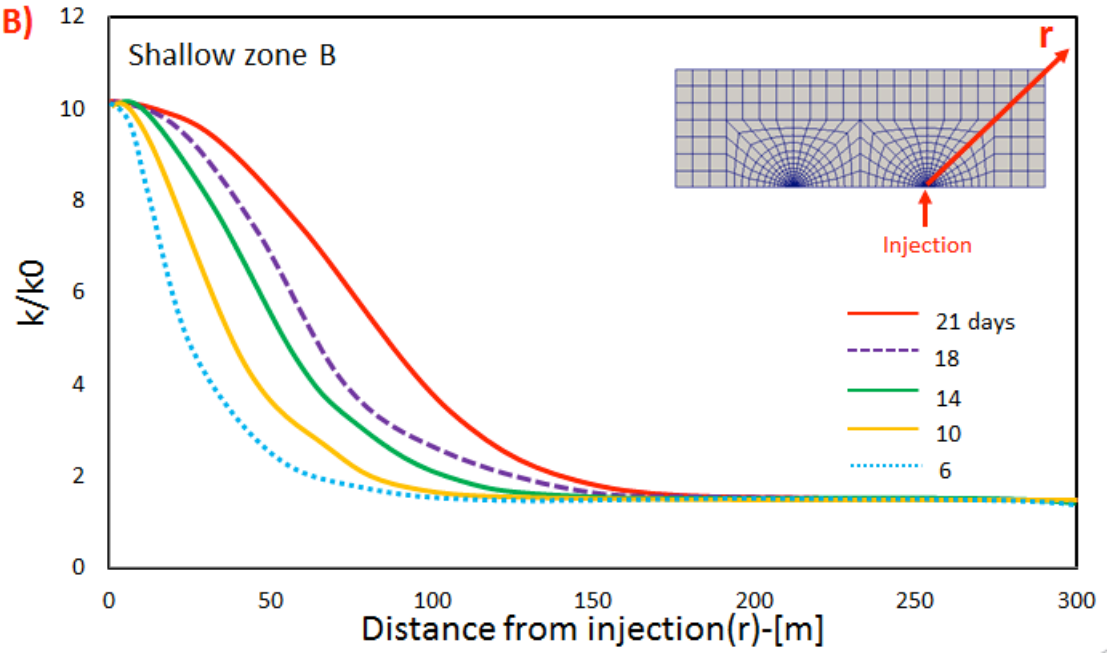
B)
Shallow zone B
r
Injection
21 days
18
14
10
6
k/k0
Distance from injection(r)-[m]
0
2
4
6
8
10
12
0
50
100
150
200
250
300

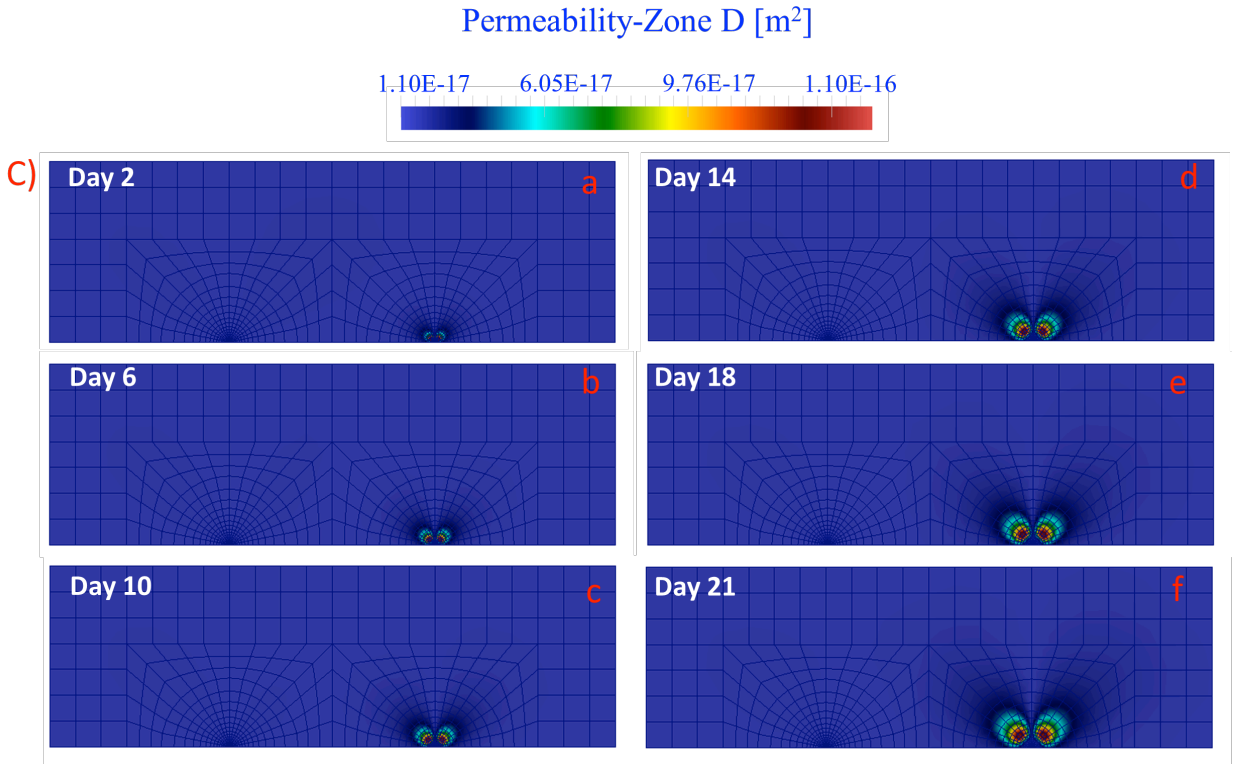
Permeability-Zone D [m²]
1.10E-17
6.05E-17
9.76E-17
1.10E-16
C)
Day 2
a
Day 14
d
Day 6
b
Day 18
e
Day 10
c
Day 21
f

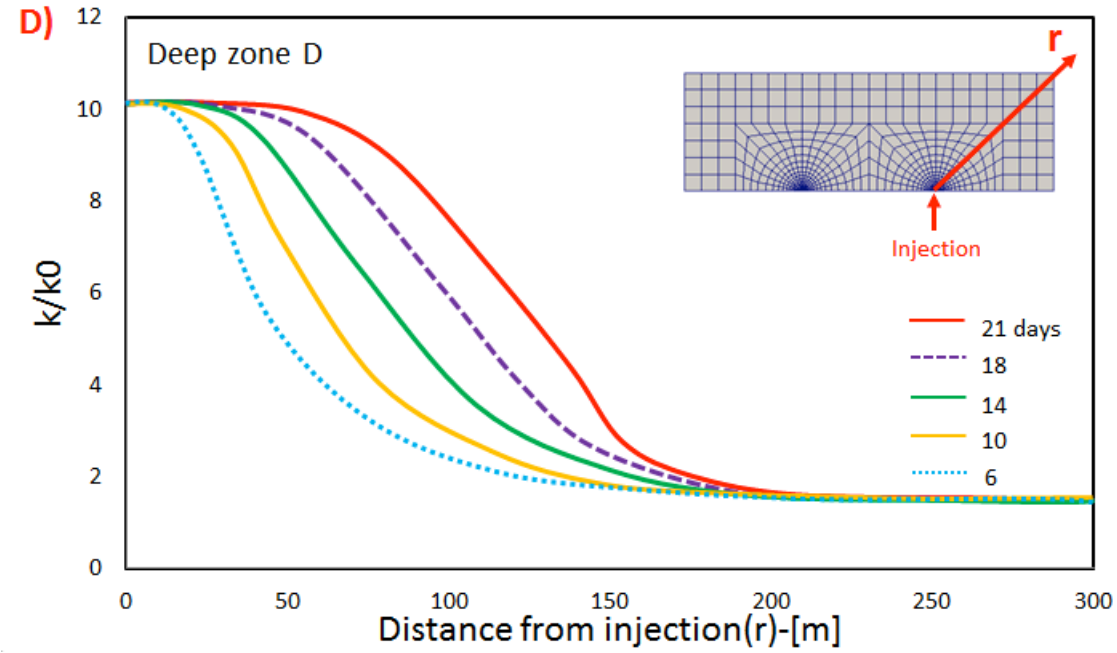

Figure 12: Evolution of permeability during short stimulation (21 days) for shallow zone B at 2000m depth and intermediate zone D at 2750m depth. Windows a, b, c, d, e and f show the permeability enhancement with time. The same network of large fractures (density of 0.003 m^{-1} and spacing 300 m) applied at both zones. A) The more closely spaced fractures have densities of 0.5 m^{-1} in the shallow zone B. B) Permeability change along the radius(r) where long fracture is located after 21 days stimulation at shallow zone B. C) Intermediate zone D with 0.9 m^{-1} fracture density. D) Permeability change along the radius(r) where large fracture is located at deep zone D. Figure A and B) Shallow zone B and fracture geometry of Figure 9-A, a, b, c, d, e, f shows the permeability enhancement with time. Figure C and D) Deep zone D and fracture geometry of Figure 9-B, a, b, c, d, e, f shows the permeability enhancement with time.

2.5 Evolution of moment magnitude during stimulation

The potential energy released within reservoirs for closely and widely spaced fracture networks is defined based on the evaluation of the elastic energy released from repeating failures of large penny-shaped fractures. The potential release of energy for different fracture networks is calculated by the summation of elastic energy released on individual penny-shaped fractures absent mechanical interaction. The potential energy release, E_p, is defined as

$$E_p = \frac{2\Delta\tau^2 a^3}{3G} \qquad (2)$$

where $\Delta\tau$ is the shear stress drop, a is the radius of the fracture in the plane of the fracture and G is shear modulus. Energy release from a pre-existing fracture increases with the square of the stress drop and the cube of the fracture size. This energy release is triggered by the evolving stress state due to pore pressures and induced thermal and chemical strains.

Energy release from fractures is most conveniently represented as a moment magnitude [*Aki*, 1967; *Kanamori*, 1977; *Keylis-Borok*, 1959]. The moment magnitude relation is defined as [*Purcaru and Berckemer*, 1978]:

$$\log M_0 = 1.5 M_s + 9.1 \qquad (3)$$

where M_0 is seismic moment and M_S is moment magnitude. In this model M_0 is the seismic energy that is derived from the elastic energy released by shear on pre-existing fractures.

We determine the spatial/temporal evolution of moment magnitude in the reservoir for the ensemble arrangement of fractures by using the above relations in **Figure 7**. For minimum (10m) and maximum (1200m) fracture radii, a maximum shear stress drop of ~3 MPa and a shear modulus of 10 GPa, the evaluated magnitude of events, M_S varies from -2 to +1.9. The largest event size (~1.9) corresponds to the largest fracture size (~1200m) within the reservoir.

During the evolution of energy release the principal difference between zones is related to the fracture density as well as the incremental stress drop that is realized and accompanies failure. The largest stress drop occurs along the large fractures and this extends furthest in comparison to that for the smaller fractures.

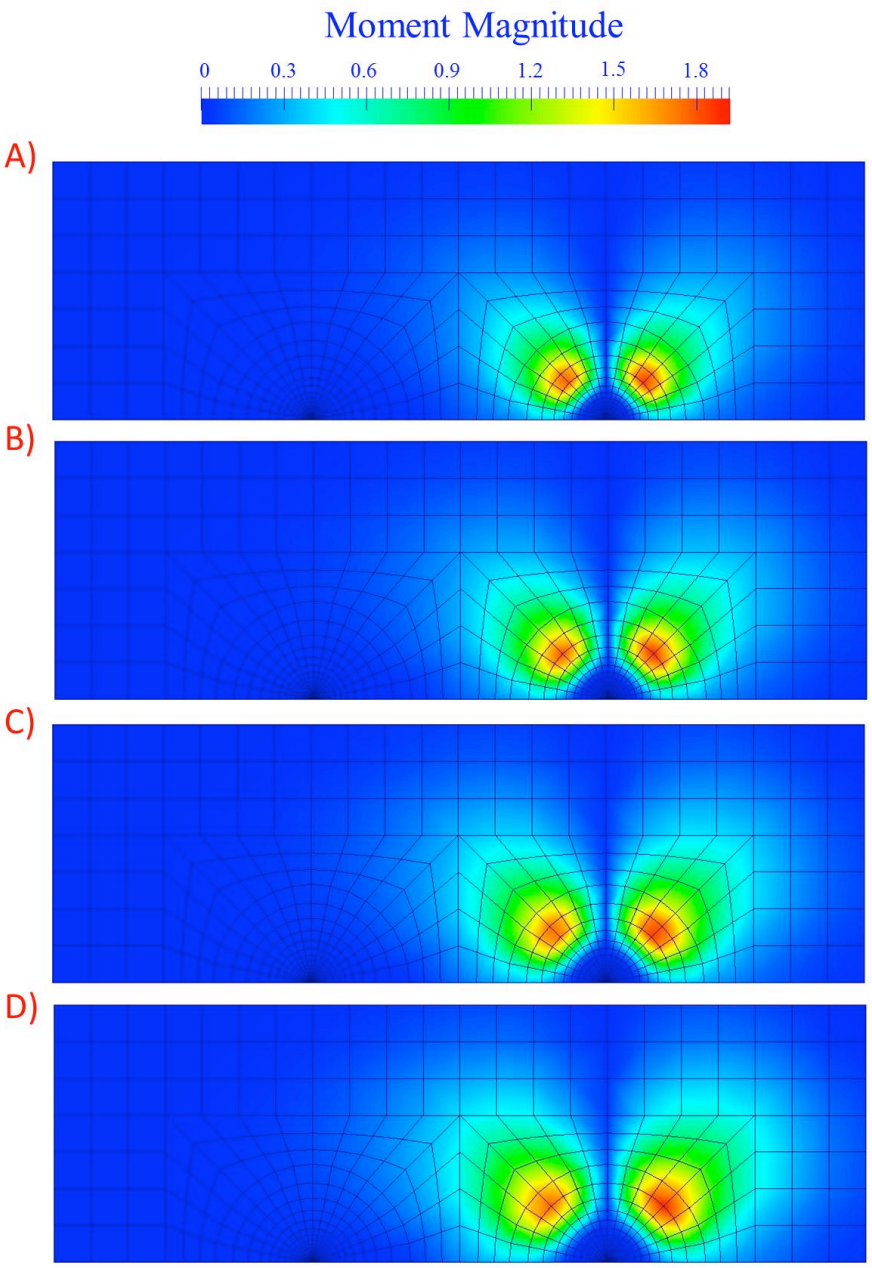

Figure 13: Evolution of moment magnitude at four different zones (shallow to deep) and at four different depths of 2000, 2500, 2750 and 3000 m after 21 day stimulation. The same network of large fractures (density of 0.003 m^{-1} and spacing 300 m) and also the same network of closely spaced fractures (densities of 0.9 m^{-1}) applied at each zone. A) Reservoir at shallow zone B. B) Intermediate zone C. C) Intermediate zone D. D) Deepest zone E.

We observe that the contours in Fig 7 are not radially distributed due to the presence of the large pervasive fractures. When we compare the potential energy released in the different zones (shallow to deep), we observe that this release begins and builds earlier, reaches further from the injection in a given time and is completed faster for intermediate zones (C and D) with the largest fracture density ($0.9m^{-1}$) compared to the zones with the smaller fracture density (B ($0.5m^{-1}$) and E ($0.26m^{-1}$)).

We then use a stress-strain fracture criterion to determine the total strain energy available for release – this energy is assumed to be shed seismically. During the rupture process the shear stress drops an amount $\Delta\tau$ from an initial value of τ_i to a final value τ_f. The total energy is

$$E_T = \int \Delta\tau^T \Delta\varepsilon dV$$

where strain changes from an initial value of ε_i to a final value ε_f where V is volume of the matrix. Here we introduce a relation to determine the number of events which occur during the failure process based on potential and total energy as

$$N_{event} = \frac{E_T}{E_p}$$

where N_{event} is the number of seismic events, E_T is the total energy and E_p is the potential energy. Simulation results are presented in a manner analogous to the conceptual models of various fracture networks (**Figure 3**) at shallow depth and intermediate fracturing (zone B with $0.5m^{-1}$ density), intermediate depth and the greatest fracturing (zones C and D with $0.9m^{-1}$ density) and the deepest zone that is least fractured (E with $0.26m^{-1}$ density).

The outcomes for induced seismicity and permeability evolution for these different cases allow comparison of the effects of various fracture spacings and stress states as a result of reservoir stimulation. For more closely spaced fractures, the migration rate of seismic events is faster, the event rate is higher and the integrated energy release is also larger than for more widely spaced fractures. That this larger cumulative energy is released in a larger number of small events is useful in limiting both event size and the related apparent influence of felt seismicity.

The characteristic event magnitude distribution that occurs in these cases is defined based on the size and location of fractures. The largest events occur close to existing large and widely spaced fractures where stress drop reaches the maximum magnitude ~3MPa. Thus the energy release from these large (~200-1200m) but widely-spaced fractures within the reservoir determines the evolution of the principal seismic event magnitude and ultimately can give significant information about the rate of propagation with time.

To determine the sensitivity of the evolution of seismic event size, rate, and position to the evolution of effective stress relative to initial stress state we examine the behavior first for the same fracture network (with $0.9m^{-1}$ density) and the stresses of zones B (2000m), C (2500m), D (2750m) and E (3000m). We then explore behavior for the stresses of zones B (2000m), C (2500m), D (2750m) and E (3000m) but for the different fracture densities of zones B ($0.5m^{-1}$), C ($0.9m^{-1}$), D ($0.9m^{-1}$) and E ($0.26m^{-1}$).

2.5.1 Influence of effective stress evolution of moment magnitude

The performance of our model - specifically following the progress of seismicity within the reservoir - is developed in terms of rates, magnitudes and locations of events and examined against observational data for two geothermal fields: Cooper Basin (Australia) and Coso geothermal field (USA) [*Izadi and Elsworth*, 2012]. We observed good agreement between our model observations and those in the Cooper Basin [Shapiro and Dinske, 2009a; Shapiro and Dinske, 2009b].

We now consider the key influence of stress state on induced seismicity when the same fracture network (high density-$0.9m^{-1}$) applies within the reservoirs but at shallow depths (2000m zone B) to greater depths (3000m zone E). This examines the stress-sensitivity of the reservoir during reservoir stimulation (~21 days). The denser fracture network (closely spaced fracture) of zones C and D provides the probability of largest seismic events during stimulation – thus we select this highest fracture density network ($0.9m^{-1}$) in this study. A representation of the fracture network geometry is shown in **Figure 3-B**. In all simulations, the only parameter that varies is the stress magnitude according to the regime (S_{hmin}=0.75 S_v).

The seismic energy released during the stimulation is illustrated in **Figure 7**. We observe a large migration of energy release as a significant population of seismic activity exists near injection and along the large fractures. Such seismic events migrate more rapidly at any given time outward from the injection point and reaching to a larger distance when the stresses on the stimulation target is largest, corresponding to the deepest zone (zone E at 3000m). But this analysis shows that by increasing the stress (reaching the deeper reservoir) the migration rate of seismic events with time and location changes little. Thus, these events may form at the same rate for shallow to deep zones when the same fracture network is applied.

2.5.2 Influence of Fracture Structure on Evolution of Moment Magnitude

We contrast the response for an invariant fracture network but with changing stress level (previous) with that for a constant initial stress but for different realizations of fracture network densities. This analysis is based on low (zone E ~$0.26m^{-1}$), intermediate (zone B ~$0.5m^{-1}$), and high (zones C and D ~$0.9m^{-1}$) fracture densities representing ranges of total numbers of 600 to 1800 fractures filling the half-reservoir. The fracture schemes that are used in simulations are displayed in **Figure 3**. For all zones we calculate the

potential energy release of fractures to determine the moment magnitude evolution during short-term stimulation (**Figure 8**).

We observe that the rate of seismic event migration within the reservoir is controlled principally by the density and spacing of the fractures. For various fracture network models (low to high density) the seismic event rate increases with increased fracture density (i.e. zones C and D with $0.9m^{-1}$) and is largely independent of stress level.

The model with the highest fracture density **Figure 8-B, C** generates both the most and the largest seismic events (M_S =1.9) within the 21 day stimulation time window. Absolute stress is largest when the stimulation target is deeper but stress drop is limited by the difference in peak and residual strength of the fractures (~3 MPa) and hence cannot be a critical parameter (**Figure 8-D)**. The reason for this behavior is related to the cumulative energy release of the fractures which scales with the size of fractures comprising the network and a roughly constant magnitude of stress drop.

We note that the rate of hydraulic and thermal transport has a considerable influence on the severity, location and timing of failure in all our models. The event rate is highest when the fracture network has the largest density ($0.9m^{-1}$) and is located at depth where the initial stresses are highest (zone D). In the next section we separately explore the influence of events driven by fluid pressure or due to thermal destressing in fractured reservoirs.

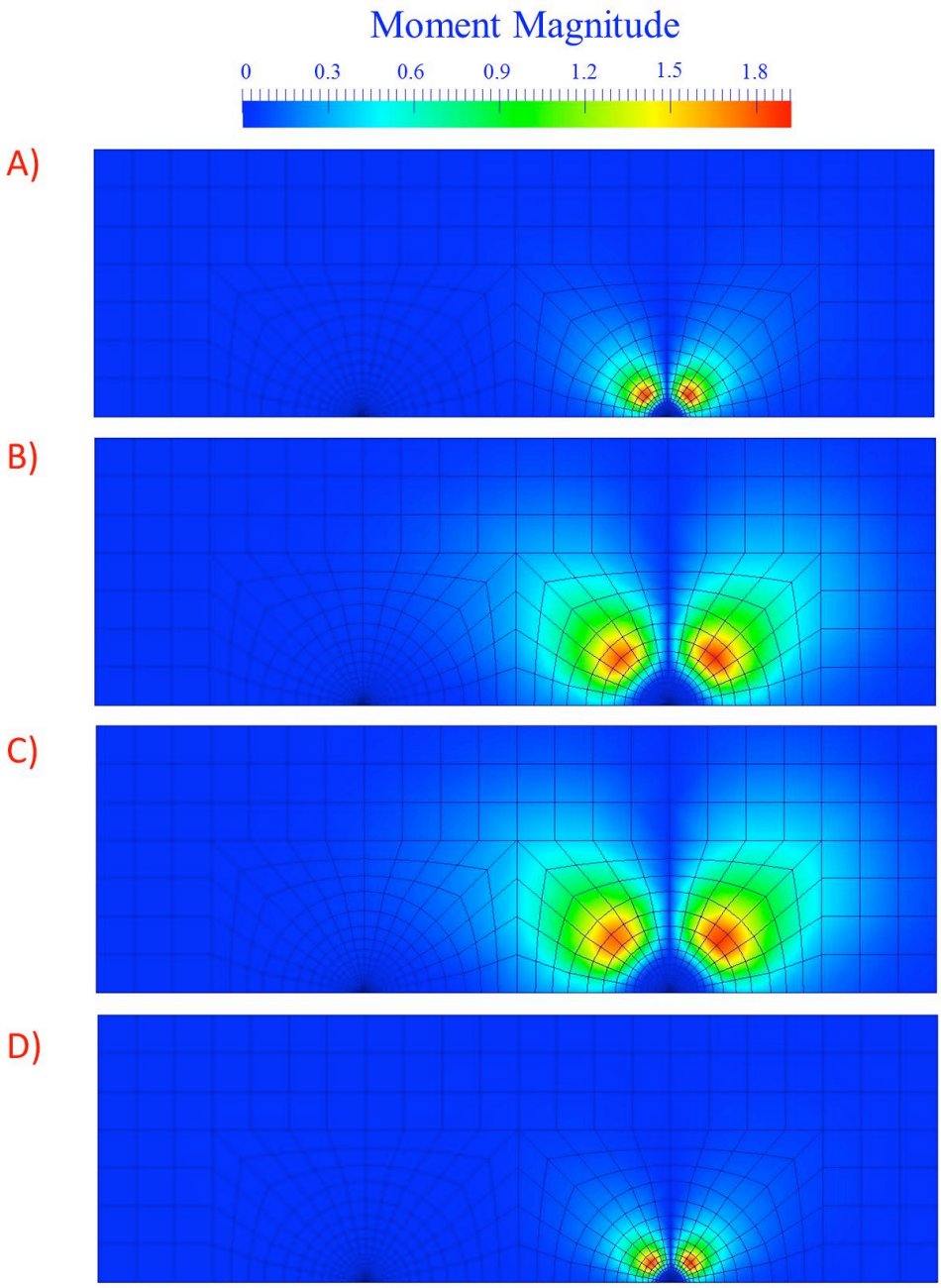

Figure 14: Evolution of moment magnitude at four different zones (shallow to deep) and at four different depths of 2000, 2500, 2750 and 3000 m after 21 day stimulation. The same network of large fractures (density of 0.003 m^{-1} and spacing 300 m) applied at each zone. A) The more closely spaced fractures have densities of 0.5 m^{-1} in the shallow zone B. B) Intermediate zone C with 0.9 m^{-1} fracture density. C) Intermediate zone D with 0.9 m^{-1} fracture density. D) Deepest zone E with 0.26m^{-1} fracture density.

2.6 Hydrodynamic and thermal front triggering of seismicity

We attempt to understand the mechanisms of seismic triggering due to fluid and thermal effects by correlating the evolution of seismicity with the transit of the hydrodynamic and thermal fronts during the 21 day stimulation. We follow the propagation of the fluid pressure, thermal and chemical fronts through the reservoir with time and determine associations of events with the various causal mechanisms.

The numerical model is used to follow the hydrodynamic and thermal fronts as they propagate through the reservoir for various fracture networks (low to high density) at low and high (shallow to deep zones) initial stresses. The location of these fronts is defined by the propagation of the fluid flow rate at any given time. The evolution of seismicity for the short-term stimulation is shown in a radius-time plot relative to the propagation of these fluid and thermal fronts in **Figure 9** (injection flow rate is set at 44 *l/s* in the simulation). This shows the progress of the fluid and thermal fronts in the reservoir together with the progress of induced seismicity. We observe that the rate of propagation of the hydrodynamic front is approximately twice as rapid as the thermal front.

The deepest penetration of the hydrodynamic front into the reservoir at any given time is recorded for the network with the most closely spaced fractures at the intermediate depths of zones C (2750m) and zone D (3000m) **Figure 9-B, C**. This increased penetration could result from two mechanisms. (i) The first is due to the immediate increase in fluid pressure and drop in effective stresses that allows the fractures to dilate. Where the initial permeabilities of the closely and widely-spaced fracture networks are initially the same, a unit change in effective stress will result in a larger permeability change for the more closely spaced network. This is because the ratio of change in aperture to initial aperture ($\Delta b/b_0$) is larger for the more closely spaced network since aperture change is the same in each case (for constant fracture stiffness). (ii) In addition, if temperatures are able to change significantly during the stimulation period, this response will be fastest for the most closely spaced fractures due to the (thermally) diffusive length scale defined by fracture spacing [*Elsworth*, 1989b; *Elsworth and Xiang*, 1989]. As we illustrate in **Figure 9** the largest event occurs at different times at each zones. The largest event occurs at the location (outward from injection) where the stress drop is highest and on the largest fracture.

To further understand the evolution of induced seismicity in space and time we separately indicate the larger event magnitudes (M_S ~1.5 to 1.9) in **Figure 10**. **Figure 10-A, B, C, and D** illustrate the progress of the fluid and thermal fronts in zones B, C, D and E (shallow to deep). Events are separated into four magnitude classifications and the largest event magnitude is also shown. We observe that the number of seismic events decays with time and distance from the injection point at each reservoir. This illustrates that most of the seismic activity is triggered by hydraulic effects at early times relative to the initiation of

stimulation. At later time, thermal effects (and possibly chemical effects as well) may contribute to the seismicity when the seismicity front then lags behind the hydrodynamic front.

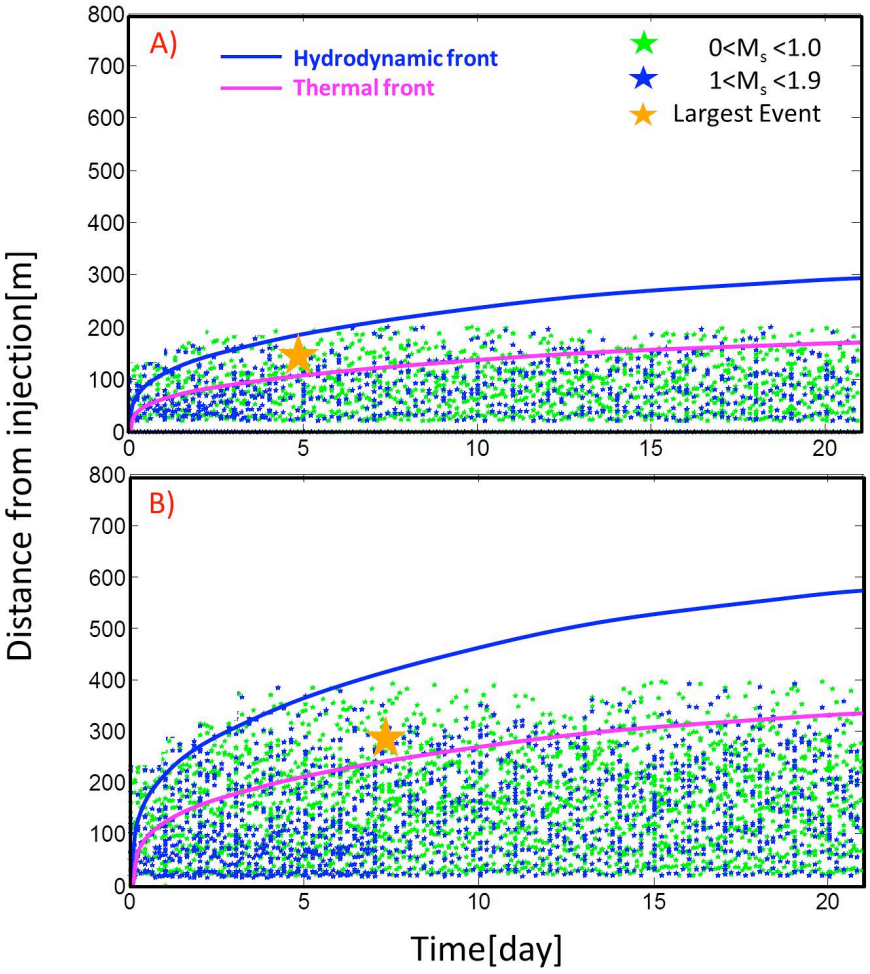

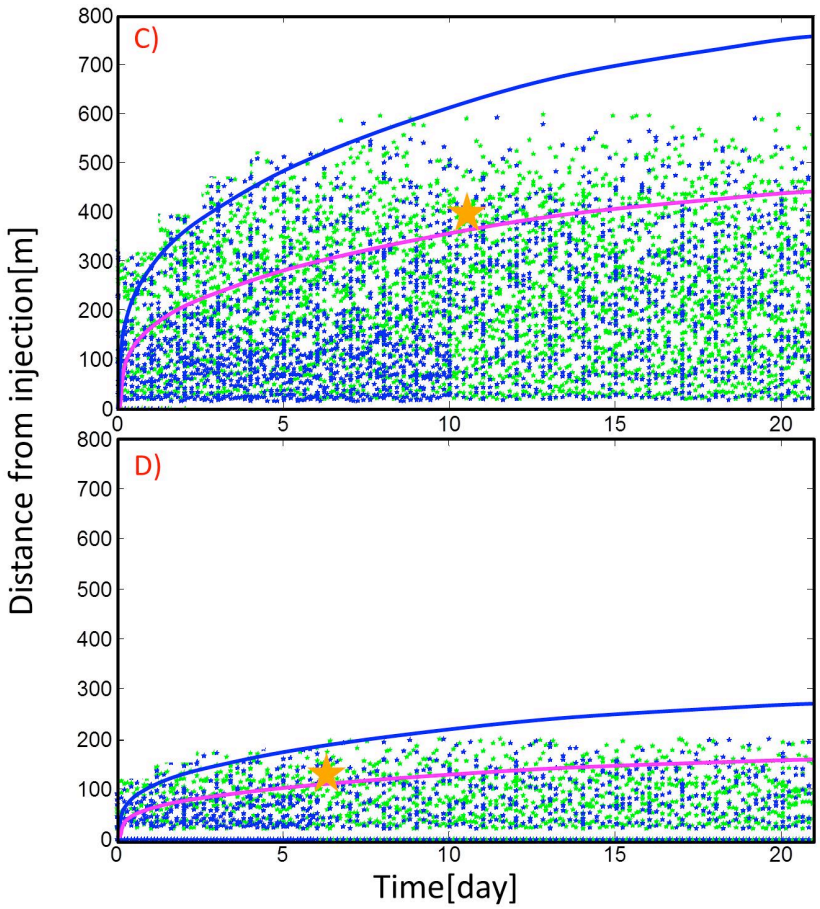

Figure 15: Radius versus time plot for short term of the progress of fluid and thermal fronts in the reservoir and of induced seismicity (Injection flow rate is 44 l/s). Seismic moment of individual events shown green: $0<M_s<1$ and blue: $1<M_s<1.9$ and the largest event is ~1.9 shown with orange star. Reservoir located at four different zones (shallow to deep) and at four different depths of 2000, 2500, 2750 and 3000 m after 21 day stimulation. The same network of large fractures (density of 0.003 m^{-1} and spacing 300 m) applied at each zone. A) The more closely spaced fractures have densities of 0.5 m^{-1} in the shallow zone B. B) Intermediate zone C with 0.9 m^{-1} fracture density. C) Intermediate zone D with 0.9 m^{-1} fracture density. D) Deepest zone E with 0.26m^{-1} fracture density.

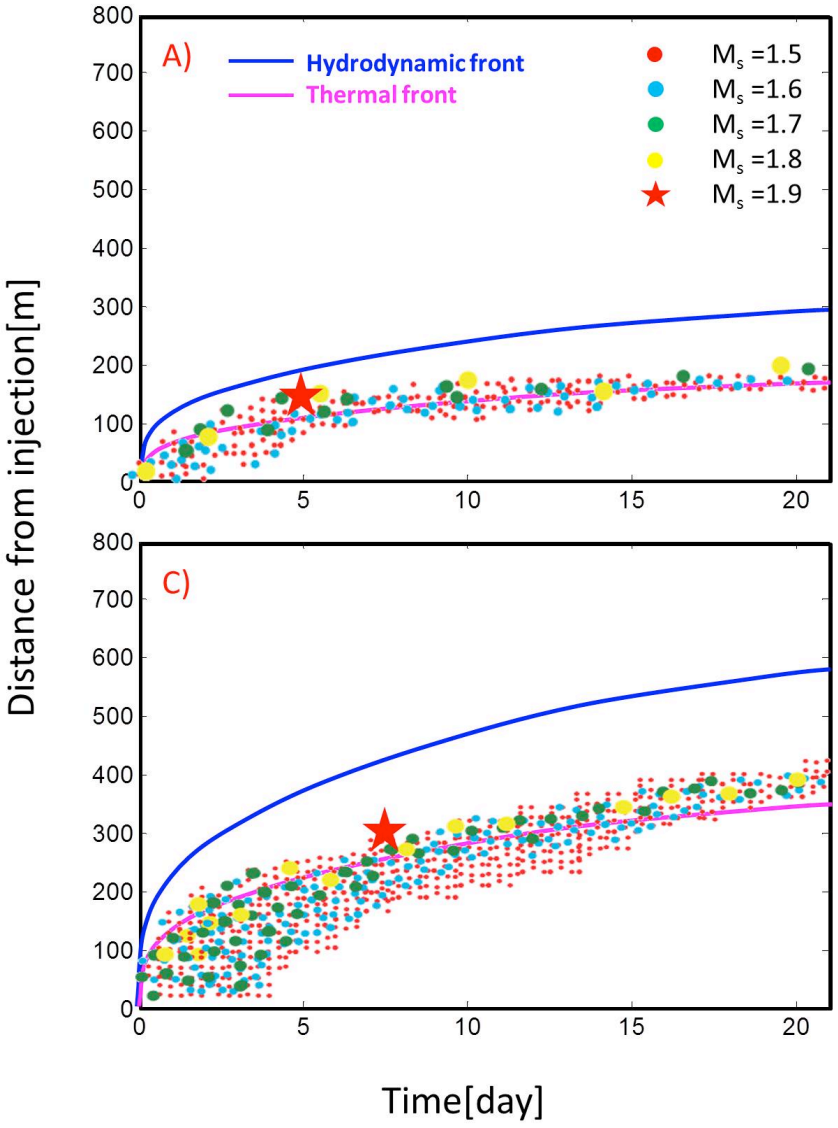
A)
Hydrodynamic front
Thermal front
M_s =1.5
M_s =1.6
M_s =1.7
M_s =1.8
M_s =1.9
C)
Distance from injection[m]
Time[day]
0
100
200
300
400
500
600
700
800
5
10
15
20

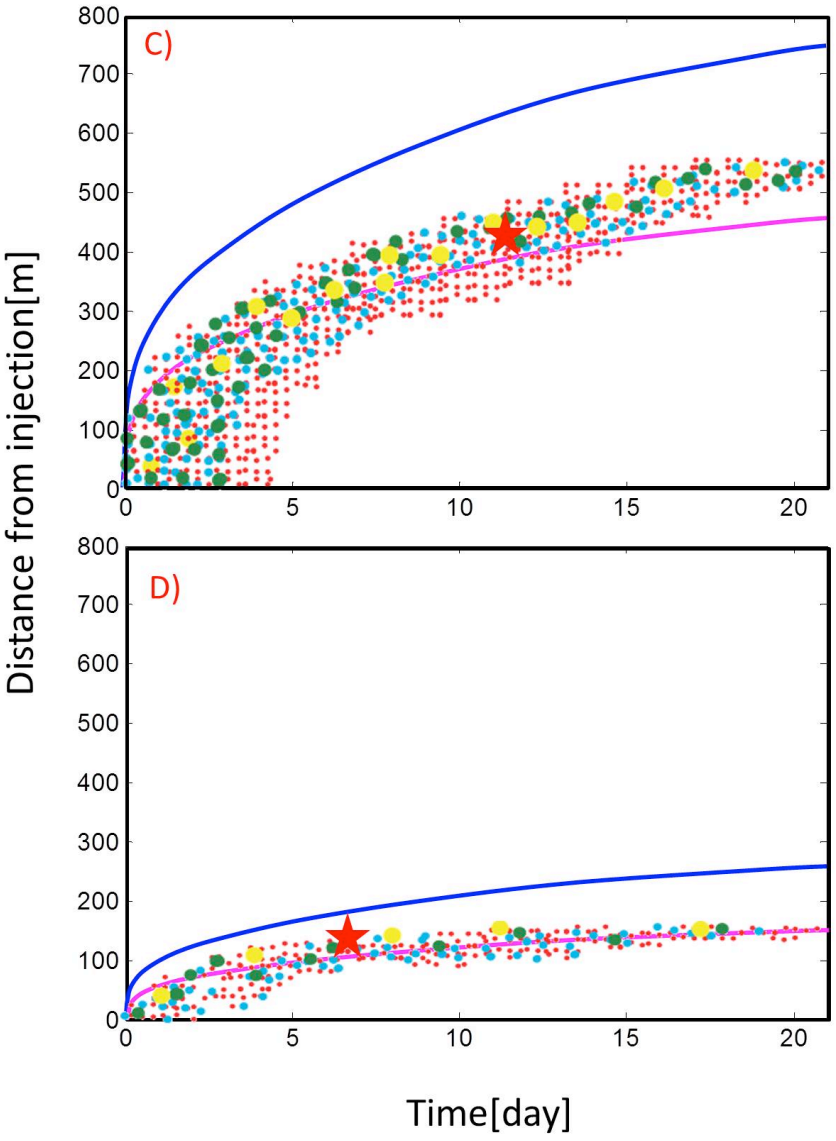

Figure 16: Radius versus time plot for short term of the progress of fluid and thermal fronts in the reservoir and of induced seismicity (Injection flow rate is 44 l/s). Reservoir located at four different zones (shallow to deep) and at four different depths of 2000, 2500, 2750 and 3000 m after 21 day stimulation. The same network of large fractures (density of 0.003 m^{-1} and spacing 300 m) applied at each zone. Larger seismic moment of individual events shown red: M_s= 1.5, blue: M_s=1.6, green: M_s=1.7, yellow: M_s=1.8 and the largest event is ~1.9 shown with red star. A) The more closely spaced fractures have densities of 0.5 m^{-1} in the shallow zone B. B) Intermediate zone C with 0.9 m^{-1} fracture density. C) Intermediate zone D with 0.9 m^{-1} fracture density. D) Deepest zone E with 0.26m^{-1} fracture density.

2.7 Empirical Relation for Seismicity Occurrence

From the Gutenberg–Richter law we model the frequency–magnitude distribution. The modeled *b*-value represents the cumulative number of seismic events at each location within the reservoir with the local magnitude evaluated from its seismic moment. Gutenberg & Richter (1944) expressed the magnitude distribution in the form $log\ N_{event} = a - bM$, where N_{event} is the number of seismic events within a magnitude interval $M \pm \Delta M$.

Here we discuss the scaling of the frequency of events N_{event} as a function of fluid pressure and temperature for stimulation at the Newberry EGS. The number of events as a function of time is controlled only by the cumulative mass of fluid injected which can cause failure and result in energy release. The greater this energy release the larger the number of events induced at a given location and therefore the greater the probability of large-magnitude events. Thus, the model above is able to predict magnitude-frequency distributions. We characterize the induced seismicity by the *b*-value for three different fracture geometries (high to low density) in **Figure 3-A, B, C**.

The anticipated approximate *b*-value for the Newberry EGS is illustrated in **Figure 11**. Apparent from these data is that the closely spaced fracture network with the higher stress regime (at the deeper level) has the largest *b*-value ~0.74 **Figure 11- C**. This shows the greater number of events induced due to the existence of a high density fracture network ($0.9m^{-1}$) and under the prescribed conditions of higher in situ stresses. We observe the lowest *b*-value ~0.67 when we stimulate the shallow zone B with the intermediate and lower fracture density ($0.5m^{-1}$). We conclude that the *b*-value describes fracture processes in the seismic region and is principally related to the fracture network density.

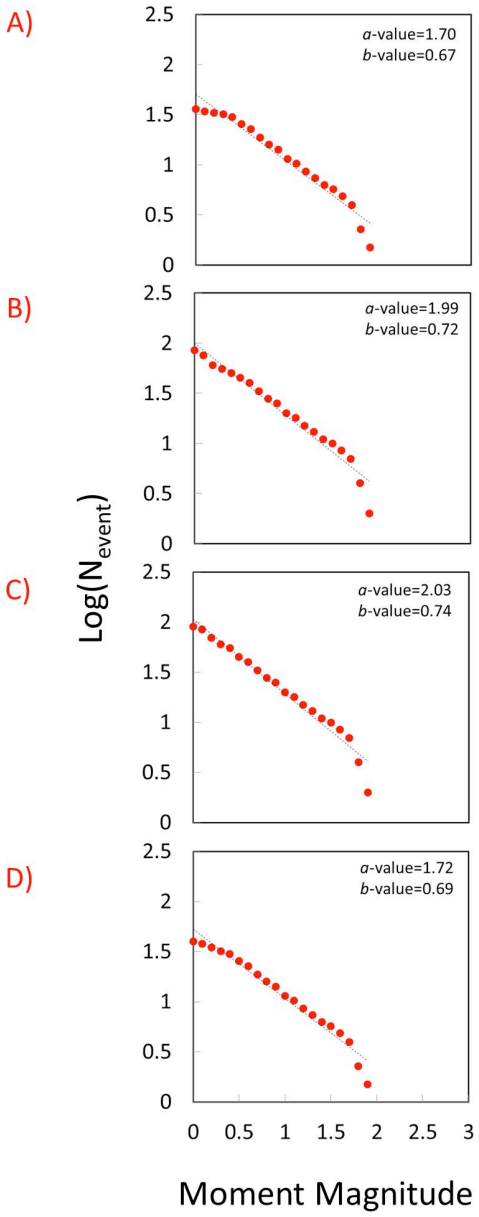

Figure 17: Number of events as a function of magnitude indicating *b*-value for moment magnitudes in the range 0-1.9 after 21 days stimulation. Reservoir located at four different zones (shallow to deep) and at four different depths of 2000, 2500, 2750 and 3000 m. The same network of large fractures (density of 0.003 m^{-1} and spacing 300 m) applied at each zone. *b*-values are evaluated for A) The more closely spaced fractures have densities of 0.5 m^{-1} in the shallow zone B (*b*~0.67). B) Intermediate zone C with 0.9 m^{-1} fracture density (*b*~0.72). C) Intermediate zone D with 0.9 m^{-1} fracture density (*b*~0.74). D) Deepest zone E with 0.26m^{-1} fracture density (*b*~0.69)

2.8 Conclusions

From our modeling experiments, permeability enhancement and induced seismicity within EGS reservoirs are each shown to be influenced by different factors during stimulation. In this study a variety of models are developed to understand the role of thermal- hydraulic- mechanical- and chemical-effects on different fractured reservoirs. Various fracture networks (low to high density) are considered and reservoir stress conditions are changed due to the depth of the reservoir (shallow to deep). We apply our models to the prospective Newberry EGS demonstration project (USA) to determine the effect of these key factors on permeability evolution and induced seismicity during the short-term (~21 day) stimulation of the reservoir.

We seed penny-shaped fractures throughout the reservoir to define fracture stiffness and shear displacement within the reservoir. Energy release from a pre-existing large single fracture increases with the square of the stress drop and the cube of the fracture size. This energy release is triggered by the evolving stress state due to pore pressures and induced thermal and chemical strains. Effective normal stresses and pore pressures are altered during injection. Then potential energy from various fracture sizes is calculated to predict seismic event magnitudes.

We observe that permeability increases by an order of magnitude during stimulation. For the closely spaced fracture network (with $0.9m^{-1}$ density) the increase of fluid circulation is higher and therefore the permeability change is propagated further from injection and occurs in shorter time than for more widely spaced fractures. Likewise for the reservoir with the highest density of fractures and high initial stresses due to greater depth - the evolution of seismicity is more rapid (higher event rate) and its distribution expands fastest with radius (zone D).

A maximum event magnitude for identical fracture distributions is M_s ~1.9 and maximum shear stress drop is prescribed as ~3MPa. We use fluid pressures and reservoir temperatures as proxies to track the hydrodynamic and thermal fronts and to define causality in the triggering of seismicity. Larger events form due to higher flow rate at early time and at later time the thermal effect also exerts an influence on the rate of events as well as event magnitude.

We separately examine the effects of thermal stresses, pore pressure and chemical effects on the evolution of seismicity in reservoirs. The most important mechanism which triggers slip and promotes seismic events and also may change the moment is the augmentation of fluid pressure at the beginning of stimulation. The influence of thermal stress may determine the rate and magnitude of seismic events when the fluid pressure is changing less rapidly (after ~5 days). Thermal effects may be the reason for the faster propagation of events clouds for the more closely spaced fracture networks. The largest event occurs

when the mean stress drop reaches the maximum prescribed stress drop (~3 MPa). Such behavior illustrates the propagation of fluid pressure and thermal fronts through the reservoir with time and associate large early-time events with the fluid front and later lower seismic magnitude events with the transit of the thermal (-chemical) front.

The *b*-value is also evaluated for different fracture networks at different depths. The *b*-value describes the fracture process within reservoirs and is related to size, location, distribution and spacing of fractures. We observe the largest *b*-value for the zone at intermediate stress level and with the greatest fracture density (zone D ~$0.9m^{-1}$). This represents the largest number of seismic events triggered with largest distribution in size. We illustrate that the penetration of the hydrodynamic front is principally controlled by the density and spacing of fractures. When we increase the density of fractures (*i.e.* more closely spaced fracture) in the system we allow the fluid flow to penetrate more rapidly during injection (zone D), thus the fluid penetrates further from the injection well at any given time. The rate of fluid penetration during injection influences the permeability evolution as well as the rate and magnitude of induced seismicity.

Acknowledgements: This work is a partial result of support from the Department of Energy Office of Energy Efficiency and Renewable Energy and Geothermal Technology Program under contract EE-10EE0002761. This support is gratefully acknowledged.

2.9 References

1 Aki, K. (1967), Scaling law of seismic spectrums, J. Geo-phys. Res., 72, 1217-1231.

2 Baisch, S., R. , E. Voeroes, H. Rothert, R. J. Stang, and R. Schellschmidt, A. n. m. f. f. i. i. s. a. (2010), I. J. R. M. M. S. Soultz-sous-Forets, 47(3), 405-413,, and doi:10.1016/j.ijrmms.2009.10.001.

3 Bruce, R. J., G. R. Foulger, and F. C. Monastero (2009), Seismic monitoring of EGS stimulation tests at the Coso geothermal field, California, using microearthquake locations and moment tensors,Thirty-Fourth Workshop on Geothermal Reservoir Engineering Stanford University, Stanford, California, February 9-11, SGP-TR-187.

4 Bryc, W. (1995), The normal distribution: characterizations with applications. Springer-Verlag. ISBN 0-387-97990-5.

5 Cladouhos, T., S. C. Petty, W. Osborn, S. Hickman, and N. Davatzes (2011), The role of stress modelling in stimulation planning at the Newberry volcano EGS demonstration project. Thirty-Sixth Workshop on Geothermal Reservoir Engineering. Stanford, CA.

6 Dinske, C., S. Shapiro, and M. Häring (2010), Interpretation of microseismicity induced by time-dependent injection pressure, SEG Expanded Abstr., 29, 2125, doi:10.1190/1.3513264.

7 Elsworth, D. (1989a), Thermal permeability enhancement of blocky rocks: One-dimensional flows, International Journal of Rock Mechanics and Mining Sciences & Geomechanics Abstracts, Volume 26, Issues 3-4, July, Pages 329-339.

8 Elsworth, D. (1989b), Theory of thermal recovery from a spherically stimulated HDR reservoir. J. Geophys. Res., Vol. 94, No. B2, pp. 1927 - 1934.

9 Elsworth, D., and J. Xiang (1989), A reduced degree of freedom model for permeability enhancement in blocky rock. Geothermics, Vol. 18, No. 5/6, pp. 691-709.

10 Elsworth, D., and H. Yasuhara (2010), Mechanical and transport constitutive models for fractures subject to dissolution and precipitation. In press. Int. J. Num. Meth. Geomechs. Vol. 34, pp. 533-549. Doi:10.1002/nag.831.

11 Evans, K., H. Moriya, H. Niitsuma, R. Jones, W. Phillips, A. Genter, J. Sausse, R. Jung, and R. Baria (2005), Microseismicity and permeability enhancement of hydrogeologic structures during massive fluid injections into granite at 3 km depth at the Soultz HDR site, Geophys. J. Int., 160(1), 388–412, doi:10.1111/j.1365-246X.2004.02474.x.

12 Goodman (1976), Methods of Geological Engineering in Discontinuous Rocks, 472 pp., West Publishing, New York.

13 Izadi, G., and D. Elsworth (2012), Mechanisms of Induced Seismicity along Reactivated Fractured Networks Due to Fluid Circulation and Heat Extraction. Submitted for Publication. TerraNova. 20 pp.

14 Jaeger, J. C., W. G. W. Cook, and R. W. Zimmerman (2007), Fundamentals of Rock Mechanics, Fourth Edition, 475 pp., Blackwell Publishing, Malden, MA.

15 Kanamori, H. (1977), The energy release in great earthquakes, d. Geophys.Res., 82, 2981-2987.

16 Keylis-Borok, V. I. (1959), On estimation of the displace-ment in an earthquake source and of source dimensions, Ann. Geofisic. 12, 205-214.

17 Murphy, H. (1982), Hot dry rock reservoir development and testing in the U.S.A. Proc. Ist Japan-U.S. Seminar on Hydraulic Fracturing and Geothermal Energy, pp. 33-38. Matrinus Nijhoff.

18 Nemat-Nasser, S. (1982), Thermally induced cracks and heat extraction from hot dry rocks, Proc. Ist Japan-U.S. Seminar on Hydraulic Fracturing and Geothermal Energy, pp. 11-31. Martinus Nijhoff, The Hague .

19 Pine, R. J., and P. A. Cundall (1985), Applications of the fluid-rock interaction program (FRIP) to the modelling of hot dry rock geothermal energy systems. Proc. Int. Syrup. on Fundamentals of Rock Joints, pp. 293-302. Centek.

20 Purcaru, G., and H. Berckemer (1978), A magnitude scale for very large earthquakes.tectonophys.49:189-198.

21 Renshaw, C. E. (1995), On the relationship between mechanical and hydraulic apertures in rough-walled fractures. J. Geophys. Res., 100: 24629-36.

22 Rutqvist, J., Y. S. Wu, C. F. Tsang, and G. Bodvarsson (2001), A modeling approach for analysis of coupled multiphase fluid flow, heat transfer, and deformation in fractured porous rock. (submitted to Int J Rock Mech Mineral Sci).

23 Shapiro, S. A., and C. Dinske (2007), Violation of the Kaiser effect by hydraulic-fracturing-related microseismicity, J. Geophys. Eng., 4, 378– 383.

24 Shapiro, S. A., and C. Dinske (2009a), Fluid-induced seismicity: Pressure diffusion and hydraulic fracturing, Geophys. Prospect., 57, 301– 310.

25 Shapiro, S. A., and C. Dinske (2009b), Scaling of seismicity induced by nonlinear fluid-rock interaction, Journal of Geophysical Research, Vol. 114, B09307, doi:10.1029/2008JB006145.

26 Shapiro, S. A., J. J. Royer, and P. Audigane (1998), Estimating the permeability from fluid-injection induced seismic emission, in Poromechanics, pp. 301–305, eds Thimus, J.-F., Abousleiman, Y., Cheng, A.H.-D., Coussy, O. & Detournay, E., Balkema, Rotterdam.

27 Taron, J., and D. Elsworth (2009a), Thermal-hydrologic-mechanical-chemical processes in the evolution of engineered geothermal reservoirs. Int J Rock Mech Min Sci, doi:10.1016/j.ijrmms.2009.01.007.

28 Taron, J., and D. Elsworth (2009b), Thermal-hydrologic-mechanical-chemical processes in the evolution of engineered geothermal reservoirs. Int J Rock Mech Min Sci, doi:10.1016/j.ijrmms.2009.01.007.

29 Taron, J., D. Elsworth, and K. B. Min (2009), Numerical simulation of thermal-hydrologic-mechanical-chemical processes in deformable, fractured porous media, International Journal of Rock Mechanics and Mining Sciences, *46*(5), 842-854.

30 Zoback, M., and H. P. Harjes (1997), Injection induced earthquakes and the crustal stress at 9 km depth at the KTB deep drilling site, Germany:Journal of Geophysical Research,102, 18477–18492.

3 CHAPTER 3: THE INFLUENCE OF THERMAL-HYDRAULIC-MECHANICAL-AND CHEMICAL EFFECTS ON THE EVOLUTION OF PERMEABILITY, SEISMICITY AND HEAT PRODUCTION IN GEOTHERMAL RESERVOIRS

Abstract

A coupled continuum model representing thermo-hydro-mechanical behaviors is applied to follow the evolution of induced seismicity within a prototypical enhanced geothermal system (EGS) reservoir. The model is applied to the potential Newberry EGS field (USA) by assuming fracture sizes of 10 to 1200 m. Models are classified by their conceptualization of the fractured reservoir geometry as networks of discrete fractures and with equivalent fractured media as fill-in. The THMC model is applied to a doublet injector-producer to explore the spatial and temporal triggering of seismicity for varied fracture network geometries both shallow (2000m) and at depth (2750m). The magnitude of the resulting seismic events is in the range -2 to +1.9. The largest event size (~1.9) corresponds to the largest fracture size (~1200m) within the reservoir. The rate of hydraulic and thermal transport has a considerable influence on the amount, location, and timing of failure, and ultimately, on the event rate. The event rate is highest when the fracture density is highest ($0.9 m^{-1}$) and the initial stresses highest (at depth). In all cases, the *a*-value decreases and the *b*-value increases with time. The *b*-value is largest (~1.34) for the highest fracture density and the highest stress regime. Thermal energy recovered during production is also greatest at depth and for the highest density of fractures.

3.1 Introduction

In enhanced geothermal systems (EGS), fluid circulation is influenced by thermal-hydro-mechanical effects in the short-term and by chemical reactions in the long-term. These effects may alter fluid transport properties and as a result enhance the permeability of fracture networks [*Elsworth*, 1989; *Goodman*, 1976a; *Polak et al.*, 2003; *Renshaw*, 1995]. Natural and induced fractures, as well as the geometry of fracture networks, have an important influence on both the evolution of permeability [*Polak et al.*, 2003; *Yeo et al.*, 1998] and on induced seismicity [*Shapiro and Dinske*, 2007].

Many field experiments [*Audigane et al.*, 2002; *Delépine et al.*, 2004; *Jung et al.*, 1996; *Rutledge and Phillips*, 2003; *Zoback and Harjes*, 1997] and models [*Rutqvist et al.*, 2001; *Shapiro et al.*, 1998 ; *Shapiro et al.*, 2002; *Taron et al.*, 2009a] have been used to determine the key factors influencing the principal processes of permeability enhancement and how they will influence induced seismicity by the action of hydraulic or thermal effects at different times [*Baisch*, 2009; *Deichmann and Giardini*, 2009; *Dinske et al.*, 2010; *Evans et al.*, 2005; *Shapiro and Dinske*, 2007; *Taron and Elsworth*, 2009; *Taron et al.*, 2009a; *Taron et al.*, 2009b; *Yasuhara et al.*, 2004]. Simulating these behaviors requires that the linkage between

the fluid and thermal behaviors and the role of fracture networks be defined within the reservoir. This work attempts to determine- how such processes will evolve through time.

Circulating fluid at elevated pressures within naturally fractured reservoirs may cause induced seismicity in the early stages of reservoir stimulation (few weeks) [*Rothert and Shapiro*, 2003; *Rutledge and Phillips*, 2003; *Shapiro et al.*, 2002]. Hydraulic effects observed during the stimulation of EGS reservoirs influence the permeability and dilation of existing fractures by altering the direction and magnitude of the reservoir stress field. Circulating fluid-induced thermal stresses may also enhance reservoir permeability by creating new fractures and by enhancing the permeability of existing fractures. Both of these effects may induce seismicity both during stimulation and later long-term production.

In this work, we apply a THMC flow-transport-deformation simulator to examine the importance of these factors on reservoir evolution and specifically on the strength of their influence. The focus of this study is to observe the evolution of dominant fracture behaviors that lead to enhanced permeability and induced seismicity during the long-term (~20 year) production of thermal energy from engineered geothermal systems (EGS). We also focus on the significant influence of fracture density and fracture spacing on long-term reservoir behavior.

This paper provides a brief description of the fracture network model and mechanisms of shear failure that result from circulating cold injection fluids at modest overpressures and under pressures. Effective stresses, modulated by fluid pressures and thermal stresses, are used to define the spatial and temporal release of seismic energy as individual fractures are reactivated in shear. The progress of fluid pressures and cooling in the reservoir is represented by the advancement- of the hydrodynamic and thermal fronts as well as the progress of pore-pressures and thermal stresses within the reservoir. The triggering of seismicity and the frequency–magnitude distribution (*a*- and *b*-values) of this seismicity is indexed to the progress of these fluid and thermal fronts. These behaviors are evaluated for parameters that broadly represent the planned Newberry Volcano EGS demonstration project and follow the anticipated evolution of the seismic event-size distribution due to fluid and thermal effects during long-term stimulation. Finally, and perhaps most importantly, the relative effects of the above mechanisms on the ultimate recovery of thermal energy from the EGS reservoir are evaluated.

3.2 Reservoir Simulation

The simulations presented in the following uses a THMC simulator [*Taron and Elsworth*, 2009] that couples the multiphase, multi-component, non-isothermal thermodynamic, reactive transport and chemical precipitation/dissolution capabilities of TOUGHREACT with the stress/deformation analysis by using the numerical modeling code FLAC^{3D}. The model incorporates the effects of fractured reservoirs

involving fracture networks of variable densities and connectivities while considering various reservoir conditions, including initial stress, temperature, and permeability – as these may exert significant influence on the evolution of permeability and seismicity.

Brittle failure on pre-existing fractures is represented as a prescribed stress drop (~3 MPa). For a prescribed frictional strength, the model calculates the shear resistance from the change of normal stress and pore pressure. Stress builds and reaches a peak strength, which then rapidly declines to a residual strength [*Goodman*, 1976b; *Jaeger et al.*, 2007]. This model is used to follow the evolution of seismic rupture within the system.

The principal assumption in this procedure is that strength will fully recover in the interseismic period, allowing the failure cycle to repeat once shear stresses have rebuilt. To define the evolution of failure in a stimulated reservoir, the failure of the seeded fractures is calculated within FLAC^{3D}. Strength is determined by comparing- the peak strength and residual shear strength, according to the Mohr-Columb criterion (see Table 2).

3.2.1 Characteristics of the reservoir

This model is now applied to a doublet geometry within a reservoir with half-symmetry (2000m×1000m×300m; Figure 1), representing the Newberry geothermal field. The Newberry demonstration EGS project is located southeast of Bend, Oregon. Data from well NWG 55-29 are used to build the reservoir model used in the subsequent simulation [*Cladouhos et al.*, 2011]. This presumed half-symmetry is approximate but represents the essence of important behaviors that act in the reservoir. A single well injects water at a constant temperature with a withdrawal well separated by 700m. Boundary stresses, in both horizontal and vertical directions, as well as pore pressure and temperature roughly corresponding to depths of 2000 and 2750 are applied to two different realizations of the geometry (Table 2) applied for this geothermal field. The characteristics and the values of the parameters in the simulation for the *in-situ* reservoir are defined in Table 1.

Prior to long-term production, the reservoir is hydraulically stimulated by elevating fluid pressures and quenching the reservoir at the injection well and withdrawal well over a period of 21 days and at an overpressure of 5 MPa [*Izadi and Elsworth*, 2014]. This dilates pre-existing fractures (fracture propagation is not considered) and allows the development of hydroshears. During the short stimulation (~21 days), four zones—at depths 2000, 2500, 2750 and 3000m—are considered for reservoir stimulation [*Izadi and Elsworth*, 2014].

During this stimulation a similar evolution of permeability and progress of seismicity is observed for both zones B (shallowest, located at 2000m depth) and E (deepest, located at 3000m depth), and for both

intermediate zones C and D (due to the similar form of the fracture networks ($0.9m^{-1}$) in zones C and D). Thus, in this study, numerical experiments are conducted for the shallow zone B (with $0.5m^{-1}$ fracture density) and deep zone D (with $0.9m^{-1}$ fracture density), alone, as representative of the reservoir. These represent behavior at two different depths of 2000m and 2750m to examine the roles of the critical influencing parameters, *viz.* fracture geometry and stress. Each of these zones requires different inputs for fracture orientations, density and spacing (Table 3). Available, but sparse, fracture data for the Newberry geothermal field [*Cladouhos et al.*, 2011] are used to build the fracture networks for the models. Following stimulation, cold fluid (20°C) is circulated within the reservoir in the doublet pattern of Figure 1. The resulting analyses examine the progress of seismicity for long-term production as the reservoir is developed in terms of rates, magnitudes and locations.

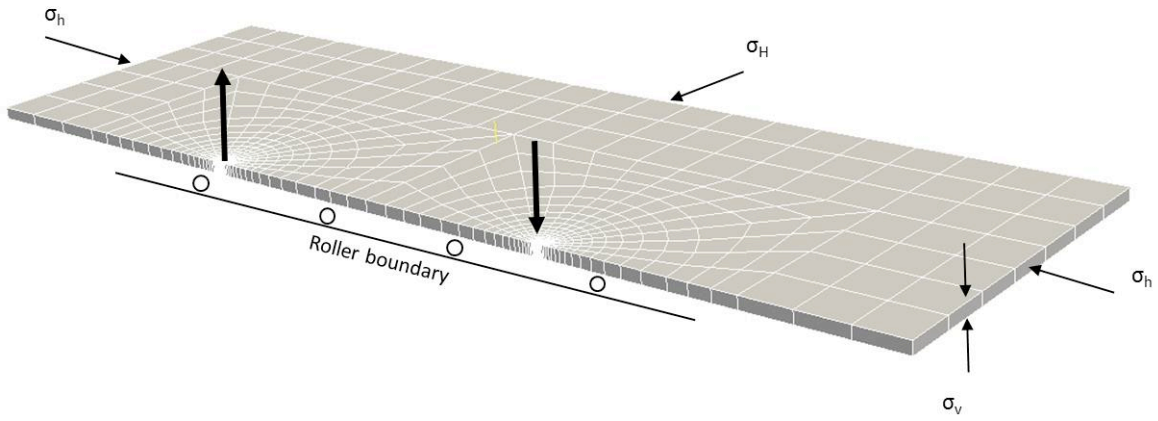

Figure 18: Geometric layout of EGS reservoir as used in the simulation. Reservoir geometry with half-symmetry (2000m×1000m×300m). The spacing between injection and production well is assumed to be 700m. A vertical and two horizontal stresses are indicated.

Table 7: Solid medium properties as used in simulations.

Parameter	Unit	Newberry
Bulk modulus of intact rock(K_m)	GPa	17
Cohesion	MPA	10
Poisson's ratio(υ)	-	0.27
Bulk modulus of fluid(k_f)	GPa	8
Bulk modulus of solid grain(K_s)	GPa	54.5
Internal friction angle(φ)	°	35
Residual friction angel(β)	°	11
Coefficient of thermal expansion(α_T)	1/°C	1.2E-5
Thermal conductivity(λ)	W/mK	2.9
Heat capacity(c_p)	J/kgK	918
Initial Permeability(k)	m^2	1.10E-17
Porosity within fractures(ϕ)	-	0.3

Table 8: Parameters utilized in the simulation.

Parameters	Unit	Depth[m]	
		2000	2750
		Zone B	Zone D
S_{hmin}	MPa	36	50
SH_{max}	MPa	48	64
S_v	MPa	48	66
$P_{injection}$	MPa	29	35
$P_{reservoir}$	MPa	24	30
$P_{production}$	MPa	19	25
Peak Strength	MPa	25	35
$T_{reservoir}$	°c	230	290
$T_{injection}$	°c	20	20
Specific Heat	kJ/kgK	4.65	5.6

Table 9: Fracture data that utilized in the simulation.

Fracture Characterization	Unit	Depth[m]	
		2000	2750
		Zone B	Zone D
Density	m^{-1}	15/30m	27/30m
Number of seeded fractures	-	1000	1800
Fracture size	m	10-1200	10-1200
Fracture spacing	m	10-300	10-300
Standard deviation($\bar{\sigma}$)	-	19	19
Mean($\bar{\mu}$)	-	360	360

3.2.2 Characteristics of the Fracture Network

The presumed fracture orientation and density representing the reservoir are defined in Table 3. The deeper zone D differs from shallower zone B because it has a larger fracture density (0.9 m^{-1} vs. 0.5 m^{-1}) and higher in situ stresses (Table 2) – two features that result in a significantly greater stimulated volume [*Izadi and Elsworth*, 2014].

Two sets of pre-existing fractures are generated in the reservoir. These comprise a set of long (200-1200m), widely spaced fractures and a set of short (10-200m), closely spaced fractures to fill-in between the larger fractures. This allows the fracture network to be generated to honor the BHTV image log data *[Cladouhos, et al., 2011]* (see Figure 2) for the Newberry reservoir.

The shallow (B) and deep (D) reservoirs have different (low and high) fracture densities. Thus different sets of fracture network models are examined to determine the important influence of the fracture density on response. Both the deeper reservoir (D), with a high density fracture network and shallow reservoir B, with low density, have the same overprinted network of large fractures (density of 0.003 m^{-1} and spacing 300 m) (Figure 2).

Permeability evolution is calculated from changes of the fracture aperture and the predefined spacing of fractures. Therefore, a sensitivity analysis is conducted to determine the influence of fracture spacing on permeability evolution. A more finely fractured representation of zones B and D (shallow and deep) is developed to examine the effect of a reduced average spacing of the large fractures on rates of seismicity and permeability evolution. Figure 3 illustrates the geometry of these two networks; the spacing of the large fractures is halved (~150m) for both zones.

The fracture characteristics listed in Table 3 represent the various fracture densities, orientations and lengths applied in the two zones and are used to examine the response of shallow(B) and deep(D) reservoirs to determine the induced seismicity during long-term (20 years) production.

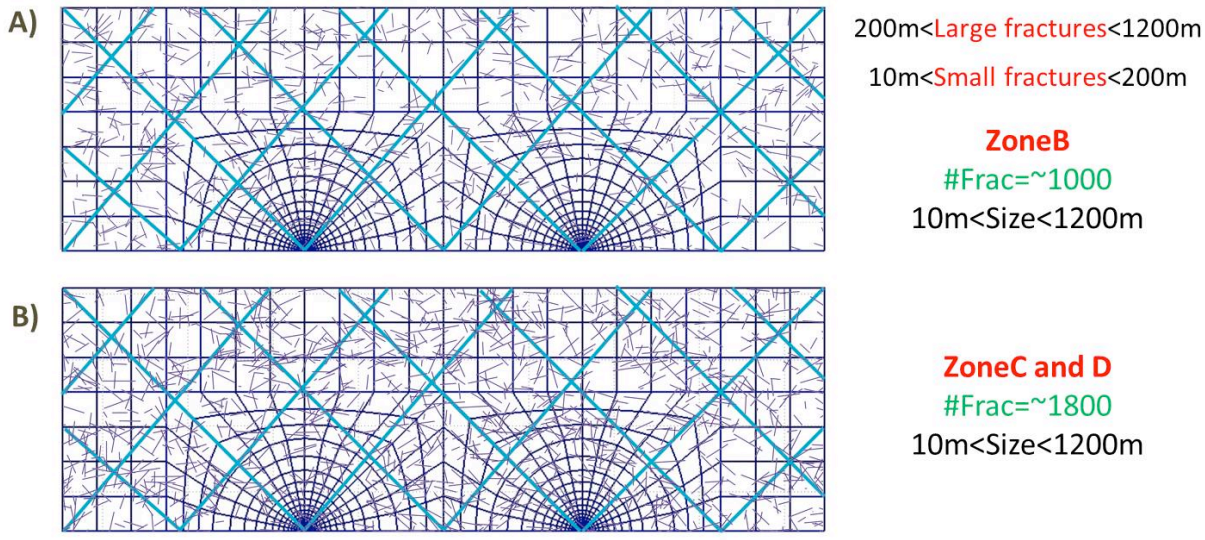

Figure 19: Fracture network structure for the Newberry EGS reservoir; fracture size varies from 10m to 1200m. The same network of large fractures (density of 0.003 m^{-1} and spacing 300 m) is defined for shallow zone B and deep zone D. A) For smaller fracture (10-200m) the fracture densities of 0.5 m^{-1} in the shallow zone B. B) Fracture density of 0.9 m^{-1}applied in the deeper zone D.

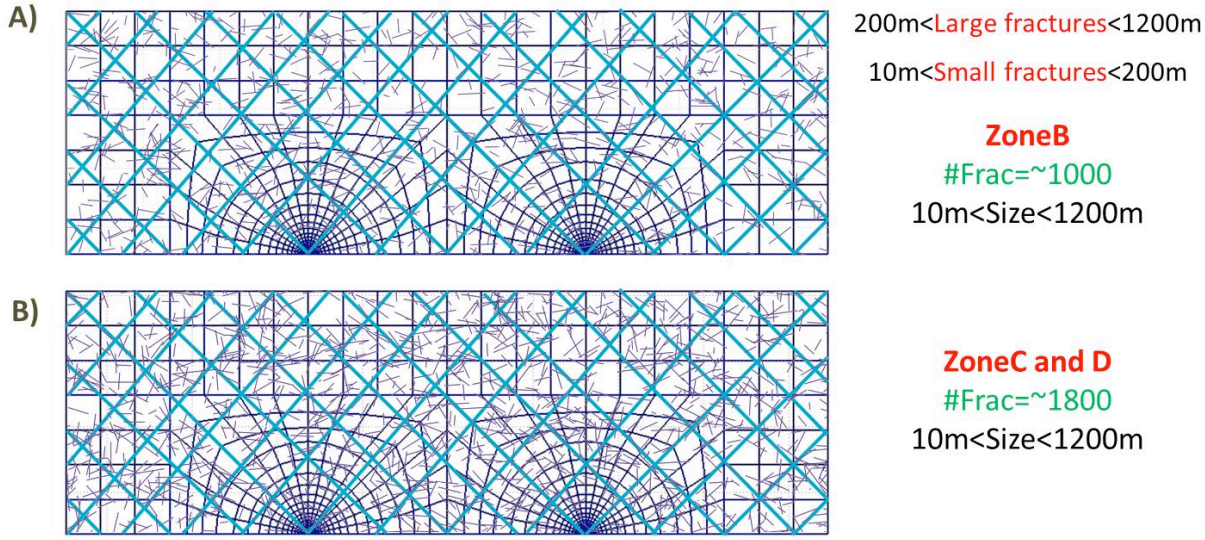

Figure 20: Fracture network structure for the Newberry EGS reservoir, fracture size varies between 10m to 1200m. The same network of large fractures (density of 0.006 m^{-1} and spacing 150 m) defined for shallow zone B and deep zone D. A) For smaller fracture (10-200m) the fracture densities of 0.5 m^{-1} in the shallow zone B. B) Fracture density of 0.9 m^{-1}applied in the deeper zone D.

3.3 Evolution of shear failure of pre-existing fractures

Shear failure calculations are handled with FLAC^{3D}. In all simulations, the friction angle on fractures is assumed constant (35^o). Stress drops resulting from the anticipated fracture networks are shown in Figure 4 (mean spacing 300m). Figure 5 (mean spacing 150m) shows stress drops for the denser network (halved spacing).

The stress drops along the large fractures are capped at the prescribed stress drop, τ. However, for the larger fracture density (smaller spacing of Figure 3), the mean stress drop is shown to be smaller than the maximum potential stress drop. This result shows that more closely spaced fractures allow the more rapid removal of heat from the blocks. In such a case failure occurs with a smaller stress drop compared to that for the larger fracture spacing.

A significantly higher rate of fracture reactivations is observed for high density fracture networks (zone D), causing an increase in stress rate compared to the low density fracture network (zone B) Figure 4. The reason for this is related to the faster propagation (two times faster) of the thermal front by advective transport as well as conductive heat transfer within the higher conductive fracture zones when the density of the fracture network is larger ($0.9m^{-1}$) compared to the lower fracture density network ($0.5m^{-1}$) in the shallow zone.

Understanding the stress drop distribution is significant for further analysis of the evolution of induced seismicity. Therefore, the following sections illustrate that the highest seismic activity will occur when the stress drop is close to that capped at the prescribed stress drop.

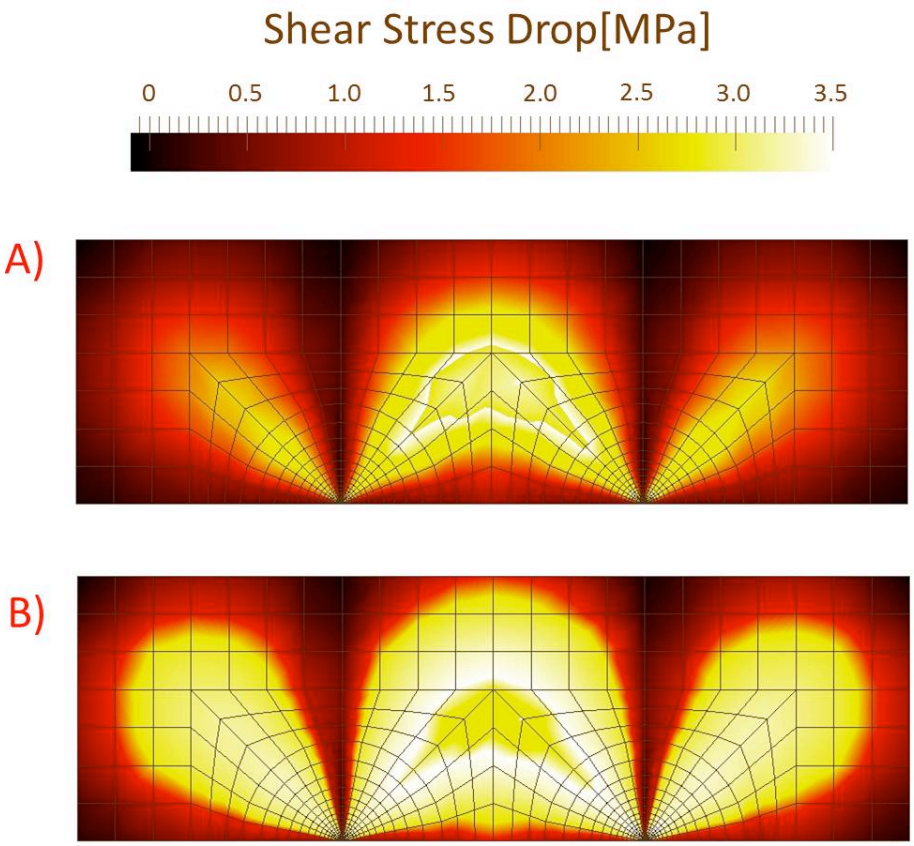

Figure 21: Development of stress drop at four different zones (shallow to deep) and at four different depths of 2000 and 2750 after 20 years of reservoir production. The same network of large fractures (density of 0.003 m^{-1} and spacing 300 m) applied at each zone. A) For smaller fracture (10-200m) the densities of 0.5 m^{-1} in the shallow zone B. B) Fracture density of 0.9 m^{-1}applied in the deeper zone D.

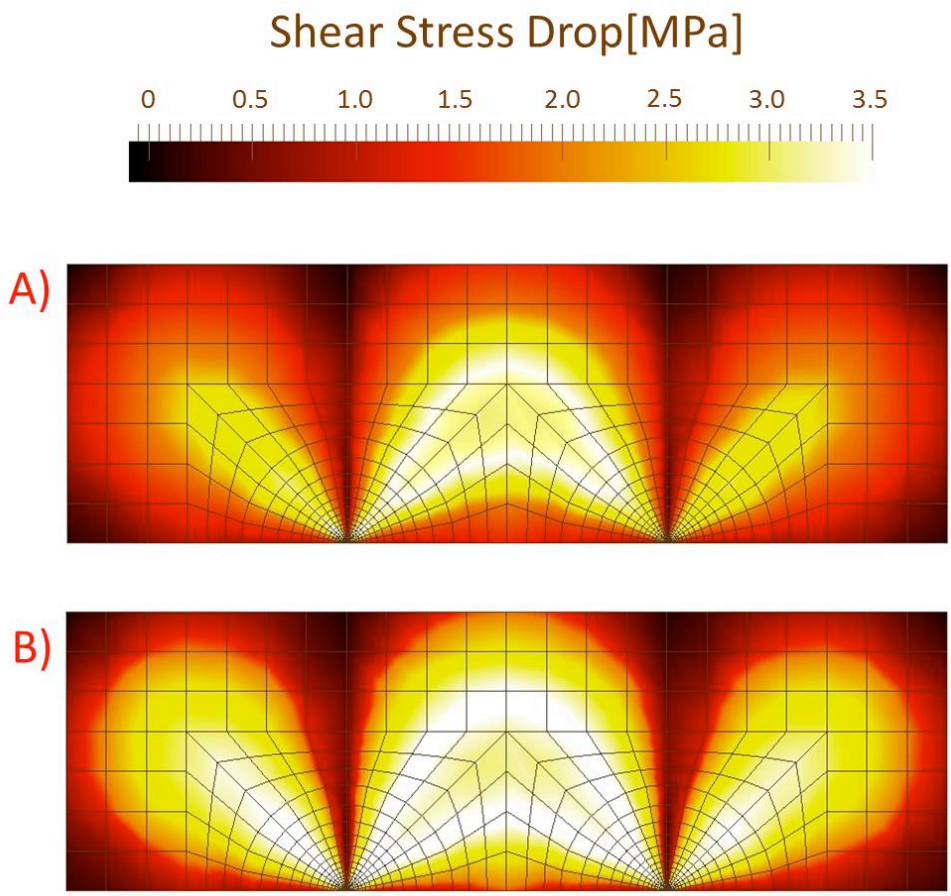

Figure 22: Development of stress drop at four different zones (shallow to deep) and at four different depths of 2000 and 2750 after 20 years of reservoir production. The same network of large fractures (density of 0.006 m^{-1} and spacing 150 m) applied at each zone. A) For smaller fracture (10-200m) the densities of 0.5 m^{-1} in the shallow zone B. B) Fracture density of 0.9 m^{-1}applied in the deeper zone D.

3.4 Evolution of moment magnitude during production

Next we evaluate the cumulative potential release of energy [*Izadi and Elsworth*, 2014] from penny shaped fractures of multiple orientations and sizes that are seeded in the reservoir . The potential energy release is a function of the shear stress drop ($\Delta\tau$), the radius of the planar fracture and also the shear modulus (G). Energy release from a pre-existing fracture increases with the square of the stress drop and the cube of the fracture size [*Izadi and Elsworth*, 2013]. It is triggered by the evolving stress state due to pore pressures and induced thermal and chemical strains. Energy release from fractures is most conveniently represented as a moment magnitude [*Aki*, 1967; *Kanamori*, 1977; *Keylis-Borok*, 1959]. The moment magnitude relation is defined as [*Purcaru and Berckemer*, 1978]:

$$\log M_0 = 1.5 M_s + 9.1 \qquad (4)$$

where M_0 is seismic moment and M_S is moment magnitude. In this model, M_0 is the seismic energy derived from the elastic energy released by the shear on pre-existing fractures.

The spatial/temporal evolution of moment magnitude in the reservoir for the ensemble arrangement of fractures is determined using the above relations. For minimum (10m) to maximum (1200m) fracture radii, a maximum shear stress drop of ~3 MPa and a shear modulus of 10 GPa, M_S varies from -2 to +1.9. The largest event size (~1.9) corresponds to the largest fracture size (~1200m) within the reservoir.

To determine the evolution of moment magnitude during long-term production, we examine the behavior of the two fracture networks models, first shallow and then at depth.

First: the same network of large fractures (density of 0.003 m^{-1} and spacing 300 m) is defined for both the shallow zone (B) and the deep zone (D). However, the smaller fractures (length 10-200m) are set with a lower fracture density (0.5 m^{-1}) in the shallow zone (B) and a higher fracture density (0.9 m^{-1}) in the deeper zone (D) (Figure 2). The evolution of moment magnitude for these sets of fracture networks is shown in Figure 6.

Second: a fractured network (Figure 3) is developed, representing the two zones (shallow zone B and deep zone D) to examine the effect of a reduced average spacing of the large fractures on the evolution of moment magnitude. Such a fracture network is modeled with both large and small fractures. The fracture density of the larger fractures is ~0.006 m^{-1} with a spacing of 150 m. The smaller fracture set (10-200m) has a fracture density of 0.5 m^{-1} in the shallow zone B and 0.9 m^{-1} in the deeper zone D. The evolution of moment magnitude for these sets of fracture networks is shown in Figure 7.

The outcomes for moment magnitude evolution for these different cases allow comparison of the effects of various fracture density, spacing and stress states as a result of reservoir production. During the evolution of energy release, the principal difference between zones B (shallow) and D (deep) for both large (~300m) and small (~150m) fracture spacing is related to first, the density of the closely spaced fracture and second, the incremental stress drop that accompanies failure. When the potential energy released in the two zones (shallow to deep) is compared, it is observed that the release begins and builds earlier and reaches further from the injection wellbore for the largest fracture density ($0.9m^{-1}$). Figure 6-B and Figure 7-B.

The response for different realizations of fracture network spacing is compared and contrasted for both shallow and deep zones. This analysis is based on small (~150m) Figure 7 and large (~300m) (Figure 6) fracture spacing for widely-spaced and large fractures in the shallow (B) and deep zones (D). The rate of seismic event migration within the reservoir is controlled principally by the density and spacing of the fractures.

The model with the higher fracture density (0.9m^{-1}) and smaller fracture spacing (150m) Figure 7-B apparently generates both the greatest number and the largest seismic events (M_S=1.9) after 20 years of reservoir production. Absolute stress is largest when the reservoir is deepest, but stress drop is limited by the difference in peak and residual strength of the fractures (~3 MPa) and hence cannot be a critical parameter. This behavior occurs because transport of fluid pressure and thermal removal from blocks is much faster for the closely spaced fractures (~150m) than for the network with widely spaced fractures (~300m). As a result, the fluid propagates faster with distance than for the more closely spaced fractures as observed in Figure 7-B in a given time. The event rate is higher when the fracture network has the larger density (0.9m^{-1}), with smaller fracture spacing (~150m), and is located at a depth where the initial stresses are higher (zone D).

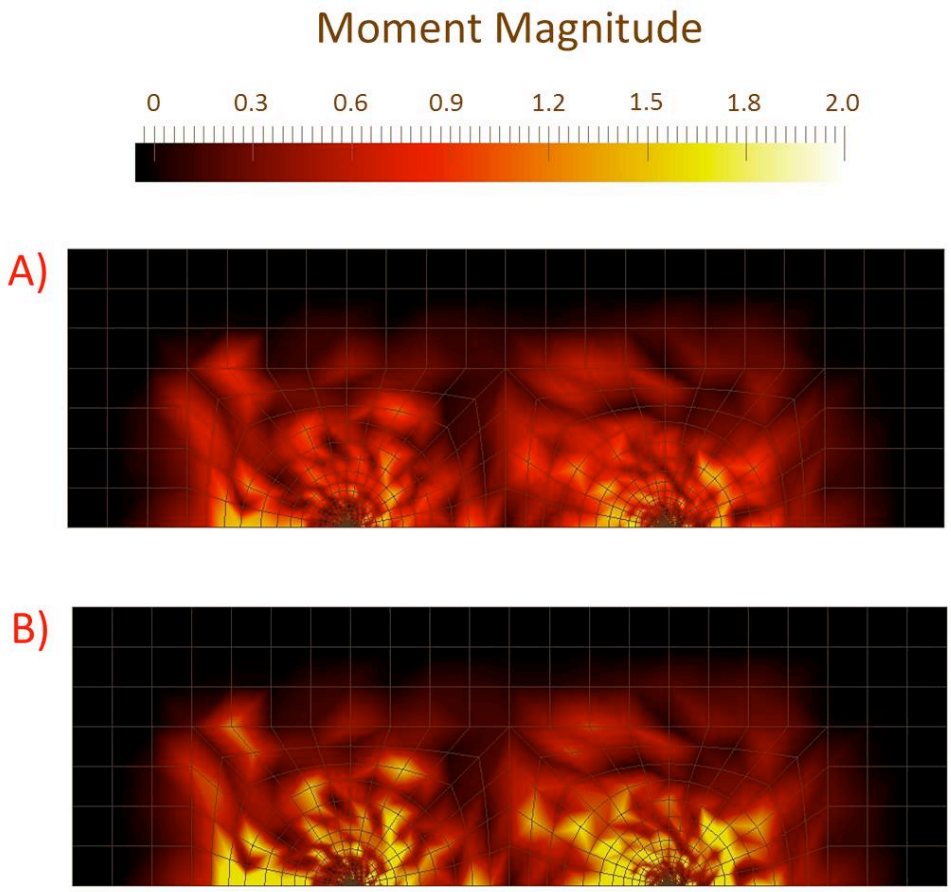

Figure 23: Evolution of moment magnitude at zones B and D (shallow to deep) and at two different depths of 2000 and 2750 after 20 years of reservoir production. The same network of large fractures (density of 0.003 m^{-1} and spacing 300 m) applied at each zone. A) For smaller fracture (10-200m) the densities of 0.5 m^{-1} in the shallow zone B. B) Fracture density of 0.9 m^{-1} applied in the deeper zone D.

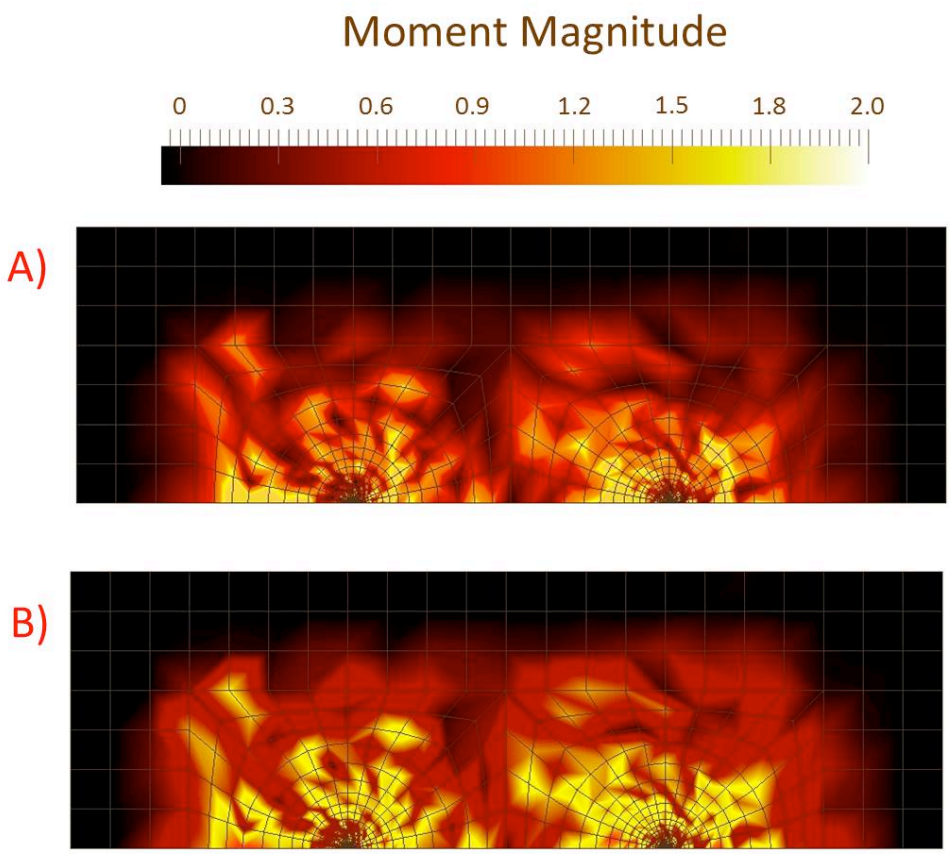

Figure 24: Evolution of moment magnitude at zones B and D (shallow to deep) and at two different depths of 2000 and 2750 after 20 years of reservoir production. The same network of large fractures (density of 0.006 m^{-1} and spacing 150 m) applied at each zone.A) For smaller fracture (10-200m) the densities of 0.5 m^{-1} in the shallow zone B. B) Fracture density of 0.9 m^{-1}applied in the deeper zone D.

3.4.1 Evolution of seismic events

Using a stress-strain fracture criterion to determine the total strain energy available for release (this energy is assumed to be shed seismically), we observe that during the rupture process the shear stress drops an amount $\Delta\tau$ from an initial value of τ_i to a final value τ_f. The total energy is calculated from the strain changes and volume of the matrix [*Izadi and Elsworth*, 2013]. A relation is introduced to determine the number of events which occur during the failure process based on potential and total energy as

$$N_{event} = \frac{E_T}{E_p} \tag{5}$$

where N_{event} is the number of seismic events, E_T is the total energy and E_p is the potential energy. The model introduced above allows the prediction of the number of seismic events during long-term stimulation. The release of seismic energy, which is generated in the proposed Newberry EGS reservoir

due to thermal, hydraulic and mechanical effects, is calculated for shallow ($0.5m^{-1}$) to deep zones ($0.9m^{-1}$) for small (~150m) to large (~300m) fracture spacing. These outcomes allow a comparison of the effects of the low and high fracture densities as well as small and large fracture spacing.

The characteristic event magnitude distribution that occurs in such cases is defined based on the size, population, location, and spacing of larger fractures (200-1200m). Results indicate that a higher density fracture network ($0.9m^{-1}$) with small fracture spacing (~150m) experiences significantly increased rates of event migration and is associated with a higher number of seismic events compared to those with larger fracture spacing (300m).

The largest events appear to occur close to existing large and widely spaced fractures where stress drop reaches the maximum magnitude ~3MPa. Thus the energy release from these large (~200-1200m) and closely spaced (~150m) fractures within the reservoir generate a higher number of seismic events with higher magnitude. This analysis gives significant information about the rate of migration of a seismic event within the reservoir and how it changes over time. The number of seismic events decreases during production by increasing the fracture density either for small or large fracture spacing. This behavior is related to evolving rates of thermal and hydraulic transport. The following section separately examines the rate of hydraulic and thermal transport within these reservoirs during long-term production.

3.5 Hydrodynamic and thermal front triggering of seismicity

This section discusses the mechanisms of seismic triggering by correlating the evolution of seismicity with the transit of the hydrodynamic and thermal fronts within the reservoir. The evolution of the seismicity from stimulation to production of a reservoir in the long term (i.e. 20 years) is illustrated by determining the propagation of fluid pressure and thermal fronts through the reservoir over time. Large magnitude events (1.5-1.9) are observed during early transit of the fluid pressure front transitioning to lower magnitude late-time events resulting from the secondary transit of the thermal front. Both temperature and pressure-diffusion may induce seismicity and may be related in a natural way to the triggering front concept [*Shapiro and Dinske*, 2007].

The hydrodynamic and thermal fronts are tracked as they propagate through the reservoir for various fracture networks of low to high density and at low and high initial stresses (shallow to deep zones). The location of these fronts is defined by the propagation of the fluid flow rate at any given time. The evolution of seismicity for long-term production (20 years) is shown in a radius-time plot relative to the propagation of the fluid and thermal fronts in Figure 8 and Figure 9 (injection flow rate is set at 44 *l/s* in the simulation). The figures show the progress of the fluid and thermal fronts in the reservoir, together

with the progress of induced seismicity in both zones B and D with closely spaced (~150m) and widely spaced (~300m) fractures.

Figures 8 and 9 also show the progress of the fluid and thermal fronts in the reservoir, together with the progress of induced seismicity. The advancement rates of the hydraulic and thermal fronts as functions of the different fracture characteristics are observed first with a fracture network density of $0.5m^{-1}$ in shallow zone B (Figure 8-A) and then with a density of $0.9m^{-1}$ in deep zone D (Figure 8-B), followed by an observation of both with the same large fracture spacing of ~300m. Further observations are made with a fracture network density of $0.5m^{-1}$ in the shallow zone B (Figure 9-A). A density of $0.9m^{-1}$ in the deep zone D (Figure 9-B) is used with the same small fracture spacing of ~150m in both zones.

The deepest penetration of the hydrodynamic front into the reservoir at any given time is recorded for the network with the most closely spaced fractures (~150) (i.e. with the larger fracture density ($0.9m^{-1}$)) and for zone D at a deeper depth (2750m) (Figure 9-B). This increased penetration could result from the larger permeability change for the more closely spaced network due to the immediate increase in fluid pressure as well as a drop in effective stresses. In addition, heat removal from the reservoir blocks are fastest for the most closely spaced fractures due to the (thermally) diffusive length scale defined by fracture spacing [*Elsworth*, 1989; *Elsworth and Xiang*, 1989].

Events are separated into three magnitude classifications (M_S ~1.5, 1.7 and 1.9). It is observed that the number of seismic events decays with time and distance from the injection point for each reservoir. This illustrates that most of the seismic activity is triggered by hydraulic effects at early times (days to month) relative to the initiation of stimulation. At a later time (months to years later), thermal effects (and possibly chemical effects) may contribute to the seismicity when the seismicity front lags behind the hydrodynamic front.

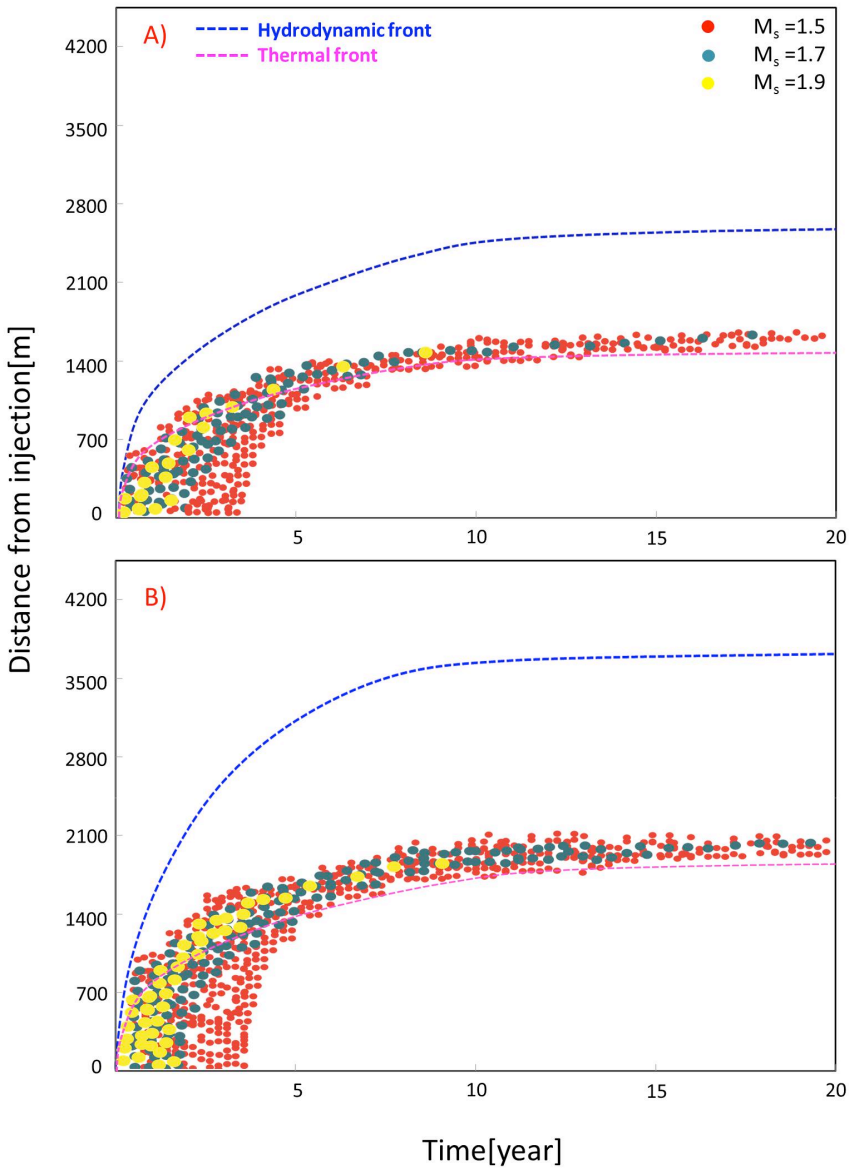

Figure 25: Radius versus time plot for short term of the progress of fluid and thermal fronts in the reservoir and of induced seismicity (injection flow rate is 44 l/s). Reservoir located at two different zones (shallow to deep) and at two different depths of 2000 and 2750 after 20 years of reservoir production. The same network of large fractures (density of 0.003 m^{-1} and spacing 300 m) applied at each zone. Larger seismic moment of individual events shown red: M_s= 1.5, blue: M_s=1.7, yellow: M_s=1.9. A) For smaller fracture (10-200m) the densities of 0.5 m^{-1} in the shallow zone B. B) Fracture density of 0.9 m^{-1}applied in the deeper zone D.

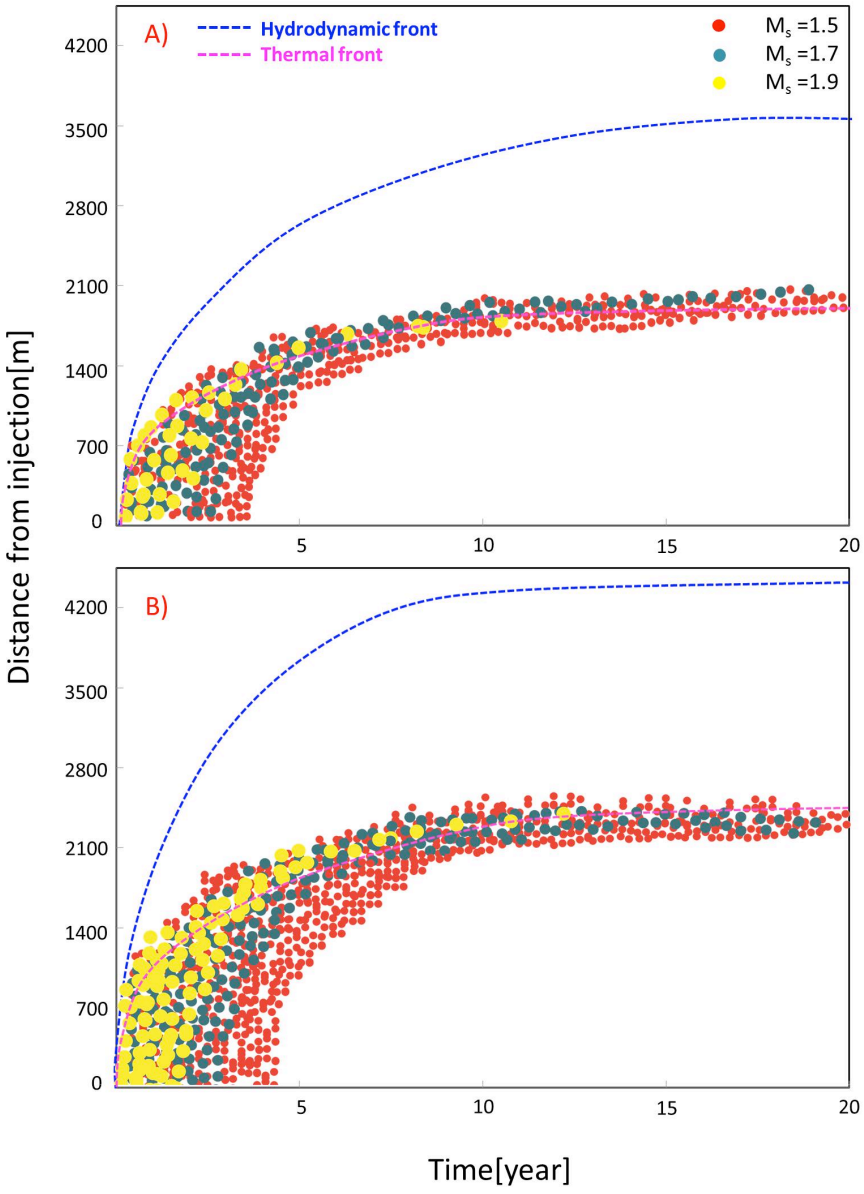

Figure 26: Radius versus time plot for short term of the progress of fluid and thermal fronts in the reservoir and of induced seismicity (injection flow rate is 44 l/s). Reservoir located at two different zones (shallow to deep) and at two different depths of 2000 and 2750 after 20 years of reservoir production. The same network of large fractures (density of 0.006 m^{-1} and spacing 150 m) applied at each zone. Larger seismic moment of individual events shown red: M_s= 1.5, blue: M_s=1.7, yellow: M_s=1.9. A) For smaller fracture (10-200m) the densities of 0.5 m^{-1} in the shallow zone B. B) Fracture density of 0.9 m^{-1}applied in the deeper zone D.

3.6 Empirical relation for seismicity occurrence during production

The cumulative number of seismic events can be expressed by the magnitude distribution [Gutenberg & Richter, 1944] in the form $log\ N_{event} = a - bM$, where N_{event} is the number of seismic events within a magnitude interval $M \pm \Delta M$. Here, a and b are constants that describe the productivity and the relative size distribution of the events, respectively.

This section discusses the scaling of event frequency, with N_{event} as a function of fluid pressure and temperature during reservoir production. The number of events as a function of time is controlled only by the cumulative mass of fluid injected, which can cause failure and result in energy release. The greater this energy release, the larger the number of events induced at a given location, and consequently the greater the probability of large-magnitude events. Thus, the model above is able to predict magnitude-frequency distributions.

The modeled *b*-value for the Newberry EGS at deeper zone D ($0.9m^{-1}$) is illustrated in Figures 10 and 11. Figure 10 corresponds to the network with larger fracture spacing (~300m), and Figure 11 is related to smaller fracture spacing (~150m).

By modeling results during stimulation [*Izadi and Elsworth*, 2014], it can be observed that the closely spaced fracture network with a higher stress regime (at the deeper level) has the largest *b*-value. This shows a greater number of events induced due to the existence of a higher density fracture network ($0.9m^{-1}$) under the prescribed conditions of higher in situ stresses compared to the lower predicted *b*-value in the shallow zone with the lower density fracture network [*Izadi and Elsworth*, 2014]. As a result, this section only considers the reservoir at the deeper level (zone D) when analyzing the change in the *b*-value during reservoir production. The main focus of this study is comparing the number of large and small seismic events associated with large and small fracture spacing when the reservoir is located at the deeper zone (D).

The largest *b*-value (~1.34) is observed during production when the reservoir is seeded with closely-spaced fractures (150m). These observations indicate that smaller fracture spacing results in both a higher *b*-value and a greater number of events; it is the dominant parameter influencing behavior.

Over longer periods of time (20 years), the largest *b*-value for the small and large fracture spacing shows more small events than large events during long-term production. The *b*-value varies from 1.14 to 1.30 for widely (300m) spaced fractures and 1.16 to 1.34 for closely (150m) spaced fractures in zone D. In both cases, the *a*-value decreases and the *b*-value increases—indicating both decreased magnitude and decreased number of events during long-term production when compared with those occurring during stimulation.

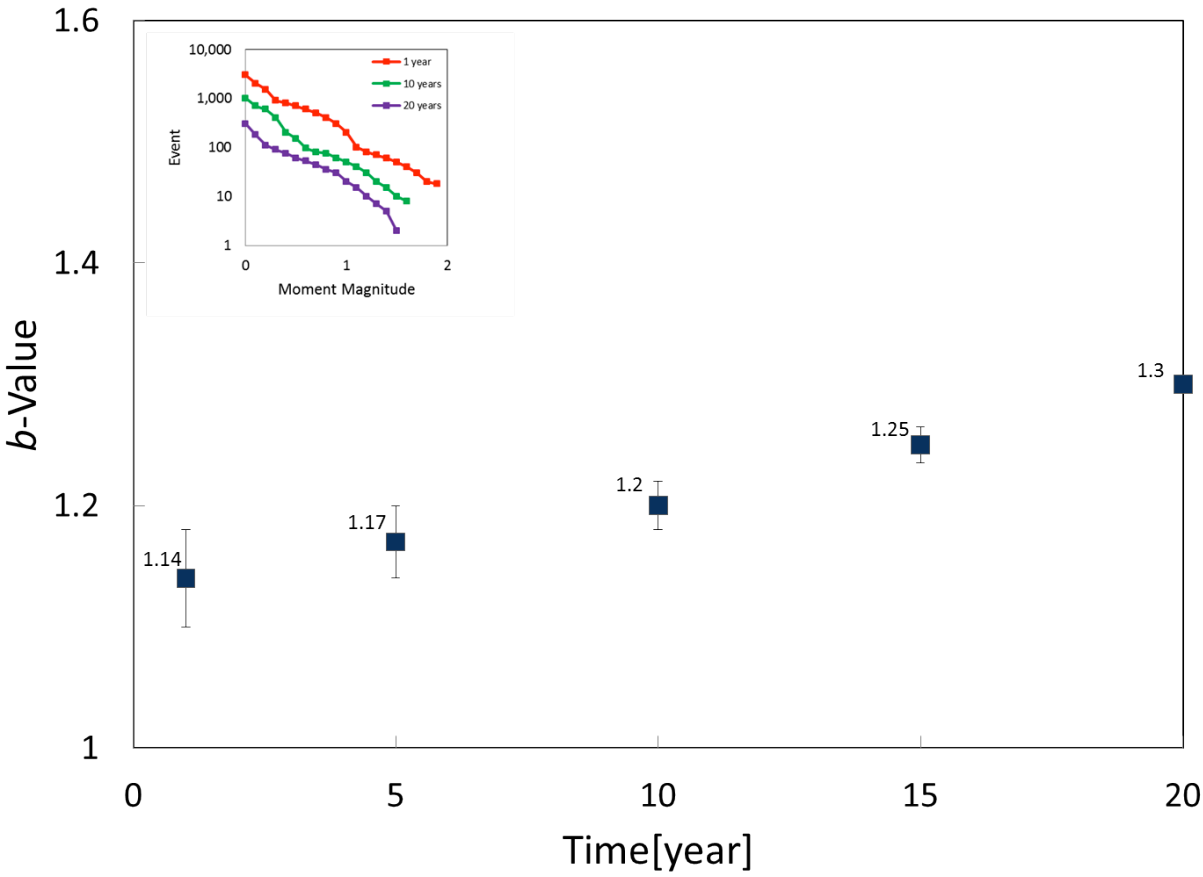

Figure 27: Number of events as a function of magnitude indicating *b*-value for moment magnitudes in the range 0-1.3 after 20 years of reservoir production. Reservoir located in shallow zone D and at depth of 2750m. *b*-values are evaluated at different times of production for the network of large fractures (density of 0.003 m^{-1} and spacing 300 m), and for the smaller fractures (10-200m) with the density of 0.9 m^{-1}.

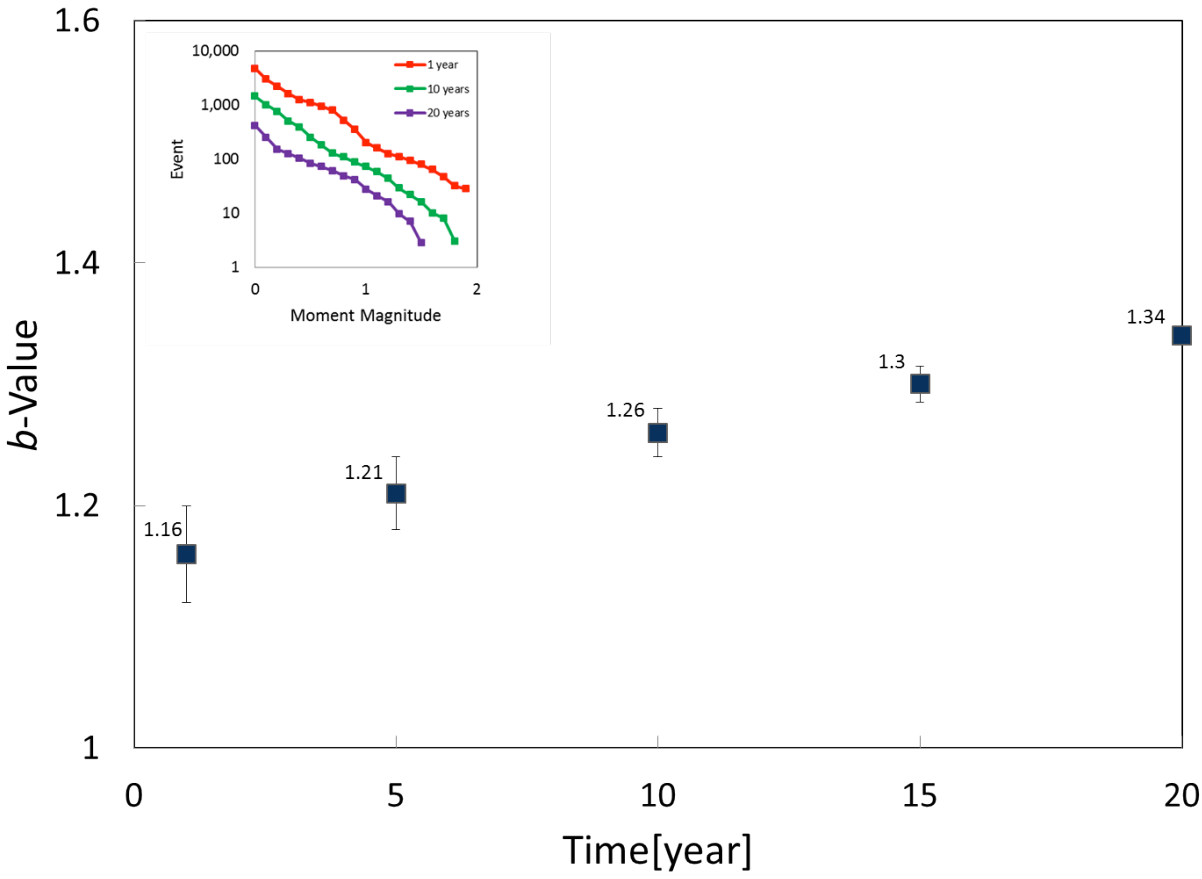

Figure 28: Number of events as a function of magnitude indicating *b*-value for moment magnitudes in the range 0-1.34 after 20 years of reservoir production. Reservoir located in shallow zone D and at depth of 2750m. *b*-values are evaluated at different times of production for the network of large fractures (density of 0.006 m^{-1} and spacing 150 m), and for the smaller fractures (10-200m) with the density of 0.9 m^{-1}.

3.7 Thermal energy

The thermal output of the reservoir is examined after 20 years of production to consider the key influence of stress state and fracture network structure on thermal production. In this circumstance, the reservoir comprises fractures with either low or high fracture density and from shallow depth (zone B) to greater depth (zone D). These models examine the sensitivity of the network with large and small fracture spacing on thermal recovery within the reservoir during long-term reservoir production.

The rate of thermal energy production is a function of the fluid mass production rate and the temperature difference between the injected and recovered fluid. The thermal energy ($E_{thermal}$) recovered from the geothermal reservoir is defined as

$$E_{thermal} = \dot{M}\, c\, \Delta T \quad (6)$$

where mass flow rate is $\dot{M}=\rho Q$, ρ is water density, Q is flow rate, and c is the specific heat capacity of the fluid. The temperature difference is $\Delta T = T_{production} - T_{injection\ fluid}$, where $T_{injection}$ is the injection fluid temperature and $T_{production}$ is the production temperature. The parameters used in the simulation are listed in Table 2. The estimated thermal energy for zones B and D, with small and large fracture spacing, is illustrated in Figure 12-C. The geometry of the reservoir for all zones is the same when the injector and producer are separated by 700m.

The flow rate and temperature profile for both shallow to deep zones (B and D) is displayed in Figures 12-A and B. The highest flow rate is observed in systems where the smallest fracture spacing (150m) and highest fracture density network ($0.9m^{-1}$) is applied. Because flow rate is a function of permeability changes as well as fracture surface area for closely spaced fractures (~150m) with higher fracture density ($0.9m^{-1}$), the migration of fluid pressures and thermal removal from blocks is much faster than for a network of widely spaced fractures (~300m).

A previous study [*Izadi and Elsworth*, 2014] illustrated that the fluid penetration in a closely spaced network (zone D) is both larger and reaches further from the injection well when compared to the wider-spaced network (zone B). Thus the increased penetration of fluid injection results in a larger initial permeability change for the more closely spaced network. The higher density network (deep zone) with a closely spaced fracture can provide a larger permeable network and lead to increased flow rates (Figure 12-A). These results illustrate that if the fracture density is increased then such a system is capable of supporting much higher flow rates, which is also beneficial for higher rates of energy recovery. Thus flow rate in the system is related to the fracture spacing and fracture density, which ultimately leads to decreased flow rates at increased fracture spacing.

Larger fracture density also increases the heat transfer area, which would significantly increase the performance of the system at an earlier time (~1 year). Higher rates of temperature decline when the zone is filled with a higher number of fractures, leading to more rapid advancement of the thermal front (Figure 12-B). By increasing the fracture spacing in shallow to deep zones, heat removal is slower compared to those with smaller fracture spacing. Such behavior illustrates that temperatures are able to change significantly during a long-term production period. This response will be fastest for the most closely spaced fractures due to the (thermally) diffusive length scale defined by fracture spacing [*Elsworth*, 1989; *Elsworth and Xiang*, 1989]. Thus, for a deeper reservoir with smaller fracture spacing (~150m), the cooling rate is fastest and the thermal transfer rate is highest.

As discussed, the more desirable system for energy recovery is achieved at early times (~1 year) when the fracture density is high and fracture spacing is small. Such a system is capable of supporting a thermal recovery close to ~10MW in zone D and ~8MW at zone B. The total thermal output of zones B, C, D and E is close to ~36MW or ~14MWe for a conversion efficiency of 40%.

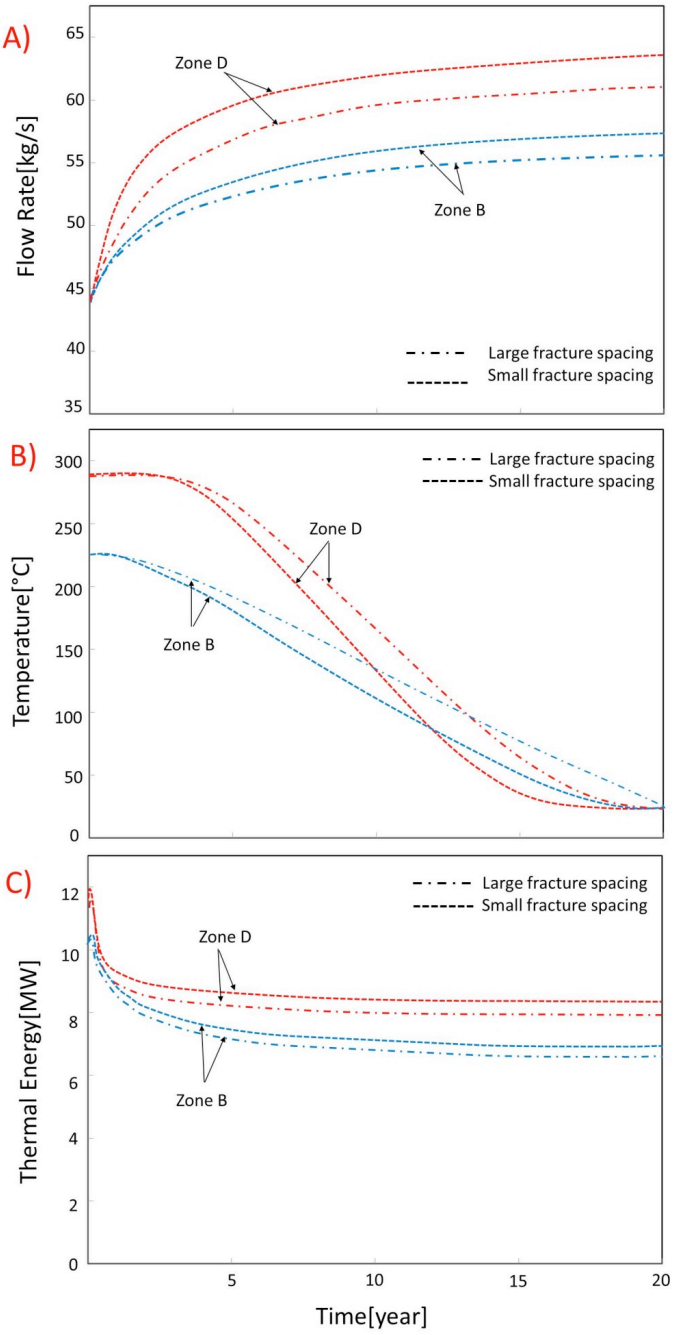

Figure 29: Flow rate, temperature? and thermal output for Newberry EGS after 20 years of production at two different depths of 2000m and 2750m. Blue dash lines relate to the network of closely and widely

spaced fractures (~150 and 300m) at shallow zone B, and red dash lines relate to the network of closely and widely spaced fractures (~150 and 300m) at deeper zone D. A) Flow rate profile. B) Temperature profile. C) Thermal recovery.

3.8 Conclusions

Using different experimental models, this paper examines the dominant behaviors influencing induced seismicity as well as heat production within EGS reservoirs during long-term production (~20 years). A THMC model is used to explore the roles of thermal- hydraulic- mechanical- and chemical-effects on different fractured reservoirs. Various fracture networks (low to high density) are considered for both closely and widely spaced fractures, and reservoir conditions change due to varying reservoir depths, shallow (2000m) to deep (2750m). These numerical models are applied to the Newberry EGS field (USA) to determine the effect of these key factors on induced seismicity during long-term (~20 years) reservoir production.

Theresults demonstrate that when a reservoir is located at greater depth and with more closely-spaced fractures (~150m), the increase of fluid circulation is higher. The permeability change is propagated further from injection and occurs in a shorter time compared to those with a widely spaced fracture network (~300m). Likewise, for the reservoir with the highest density of fractures and high initial stresses (due to greater depth) — the evolution of seismicity is more rapid (higher event rate), and its distribution expands faster with radius (zone D).

A maximum event magnitude for identical fracture distributions is M_s~1.9, a magnitude directly related to the largest fracture size (~1200m) and maximum prescribed shear stress drop (~3MPa) in the reservoir.

The hydrodynamic and thermal fronts are also defined for different fracture structure (with closely-widely spaced fractures) to determine seismicity triggering during long-term production. A higher migration rate and a quicker advancement of these fronts is observed when the zone is filled with closely spaced fractures (~150m) under the prescribed conditions of higher in situ stresses (deeper zone). As a result, larger numbers of seismic events are created due to higher flow rates when the fracture spacing is smallest.

There is a significant increase in both the number and magnitude of seismic events when the fracture density increases and fracture spacing decreases. The effects of thermal stress and pore pressure on the evolution of seismicity in reservoirs is examined separately and indicates that the most important mechanism triggering slip and promoting both the number of seismic events and the moment magnitude, is the augmentation of fluid pressure. The penetration of the hydrodynamic front is observed to be controlled principally by the size, number, location, and spacing of fractures.

When the spacing of fractures in the system is decreased, the fluid flow is able to penetrate more rapidly during injection.

We observe the propagation of fluid pressure and thermal fronts generate seismic events thorough reservoir with time. Large events at early-time (days to month) occurs due to the fluid front. Over longer periods of time (month to years) smaller seismic magnitude formed as a result of thermal (-chemical) front within reservoir.

The network with small (~150m) fracture spacing is capable of generating the highest flow rate and as a result is the fastest propagating hydrodynamic front observed. This behavior allows the system to create a large number of events with highest magnitude (1.9) from months to years after the start of injection.

We then modeled the *b*-value for different fracture networks with different fracture spacing (the *b*-value describes the fracture process within reservoirs and is related to the size, location, distribution, and spacing of fractures) and characterized the induced seismicity by the *b*-value for shallow (B) to deep zones (D). The largest *b*-value was observed at zone D, indicating a larger number of triggered seismic events (also with a larger distribution in location). The approximate *b*-value for the Newberry EGS in the deepest zone (D) for two different fracture spacing shows that the smaller fracture spacing (~150m) has the highest *b*-value. The *b*-value regime in small and large fracture spacing indicates a higher number of events when the spacing is decreased.

The temperature and flow rate profile for shallow and deep zones B and D with small and large fracture spacing was examined to evaluate the thermal recovery from these zones after 20 years of reservoir production. The highest thermal output is from the deeper zone D with a closely spaced fracture network. A high number of fractures in the system with small spacing between fractures increases the rate of cooling and contributes to having a quicker decline in temperature and also to generating a fluid flow path for a higher system flow rate. Based on the information discussed above, this paper concludes that the total thermal output for Newberry EGS at four shallow to deep zones B, C, D and E is close to ~36MW or ~14MWe.

Acknowledgements

This work is a partial result of support from the Department of Energy Office of Energy Efficiency and Renewable Energy and Geothermal Technology Program under contract EE-10EE0002761. This support is gratefully acknowledged.

3.9 References

1 Aki, K. (1967), Scaling law of seismic spectrums, J. Geo-phys. Res., 72, 1217-1231.

2 Audigane, P., J. Royer, and H. Kaieda (2002), Permeability characterization of the Soultz and Ogachi large-scale reservoir using induced microseismicity:Geophysics,67, 204–211.

3 Baisch, S. (2009), Deep heat mining basel—Seismic risk analysis, technical report, Serianex, Bad Bergzabern, Germany.

4 Cladouhos, T., S. C. Petty, W. Osborn, S. Hickman, and N. Davatzes (2011), The role of stress modelling in stimulation planning at the Newberry volcano EGS demonstration project. Thirty-Sixth Workshop on Geothermal Reservoir Engineering. Stanford, CA.

5 Deichmann, N., and D. Giardini (2009), Earthquakes induced by the stimulation of an enhanced geothermal system below Basel (Switzerland), Seismol. Res. Lett., 80(5), 784–798.

6 Delépine, N., N. Cuenot, E. Rothert, M. Parotidis, S. Rentsch, and S. Shapiro (2004), Characterization of fluid transport properties of the Hot Dry Rock reservoir Soultz-2000 using induced microseismicity, Journal of Geophysics and Engineering Volume 1 Number 1.

7 Dinske, C., S. Shapiro, and M. Häring (2010), Interpretation of microseismicity induced by time-dependent injection pressure, SEG Expanded Abstr., 29, 2125, doi:10.1190/1.3513264.

8 Elsworth, D. (1989), Theory of thermal recovery from a spherically stimulated HDR reservoir. J. Geophys. Res., Vol. 94, No. B2, pp. 1927 - 1934.

9 Elsworth, D., and J. Xiang (1989), A reduced degree of freedom model for permeability enhancement in blocky rock. Geothermics, Vol. 18, No. 5/6, pp. 691-709.

10 Evans, K., H. Moriya, H. Niitsuma, R. Jones, W. Phillips, A. Genter, J. Sausse, R. Jung, and R. Baria (2005), Microseismicity and permeability enhancement of hydrogeologic structures during massive fluid injections into granite at 3 km depth at the Soultz HDR site, Geophys. J. Int., 160(1), 388–412, doi:10.1111/j.1365-246X.2004.02474.x.

11 Goodman (1976a), Methods of Geological Engineering in Discontinuous Rocks. New York: West Publishing.

12 Goodman (1976b), Methods of Geological Engineering in Discontinuous Rocks, 472 pp., West Publishing, New York.

13 Izadi, G., and D. Elsworth (2014), Reservoir Stimulation and Induced Seismicity: Roles of Fluid Pressure and Thermal Transients on Reactivated Fractured Networks. Geothermics, Volume 51 , Pages 368-379.

14 Izadi, G., and D. Elsworth (2013), The effects of thermal stress and fluid pressure on induced seismicity during stimulation to production within fractured reservoirs. TerraNova. Volume 25, Issue 5, pages 374–380, DOI: 10.1111/ter.12046.

15 Jaeger, J. C., W. G. W. Cook, and R. W. Zimmerman (2007), Fundamentals of Rock Mechanics, Fourth Edition, 475 pp., Blackwell Publishing, Malden, MA.

16 Jung, R., F. Cornet, F. Rummel, and J. Willis-Richard (1996), Hydraulic stimulation results 1992/1993, in Baria R., Baumgärtner J., and Gérard A., eds.,European Hot Dry Rock programme, 1992–1995: Extended Summary of the Final Report to the European Community (DG XII), Contract N JOU2-CT92-0115, 31–41.

17 Kanamori, H. (1977), The energy release in great earthquakes, d. Geophys.Res., 82, 2981-2987.

18 Keylis-Borok, V. I. (1959), On estimation of the displace-ment in an earthquake source and of source dimensions, Ann. Geofisic. 12, 205-214.

19 Polak, A., D. Elsworth, H. Yasuhara, and e. al. (2003), Permeability reduction of a natural fracture under net dissolution by hydrothermal fluids. Geophys Res Lett, 30(20).

20 Purcaru, G., and H. Berckemer (1978), A magnitude scale for very large earthquakes.tectonophys.49:189-198.

21 Renshaw, C. E. (1995), On the relationship between mechanical and hydraulic apertures in rough-walled fractures. J. Geophys. Res., 100: 24629-36.

22 Rothert, E., and S. A. Shapiro (2003), Microseismic monitoring of borehole fluid injections: Data modeling and inversion for hydraulic properties of rocks, doi: 10.1190/1.1567239 Geophysics, v. 68 no. 2 p. 685-689.

23 Rutledge, J. T., and W. S. Phillips (2003), Hydraulic stimulation of natural fractures as revealed by induced microearthquakes, Carthage Cotton Valley gas field, east Texas.:Geophysics,68, 441–452. .

24 Rutqvist, J., Y. S. Wu, C. F. Tsang, and G. Bodvarsson (2001), A modeling approach for analysis of coupled multiphase fluid flow, heat transfer, and deformation in fractured porous rock. (submitted to Int J Rock Mech Mineral Sci).

25 Shapiro, S. A., and C. Dinske (2007), Violation of the Kaiser effect by hydraulic-fracturing-related microseismicity, J. Geophys. Eng., 4, 378– 383.

26 Shapiro, S. A., J. J. Royer, and P. Audigane (1998), Estimating the permeability from fluid-injection induced seismic emission, in Poromechanics, pp. 301–305, eds Thimus, J.-F., Abousleiman, Y., Cheng, A.H.-D., Coussy, O. & Detournay, E., Balkema, Rotterdam.

27 Shapiro, S. A., E. Rothert, V. Rath, and J. Rindschwentner (2002), Characterization of fluid transport properties of reservoirs using induced microseismicity:Geophysics,67, 212–220.

28 Taron, J., and D. Elsworth (2009), Thermal-hydrologic-mechanical-chemical processes in the evolution of engineered geothermal reservoirs. Int J Rock Mech Min Sci, doi:10.1016/j.ijrmms.2009.01.007.

29 Taron, J., D. Elsworth, and K.-B. Min (2009a), Numerical simulation of thermal-hydrologic-mechanical-chemical processes in deformable, fractured porous media, *International Journal of Rock Mechanics and Mining Sciences*, doi:10.1016/j.ijrmms.2009.1001.1008.

30 Taron, J., D. Elsworth, and K. B. Min (2009b), Numerical simulation of thermal-hydrologic-mechanical-chemical processes in deformable, fractured porous media, International Journal of Rock Mechanics and Mining Sciences, *46*(5), 842-854.

31 Yasuhara, H., D. Elsworth, and A. Polak (2004), Evolution of permeability in a natural fracture: Significant role of pressure solution, *Journal of Geophysical Research*, *109*(B3).

32 Yeo, I. W., M. H. De Freitas, and R. W. Zimmerman (1998), Effect of shear displacement on the aperture and permeability of a rock fracture. Int. J. Rock Mech. Min. Sci.; 35(8): 1051-1070.

33 Zoback, M., and H. P. Harjes (1997), Injection induced earthquakes and the crustal stress at 9 km depth at the KTB deep drilling site, Germany:Journal of Geophysical Research,102, 18477–18492.

4 CHAPTER 4: ANAMALOUS DISTRIBUTION OF MICROEARTHQUAKES IN THE NEWBERRY GEOTHERMAL RESERVOIR: MECHANISMS AND IMPLICATIONS

Abstract

Stimulation of enhanced geothermal system (EGS) reservoirs by fluid injection can enhance the reservoir permeability but may also result in undesired microearthquakes (MEQs). A bimodal depth distribution of fluid-injection-induced MEQs was observed in the 2012 stimulation phase of the Newberry Volcano EGS Demonstration project in Oregon, US. During 7 weeks of hydraulic stimulation of well NWG 55-29, 90% of MEQs occurred in the shallow reservoir (~ 500 m to ~1800 m), only a few occurred adjacent to the bottom of the open borehole (~ 2500 to ~3000 m) while almost no seismicity was observed in the intervening interval (~1800 m to ~2500 m). Our analysis of frictional stability using spatial models for fluid pressure diffusion of injected fluids show that the distribution of MEQs is consistent with observed casing damage, and a possible leak at ~ 700 m, and is inconsistent with migration of fluids from the casing shoe. The role of fluid injection through the ruptured casing is further supported by the analyses of shear failure and pore-pressure diffusion. Finally, the absence of seismicity at intermediate depths is consistent with our laboratory determinations of frictional stability, showing velocity strengthening frictional behavior for samples from intermediate depths, bracketed by velocity neutral and weakening behavior for samples from shallower and greater depths.

4.1 Introduction

Enhanced Geothermal Systems (EGS) technology has great potential to utilize Earth's vast thermal resources to meet the world's growing need for energy. Since natural-fractured, high-temperature geothermal systems do not necessarily have high permeability for efficient fluid circulation, they are typically stimulated via hydroshearing to recover geothermal energy sustainably and economically. Hydroshearing is achieved by injecting water at a stimulation pressure that is above the local hydrostatic pore-pressures but below the minimum principal stress. This process induces shear failure of preexisting fractures and self-propped Mode II or Mode III cracks, resulting in zones of enhanced permeability in otherwise typically low permeability crystalline rock (Evans et al., 2005; Tester, 2007). The resulting increased heat exchange area and residence time of injected fluids allows these fluids to reach optimum production temperature (Hubbert and Rubey, 1959; Majer and Peterson, 2007), increasing the production of geothermal energy.

A drawback of the hydroshearing technique is that the elevated pore-pressures during fluid injection can induce low magnitude (M_w) microearthquakes (MEQs) in the reservoir where faults are absent in the stimulated region (Bachmann et al., 2011; Majer et al., 2007; Zoback and Harjes, 1997). Additionally, the

short-term thermal cooling of the hot reservoir rock and long-term chemical interactions between the rock and the circulating fluid can also induce shear failure or even tensile failure, further enhancing the occurrence of MEQs (Elsworth and Goodman, 1986; Rutqvist et al., 2008). Clearly, the occurrence of MEQs is the result of complex coupled thermal-hydro-mechanical-chemical processes during the development of EGS.

MEQs, while posing a threat to public acceptance of EGS, provide crucial feedback on the progress of subsurface activities in EGS reservoir stimulation (e.g., crack propagation, permeability evolution, and temperature changes (Izadi and Elsworth, 2013; Majer et al., 2007). Particularly, the spatial distribution and timing of MEQs are of significance, potentially providing reliable constraints on the progress and effectiveness of stimulation, guiding optimum production of the reservoir, and ensuring the economic maintenance of reservoir life. Of particular interest in this respect are EGS sites where the seismicity distribution is anomalous. Such an anomalous distribution of MEQs was observed in an EGS Demonstration Project at Newberry Volcano, Oregon that has been operated by *AltaRock Energy Inc*. since 2009. The stimulation well (NWG 55-29) of the Newberry EGS system consists of a cased portion to ~1800 m depth followed by an open section to ~3000 m depth and was stimulated in 2012 by fluid-injection. In contrast to the expected MEQ distribution adjacent to the borehole along its entire open zone (**Figure 1a**) - including the widely observed progressive movement to greater depths of induced seismicity with time (Fehler, 1989), - the seismicity at the Newberry Geothermal Reservoir exhibited a bimodal depth distribution of MEQs (**Figure 1b**). During the seven weeks of hydraulic stimulation, a few MEQs occurred adjacent to the bottom of the open hole (within the initial 4 days) while almost no seismicity was observed in the principal stimulation zone (~1800 m to ~2500 m depth). Anomalously, 90% of the MEQs occurred above the casing shoe (at depths between 500m and 1800m over the next 46 days) adjacent to the cased portion of the well.

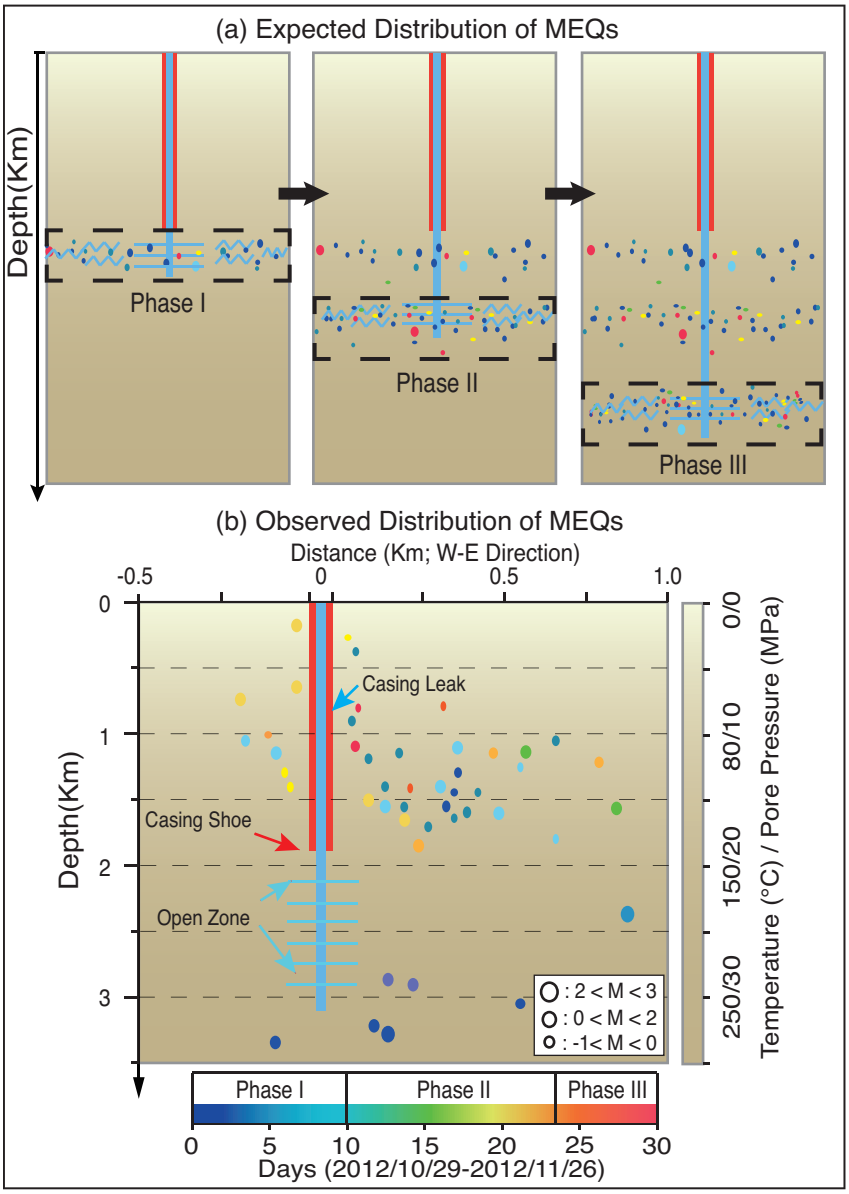

Figure 1. 2012 stimulation of Well NWG 55-29 was completed through three phases. **(a)** Expected distribution pattern of MEQs in each of stimulation phase. **(b)** Observed distribution of MEQs, showing both spatial and temporal anomalies.

We propose that the enigmatic distribution of MEQs during the stimulation may have resulted from two alternative causes: (1) Fluid injection through a leak in the casing. A segment of the casing may have been damaged in the shallow reservoir. The resulting leak would have introduced fluid overpressures and thermal stresses that could reactivate fractures. This fluid diversion in the wellbore would reduce pressures in the deep borehole (~1800 to ~3000 m depth) and staunch the potential for hydroshearing.

Alternatively, (2) the shallow casing leak may have been minimal, but migration of the injected fluid from the casing shoe (~1800 m depth) to the shallow zone (~500 m to ~1800 m depth) triggered local seismic events that began after ~5 days - again as a result of elevated pore-pressures and thermal stress.

In this study, we employ both brittle failure analyses and friction experiments to explore the mechanisms behind and implications of the observed anomalous spatial and temporal distribution of seismicity at the Newberry geothermal reservoir. Our results suggest that the bimodal seismicity distribution is due to leakage from the well at shallow depth. Moreover, we show that the absence of seismicity at intermediate depths cannot be explained by the observed stress and presumed stability regime but is consistent with alternate distributions of frictional strength and stability.

We begin with a description of the geological setting of the Newberry Geothermal Reservoir. Next, we provide the rationale behind and approach of various analyses that we conducted to obtain insight into the cause of the anomalous distribution of seismicity in the Newberry Geothermal Reservoir. Our analysis consists of four consecutive steps: we (i) define the controls on frictional stability within the shallow crust, (ii) define the anticipated timing of these events if driven by fluid migration, (iii) use the depth-stability analysis to show that if MEQs occur at depth, then they should also be present at all depths, and then (iv) explore reasons for the missing seismicity through inferred strain-hardening/velocity-strengthening behavior, constrained by experimental characterization. We assume constant frictional properties in efforts (i)-(iii) and test this assumption via the shear experiments (part (iv)). In addition, throughout theoretical analyses (i-iii), we adopt the in-situ stresses and pore-pressures as estimated in the geological setting and treat these quantities as constants.

4.2 Geological setting and methods

4.2.1 Geological setting

The Newberry Volcano has been active for 0.5 Myr and is located in Deschutes County, Oregon, ~ 40 km south of Bend and ~ 56 km east of the crest of the Cascade Range. Well NWG 55-29 cuts through a thick flat-lying sequence of tuffs and reaches a depth of ~3km west of the caldera rim of Newberry Volcano (**Figure 2a**) (Cladouhos et al., 2011). Neither ring fractures nor faults transect the stimulated injection well (Davatzes and Hickman, 2011), eliminating the possibility of vertical conduits to transmit fluids. However, pre-existing fractures are observed in the borehole (Davatzes and Hickman, 2011). We consider a normal faulting stress regime according to the World Stress Map (Heidbach et al., 2010) and take the vertical σ_v, maximum horizontal σ_H, and minimum horizontal σ_h, stresses to be zero at the surface and use gradients of 24.1, 23.5 (N-S) and 14.9-15.8 (E-W) MPa/km, respectively with an initial hydrostatic pore-pressure P_f gradient of 8.8 MPa/km. The volcanic stratigraphy and the in-situ stress regime are indicated

in **Figure 2b**. The average wellhead pressure during the stimulation was ~6 MPa (Cladouhos et al., 2011; Davatzes and Hickman, 2011).

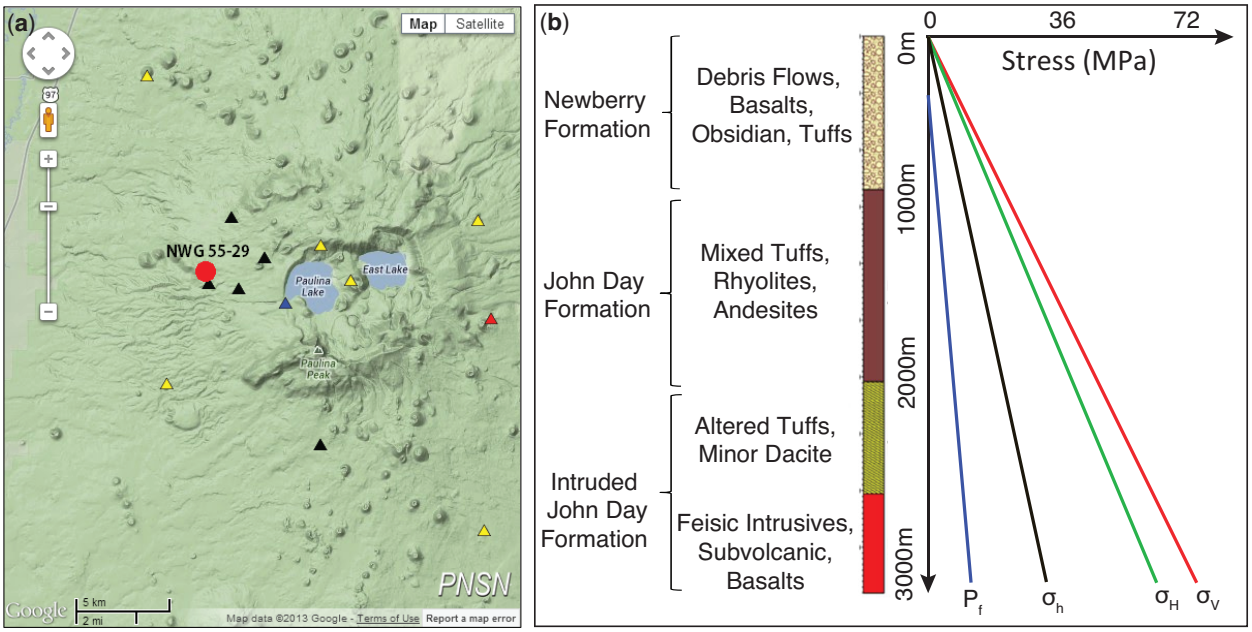

Figure 2. (a) Location of well NWG 55-29 (from Google Earth). **(b)** Stratigraphy and stress regime of well NWG 55-29.

4.2.2 Shear failure analysis

Observations such as in-situ stress measurements in deep boreholes (Zoback and Healy, 1992), seismicity induced by fluid injection (Pine et al., 1983; Raleigh et al., 2013) and earthquake triggering of secondary earthquakes (Stein et al., 1992) all suggest a state of dynamic equilibrium within the upper continental crust (Townend and Zoback, 2000). Here, we explore the potential for shear failure of critically stressed fractures throughout the depth of the geothermal reservoir. We use the Mohr-Coulomb failure criterion (**Figure 3**) to define the shear strength, τ_s, for brittle failure of pre-existing fractures:

$$\tau_s = C_0 + \mu_s \cdot \sigma_{neff} = C_0 + \mu_s \cdot (\sigma_{tot} - \alpha_b \cdot P_f) \quad (1)$$

where C_0 is cohesion; μ_s is the coefficient of friction (tangent of friction angle φ); σ_{neff} is the effective normal stress; σ_{tot} is the total normal stress; and α_b is the Biot coefficient.

The pre-existing fractures are considered to be optimally oriented for shear failure with the fracture normal at an angle θ to the maximum principal stress σ_1 (**Figure 3**).

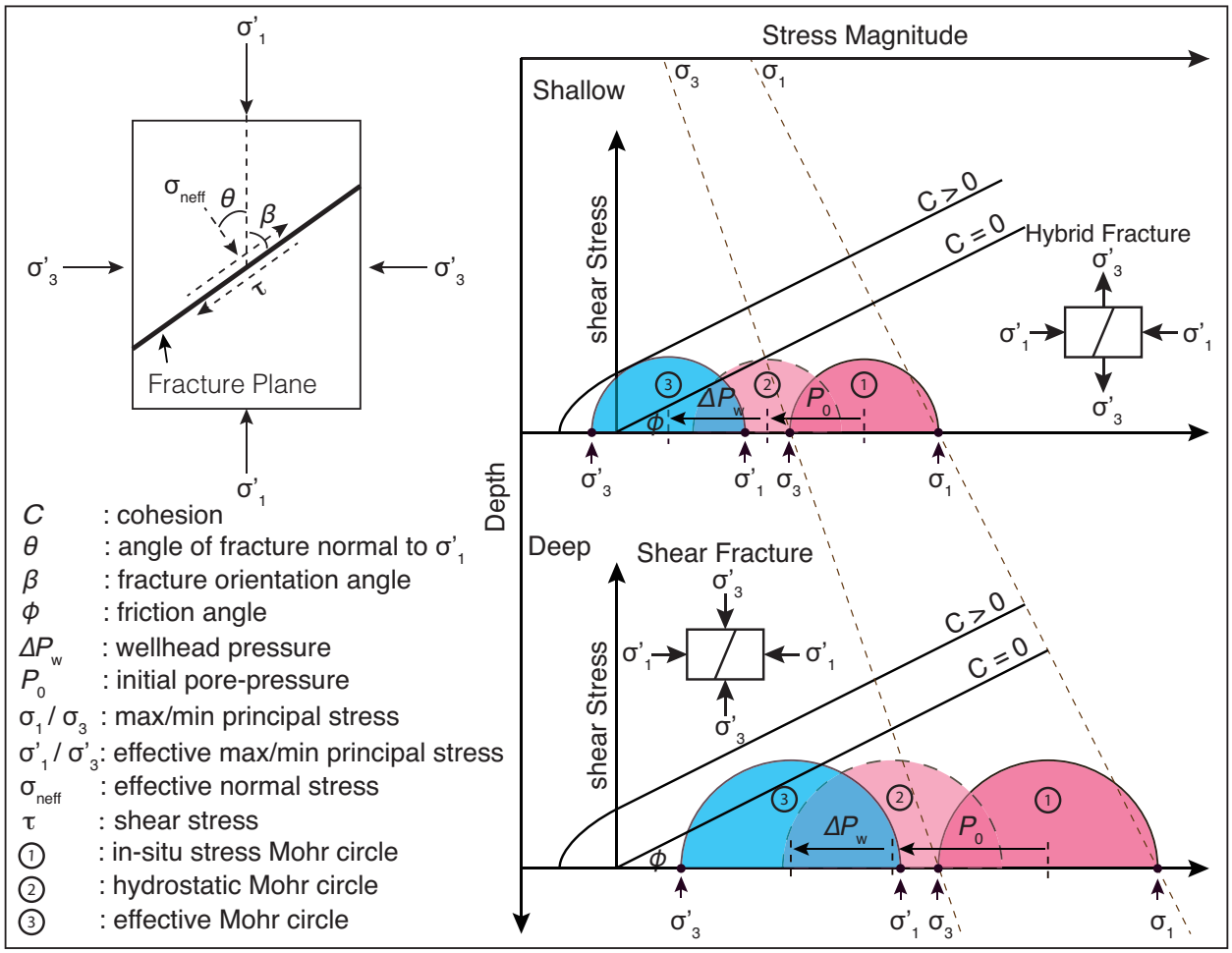

Figure 3. Schematic fracture plane with respect to stress configuration (left side) and depth and fluid pressure dependent Mohr circles (right side)

Thus, we have:

$$\sigma_{neff} = \frac{(\sigma_1' + \sigma_3')}{2} + \frac{(\sigma_1' - \sigma_3')}{2}\cos 2\theta \tag{2}$$

$$\tau = -\frac{\sigma_1' - \sigma_3'}{2}\sin 2\theta \tag{3}$$

where τ is the critical shear stress; σ_1' and σ_3' are the effective maximum and minimum principal stresses, respectively; and 2θ is equal to $\varphi+\pi/2$. In this study, σ_1 and σ_3 denote the vertical and minimum horizontal stresses, respectively. Combining Eq.(1) and Eq.(3), yields:

$$\frac{\sigma_1'}{\sigma_3'} = \frac{(\mu_s^2+1)^{1/2} + \mu_s + 2C/\sigma_3'}{(\mu_s^2+1)^{1/2} - \mu_s} \tag{4}$$

Extending the principal stress as a function of in-situ stress gradients, reservoir depth, initial hydrostatic pore-pressure, and applied wellhead pressure, we can rewrite Eq. (4) as follows:

$$F_{pot} = \frac{\sigma_1'}{\sigma_3'} = \frac{(\gamma_1 - \alpha_b \cdot \gamma_f)\cdot z - \alpha_b \cdot \Delta P_w}{(\gamma_3 - \alpha_b \cdot \gamma_f)\cdot z - \alpha_b \cdot \Delta P_w} \tag{5}$$

$$F_{crt} = \frac{(\mu_s^2+1)^{1/2} + \mu_s + 2C/\sigma_3'}{(\mu_s^2+1)^{1/2} - \mu_s} = \frac{(\mu_s^2+1)^{1/2} + \mu_s + 2C/[(\gamma_3 - \alpha_b \cdot \gamma_f)\cdot z - \alpha_b \cdot \Delta P_w]}{(\mu_s^2+1)^{1/2} - \mu_s} \tag{6}$$

where γ_1, γ_3, and γ_f, represent the gradients of σ_1, σ_3, and P_f, respectively; z is the reservoir depth and ΔP_w is the local wellhead pressure (**Figure 3**). We define Eq. (5) as the shear failure potential F_{pot} and Eq. (6) as the critical failure index F_{crt} to determine whether a critically stressed fracture would fail at a given reservoir depth. If the cohesion C_0 is null, then the critical failure index F_{crt} is controlled only by the coefficient of friction of the pre-existing fractures.

Before stimulation, F_{pot} is a constant value defined by the initial in-situ pore-pressure and in-situ stresses. During fluid injection, F_{pot} becomes a function of both depth and the fluid pressure. More realistically, injecting cold fluid in the hot reservoir induces thermal contraction of the rock, reducing the effective stresses acting on the fracture. The upper-bound for the induced thermal stress is approximated as:

$$\sigma_{thermal} = \alpha \cdot \Delta T \cdot E \tag{7}$$

where α is the linear thermal coefficient; ΔT is temperature change; E is the Young's modulus of the reservoir rocks and a full displacement constraint is assumed. This yields the shear failure potential:

$$F_{pot} = \frac{(\gamma_1 - \alpha_b \cdot \gamma_f)\cdot z - \alpha_b \cdot \Delta P_w - \sigma_{thermal}}{(\gamma_3 - \alpha_b \cdot \gamma_f)\cdot z - \alpha_b \cdot \Delta P_w - \sigma_{thermal}} \tag{8}$$

Thus the relation between F_{pot} and F_{crt} with respect to the shear failure events in the geothermal reservoir can be described as: (1) If F_{pot} is equal to or greater than F_{crt}, then shear failure may occur. (2) If F_{pot} is less than F_{crt}, then no failure occurs.

For the scenario of a casing leak in the shallow reservoir, we assume that the wellhead pressure in the leaking window is transmitted to the open zone. Thus, we use this method to examine the shear failure potential on pre-existing fractures exposed to the same ΔP_w.

4.2.3 Pore-Pressure diffusion analysis

In well injection scenarios, pore-pressure diffusion is an important factor that may influence the timing of seismicity (Evans et al., 2005; Lee and Wolf, 1998; Shapiro et al., 1997). In the low-frequency limit of Biot's (1962) equations, the pore-pressure diffusion from a borehole in a fluid-saturated porous medium is expressed as (Biot, 1956; Shapiro et al., 2002):

$$\beta\phi\frac{\partial p}{\partial t}=\frac{\partial}{\partial r}\left[\frac{\kappa}{\eta}\cdot r^2\cdot\left(\frac{\partial p}{\partial r}\right)\right] \tag{9}$$

where β is the compressibility coefficient; Φ is the porosity; p is the pressure; t is the diffusion time; r is the diffusion length; η is the viscosity of the fluid; κ is the permeability. The solution to Eq. (9) for a Heaviside pressure pulse applied at the origin (Shapiro et al., 1997) suggest that the distance from the injection point to the triggering front can be described as:

$$r^2=4\pi Dt=4\pi t\frac{N\kappa}{\eta} \tag{10}$$

where D is the hydraulic diffusivity and N is a poroelastic modulus defined as follows (Delépine et al., 2004; Lachenbruch, 1980; Shapiro et al., 1997):

$$N=[\frac{\phi}{K_f}+\frac{\alpha}{K_g}]^{-1} \tag{11}$$

where α =1-K_d/K_g; K_d is the drained bulk modulus of the dry frame; K_g is the bulk modulus of the grains; and K_f is the bulk modulus of the fluid.

We use Eq. (10) to estimate the time necessary for injected fluid to diffuse from the top of the open hole (base of the casing) to the shallow reservoir and test whether this can explain the observed timing of anomalous seismicity at shallow depths in the reservoir. We assume spherical pore-pressure diffusion in a homogeneous medium, and we focus on upward diffusion along a vertical path as this is the shortest distance to reach the shallow reservoir and thus defines the shortest critical diffusion time t_c.

4.2.4 Friction experiments

In the foregoing analyses, we have assumed constant frictional properties of the geothermal reservoir rocks. However, in reality, the frictional characteristics are expected to depend on factors such as rock composition and the depth-dependent in-situ pressure and temperature conditions (den Hartog and Spiers, 2013). Hence, we performed friction experiments to determine the frictional properties of pre-existing

fractures as a function of depth and as such provide insight into the mechanisms of the anomalous distribution of seismicity.

Sample material and experimental procedure

We collected 5 samples from drilling cuttings from well NWG 55-29 for friction experiments. Samples 1 and 2 were collected from the shallow reservoir where abundant MEQs occurred, while samples 3 to 5 were taken from the missing seismic zone at depths between ~1800 m and ~3000 m. After cleaning the samples to remove the drilling mud and possible drill bit fragments, the samples were crushed and powdered in a disc mill, and finally sieved to a particle size less than 150 μm. The mineralogical composition of the samples was characterized via X-Ray Diffraction analysis (XRD), which shows that the samples were dominated by three groups of minerals: carbonate (mainly calcite), phyllosilicates and tectosilicates (**Table 1**).

Table 1. Information of drilling core samples from stimulation well NWG 55-29

No.	Depth (m)	Formation	Mineral Compositions
S1	~701	Newberry	81% albite, 17% clinopyroxene, 2% hematite
S2	~1407	John Day	49% andesine, 14% calcite, 13% montmorillorite, 11% clinochlore, 7% quartz, 3% vermiculite
S3	~2139	Intruded John Day	60% albite, 20% quartz, 14.8% clinochlore, 3.5% calcite, 2.6% muscovite
S4	~2603	Intruded John Day	70% albite, 12% quartz, 11% phlogopite, 2.5% chlorite, 2.1% stilbite, 0.5% calcite, 1.9% others
S5	~2904	Intruded John Day	56.4% albite, 23.6% quartz, 14.6% orthoclase, 4.4% clinochlore, 0.6% muscovite, 0.4% calcite

The experiments were performed with a biaxial testing apparatus (**Figure 4a**), using the same set-up and following similar procedures as (Samuelson et al., 2008). In this machine, two gouge layers are sandwiched between three roughened steel forcing blocks with a contact area of 50 x 50 mm^2. We performed experiments at room temperature on water-saturated gouge layers with an initial thickness of 5

mm. To ensure that gouge layers were flat and identical in each experiment, they were constructed using a leveling jig and a measured mass (Frye and Marone, 2002).

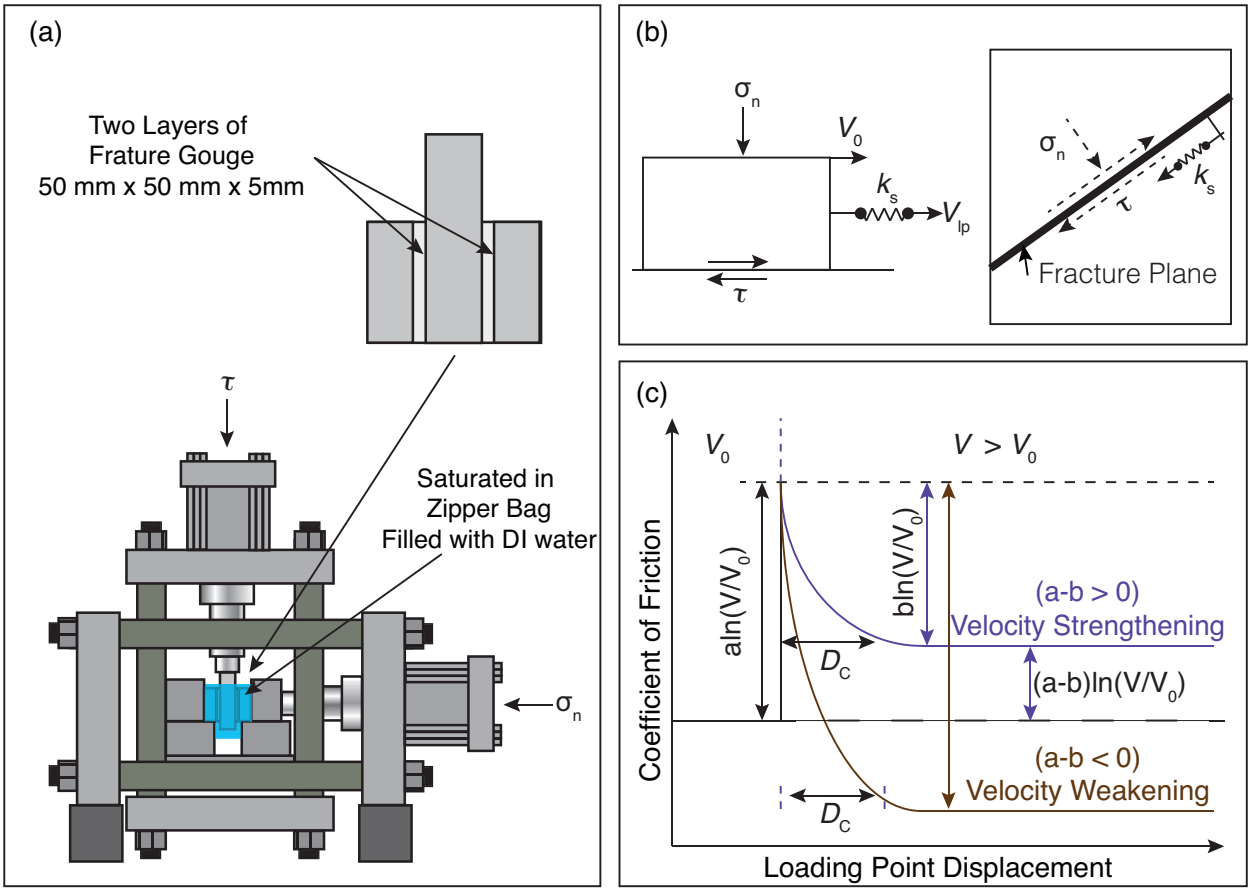

Figure 4. **(a)** Double-direct shear geometry in a biaxial load frame. **(b)** Conceptual sliding model representing the fracture/fault sliding behavior. **(c)** Idealized RSF friction response to an increased velocity step showing two alternative frictional behaviors: velocity strengthening and velocity weakening.

Shear loading was attained by forcing the central block down at a constant velocity of 10 μm/s, while applying a normal load of 15 MPa perpendicular to the shear direction. After the achievement of steady-state friction, the sliding velocity was stepped in the range from 1 μm/s to 300 μm/s until a displacement of 9 mm was reached. The normal stress was next raised to 45 MPa and the velocity sequence was repeated, reaching a final displacement of 18-20 mm. The effect of calcite on the frictional properties of the Newberry samples was tested by performing additional experiments on samples 2 and 4 after leaching with 12% hydrochloric acid to remove the calcite.

Data analysis

We calculated the coefficient of friction μ as a function of shear displacement for our experiments using $\mu = \tau / \sigma_n$. The velocity dependence of friction was interpreted in the framework of the rate and state friction (RSF) theory (**Figure 4b**) (Dieterich, 1979, 1978; Ruina, 1983). In the RSF approach to modeling fracture slip, the friction coefficient is written as (Dieterich, 1978; Marone, 1997; Scholz, 1998):

$$\mu = \mu_0 + a \ln\left(\frac{V}{V_0}\right) + b \ln\left(\frac{V_0 \theta}{D_c}\right) \tag{12}$$

$$\frac{d\theta}{dt} = 1 - \frac{V\theta}{D_c} \tag{13}$$

where μ_0 is the coefficient of friction at a reference velocity V_0; θ is a state variable, a and b are friction parameters which represent, respectively, the effect of instantaneous and displacement-dependent changes in friction from V_0 to V=eV_0; and D_c is the critical slip distance over which evolution to a new steady state takes place. Frictional slip instability is determined in part by the parameter (a-b) derived from Eq. (12) for a finite step in velocity, yielding (Dieterich, 1979; Ruina, 1983; Scholz, 1998):

$$a - b = \frac{\Delta \mu_{ss}}{\Delta \ln V} \tag{14}$$

A positive value of (a-b) denotes velocity-strengthening behavior indicative of stable, aseismic slip (Gu et al., 1984), while a negative a-b indicates velocity-weakening behavior, which is potentially unstable (**Figure 4c**). The RSF friction parameters were determined from our experiments by solving Eqns. (12) and (13), coupled with an equation describing elastic interaction with the testing machine, using the fitting method described by Marone (1998) and Blanpied et al. (1998).

Frictional stability depends on the critical stiffness K_c defined as:

$$K_c = \frac{\sigma_n (b - a)}{D_c} \tag{15}$$

As shown by Gu et al. (1984), instability may occur if the loading stiffness K is smaller than the effective-rheologic stiffness K_c.

If we assume a circular dislocation (fracture) in a homogeneous medium, the effective shear stiffness around a fracture of diameter L is (Chinnery, 1969; Scholz, 2002; Starr, 1928):

$$K = \eta \cdot \frac{G_s}{L} \tag{16}$$

where η is a geometric factor and G_s is the shear modulus. Assuming the crack in the reservoir is penny-shaped, η has the value of $7\pi/24$. Combing Eq. (15) and Eq. (16), we find that the critical fracture length L_c for instability is:

$$L_c = \eta \cdot \frac{G_s \cdot D_c}{\sigma_n \cdot (b - a)} \tag{17}$$

For fractures smaller than L_c, (i.e., $K > K_c$) stable sliding will occur, while for those larger than L_c (i.e., $K < K_c$), unstable slip can result.

4.3 Results

4.3.1 Shear failure analysis

Failure may be induced on critically oriented fractures in the reservoir by the application of sufficient wellhead pressure. **Figure 5a** shows that when the friction angle of fractures is 30° and the wellhead pressure is 3 MPa, the F_{pot} at each depth is larger than that of F_{crt}, implying that all the critically stressed fractures will fail to slip at all depths. If fractures are frictionally stronger, the F_{crt} in the deeper reservoir will be larger than F_{pot}, resulting in a stable region in the deep reservoir, but rendering the shallow reservoir unstable ($F_{pot} > F_{crt}$). Increasing wellhead pressure (e.g., from 3 MPa to 6 MPa) can both enlarge the regions of hybrid fracturing (shear failure and tensile failure) and hydroshearing where $F_{pot} > F_{crt}$ (**Figure 5b**). In addition, when thermal stresses are considered at each depth (quenching), the zones of instability spread.

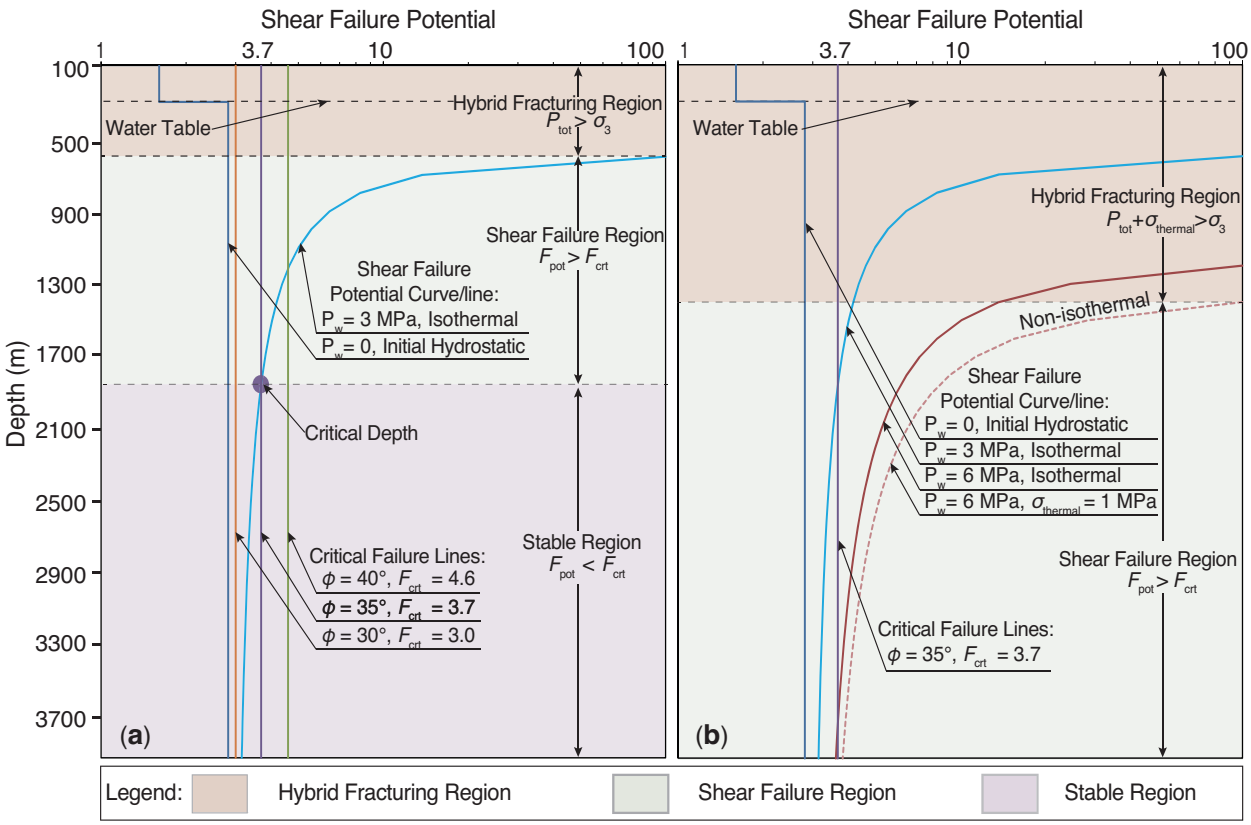

Figure 5. Shear failure potential and critical failure as a function of depth for wellhead pressure applied at all depths. **(a)** Effect of coefficient of friction of pre-existing fractures. Assuming the friction angle is 35°, the value of shear failure potential (blue curve) is greater than that of the critical failure line (purple line) above the critical depth at ~1900 m, while it is smaller below this depth. If the fracture has a larger (or smaller) friction angle than 35° (or 30°), the stability region will increase (or decrease). **(b)** Effects of magnitude of wellhead pressure and thermal stress. When wellhead pressure increases from 3 MPa to 6 MPa, the shear failure region will be enlarged with depth. Thermal stress will enhance the instability along the depth.

4.3.2 Pore-Pressure diffusion

We consider a possible migration of fluids from the deep open zone (top of the open zone at ~ 2000m) to the shallow seismic zone and calculate pressure-diffusion under two end-member permeability scenarios: 1) migration through high permeability fractures (k = 10 mD) and 2) migration through low permeability matrix (k =10 μD). During the stimulation, injection of water was completed in three cycles: about 7 days for the first cycle, then 7 days for the second cycle and 14 days for the third cycle after a hiatus of 7 days (**Figure 6a**). The depths of seismic events with time are indicated in **Figure 6b**. The timing of these

seismic events indicates an appropriate synchronous response to the injected wellhead pressure. The rate of pore-pressure diffusion in the fractures and rock matrix shows a significant difference that in the first injection cycle, the vertical distances from the depths of all seismic events to the reference depth are larger the pore-pressure diffusion length through the matrix.

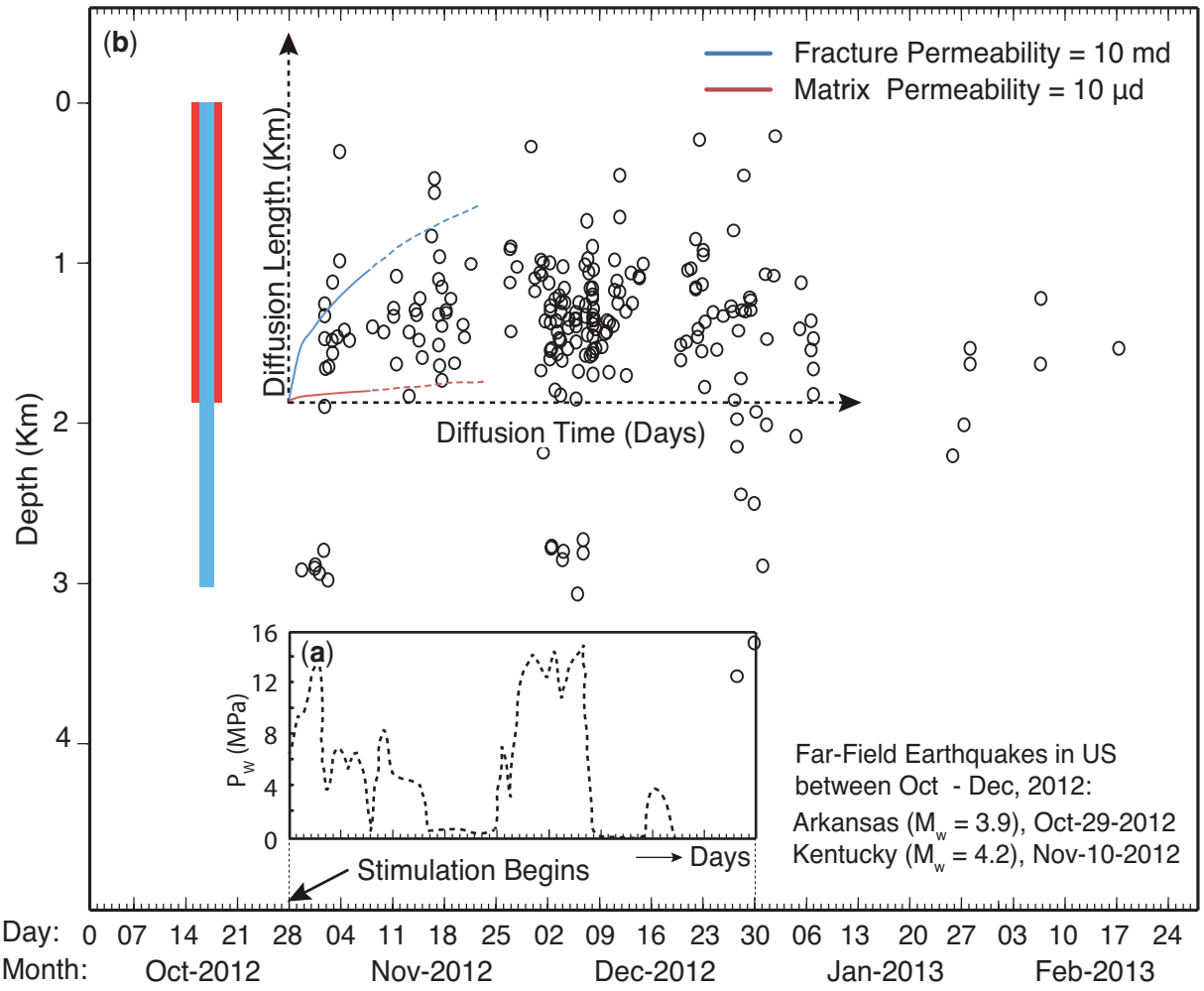

Figure 6. (**a**) Injection wellhead pressure with time. (**b**) Pore-pressure diffusion length with time compared with elevations of seismic events with time. The vertical distances between the top of uncased wellbore portion and some seismic events in shallow reservoir (above 1000 m) are beyond the maximum diffusion front when reservoir permeability is 10 md.

4.3.3 Friction experiments

A preliminary appraisal of the observed seismicity by both lithostatic (Section 3.1) and distributed parameter models (Section 3.2) suggests that if shear failure occurred in the deep reservoir (~3000 m) it

should also occur in the upper open zone. Thus the observed bimodal distribution of seismicity cannot be fully explained by a model with uniform frictional properties with depth. Therefore, we determined the frictional slip stability as a function of depth from our shear experiments to clarify the distribution of MEQs.

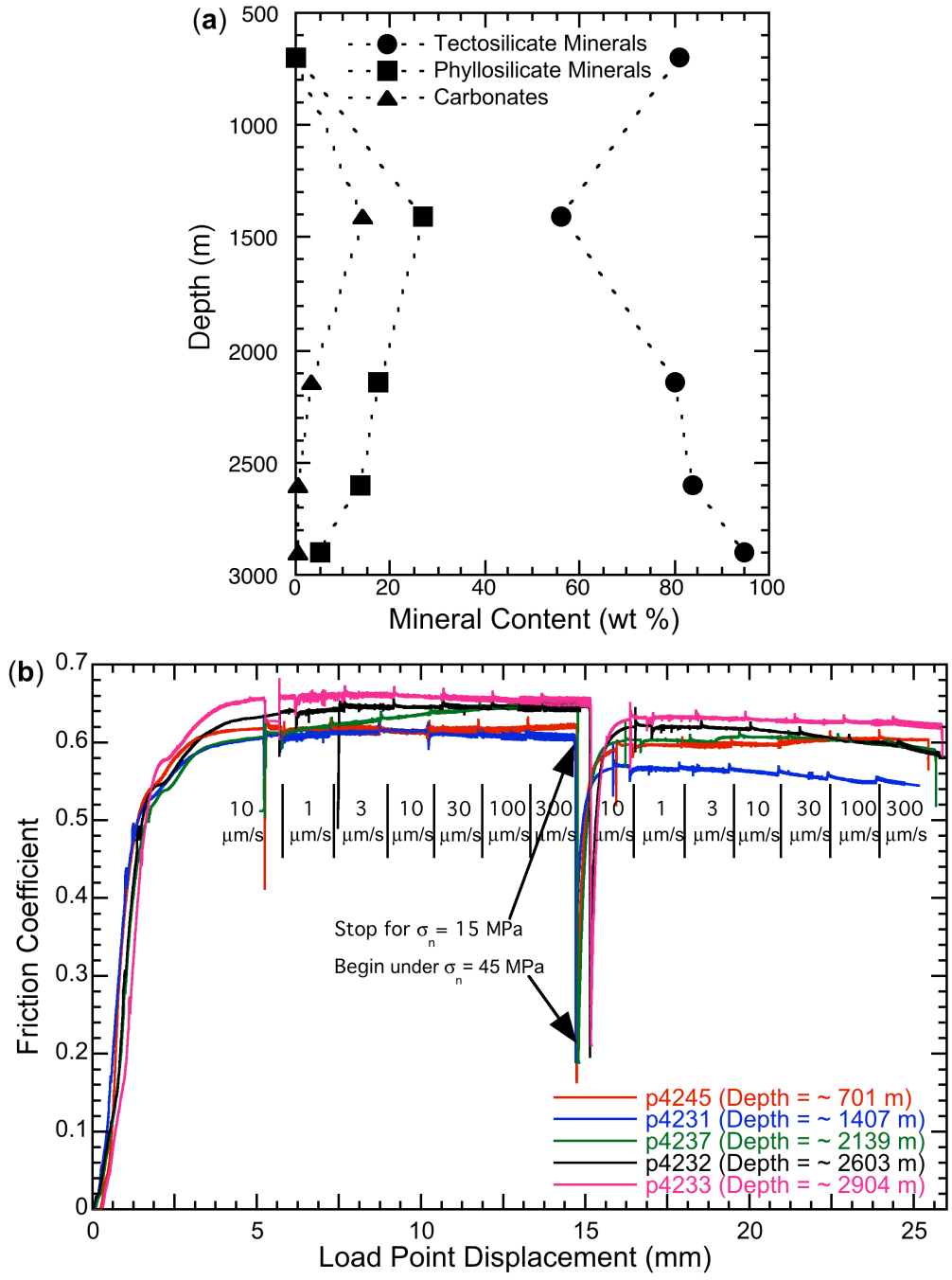

Figure 7. **(a)** Mineral contents with depths. **(b)** Friction-load point displacement curves of examined samples under normal stresses of 15 MPa and 45 MPa, respectively.

The composition of the samples used for the experiments is plotted versus depth in **Figure 7a**. All samples are dominated by tectosilicates with lesser amounts of phyllosilicates and calcite. The phyllosilicates and calcite contents reach a maximum at a depth of ~1500 m while the amount of tectosilicates is lowest at this depth. The friction curves of all shear experiments were similar (**Figure 7b**). The friction coefficient measured at the end of each constant normal stress portion (i.e. at displacements of 9 and 18 mm for 15 and 45 MPa, respectively) are plotted in **Figure 8** versus depth, while (*a*-*b*) values at 15 and 45 MPa normal stress are shown versus depth in **Figure 9** and **10.**

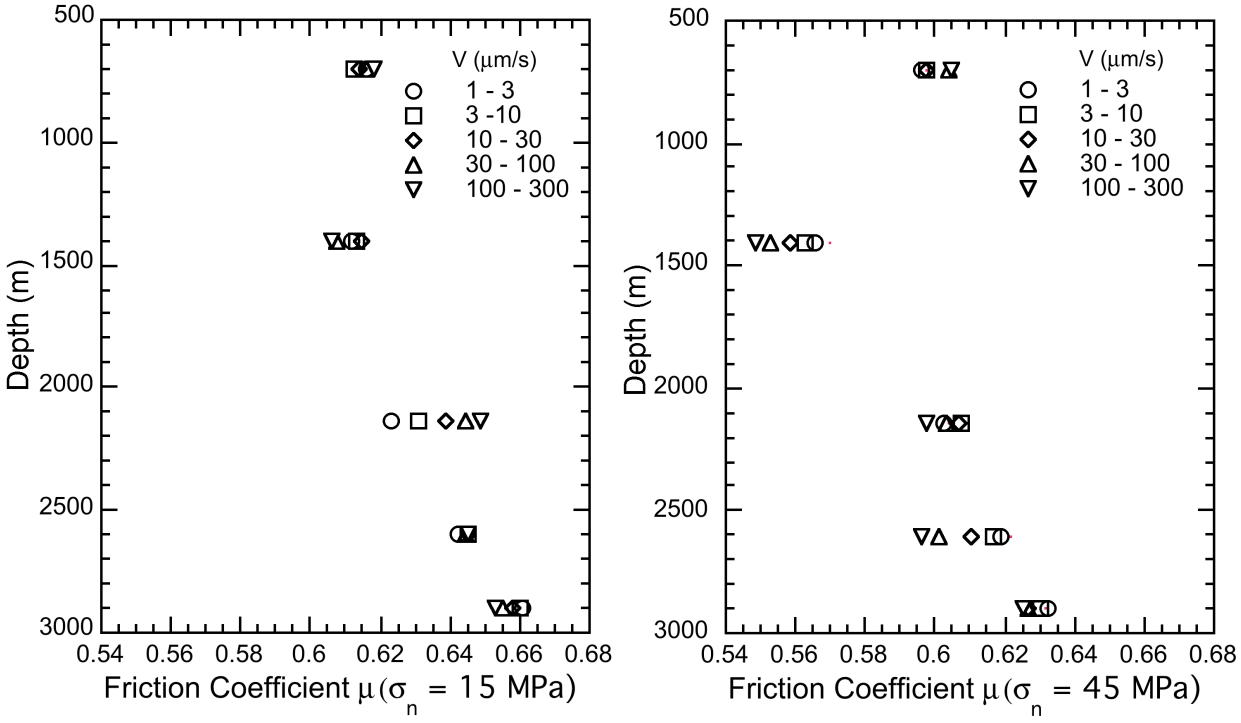

Figure 8. Steady sliding friction μ of examined samples with depths before each velocity step under normal stresses of 15 MPa and 45 MPa, respectively.

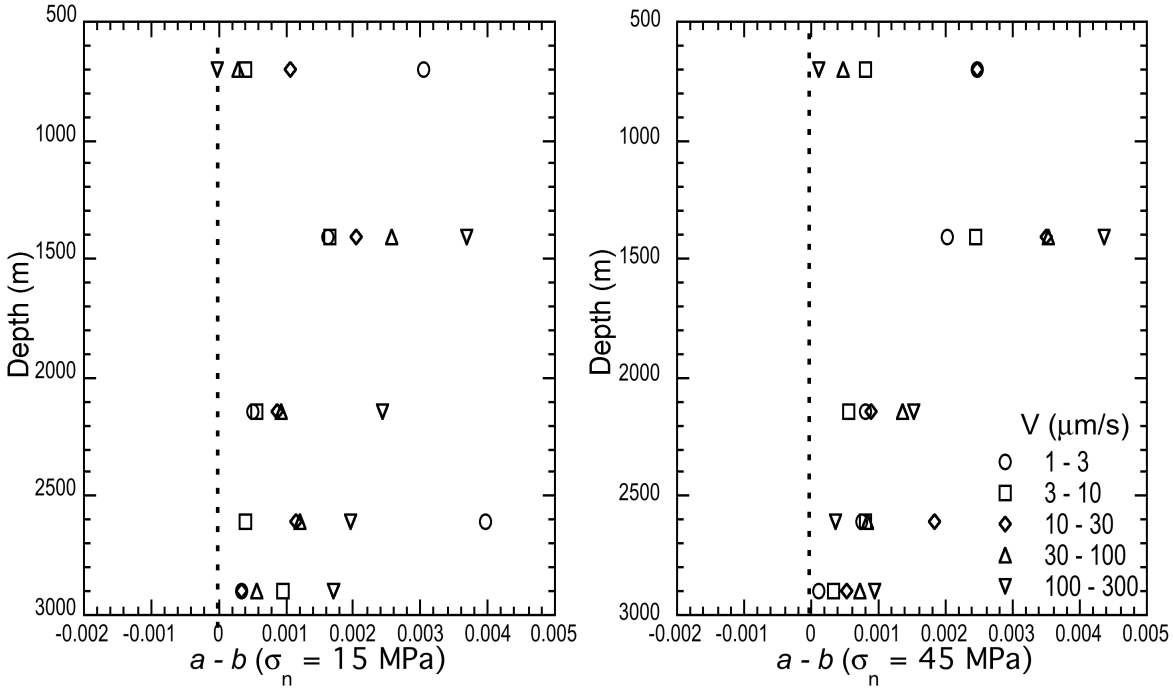

Figure 9. Friction parameter (*a*-*b*) of examined samples with depths for each velocity step under normal stresses of 15 MPa and 45 MPa, respectively.

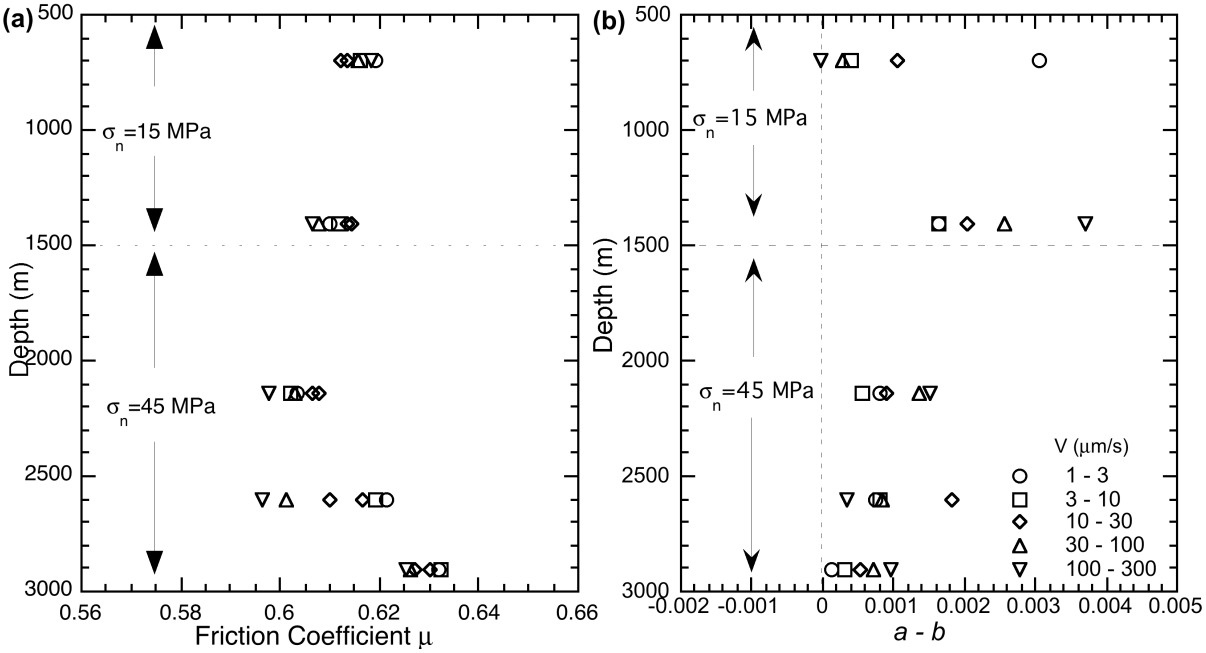

Figure 10. **(a)** Friction coefficient μ and **(b)** parameter (*a*-*b*) with depths of approximate in-situ normal stress.

The measured (*a*-*b*) values of samples are predominantly positive (velocity strengthening) at the conditions of our experiments. At shallow depth (~700 m) and at the base of the open zone (~ 2900 m), the (*a*-*b*) magnitudes are near zero or close to velocity neural, while at ~1400 m, (*a*-*b*) is more positive, representing more velocity strengthening behavior. The (*a*-*b*) values of samples with/without calcite at 15 MPa and 45 MPa normal stress are shown in **Figure 11**.

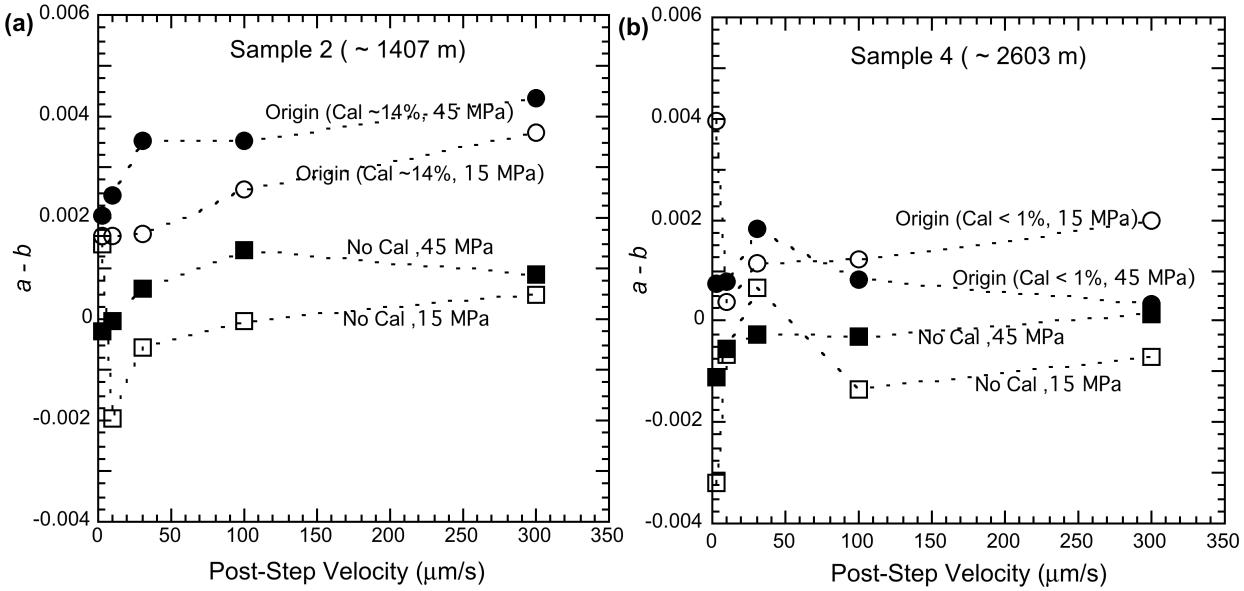

Figure 11. Comparison of frictional parameter (*a*-*b*) between calcite contained and calcite removed sample 2 and 4.

The results show similar trends of composition of samples and friction properties with depth, suggesting a possible mineralogical control on the MEQs at intermediate depth. The critical friction slip distance increases with post-step velocity (**Figure 12a**). We used the modeled RSF parameters along with a bulk modulus of 17 GPa and Poisson ratio of 0.27 (Izadi and Elsworth, 2013; Li et al., 2012) to estimate the critical fracture radius L_c for frictional instability and earthquake nucleation. The fracture length increases with increasing sliding velocity (**Figure 12b**). Our data suggest a minimum fracture radius of ~7 m.

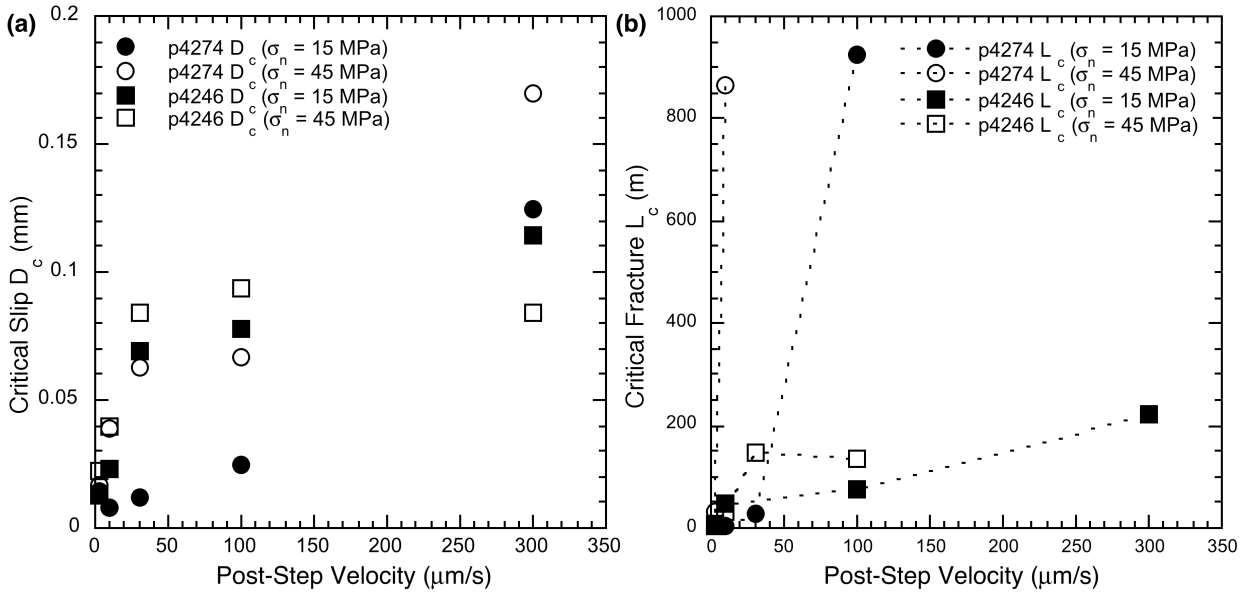

Figure 12. **(a)** Critical slip distance and **(b)** critical fracture length with increasing velocity.

4.4 Discussion

Considering the first possible cause that the casing leak in the shallow reservoir may contribute to the bimodal distribution of the MEQs, shear failure analysis indicates that the newly introduced fluid penetrating the shallow reservoir (above ~ 1800 m) due to casing leak will enhance local instability of fractures and induce MEQs. The less critically oriented fractures in the shallow reservoir could also be reactivated due to the higher shear potential F_{pot} compared to that of the deep reservoir (~ 3000 m), resulting in more seismic events. Meanwhile, wellhead pressure ΔP_w in the open zone (below ~ 2000 m) will decrease due to the shallow casing leak. As a result, the residual ΔP_w in the open zone may not be sufficient to continue reactivating local pre-existing fractures, which explains why the MEQs diminish in the deep zone (~ 3000 m).

For the second possible cause, pore-pressure diffusion analysis demonstrates that, for reservoir fractures with a permeability of 10 mD, the estimated fluid migration time does not match the timing of the observed shallow MEQs within the initial 4 days of stimulation. Furthermore, the previous logging and testing of well NWG 55-29 suggests that the pre-existing fractures lack significant permeability (estimated at ~10 μD in impermeable zone and ~3.25 mD in permeable zone) (Petty et al., 2013; Spada et al., 2013). Hence, a realistic diffusion length should be considerably shorter than the upper-limit end-member scenario and it is plausible that the water cannot migrate upwards and generate critical overpressures sufficiently quickly. As a result, the unmatched timing between MEQs and fluid migration

(**Figure 6**) implies that the deep injected fluid is unlikely to be the major cause of early shallow seismic events.

Based on our friction experiments, and previous studies, we consider four factors that may be important to explain the missing seismicity at intermediate depths: *viz.* contrasting mineral compositions, pore-pressures, temperatures and fracture sizes at the sampled depths in the reservoir. In terms of mineralogy, frictional strength μ shows the opposite trend compared to parameter (*a*-*b*) with depth. The phyllosilicate-rich materials exhibit low frictional strength and velocity-strengthening behavior while tectosilicate-rich materials show high frictional strength with velocity-neutral (or minimum velocity-weakening behavior) (**Figure 7a** and **Figure 10**) suggesting that (*a*-*b*) and μ are strongly mineral group dependent. This relation is also observed in previous studies (Ikari et al., 2011; Kohli and Zoback, 2013; Niemeijer and Collettini, 2013). The comparison of (*a*-*b*) values between samples with calcite and those in which the calcite was removed shows that dissolving the calcite decreases (*a*-*b*) at room temperature (**Figure 11**), implying that the dissolution of calcite can decrease frictional stability. Because wet calcite-rich fault gouge exhibits stable slip below 80°C ~100°C, unstable slip at 100°C ~ 550°C, and is stable again at 590°C (Verberne et al., 2014), (*a*-*b*) values of samples at in-situ temperatures (100°C ~ 250°C) are expected to be lower than the values measured in the current experiments conducted at room temperature. However, the effects of calcite on (*a*-*b*) values are expected to be minimal in the deep reservoir where the calcite content is negligible. This is supported by our result showing similar (*a*-*b*) values for sample with and without (~0.5%) calcite.

Pore pressure is another important factor that may influence frictional slip stability (Scholz, 1998). In our experiments, we observed that the (*a*-*b*) values of samples from the shallow reservoir are slightly lower when deformed at a normal stress of 15 MPa as opposed to 45 MPa. Samples from the deep reservoir, on the other hand, show slightly higher values at 15 MPa than at 45 MPa. Although the differences are small, they suggest that a reduction of the effective normal stress brought about by an increase in the pore pressure due to plausible casing leak in the shallow reservoir may result in a lower local (*a*-*b*) value, while increasing the pore pressure due to fluid injection in the deep reservoir can increase the local (*a*-*b*) value.

In summary, from the above we infer that the *in-situ* frictional slip stability of the shallow reservoir could have been less than implied by our measured (*a*-*b*) data, because: 1) the temperature of the calcite-rich shallow reservoir (~1400 m) is about 100°C and previous studies suggest that (*a*-*b*) values are lower at this higher temperature; 2) An abrupt increase in fluid pressure as a result of casing leak in this calcite-rich region also decreases frictional stability and 3) low temperature leaking fluid dissolves the calcite, resulting in a further reduction of (*a*-*b*). In addition, (*a*-*b*) values at these depths are very small and close

to velocity neutral. Thus the perturbation by the increased pore-pressure as well as the temperature effect may result in a shift of local *a-b* magnitudes from positive to negative.

In the zone where seismic events are absent, the calcite content of samples decreases with depth and is negligible at the base of the open zone. Thus the measured positive (*a-b*) values in the deep reservoir may be slightly influenced by the temperature that promotes velocity-weakening behavior in calcite (i.e., (*a-b*) values may be slightly lower than the measured ones). However, this slight effect is offset by the pore-pressure perturbation that increasing local fluid pressure (or decreasing effective normal stress) at greater depths will have, thereby increasing local *a-b* values (i.e., local frictional stability is enhanced). As a result, the measured positive *a-b* values may be close to the in-situ values, implying that only aseismic events could occur in the deep zone. Furthermore, the migration of cold injected fluid through the fractures could remove the retrograde-soluble calcite and may gradually decrease the (*a-b*) values. In this manner the initial velocity strengthening properties of preexisting fractures could be transformed to velocity weakening, with the potential for frictional instability.

In addition to mineralogical influences on stability, the distribution of fracture sizes is an important factor to determine the potential for instability when (*a-b*) values are negative. Our results suggest that only fractures with negative (*a-b*) values and lengths (radius) greater than ~7 m may slip unstably. However, fractures with length less than 7 m are conditionally stable. If *in-situ* fault creep velocities are slower than the experimental sliding velocity, the real critical fracture length could be smaller than the lowest fracture length derived from our data. Based on this analysis, we can speculate that, if the (*a-b*) values of the preexisting fractures were initially negative, then fracture lengths in the stable aseismic zone must be smaller than this threshold of ~7 m. This speculation needs to be validated by further *in-situ* reservoir fracture characterization.

4.5 Conclusion

Differing from other expected distribution patterns of induced MEQs with depth, this bimodal depth distribution of MEQs at the Newberry geothermal reservoir suggests unusual controls by fluid permeation and reservoir mineralogy and state. Our analyses introduce the following conclusions: (1) The unusual and unexpected penetration of excess fluid pressures in the shallow zone is plausible mainly due to the casing leak in the shallow reservoir. This result is further confirmed by the second observation that indeed the casing is damaged at shallow depth (~700 m). (2) The diminished seismicity in the deep open zone is plausibly associated by fluid loss (wellhead pressure drop) as a result of the shallow leak. (3) An upward-migrating fluid pressure pulse is incapable of inducing seismicity in the shallow reservoir (above ~1000 m), but may partially contribute to the occurrence of seismicity near the top of casing shoe (~1800 m). (4) The observation of missing seismic events between ~1800 m and ~2500 m during the stimulation

plausibly results from slight velocity strengthening properties in the reservoir and in particular on local preexisting fractures. Aseismic events may still occur in this intermediate zone, in the form of slow sliding slip or creep events, but may be below the threshold observed by the seismic monitoring.

Acknowledgement

This work is the result of partial support provided by DOE Grant DE-EE002761 and NSF grants EAR1045825, and EAR1215856. This support is gratefully acknowledged.

4.6 References

1 Bachmann, C.E., Wiemer, S., Woessner, J., Hainzl, S., 2011. Statistical analysis of the induced Basel 2006 earthquake sequence: Introducing a probability-based monitoring approach for Enhanced Geothermal Systems. Geophys. J. Int. 186, 793–807. doi:10.1111/j.1365-246X.2011.05068.x

2 Biot, M.A., 1956. Theory of Propagation of Elastic Waves in a Fluid-Saturated Porous Solid. II. Higher Frequency Range. J. Acoust. Soc. Am. doi:10.1121/1.1908241

3 Blanpied, M.L., Marone, C.J., Lockner, D.A., Byerlee, J.D., King, D.P., 1998. Quantitative measure of the variation in fault rheology due to fluid-rock interactions. J. Geophys. Res. Solid Earth 103, 9691–9712. doi:10.1029/98JB00162

4 Chinnery, M.A., 1969. Theoretical fault models, in A symposium on Processes in the Focal Region, 37, edited by K. Kasahar and A.E. Stevens. Publ. Dom. Obs. Ottawa 211–223.

5 Cladouhos, T.T., Petty, S., Callahan, O., Osborn, W., Hickman, S., Davatzes, N., 2011. The Role of Stress Modeling in Stimulation Planning at the Newberry Volcano EGS Demonstration Project, in: Thirty Sixth Workshop on Geothermal Reservoir Engineering. Stanford University, Stanford, California, 8 p.

6 Davatzes, N.C., Hickman, S.H., 2011. Preliminary analysis of stress in the Newberry EGS Well NWG 55-29.

7 Delépine, N., Cuenot, N., Rothert, E., Parotidis, M., Rentsch, S., Shapiro, S.A., 2004. Characterization of fluid transport properties of the Hot Dry Rock reservoir Soultz-2000 using induced microseismicity. J. Geophys. Eng. doi:10.1088/1742-2132/1/1/010

8 Den Hartog, S.A.M., Spiers, C.J., 2013. Influence of subduction zone conditions and gouge composition on frictional slip stability of megathrust faults. Tectonophysics 600, 75–90. doi:http://dx.doi.org/10.1016/j.tecto.2012.11.006

9 Dieterich, J.H., 1978. Time-dependent friction and the mechanics of stick-slip. Pure Appl. Geophys. PAGEOPH 116, 790–806. doi:10.1007/BF00876539

10 Dieterich, J.H., 1979. Modeling of rock friction 1. Experimental results and constitutive equations, in: Journal of Geophysical Research: Solid Earth. pp. 2161–2168. doi:10.1029/JB084iB05p02161

11 Elsworth, D., Goodman, R.E., 1986. Characterization of rock fissure hydraulic conductivity using idealized wall roughness profiles. Int. J. Rock Mech. Min. Sci. Geomech. Abstr. 23, 233–243. doi:http://dx.doi.org/10.1016/0148-9062(86)90969-1

12 Evans, K.F., Genter, A., Sausse, J., 2005. Permeability creation and damage due to massive fluid injections into granite at 3.5 km at Soultz: 1. Borehole observations. J. Geophys. Res. Earth 110. doi:Artn B04203 Doi 10.1029/2004jb003168

13 Fehler, M.C., 1989. Stress control of seismicity patterns observed during hydraulic fracturing experiments at the Fenton Hill hot dry rock geothermal energy site, New Mexico. Int. J. Rock Mech. Min. Sci. Geomech. Abstr. 26, 211–219. doi:http://dx.doi.org/10.1016/0148-9062(89)91971-2
14 Frye, K.M., Marone, C., 2002. Effect of humidity on granular friction at room temperature. J. Geophys. Res. Earth 107. doi:Artn 2309 Doi 10.1029/2001jb000654
15 Gu, J.-C., Rice, J.R., Ruina, A.L., Tse, S.T., 1984. Slip motion and stability of a single degree of freedom elastic system with rate and state dependent friction. J. Mech. Phys. Solids 32, 167–196. doi:http://dx.doi.org/10.1016/0022-5096(84)90007-3
16 Heidbach, O., Tingay, M., Barth, A., Reinecker, J., Kurfeß, D., Müller, B., 2010. Global crustal stress pattern based on the World Stress Map database release 2008. Tectonophysics 482, 3–15. doi:10.1016/j.tecto.2009.07.023
17 Hubbert, M.K., Rubey, W.W., 1959. Role of fluid pressure in mechanics of overthrust faulting I. Mechanics of fluid-filled porous solids and its application to overthrust faulting. Geol. Soc. Am. Bull. 70, 115–166.
18 Ikari, M.J., Marone, C., Saffer, D.M., 2011. On the relation between fault strength and frictional stability. Geology 39, 83–86. doi:10.1130/g31416.1
19 Izadi, G., Elsworth, D., 2013. The effects of thermal stress and fluid pressure on induced seismicity during stimulation to production within fractured reservoirs. Terra Nov. 25, 374–380. doi:10.1111/ter.12046
20 Kohli, A.H., Zoback, M.D., 2013. Frictional properties of shale reservoir rocks. J. Geophys. Res. Earth 118, 5109–5125. doi:Doi 10.1002/Jgrb.50346
21 Lachenbruch, A.H., 1980. Frictional heating, fluid pressure, and the resistance to fault motion. J. Geophys. Res. doi:10.1029/JB085iB11p06097
22 Lee, M.K., Wolf, L.W., 1998. Analysis of fluid pressure propagation in heterogeneous rocks: Implications for hydrologically-induced earthquakes. Geophys. Res. Lett. 25, 2329–2332. doi:Doi 10.1029/98gl01694
23 Li, Y., Wang, J., Jung, W., Ghassemi, A., 2012. Mechanical Properties of Intact Rock and Fractures in Welded Tuff from Newberry Volcano, in: Thirty-Seventh Workshop on Geothermal Reservoir Engineering. Stanford University, Stanford, California, 12 p.
24 Majer, E.L., Baria, R., Stark, M., Oates, S., Bommer, J., Smith, B., Asanuma, H., 2007. Induced seismicity associated with Enhanced Geothermal Systems. Geothermics 36, 185–222. doi:http://dx.doi.org/10.1016/j.geothermics.2007.03.003
25 Majer, E.L., Peterson, J.E., 2007. The impact of injection on seismicity at The Geysers, California Geothermal Field. Int. J. Rock Mech. Min. Sci. 44, 1079–1090. doi:http://dx.doi.org/10.1016/j.ijrmms.2007.07.023
26 Marone, C., 1997. On the rate of frictional healing and the constitutive law for time- and slip-dependent friction. Int. J. Rock Mech. Min. Sci. Geomech. Abstr. 34, 347. doi:10.1016/S1365-1609(97)00054-3
27 Marone, C., 1998. Laboratory-derived friction laws and their application to seismic faulting. Annu. Rev. Earth Planet. Sci. 26, 643–696. doi:Doi 10.1146/Annurev.Earth.26.1.643
28 Niemeijer, A., Collettini, C., 2013. Frictional Properties of a Low-Angle Normal Fault Under In Situ Conditions: Thermally-Activated Velocity Weakening. Pure Appl. Geophys. 1–24. doi:10.1007/s00024-013-0759-6
29 Petty, S., Nordin, Y., Glassley, W., Cladouhos, T.T., Swyer, M., 2013. Improving Geothermal Project Economics with Multi-zone Stimulation: Results from the Newberry Volcano EGS Demonstration, in: PROCEEDINGS, Thirty-Eighth Workshop on Geothermal Reservoir Engineering. Stanford University, Stanford, California.
30 Pine, R.J., Ledingham, P., Merrifield, C.M., 1983. In-situ stress measurement in the Carnmenellis granite—II. Hydrofracture tests at Rosemanowes quarry to depths of 2000 m. Int. J. Rock Mech. Min. Sci. Geomech. Abstr. 20, 63–72. doi:10.1016/0148-9062(83)90328-5

31 Raleigh, C.B., Healy, J.H., Bredehoeft, J.D., 2013. Faulting and Crustal Stress at Rangely, Colorado, in: Flow and Fracture of Rocks. American Geophysical Union, pp. 275–284. doi:10.1029/GM016p0275
32 Ruina, A., 1983. Slip instability and state variable friction laws. J. Geophys. Res. Solid Earth 88, 10359–10370. doi:10.1029/JB088iB12p10359
33 Rutqvist, J., Freifeld, B., Min, K.B., Elsworth, D., Tsang, Y., 2008. Analysis of thermally induced changes in fractured rock permeability during 8 years of heating and cooling at the Yucca Mountain Drift Scale Test. Int. J. Rock Mech. Min. Sci. 45, 1373–1389. doi:http://dx.doi.org/10.1016/j.ijrmms.2008.01.016
34 Samuelson, J., Marone, C., Voight, B., Elsworth, D., 2008. Laboratory investigation of the frictional behavior of granular volcanic material. J. Volcanol. Geotherm. Res. 173, 265–279. doi:http://dx.doi.org/10.1016/j.jvolgeores.2008.01.015
35 Scholz, C.H., 1998. Earthquakes and friction laws. Nature 391, 37–42. doi:Doi 10.1038/34097
36 Scholz, C.H., 2002. The Mechanics of Earthquakes and Faulting, 2nd Edition. ed. Cambridge University Press.
37 Shapiro, S.A., Huenges, E., Borm, G., 1997. Estimating the crust permeability from fluid-injection-induced seismic emission at the KTB site. Geophys. J. Int. 131, F15–F18. doi:Doi 10.1111/J.1365-246x.1997.Tb01215.X
38 Shapiro, S.A., Rothert, E., Rath, V., Rindschwentner, J., 2002. Characterization of fluid transport properties of reservoirs using induced microseismicity. Geophysics. doi:10.1190/1.1451597
39 Spada, M., Tormann, T., Wiemer, S., Enescu, B., 2013. Generic dependence of the frequency-size distribution of earthquakes on depth and its relation to the strength profile of the crust. Geophys. Res. Lett. 40, 709–714. doi:Doi 10.1029/2012gl054198
40 Starr, A.T., 1928. Slip in a crystal and rupture in a solid due to shear. Math. Proc. Cambridge Philos. Soc. 24, 489–500. doi:doi:10.1017/S0305004100014626
41 Stein, R.S., King, G.C., Lin, J., 1992. Change in failure stress on the southern San Andreas fault system caused by the 1992 magnitude = 7.4 Landers earthquake. Science 258, 1328–1332. doi:10.1126/science.258.5086.1328
42 Tester, J., 2007. The Future of Geothermal Energy: Impact of Enhanced Geothermal Systems (EGS) on the United States in the 21st Century. MIT.
43 Townend, J., Zoback, M.D., 2000. How faulting keeps the crust strong. Geology 28, 399–402. doi:10.1130/0091-7613(2000)28<399:HFKTCS>2.0.CO
44 Verberne, B.A., Spiers, C.J., Niemeijer, A.R., De Bresser, J.H.P., De Winter, D.A.M., Plümper, O., 2014. Frictional Properties and Microstructure of Calcite-Rich Fault Gouges Sheared at Sub-Seismic Sliding Velocities. Pure Appl. Geophys. 171, 2617–2640. doi:10.1007/s00024-013-0760-0
45 Zoback, M.D., Harjes, H.-P., 1997. Injection-induced earthquakes and crustal stress at 9 km depth at the KTB deep drilling site, Germany. J. Geophys. Res. Solid Earth 102, 18477–18491. doi:10.1029/96JB02814
46 Zoback, M.D., Healy, J.H., 1992. In situ stress measurements to 3.5 km depth in the Cajon Pass Scientific Research Borehole: Implications for the mechanics of crustal faulting. J. Geophys. Res. doi:10.1029/91JB02175

5 CHAPTER 5: ANALYSIS OF FLUID INJECTION-INDUCED FAULT REACTIVATION AND SEISMIC SLIP IN GEOTHERMAL RESERVOIRS

Abstract:

We explore the issue of fault reactivation induced in Enhanced Geothermal Systems (EGS) by fluid injection. Specifically we investigate the role of late stage activation by thermal drawdown. A THM (Thermal-Hydrological-Mechanical) simulator incorporating a ubiquitous joint constitutive model is used to investigate the elastic-plastic behavior of an embedded fault. We apply this new THM model to systematically simulate the seismic slip of a critically-stressed strike-slip fault embedded within the reservoir. We examine the effects of both pore pressure perturbation and thermal shrinkage stress on the magnitude of the resulting events and their timing. We analyze the sensitivity of event magnitude and timing to changes in the permeability of the fault and fractured host, fracture spacing, injection temperature, and fault stress obliquity. From this we determine that: (1) the fault permeability does not affect the timing of the events nor their size, since fluid transmission and cooling rate is controlled by the permeability of the host formation. (2) When the fractured medium permeability is reduced (e.g. from 10^{-13} to 10^{-16} m^2), the timing of the event is proportionately delayed (by a corresponding three orders of magnitude), although the magnitude of the seismic event is not impacted by the change in permeability. (3) Injection temperature has little influence on either the timing or size of the early hydro-mechanically induced events, but it does influence the magnitude but not the timing of the secondary thermal event. The larger the temperature differences between that of the injected fluid and the ambient rock, the larger the magnitude of the secondary slip event. (4) For equivalent permeabilities, changing the fracture spacing (*10m-50m-100m*) primarily influences the rate of heat energy transfer and thermal drawdown within the reservoir. Smaller spacing between fractures results in more rapid thermal recovery but does not significantly influence the timing of the secondary thermal rupture.

5.1 Introduction

Massive water injection has the potential to elevate pore pressures within porous and fractured formations and to reactivate faults, either seismically or aseismically [*Cappa*, 2010; *Cappa and Rutqvist*, 2012; *Cappa et al.*, 2009; *Scholz*, 1990; *Segall and Rice*, 1995]. Extensive studies have explored the response of injection-induced activity in enhanced-geothermal systems (EGS): some evidence shows that the stress perturbation and the elevation of fluid pressures may induce distributed seismic events on fractures [*Zoback and Harjes*, 1997]. However, reactivation, especially on large faults, may result in large seismic events [*Garagash and Germanovich*, 2012], depending on the weakening characteristics of the feature [*Miller*, 2004; *Segall and Rice*, 1995].

Possible mechanisms of fault reactivation are not limited to hydro-mechanical effects. In geothermal systems where the reservoir is chilled with the forced-circulation of cold fluid, the induced thermal shrinkage stress will also control changes in effective stress and may cause fault activation and induced seismicity [*Rutqvist and Oldenburg*, 2007; *Rutqvist et al.*, 2008], Stresses reduce as convective transport drains heat from the rock matrix and it thermally shrinks and decompresses along the unloading curve according to the equivalent elastic properties of the fractured medium [*Bažant et al.*, 1979; *Boley*, 1960; *Sandwell*, 1986].

Since energy release is proportional to fracture aperture to the third power - representing the effective volume destressed by the slip - large faults are of significant concern when understanding reactivation. Large faults (finite-thickness) typically have a specific architecture including heterogeneous properties of a fault core zone and damage zone [*Caine*, 1996] that exert a strong influence on fluid transport behavior. This includes a low permeability fault core that is a flow barrier across the fault and flanked by higher (than the host) permeability zones [*Faulkner et al.*, 2003; *Kim et al.*, 2004; *Vermilye and Scholz*, 1998]. The fault core is typically gouge-filled with low permeability (in the range 1.0×10^{-17} to 1.0×10^{-21} m^2). Significantly, the impermeable fault acts as a barrier to prevent water from penetrating through the fault although fault-parallel transmission is possible. Fault reactivation is a complex process involving the interaction of total stresses and fluid pressures and transformations in stiffness and permeability. In this work we focus on the additional impact of delayed thermal stresses on the timing and magnitude of any induced instability.

We use a coupled Thermal-Hydrological-Mechanical (THM) model [*Taron and Elsworth*, 2009; 2010] to explore the different factors governing fault reactivation of a critically-stressed strike-slip fault. The critical controlling parameters that are examined include fault permeability, fractured medium permeability, fracture spacing and stress obliquity relative to the fault. Finally we control the temperature of the injected water as a method to scale the impact of thermal effects.

5.2 Model setup

In order to investigate the influence of fluid pressures and thermal stresses on the reactivation of critically-stressed faults, we analyze anticipated stress changes using a simple model for a fault acted upon by far-field stresses. This defines the stress drop, which in turn may be used to define the seismic energy release and related event magnitude. We then follow the development of stresses around faults oriented with different stress obliquities using a suitable simulator that couples the effects of fluid transport and changes in total stresses. This method is used to evaluate the timing and magnitude of the resulting slip events.

5.2.1 Analytical stress analysis

Normally, fault instability is governed by contemporary principal stress orientations relative to the pre-existing fault planes [*Streit and Hillis*, 2004]. Based on effective stress theory and the Coulomb failure criterion, the basic equation for slip on a plane is defined as,

$$\tau = C + \mu_s(\sigma_n - p) = C + \mu_s \sigma_{neff} \tag{1}$$

where C is the cohesion, p is the fluid pressure, μ_s is the coefficient of friction, σ_n is the normal stress and τ is the shear stress [*Scholz*, 1990].

To allow the analysis of failure due to an applied oblique stress on the failure of a pre-existing fault [*Jaeger*, 1979] the effective normal stress σ_{neff} and shear stress τ along the fault may be defined as (see Figure. 1),

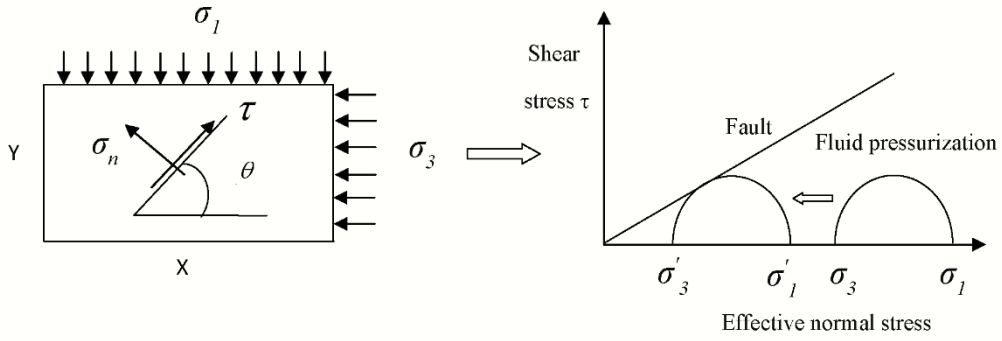

Figure 5. Fault plane stress analysis and slip failure mechanism by fluid pressurization.

$$\sigma_{neff} = \frac{\sigma_x + \sigma_y}{2} + \frac{\sigma_x - \sigma_y}{2}\cos 2(\frac{\pi}{2} - \theta) - \tau_{xy}\sin 2(\frac{\pi}{2} - \theta) - p \tag{2}$$

$$\tau = \frac{\sigma_x - \sigma_y}{2}\sin 2(\frac{\pi}{2} - \theta) - \tau_{xy}\cos 2(\frac{\pi}{2} - \theta) \tag{3}$$

To allow stability to be determined when combined with the strength criterion,

$$\tau_s = \sigma_{neff} * \mu_s \tag{4}$$

This enables strength of a rock mass incorporating a single plane of weakness to be straightforwardly evaluated [*Jaeger*, 1979]. Where we assume that failure may occur on the most critically oriented plane

(Figure 1 b) then the ratio of maximum and minimum principal effective stresses is given by [*Rutqvist et al.*, 2007]

$$\frac{\sigma_1'}{\sigma_3'} = \frac{\sigma_1 - \alpha p}{\sigma_3 - \alpha p} \le q = \left[(\mu_s^2 + 1)^{1/2} + \mu_s \right]^2 \quad (5)$$

where q represents the effective stress limiting difference ratio, where we adopt Biot effective stress theory [*Biot*, 1941] to calculate the horizontal effective maximum in-situ and minimum in-situ stress. When the left hand side ratio exceeds q, then the fault begins to slip. In our study, the Biot coefficient is set as 0.8, the internal fault friction angle is equal to 28 degrees and therefore [*Biot*, 1941; *Byerlee*, 1978], so the value of q is 2.76, and the friction angle of the intact host rock is 30 degrees, then the corresponding value q is 3. Correspondingly, for the stress regime of $\sigma_1 = 45.5MPa, \sigma_3 = 28.6MPa, p = 18.1MPa$ the stress obliquity is,

$J = \sigma_1' / \sigma_3' = 2.2 < q = 2.76.$

Therefore the fault is set as initially stable, while critically stressed. An approach to describe the fault slip potential could use the parameter Δ,

$$\Delta = \Delta\sigma_1' - 2.76\Delta\sigma_3' \quad (6)$$

where $\Delta\sigma_1'$ represents the change in maximum principal effective stress and $\Delta\sigma_3'$ is the change in minimum principal effective stress.

In this work, the failure potential is estimated using a friction angle of 28° and zero cohesion, therefore failure occurs when the effective stress ratio $J = \sigma_1' / \sigma_3'$ is greater than 2.76.

5.2.2 TOUGH-FLAC simulator introduction

We use a coupled THMC model [*Taron and Elsworth*, 2009] capable of representing the mechanical response of the fractured porous subsurface due to fluid injection and recovery. This model satisfies the requirement of representing the coupled elastic-plastic behavior of the fault. The simulator couples analysis of mass and energy transport in porous fractured media (TOUGH) and combines this with mechanical deformation (FLAC3D) as noted in Figure 2 [*Xu et al.*, 2003; *Xu et al.*, 2004; *Xu et al.,* 2001]. The same meshes are used for each of these codes although TOUGH has block-centered nodes and FLAC3D nodes at the block corners (see Figure 1-2). Thus interpolation is required between pressures defined in the transport model to be applied as effective stresses in the mechanical code (TOUGHREACT). Evolving effective stresses are used, together with an appropriate constitutive model

to define the evolution of fracture apertures in the medium and to thereby determine the change in permeability.

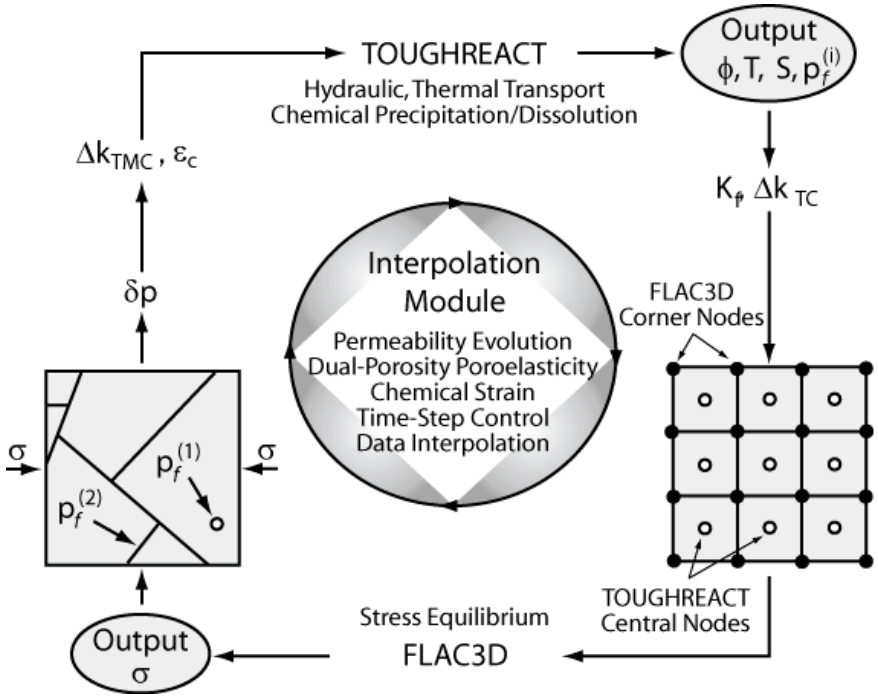

Figure 1 Flac-Tough model simulation flow chart [*Taron and Elsworth*, 2009]

5.2.3 Fault modeling approach

Generally there are three approaches to model fault characteristics [*Cappa,* 2010; *J Rutqvist, Y.-S. Wu, C.-F. Tsang and G. Bodvarsson,* 2002]: the fault could be characterized as a mechanical interface with zero-thickness, by representation with solid elements and double interfaces, or by combination of solid elements and ubiquitous joints as weak plane (see Figure 3). Fault modeling as an interface could be an appropriate approach if the thickness of the fault is negligible compared to the scale of the entire reservoir. To successfully couple fault slip with fluid pressurization in an interface model, it is necessary to add hydraulic elements along the interface, because the hydraulic elements must update the effective normal stress and shear strength by interpolating accurate fault pressure. However, this approach is difficult in building the fault gridding in TOUGH; and it cannot model the heterogeneous character of the fault. The continuum approach with a ubiquitous joint constitutive model in FLAC3D is easier in building meshes for TOUGH; furthermore this approach can represent the anisotropic plasticity of the fault by accounting for the presence of a weak plane. Therefore we adopt this third approach to model the fault.

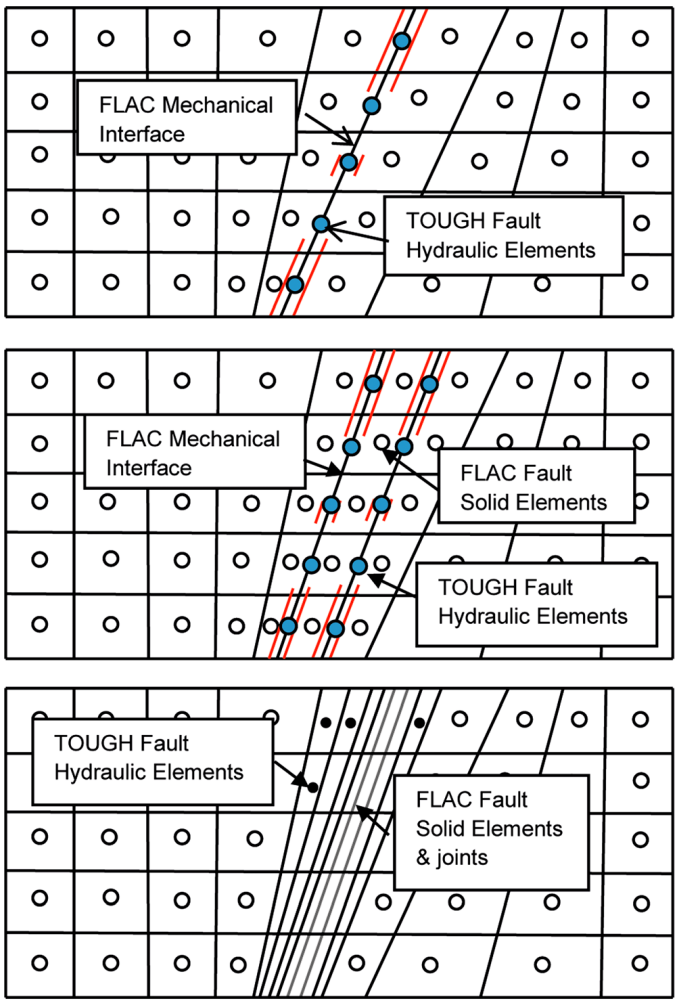

Figure 2 Available approaches for fault modeling in TOUGHREACT.

5.2.4 Moment magnitude scaling

The seismic energy released by shear slip on a pre-existing fault plane is quantified by the event moment M_0. The moment magnitude scale M_S is used to measure the strength of the seismic event. The M_S - M_0 relationship is defined [*Kanamori and Abe*, 1979; *Purcaru and Berckhemer,* 1982] as,

$$\log M_0 = 1.5M_s + 16.1 \tag{7}$$

where M_0 is seismic moment and M_s is moment magnitude.

The moment M_0 is also defined by the relation [Aki, 1967],

$$M_0 = \mu LWD_c \tag{8}$$

where L=fault length, W= fault rupture width, $\mu = \text{rigidity}$, $D_c = \text{slip distance}$.

The fault seismic moment is a function of slip distance and fault rigidity when the fault rupture area is constant. Since the different patches on the fault undergo different slip distances due to the decaying propagation of the rupture front along the fault, we define the moment by the following equation,

$$M_0 = \int_0^L \mu LWdD_c \tag{9}$$

In order to obtain moment magnitudes that are appropriate to the 3D representation of the fault (fault area of 442m × 442m) we use the results from the 2D plane strain model and extrapolate these over the fault area. This switch between the 2D slip model and the 3D fault ignores the clamped boundaries (zero displacement) at the top and base of the fault and would slightly overestimate the moment magnitude – relative to the real case where the edges of the fault are clamped.

5.2.5 Model configuration

The model is used to represent conditions prototypical to an enhanced geothermal system (EGS). The reservoir geometry is a pseudo 3-D doublet (1500m × 600m × 15m) (see Figure 4). The initial temperature distribution is homogeneous with an initial rock temperature of 250 C. The minimum in-situ stresses are imposed at 28.8 MPa in the W-E direction, and maximum in-situ stresses are subjected to a constant 45 MPa in the N-S direction. A strike-slip fault is located in the center of reservoir with the injection well and withdrawal well distributed to the east and west of the fault, respectively. In this configuration the fault acts as a barrier for the propagation of the fluid front from the injection to the recovery well. The model boundaries are set as no-flow boundaries with applied constant stresses.

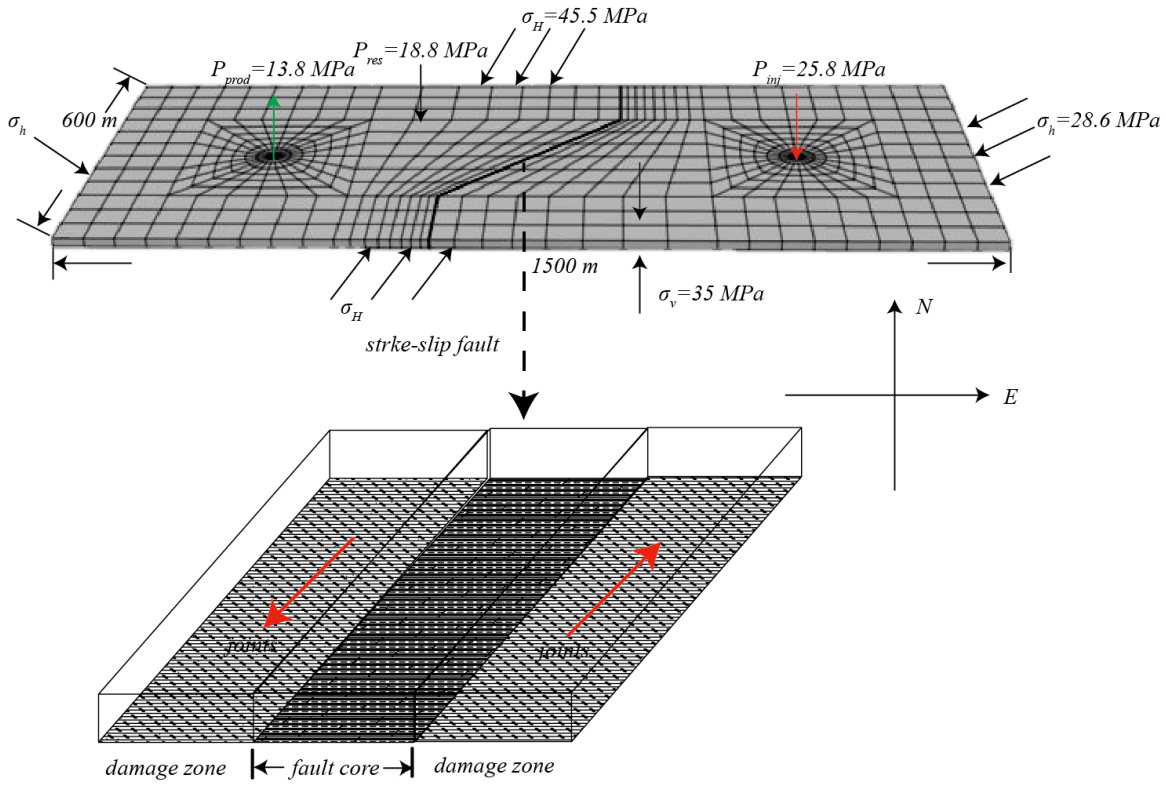

Figure 3 (a) Model geometry and applied stress boundary condition, initial condition, (b) strike-slip fault geometry in model.

The strike-slip fault comprises a low permeable core (thickness 0.8m) and flanked by higher permeability damage zones (thickness 1.2 m). The ubiquitous joint model represents the elastic-plastic behavior of the fault. The joints and host rock have the same initial internal frictional angle of 28° (see Table 1). We adopt a linear strain-softening relationship that implies that the friction angle decreases with an increase in the plastic strain.

Table 1 Material properties input in model [*Rutqvist et al.*, 2013].

Parameters	In-tact rock	Damage zone	Core zone
Young's modulus (GPa)	8	1.5	1.5
Shear modulus (GPa)	5.5	1	1
Permeability (m^2)	1×10^{-13}--1×10^{-16}	1×10^{-14}--1×10^{-17}	1×10^{-19}
Poisson's ratio	0.2	0.2	0.2
Friction angle	30	28	28
Fracture porosity	0.8	0.8	0.8

5.3 Validation result

We use the geometry of Figure 4 (a) to validate the model. The simulation results in induced fault seismic slip due to over pressurization by the fluid (2MPa). The parameter $J = \sigma_1' / \sigma_3'$ is utilized to describe the distribution of shear failure potential (see Figure 5) around the pressurized fault. When the fault friction angle is equal to 28 degrees, the fault and areas ahead of the tip show a high potential for slip – as illustrated by $J > 2.76$ (Figure 5(a)). This strength is applied on the fault, but the strength in the surrounding matrix corresponds to a friction angle equal to 30 degrees with $J = 3$ - that remains unfailed in the matrix. Where strength of the fault is raised to 35 degrees and the analysis completed – the fault is now stable (Figure 5(b) with $J > 3.7$ required for failure) despite the same 2MPa over pressurization.

During failure, the control point in the center of the fault has the largest relative seismic slip distance of 0.35 m (see Figure 6b). The corresponding seismic moment magnitude is 3.1. When the rupture front migrates away from the center of the fault to the fault tips, the slip distance of each patch decreases. When the slip occurs, the corresponding Coulomb Stress ratio is equal to the tangent of the friction angle tan28° (see Figure 6c).

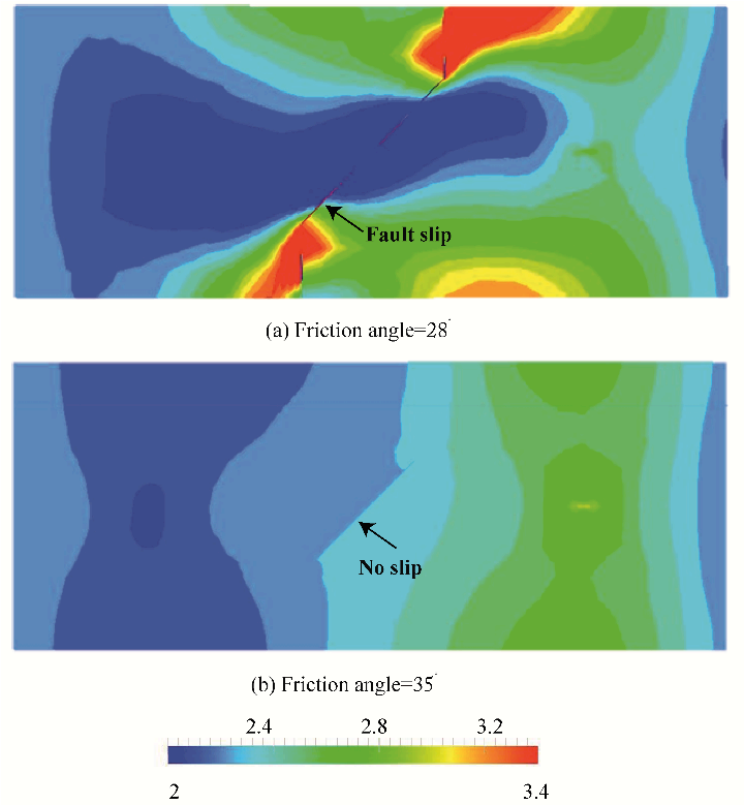

Figure 4 Spatial distribution of the fault failure potential, J under isothermal injection

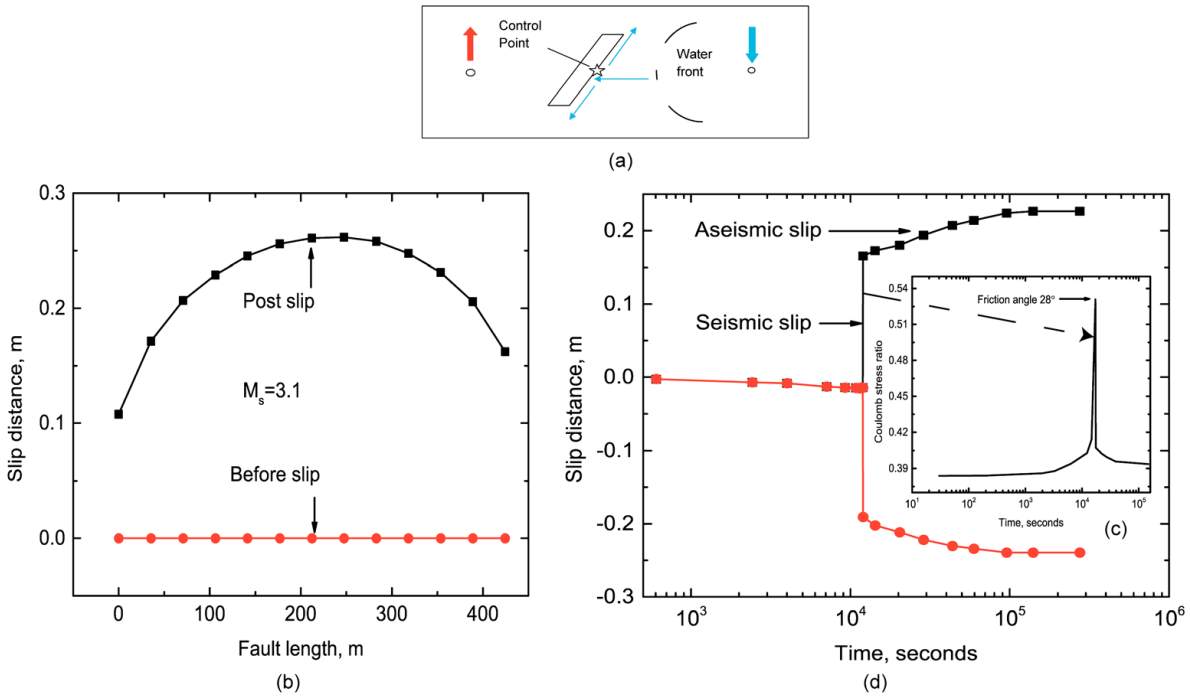

Figure 5 Response at control points (a) located at mid length on the fault and (b) resulting fault slip distance distribution for cases both before and after slip. (c) Evolution of Coulomb stress ratio at mid length along the fault. (d) Slip distance along the fault under isothermal injection.

5.4 Parametric analysis

To understand the principal factors that influence event magnitude and timing during fault reactivation, we examine the influence of fault and host permeability, fracture spacing of the host, injection temperature and stress obliquity. These factors are evaluated during the full loading cycle including the influences of fluid pressure and thermal stresses, respectively at early and late times during reservoir production.

5.4.1 Fault permeability

The hydraulic characteristics of the fault are represented by a low permeability core [*Caine*, 1996] flanked by damage zones with elevated permeability and embedded within the host medium of defined intermediate permeability. The permeability of the fault damage zone is varied from 10^{-14} m^2 to 10^{-17} m^2, with the fracture permeability of the host is 10^{-14} m^2.

Figure 7a shows the evolution of the fault slip distance at the control point for different fault damage zone permeability values. The overpressure required to induce slip is sensibly constant in all cases (total stresses do not change significantly) and since pressure build-up in the fault is controlled principally by supply of fluid through the moderate permeability (10^{-17} m^2) fractured host, then the timing of fault slip is the same for different fault permeabilities. In all cases the slip occurs ~3.9 hours (1.4×10^4 s) after the initiation of pumping (see Figure 7b).

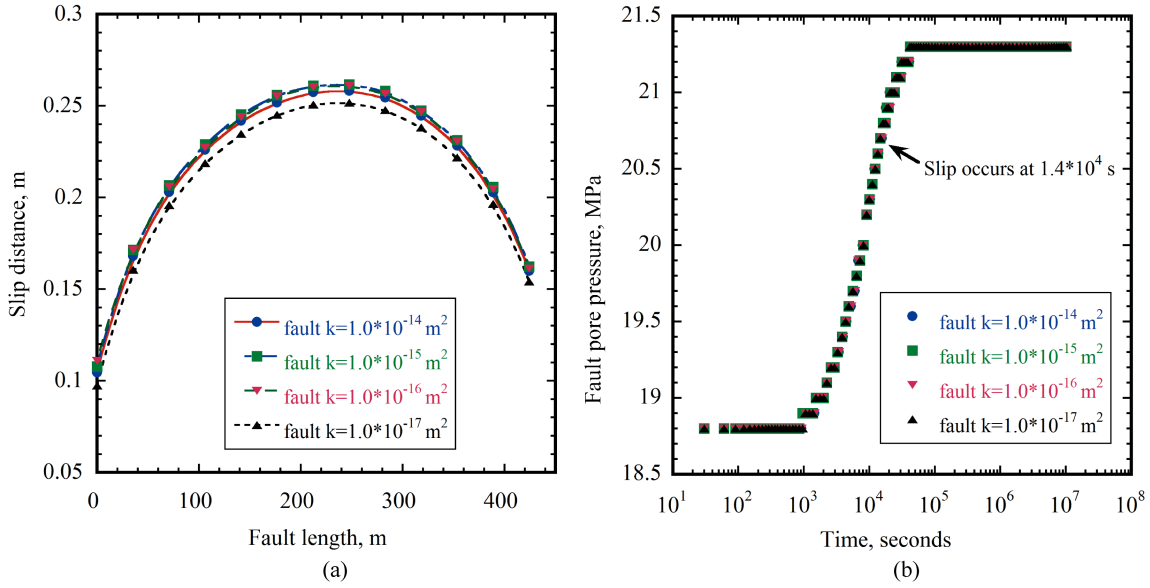

Figure 6 (a) Fault slip distance distribution comparison under different fault permeability (b) fault pore pressure evolution comparison under different fault permeability.

5.4.2 Fractured medium permeability

As noted previously, the permeability of the fractured host controls pressure build-up in the system by limiting the supply of fluid to the embedded fault. Thus, where permeability of the host is either initially elevated, or where it is similarly increased by artificial stimulation, then this will influence the rate of fluid supply to the fault. This further modulates the timing of slip. For a fractured medium the growth in the fracture aperture may be defined by an empirical function of non-linear fracture stiffness α and applied effective stress σ [*J Rutqvist, Y.-S. Wu, C.-F. Tsang and G. Bodvarsson*, 2002] as,

$$b_m = b_{mr} + (b_{mo} - b_{mr})\exp(-\alpha\sigma) \tag{10}$$

where b_m denotes the hydraulic aperture due to mechanical stress effect alone, b_{mo} is the aperture without mechanical stress effect and b_{mr} is the residual aperture solely under the mechanical stress. Assuming the mechanical aperture is approximately equivalent to the hydraulic aperture ($b \sim b_m$) in an orthogonally fractured medium, then the permeability may be defined as,

$$k = \frac{b^3}{12s} + \frac{b^3}{12s} = \frac{b^3}{6s} \tag{11}$$

where s is the fracture spacing, and b is fracture aperture. The fracture permeability is dynamic due to controls on the evolution aperture exerted by mechanical stress effects.

We examine the influence of feasible permeabilities of fractured host in the range $10^{-13} - 10^{-16} m^2$ on the magnitude and timing of fault slip where the permeability of the fault damage zone is maintained constant at 10^{-15} m^2. In all cases the fracture spacing is retained constant at 10 m.

Figure 1-8 shows that high fracture permeabilities concomitantly decrease the time taken for the pressure front to arrive at the fault and to build to the required fault reactivation pressure of 20.7 MPa. For this pressure-controlled system the delay in fault reactivation increases by almost an order of magnitude for each one-order decrease in fracture permeability: the fault slips at 0.38 hours ($1.4\times10^{3} s$) when the host permeability is 10^{-13} m^2, and three orders of magnitude later 16.2 days ($1.4\times10^{6} s$) when the host permeability is decreased to 10^{-16} m^2. However, although slip occurs earlier as the permeability is increased, the relative slip-distance of the fault remains the same – resulting in no change in moment magnitude with this change in host permeability (Figure 8(a)).

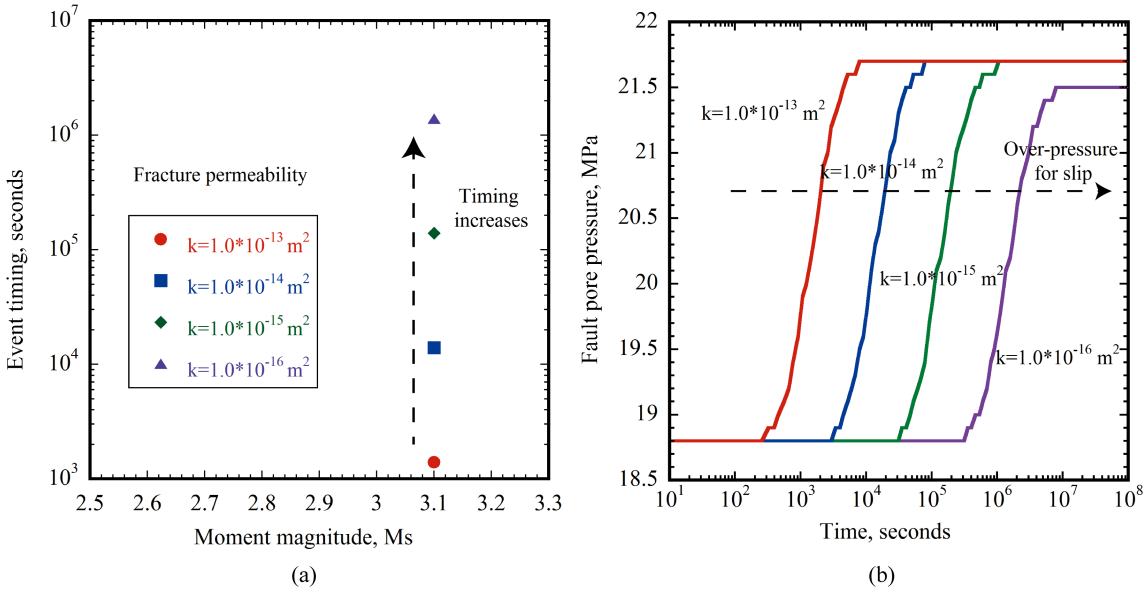

Figure 7 Fault seismic slip event timing vs. magnitude under different fracture permeabilities (b) fault pore pressure evolution under different fracture permeabilities.

5.4.3 Injection temperature

With the prior influence of isothermal injection examined for differences in permeability of both the fault and the host – we now examine the influence of thermal drawdown (non-isothermal injection) on fault

reactivation. Specifically we are interested in the potential for late-time reactivation due to the stresses induced by thermal drawdown.

Figure 9 confirms that indeed late time seismic events may occur within the 30-year injection history when fluid is injected at 50 $^{\circ}$C into a host of 250 $^{\circ}$C, where the fracture host permeability is kept as 10^{-14} m^2, and the fault permeability is 10^{-17} m^2. The first seismic slip event occurs due to hydro-mechanical effects at $1.4\times10^{4} s$ (3.9 hours), and the second slip occurs at $1.4\times10^{8} s$ (4.4 years) when the thermal front arrives at the fault and causes significant temperature drawdown. The magnitude of the second slip event that is induced by the thermal shrinkage stress is weaker than the first event induced by hydro-mechanical effects. The first event has a relative slip distance of 36 cm and a magnitude of 3.1 with the second event displacing only 6 cm with a magnitude of 2.6.

When the hot reservoir rock is cooled, the thermal stress induced by shrinkage results in unloading by decreasing the maximum in-situ stress; and in turn the fault shear strength decreases. The associated decrease in shear strength in the cooling regime facilitates fault reactivation. Figure 1-10a shows that the seismic slip induced by the thermal stress occurs when the rate of temperature drawdown gradient reached to the maximum point. Figure 10c indicates that the maximum drawdown gradient at an injection temperature $T = 50\ ^{o}C$ is a critical transition point for inducing late-stage seismicity. In this particular instance the maximum absolute value of the thermal drawdown gradient is equal to $6\times10^{-7}\ ^{\circ}C/s$. Figure 1-10b shows that the fault temperature begins to be drawn down after 8.0×10^{7} seconds (2.5 years) and this continues until the reservoir is depleted after 1.6×10^{9} seconds (50.7 years).

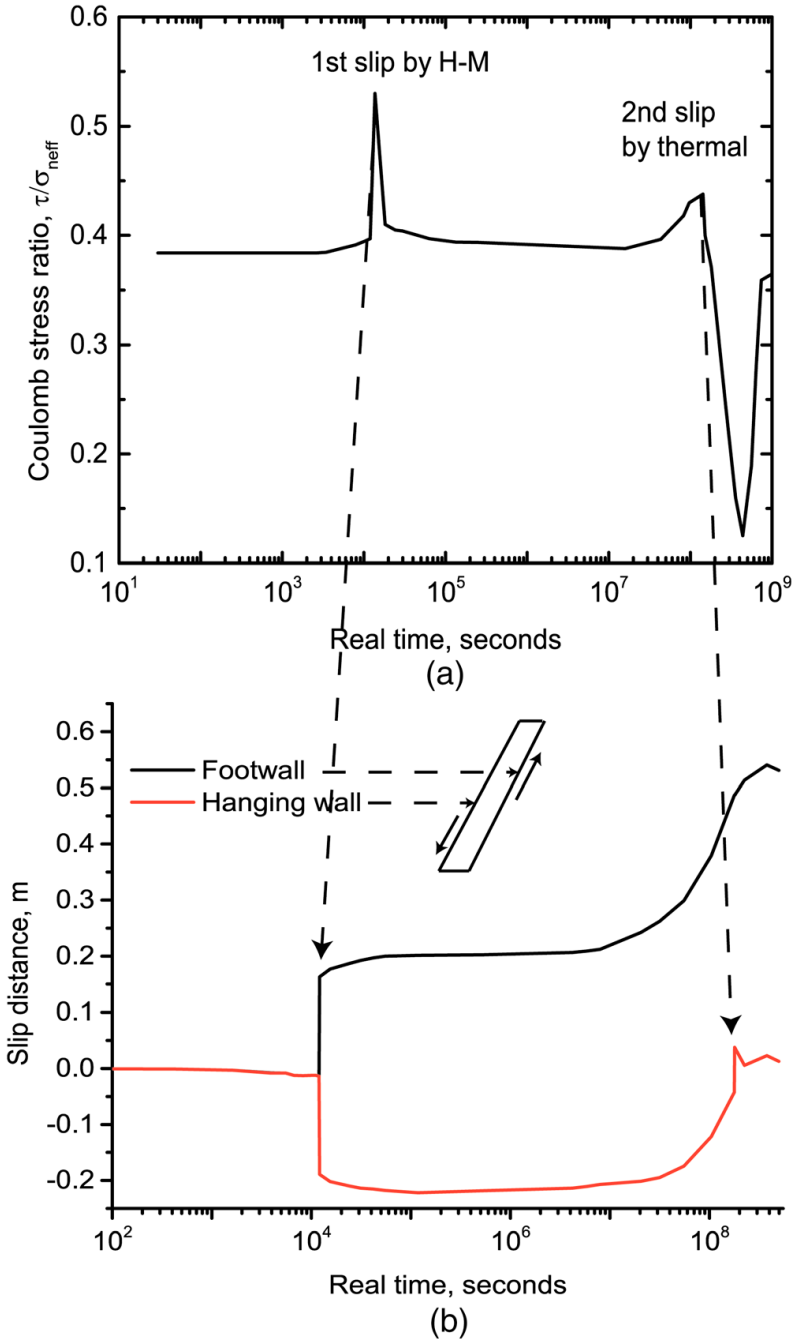

Figure 8 Two fault seismic slips occurred within 20 years induced by H-M effect and by cooling stress effect. (a) The evolution of fault Coulomb stress ratio. (b) Slip distance evolution of both footwall (green line) and hanging wall (blue line).

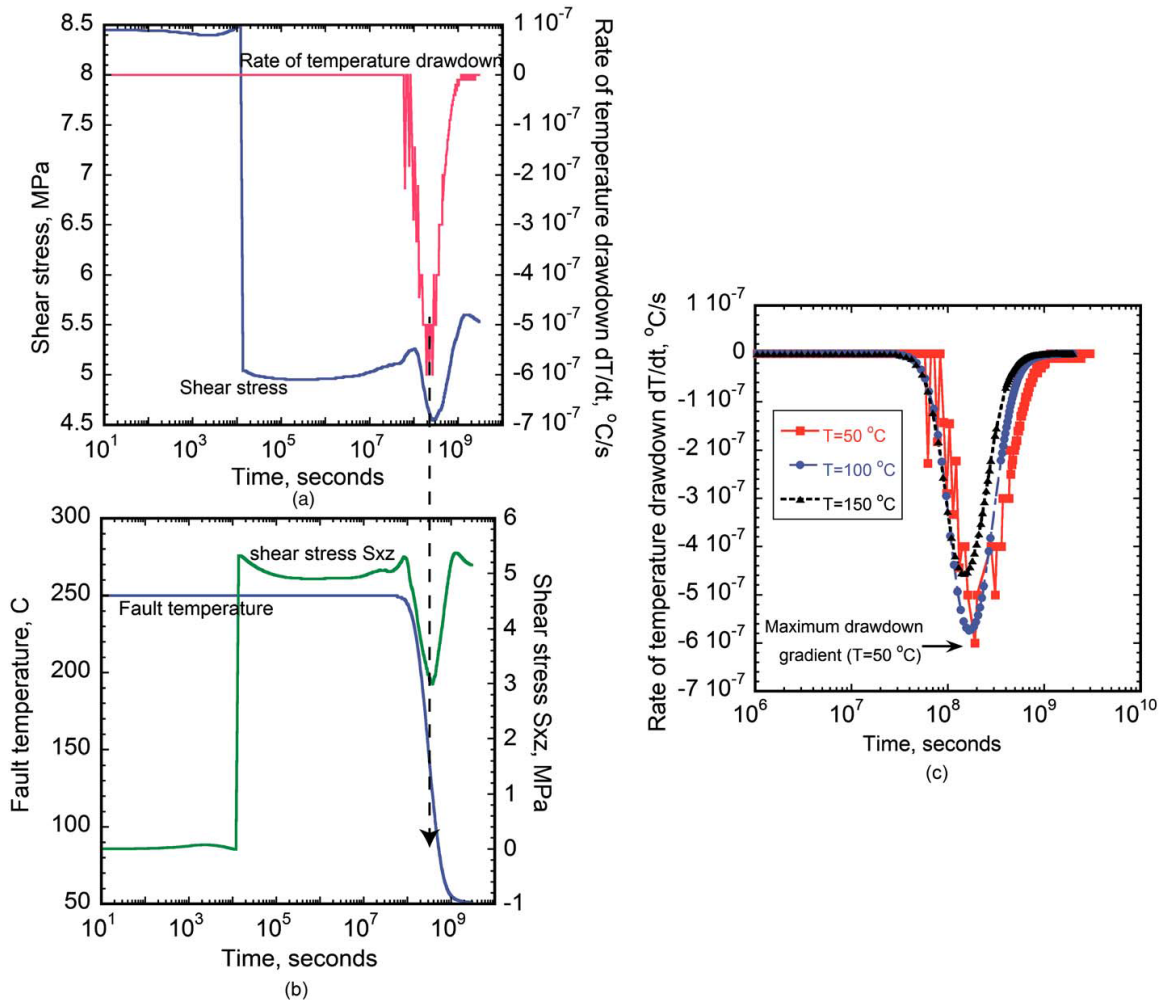

Figure 9 (a) Fault shear stress (blue) and fault temperature drawdown gradient (red) evolution (b) the evolution of fault temperature +(blue) (c) comparison of fault thermal drawdown gradient under different water injection temperatures ($T = 50^{\circ}C,\ 100^{\circ}C,\ 150^{\circ}C$).

The effect of the thermal shrinkage stress is most pronounced at the thermal boundary between the hot and cooling regions where stress gradients are largest. Displacements in the direction of the minimum principal stress indicate a net displacement into the cooled region as that region thermally-compacts (see Figure 1-11). Slip occurs when the advancing cooling front reaches the fault and the rate of stress change, both in space and in time, is particularly high (Figure 10). Therefore we primarily investigate the influence of injected fluid temperature in the range $50^{\circ}C - 250^{\circ}C$ on the magnitude and timing of fault slip and thermal energy recovery efficiency. Figure 1-12 shows that the timing and magnitude of the first seismic slip event is not affected by the injection temperature, because the hydraulic front diffuses faster than the thermal front, so the first seismic slip event induced by hydraulic-mechanical effects are not

affected by the temperature variation of the injected fluid. However, it is observed that only the colder injection ($T=50^{\circ}C$) cause sufficient fault shear strength reduction and in turn slips at $t=1.4\times10^{8}s$ (4.4 years) and, as expected, the injected fluid with hotter temperature does not generate the later time seismic slip event. The greater temperature difference between the injected fluid and the ambient rock results in larger thermal stress, which reduces the fault shear strength to a larger extent. Thus, only the colder injection leads to a larger seismic fault reactivation.

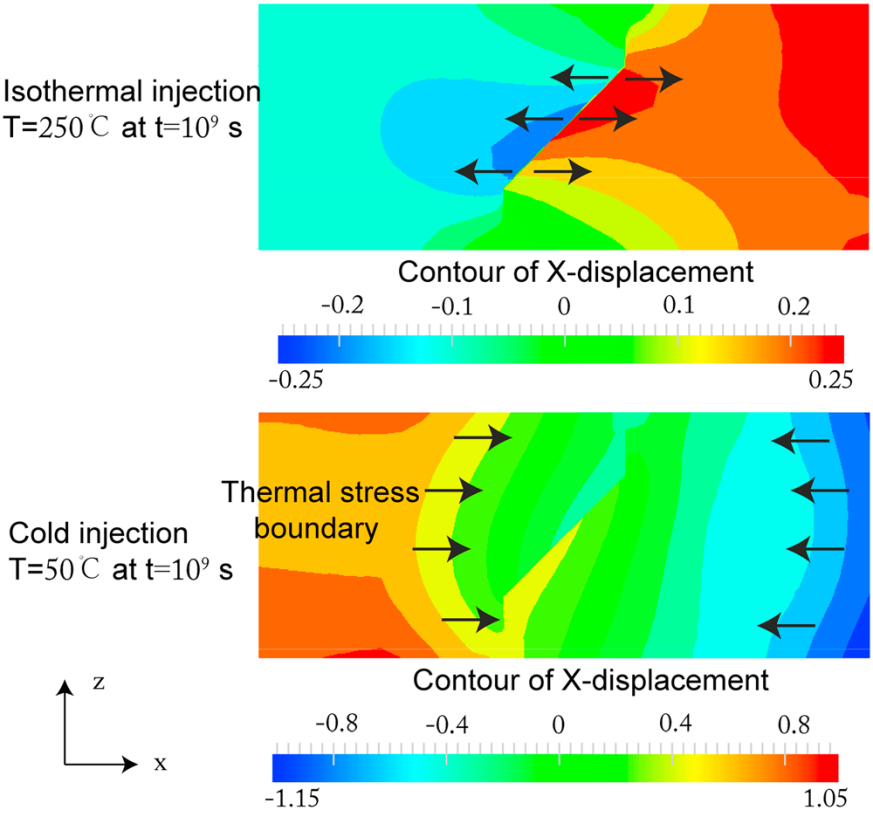

Figure 5-10 Field x-displacement distribution for isothermal injection and cold injection at $t=10^{9}s$.

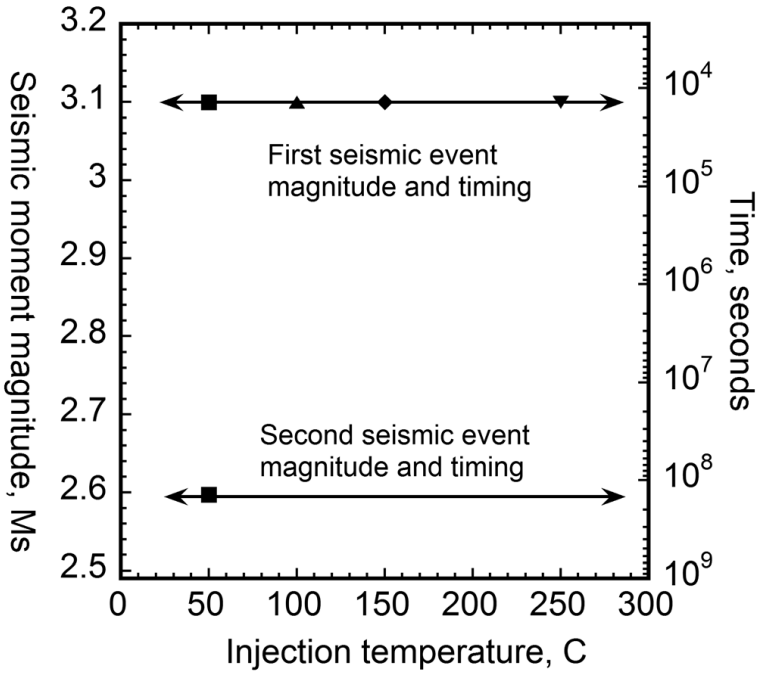

Figure 11 Fault seismic event magnitude and timing result comparison under different injection temperature $50^{\circ}C$, $100^{\circ}C$, $150^{\circ}C$, $250^{\circ}C$. The arrows in left direction show the results of event magnitude, and the arrows in right direction shows the results of event timing.

Fracture spacing

The injected fluid flows only in the fractures and the fracture spacing directly controls thermal conduction from the matrix to the fluid in the fractures. Here we investigate the influence of fracture spacing (10m 50m and 100m) in both fault reactivation and heat energy recovery efficiency, while the fracture permeability is retained constant at 10^{-14} m^2.

To determine the impact of fracture spacing on thermal recovery and fault slip we compare the results for isothermal injection ($T = 250^{\circ}C$) to those for cold injection ($T = 50^{\circ}C$) and with different fracture spacing. Figure 1-14 illustrates that the variation in fracture spacing has no impact on the timing and magnitude of fault reactivation – in all cases the fault slips after ~ $1.4\times10^4 s$ (3.89 hours) under isothermal injection $T = 250^{\circ}C$. Similarly, they are unchanged for cold injection - the timing of the second (thermally activated) slip for all the fracture spacing cases (10m-50m-100m) remains unchanged at ~$1.4\times10^8 s$ (4.43 years), and the corresponding seismic moment magnitude is 2.6. Figure13(a) shows that the thermal front propagates uniformly at small fracture spacing (10m) in the reservoir and the second (thermally activated) slip event is triggered as soon as the thermal front arrives at the fault at ~$1.4\times10^8 s$

(4.43 years). Conversely, when the fracture spacing is increased to 100m, the reservoir temperature decreases uniformly across the reservoir without the presence of a distinct thermal front. The spatial thermal gradient around the fault is the principal factor to determine whether the second slip event actually occurs (Figure 13(b) and (c)). It indicates that the spatial thermal gradient is maximum at $\sim 1.4\times10^{8} s$ (4.43 years) and is similar for fracture spacing between 50 m and 100m.

Further investigation of the temperature profiles reveals that the denser fracture spacing increases the residence time of the cold fluid circulating within the hot reservoir and the smaller fracture spacing allows more rapid recovery of heat from the matrix blocks. Figure 15(a) shows the evolution of fluid temperature within the reservoir for different fracture spacing ($T = 50^{\circ}C$). As fracture spacing increases the chilled region adjacent to the injector is reduced in size (see Figure 15(b)). Thus the more closely-spaced fractures result in a faster recovery of heat from the reservoir.

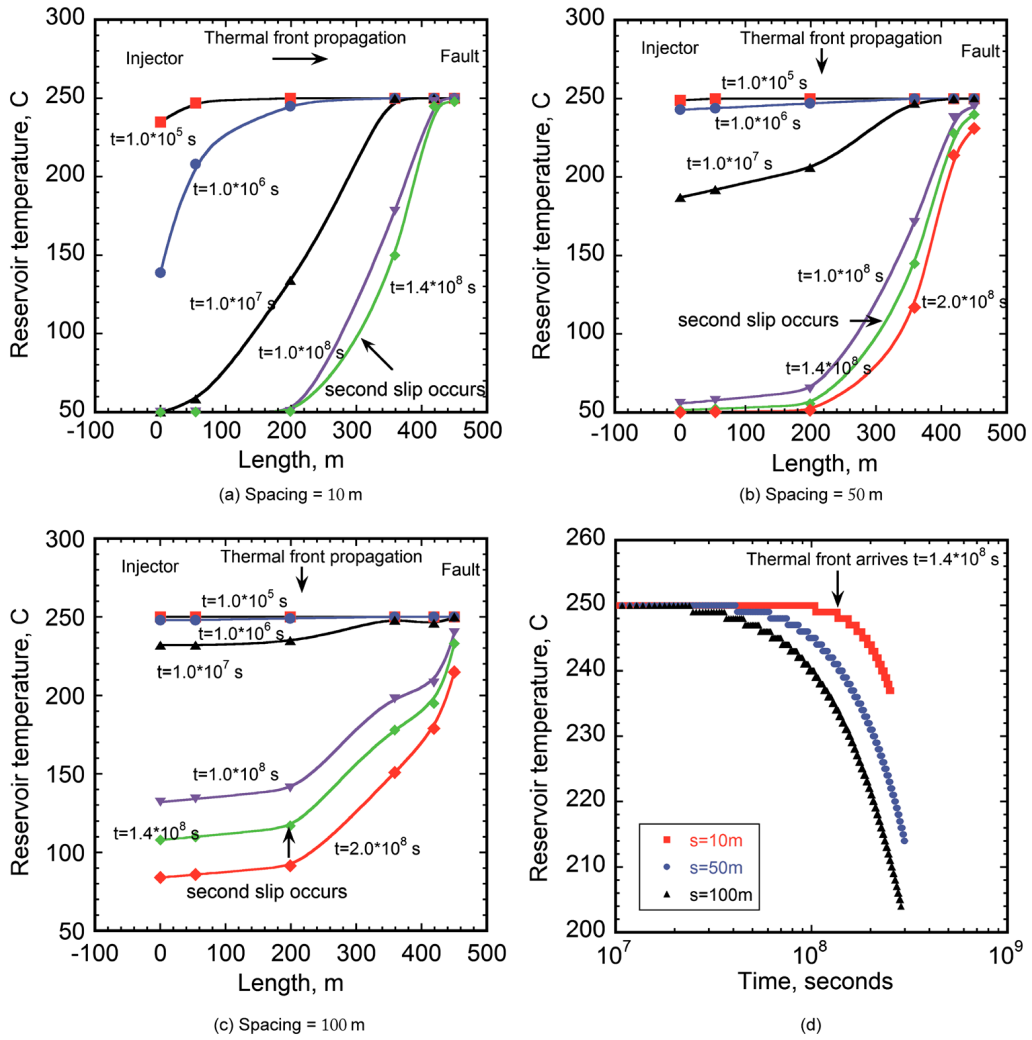

Figure 12 (a) Reservoir temperature evolution under fracture spacing=10 m. (b) reservoir temperature evolution under fracture spacing=50 m, (c) reservoir temperature under fracture spacing=100 m, (d0 fault temperature evolution under 10m-50m-100m fracture spacing.

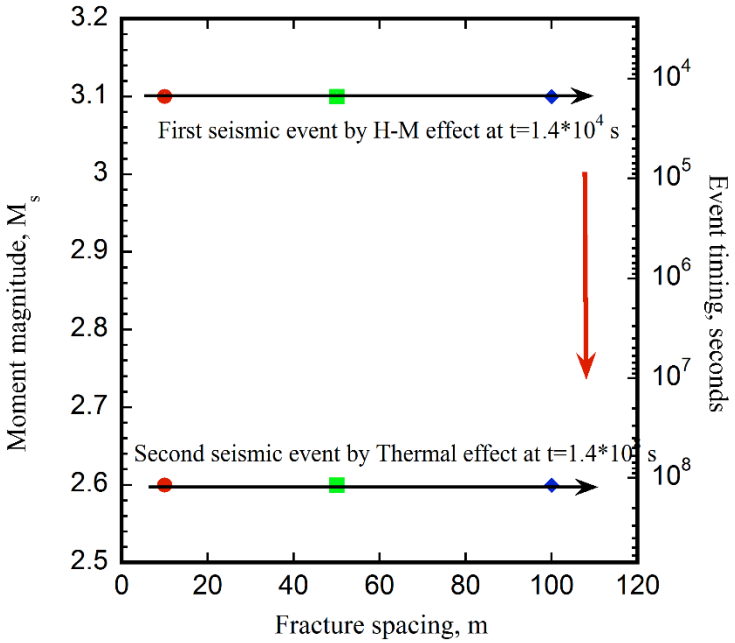

Figure 13 Fault seismic slip event magnitude and timing comparison under different fracture spacing (injection temperature T= 50 C).

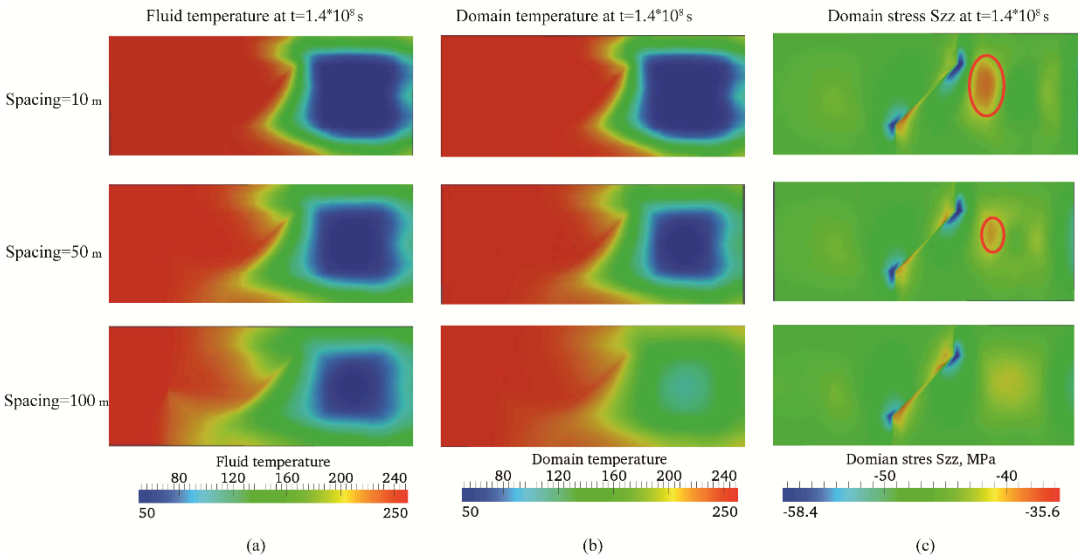

Figure 14 (a) Fluid temperature distribution at 4.4 years and 31 years under different fracture spacing (10m-50m-100m) under the same injection pressure, (b) domain temperature comparison at 4.4 year under different fracture spacing (10*m*-50*m*-100*m*) (b) domain stress Szz at 4.4 year under different fracture spacing.

5.4.4 Stress obliquity

Fault orientation plays an important role in modulating the stress state on the fault plane and in controlling the fluid over-pressurization required for fault reactivation. We compare different fault orientation scenarios while maintaining the distance between the fault center and injection well as constant. During this the fault plane angle is varied from 30 degrees to 75 degrees (see Figure 16(a)).

The fault is stable when the fault is inclined at only 30 degrees, but fails with the largest slip distance (6 cm) and moment magnitude (2.5) occurring after $1.4\times10^4 s$ (3.9 hours) when inclined at 60 degrees to the minimum principal stress (Figure 16(b)). This is for H-M effects only.

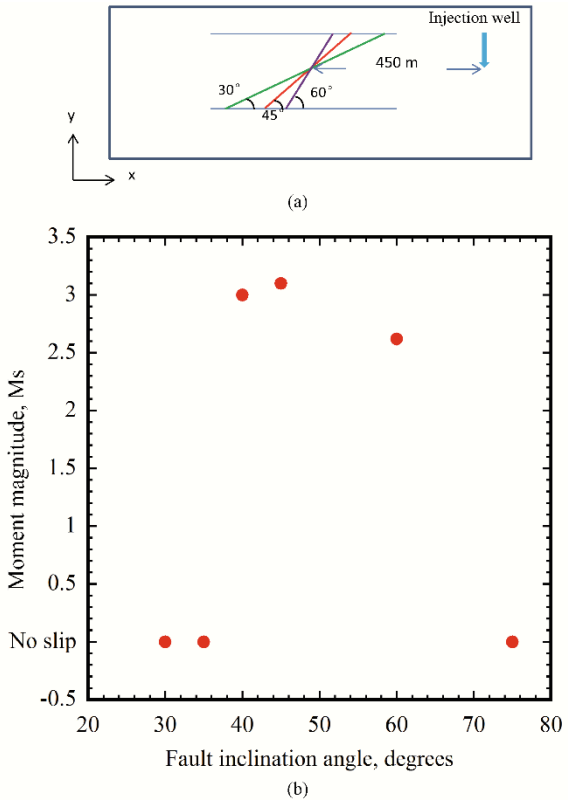

Figure 15 (a) Schematic figure of different fault inclination angles (b) Fault seismic slip moment magnitude comparison under different fault inclination angles.

5.5 Conclusions

We explore the potential for reactivation of a major strike-slip fault in an enhanced geothermal systems (EGS) reservoir. We systematically investigate the mechanisms causing fault reactivation and seismic slip together with the critical controlling factors influencing slip magnitude and timing. The results indicate the primary influence of mechanical and hydrological effects in the short-term fault reactivation, and the impact of thermal stress in causing long-term seismic slip.

The timing and magnitude of the initial H-M slip is insensitive to the permeability of the fault. This is because the transmission of fluid to the fault, from the injection well, is controlled by the permeability of the stimulated host medium. When the host fracture permeability is constant, the progression of the stress ratio between injection and fault due to hydraulic effect is similar in the magnitude and timing. Increasing the permeability of the host by an order of magnitude decreases the time to the first H-M event by an order of magnitude. For equivalent permeabilities, the rate of thermal recovery is controlled by the fracture spacing. Smaller fracture spacing results in faster thermal drawdown and more rapid energy recovery.

However, in terms of cold water injection, the induced thermal shrinkage stress does play an important role in unloading of the stress field by reducing the maximum in-situ stress, and thereby reduce the shear strength. This stress change is shown to result in secondary seismic slip, even when no strengthening of the fault is considered. The magnitude of the second seismic slip event is governed by the temperature difference between the injected fluid temperature and the ambient domain temperature. This is because the magnitude of thermal shrinkage stress is also proportional to the temperature difference. The larger temperature difference leads to a larger late stress ratio rise. In our results, where cold fluid is injected at 50 C, this results in a late stage event of M_s=2.6 with a seismic slip distance of 6 cm. The fracture spacing does not affect the timing and magnitude of seismic slip when the permeability of the fractured medium is retained constant. This is surprising as the effectiveness of energy recovery and therefore the rate of cooling is increased with a decrease in fracture spacing. However this does not significantly affect the timing of these secondary thermal events (Figure 1-14). Finally, the orientation angle of the fault directly determines the stress state applied by the injected fluid and controls the magnitude of the resulting event, but not its timing. Faults with the largest stress obliquity fail with the largest moment magnitude.

Acknowledgement

This work is the result of partial support from the US Department of Energy under project DOE-DE-EE0002761. This support is gratefully acknowledged.

5.6 References

Aki, K. (1967), Scaling law of seismic spectrum, J. Geophys. Res., 72(4), 1217–1231, doi:10.1029/JZ072i004p01217.

Bažant, Z., H. Ohtsubo, and K. Aoh (1979), Stability and post-critical growth of a system of cooling or shrinkage cracks, *Int. J. Fract.*, 15(5), 443–456.

Biot, M. (1941), General theory of three-dimensional consolidation, J. Appl. Phys., 12(2), 155–164.

Boley, B. A. (1960), Theory of Thermal Stresses, John Wiley, New York.

Byerlee, J. (1978), Friction of rocks, *Pure Appl. Geophys.*, 116(4–5), 615–626.

Caine, J. S., J. P. Evans, and C. B. Forster (1996), Fault zone architecture and permeability structure, *Geology*, 18, 1025–1028.

Cappa, F. (2010), Modeling of coupled deformation and permeability evolution during fault reactivation induced by deep underground injection of CO2, edited.

Cappa, F., and J. Rutqvist (2012), Seismic rupture and ground accelerations induced by CO2 injection in the shallow crust, *Geophys. J. Int.*, 190(3), 1784–1789.

Cappa, F., J. Rutqvist, and K. Yamamoto (2009), Modeling crustal deformation and rupture processes related to upwelling of deep CO2-rich fluids during the 1965–1967 Matsushiro earthquake swarm in Japan, *J. Geophys. Res.*, 114, B10304, doi:10.1029/2009JB006398.

Faulkner, D. R., A. C. Lewis, and E. H. Rutter (2003), On the internal structure and mechanics of large strike-slip fault zones: Field observations of the Carboneras fault in southeastern Spain, *Tectonophysics*, 367(3–4), 235–251.

Garagash, D. I., and L. N. Germanovich (2012), Nucleation and arrest of dynamic slip on a pressurized fault, *J. Geophys. Res*., 117, B10310, doi:10.1029/2012JB009209,.

Jaeger, J. C. (1979), Fundamentals of Rock Mechanics, 3rd ed., Capman 1 Hall, New York.

Kanamori, H., and K. Abe (1979), Reevaluation of the turn-of-the-century seismicity peak, *J. Geophys. Res.*, 84(B11), 6131–6139, doi:10.1029/JB084iB11p06131.

Kim, Y.-S., D. C. P. Peacock, and D. J. Sanderson (2004), Fault damage zones, *J. Struct. Geol.*, 26(3), 503–517.

Miller, S. A., C. Collettini, L. Chiaraluce, L. Cocco, M. Barchi, and M. Kaus (2004), Aftershocks driven by a high-pressure CO2 source at depth, *Nature*, 427, 724–727.

Purcaru, G., and H. Berckhemer (1982), Quantitative relations of seismic source parameters and a classification of earthquakes, *Tectonophysics*, 84(1), 57–128.

Rutqvist, J., and C. Oldenburg (2007), Analysis of cause and mechanism for injection-induced seismicity at the Geysers Geothermal Field, California, *GRC Trans*., 31, 441–445.

Rutqvist, J., Y.-S. Wu, C.-F. Tsang, and G. Bodvarsson (2002), A modeling approach for analysis of coupled multiphase fluid flow, heat transfer, and deformation in fractured porous rock, *Int. J. Rock Mech. Min. Sci.*, 39, 429–442.

Rutqvist, J., J. Birkholzer, F. Cappa, C. Oldenburg, and C.-F. Tsang (2008), Shear-slip analysis in multiphase fluid-flow reservoir engineering applications using TOUGH-FLAC, edited.

Rutqvist, J., A. P. Rinaldi, F. Cappa, and G. J. Moridis (2013), Modeling of fault reactivation and induced seismicity during hydraulic fracturing of shale-gas reservoirs, *J. Pet. Sci. Eng.*, 107(0), 31–44.

Sandwell, D. T. (1986), Thermal stress and the spacings of transform faults, *J. Geophys. Res*., 91(B6), 6405–6417, doi:10.1029/JB091iB06p06405.

Scholz, C. H. (1990), The Mechanics of Earthquakes and Faulting, Cambridge Univ. Press, Cambridge, New York, Port Chester, Melbourne, Sydney.

Segall, P., and J. R. Rice (1995), Dilatancy, compaction, and slip instability of a fluid-infiltrated fault, *J. Geophys. Res.*, 100(B11), 22,155–22,171, doi:10.1029/95JB02403.

Streit, J. E., and R. R. Hillis (2004), Estimating fault stability and sustainable fluid pressures for underground storage of CO2 in porous rock, *Energy*, 29(9–10), 1445–1456.

Taron, J., and D. Elsworth (2009), Thermal–hydrologic–mechanical–chemical processes in the evolution of engineered geothermal reservoirs, *Int. J. Rock Mech. Min. Sci*., 46(5), 855–864.

Taron, J., and D. Elsworth (2010), Coupled mechanical and chemical processes in engineered geothermal reservoirs with dynamic permeability, *Int. J. Rock Mech. Min. Sci*., 47(8), 1339–1348.

Vermilye, J. M., and C. H. Scholz (1998), The process zone: A microstructural view of fault growth, *J. Geophys. Res.*, 103(B6), 12,223–12,237, doi:10.1029/98JB00957.

Xu, T., E. Sonnenthal, N. Spycher, K. Pruess, G. Brimhall, and J. Apps (2001), Modeling multiphase non-isothermal fluid flow and reactive geochemical transport in variably saturated fractured rocks: 2. Applications to supergene copper enrichment and hydrothermal flows, *Am. J. Sci.*, 301(1), 34–59.

Xu, T., J. A. Apps, and K. Pruess (2003), Reactive geochemical transport simulation to study mineral trapping for CO2 disposal in deep arenaceous formations, *J. Geophys. Res.*, 108(B2), 2071, doi:10.1029/2002JB001979.

Xu, T., E. Sonnenthal, N. Spycher, and K. Pruess (2004), TOUGHREACT User's Guide: A simulation program for non-isothermal multiphase reactive geochemical transport in variable saturated geologic media, Earth Sciences Division, Lawrence Berkeley National Laboratory, Univ. of California, Berkeley, Calif.

Zoback, M. D., and H.-P. Harjes (1997), Injection-induced earthquakes and crustal stress at 9 km depth at the KTB deep drilling site, Germany, *J. Geophys. Res*., 102(B8), 18,477–18,491, doi:10.1029/96JB02814.

6 CHAPTER 6 THERMAL DRAWDOWN AND LATE-STAGE SEISMIC SLIP FAULT-REACTIVATION IN ENHANCED GEOTHERMAL RESERVOIRS

Abstract

Late-stage seismic-slip in geothermal reservoirs has been shown as a potential mechanism for inducing seismic events of magnitudes to ~2.6 as late as two decades into production. We investigate the propagation of fluid pressures and thermal stresses in a prototypical geothermal reservoir containing a centrally-located critically-stressed fault from a doublet injector and withdrawal well to define the likelihood, timing and magnitude of events triggered by both fluid pressures and thermal stresses. We define two bounding modes of fluid production from the reservoir. For injection at a given temperature, these bounding modes relate to either low- or high-relative flow rates. At low relative dimensionless flow rates the pressure pulse travels slowly, the pressure-driven changes in effective stress are muted, but thermal drawdown propagates through the reservoir as a distinct front. This results in the lowest likelihood of pressure-triggered events but the largest likelihood of late-stage thermally-triggered events. Conversely, at high relative non-dimensional flow rates the propagating pressure pulse is larger and migrates more quickly through the reservoir but the thermal drawdown is uniform across the reservoir and without the presence of a distinct thermal front, and less capable of triggering late-stage seismicity. We evaluate the uniformity of thermal drawdown as a function of a dimensionless flow rate Q_D that scales with fracture spacing s (m), injection rate q (kg/s), and the distance between the injector and the target point L^* ($Q_D \propto qs^2 / L^*$). This parameter enables the reservoir characteristics to be connected with the thermal drawdown response around the fault and from that the corresponding magnitude and timing of seismicity to be determined. These results illustrate that the dimensionless temperature gradient adjacent to the fault dT_D / dx_D is exclusively controlled by the factor Q_D. More significantly, this temperature gradient correlates directly with both the likelihood and severity of triggered events, enabling the direct scaling of likely magnitudes and timing to be determined a priori and directly related to the characteristics of the reservoir. This dimensionless scaling facilitates design for an optimum Q_D value to yield both significant heat recovery and longevity of geothermal reservoirs while minimizing associated induced seismicity.

6.1 Introduction

Harvesting geothermal energy from deep fractured low-permeability formations has become a feasible method to ease the demand on fossil energy. Predicting mass rates and temperatures of fluid production and assessing induced seismicity are intimately connected topics that require an intimate and complete

understanding of subsurface coupled THMC (Thermal-Hydrological-Mechanical-Chemical) processes [*Taron and Elsworth*, 2010]. The associated thermal drawdown response of the rock mass results from the circulation of a heat-transfer fluid [*Bodvarsson*, 1969; *Bödvarsson and Tsang*, 1982]. Thermal drawdown in the fractured porous medium may be determined by accommodating the essential components of the reservoir – heat transfer from the reservoir matrix to the fluid by conduction and then advection across the reservoir – for which a variety of analytical approaches are available [*Elsworth*, 1989a; b; 1990; *Ganguly and Mohan Kumar*, 2014; *Gringarten and Witherspoon*, 1973; *Gringarten et al*., 1975; *Pruess*, 1983; *Pruess and Wu*, 1993; *Ghassemi et al*., 2003]. These approaches are based on the assumptions of locally 1-D heat conduction in an infinite medium, and that the fluid flow in the fractured medium instantaneously reaches local thermal equilibrium [*Shaik et al*., 2011].

To accommodate more general flow geometries, including the inclusion of heterogeneity, a variety of numerical methods are available to represent response. Such models also accommodate key process of heat transfer in the subsurface in accommodating dual porosity to describe heat exchange between the porous fracture and the low porosity rock [*Xu et al*., 2003; *Xu et al*., 2004; *Xu et al*., 2001; *Elsworth*, 1989a, 1989b; *Elsworth and Xiang*, 1989]. The principal heat transfer processes include first heat conduction between the matrix and fluid within the fractures then the advection of that heat across and then out from the reservoir. Depending on the fluid velocity in the fracture, the temperature gradient between the circulating fluid and the adjacent rock varies significantly. In general, the amount of heat energy transferred from the rock is controlled by the heat transfer area, the temperature difference between rock and fluid and the velocity of the circulating fluid [*Holman*, 2002].

In addition to exploring thermal drawdown in the reservoir, and its influence on effluent fluid temperatures, the spatial distribution of reservoir temperature is also influenced by rates of fluid circulation. This thermal drawdown of the rock is also capable of inducing thermal stresses, which in turn are implicated in the potential for induced seismicity and increase the likelihood of late stage fault reactivation [*Gan and Elsworth*, 2014]. The role of thermal stresses in reservoirs has been explored with respect to the evolution of permeability [*Elsworth*, 1989] and of stresses [*Segall and Fitzgerald*, 1998]. Thermally-driven tress changes in geothermal reservoirs are known to be potentially significant. In this work we specifically explore rates of stress generation and their propagation through the reservoir as controlled by thermal capacitance of a dual porosity system, and ultimately on the potential to develop unstable slip. In this, the induced thermal stresses cause the unloading of the fault by reducing maximum in-situ stress, thereby reducing shear strength and therefore enabling slip reactivation as a potentially seismic event. The severity of the reactivation event appears directly related to the spatial gradient of rock temperature that develops in the reservoir [*Gan and Elsworth*, 2014] _ a uniform reduction in temperature

will have a muted change in thermal stresses. Hence, in this work we explore the impact of fluid circulation rates on the heterogeneity of thermal drawdown that may develop within the reservoir and its potential impact on the timing and magnitude of induced seismicity.

The following develops a dimensionless semi-analytical model which incorporates the reservoir scale, fracture spacing and injection mass flow rate to determine thresholds for the evolution of uniform or shock-front distributions of thermal drawdown within the rock comprising the reservoir. The semi-analytical model is derived based on the balance of heat conduction within the fractured medium and the Warren-Root fracture model. Key variables are prescribed that may then be used to assess the propagation of stress fronts through the reservoir and from that define the likelihood, timing and magnitude of late stage events that might occur on reactivated faults.

6.2 Mathematical formulation

To assess and elucidate the fundamental heat transfer processes within the fractured-porous medium, a basic model is presented in Figure 2-1 for the following analytical study. The two-dimensional reservoir is characterized by an orthogonal fracture network with uniform fracture spacing s (m) in both x and z directions and with a uniform fracture aperture b (m). The fractures are the sole conduits for fluid circulation within the reservoir. This parallel fracture model (PFM) has been validated to effectively characterize heat recovery from an arrangement of prismatic blocks, which are thermally isolated from the geologic host medium [*Elsworth*, 1990].

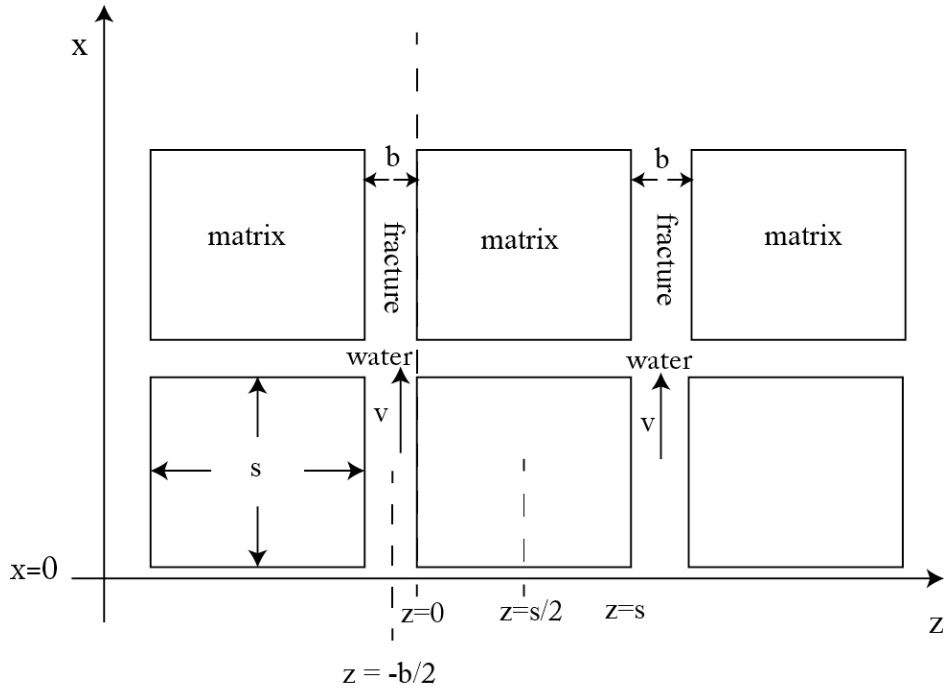

Figure 1 Schematic of analytical heat conduction within fractured medium, the identical fractures with aperture b are equally separated at the spacing s.

Here we relax the restrictions imposed by prior analytical solutions by imposing the following assumptions:

1. The initial temperature of the reservoir and interstitial fluid is uniform at T_0 with cold water injected at constant rate and at constant temperature T_{inj} .

2 Heat conduction occurs primarily in z- directions along the fractures with thermal conductivity K_r and with heat transfer in the vertical direction neglected. We assume that the majority of heat transfer occurs normal to the direction from injection well to production well. There is no heat transfer by radiation within the fractures. The diffusion of heat in the rock matrix occurs only in the direction orthogonal to the fracture plane.

3 The density and heat capacity for both the rock and fluid are constant. Also the thermal conductivity of the rock matrix is assumed constant.

The differential equations governing heat transfer in the fracture are based on the balance of heat energy in the control volume of fractures, defined as

$$\rho_w c_w \frac{\partial T_w(x,t)}{\partial t} = -\upsilon \rho_w c_w \frac{\partial T_w(x,t)}{\partial x} + \frac{2K_r}{b} \frac{\partial T_r(x,z,t)}{\partial z}\bigg|_{z=b/2} \quad (1).$$

where υ is the fluid velocity (m/s), $T_w(x,t)$ is the temperature of water, $T_m(x,z,t)$ is the temperature of the rock matrix, b is the fracture aperture (m), c_w is the heat capacity of water ($J/\mathrm{kg}/^{o}C$), ρ_w is the density of water, and K_r is the thermal conductivity of the rock ($J/s/m/^{o}C$).

The temperature of the rock matrix is governed by the one-dimensional heat conduction equation:

$$\frac{\partial^2 T_r(x,z,t)}{\partial z^2} = \frac{\rho_r c_r}{K_r} \frac{\partial T_r(x,z,t)}{\partial t} \quad (2).$$

where ρ_r is the density of the rock matrix, and c_r is the heat capacity of the rock.

The thermal drawdown response may be determined under a variety of different reservoir configurations by using a unified dimensionless analytical model. We redefine the governing equations in terms of the non-dimensional variables of dimensionless flow rate, Q_D, mean temperatures of the rock, T_{Dr} , and water, T_{Dw} , time, t_D and length_scales, x_D and z_D , as,

$$Q_D = \frac{\rho_w c_w}{K_r}\left(\frac{q_1}{L^*}\right)s \tag{3}$$

$$q_1 = \frac{q}{\rho_w \frac{W}{s} H} = \frac{qs}{\rho_w HW} \tag{4}$$

where q is the injection rate (kg/s), q_1 is the volumetric flow rate per fracture per unit thickness (m^2/s), the terms H and W are the height and width of the reservoir respectively and L^* is the distance between the injector and the target point. Substituting equation (4) into equation (3) defines the dimensionless flow rate as,

$$Q_D = \frac{qs^2 c_w}{K_r HL^* W} \tag{5}$$

Dimensionless time t_D is defined as,

$$t_D = \frac{\rho_w c_w}{K_r}\frac{\rho_w c_w}{\rho_r c_r}\left(\frac{q_1}{L^*}\right)^2 t = \frac{t}{K_r \rho_r c_r}\left(\frac{qsc_w}{HWL^*}\right)^2 \tag{6}$$

The dimensionless rock temperature T_{Dr} is defined as,

$$T_{Dr} = \frac{T_{inj} - T_r}{T_{inj} - T_0} \tag{7}$$

The dimensionless outlet water temperature T_{Dw} is defined as,

$$T_{Dw} = \frac{T_{inj} - T_w}{T_{inj} - T_0} \tag{8}$$

The dimensionless lengthscales x_D and z_D are defined separately as,

$$x_D = \frac{x}{L^*} \tag{9}$$

$$z_D = \frac{z}{s} \tag{10}$$

$$\eta_w = \frac{L^* K_r}{\upsilon \rho_w c_w sb} = \frac{1}{Q_D} \tag{11}$$

These defined non-dimensional parameters, Q_D , t_D , T_{Dr} , T_{Dw} , lengthscales x_D and z_D are used to transform and simplify the governing equations. By assuming that heat storage term in the fracture is negligible, the corresponding dimensional governing equations of (1) and (2) could be represented in dimensionless form as,

$$\frac{\partial T_{Dw}(x,t)}{\partial x_D} = 2\eta_w \frac{\partial T_{Dr}(x,z,t)}{\partial z_D}\bigg|_{z=b/2} \tag{12}.$$

$$\frac{\partial^2 T_{Dr}(x,z,t)}{\partial z_D{}^2} = \eta_w{}^2 \frac{\partial T_{Dr}(x,z,t)}{\partial t_D} \tag{13}.$$

6.3 Model description

This present work is a continuation of prior characterizations that defines the potential for late-stage fault reactivation in geothermal reservoirs [*Gan and Elsworth*, 2014]. This extension is to codify the likelihood, timing and magnitude of potential events as a function of fracture geometry and fluid transmission characteristics and applied flow-rates. The heat transfer problem is approached using semi-analytical and numerical methods and this then applied to define the propagation of stress fronts and their impact on seismicity. Calculations are completed using a numerical simulator that couples the analysis of mass and energy transport in porous fractured media (TOUGH) with mechanical deformation (FLAC3D) [*Taron and Elsworth*, 2009; 2010; *Xu et al*., 2004]. These analyses are completed using the non-dimensional parameters noted in equation (5) through (8).

The reservoir geometry includes a 2-D rectangular (1500m × 600m × 15m) reservoir containing three sets of orthogonal fractures (see the mesh in Figure 2). A strike-slip fault is located in the center of reservoir flanked by equidistant injection and withdrawal wells. The initial distribution of reservoir temperature is uniform with an initial rock and fluid temperature of 250 $^\circ C$, an initial reservoir pressure of 18.8 MPa, and with cold water injected under constant mass flow rate with a constant enthalpy of $2.0\times10^5 J/kg$ (equivalent to 43 $^\circ C$) and with the production well operated under a constant pressure of 13.8 MPa. A minimum in-situ stress of 28.8 MPa is imposed in the W-E direction and the maximum horizontal stress of 45 MPa is applied in the N-S direction. The model boundaries are set as no-flow boundaries with applied constant stresses.

The inserted strike-slip fault is finely discretized to represent the anticipated mechanical and transport characteristics of a fault with a low permeability core (thickness 0.8m) flanked by higher permeability damage zones (thickness 1.2 m). The fault acts as flow conduit along its axis but as a barrier/impediment for the propagation of the fluid front from the injection to the recovery well. A ubiquitous-joint

constitutive model is applied to represent the elastic-plastic behavior of the fault. The fractures comprising the fracture network and host rock have the same initial angle of internal friction of 30° (see Table 1) [*Biot*, 1941; *Byerlee*, 1978]. The friction angle of the fault joint is 30° . We adopt a linear strain-softening relationship that implies that the friction angle decreases with an increase in the plastic strain.

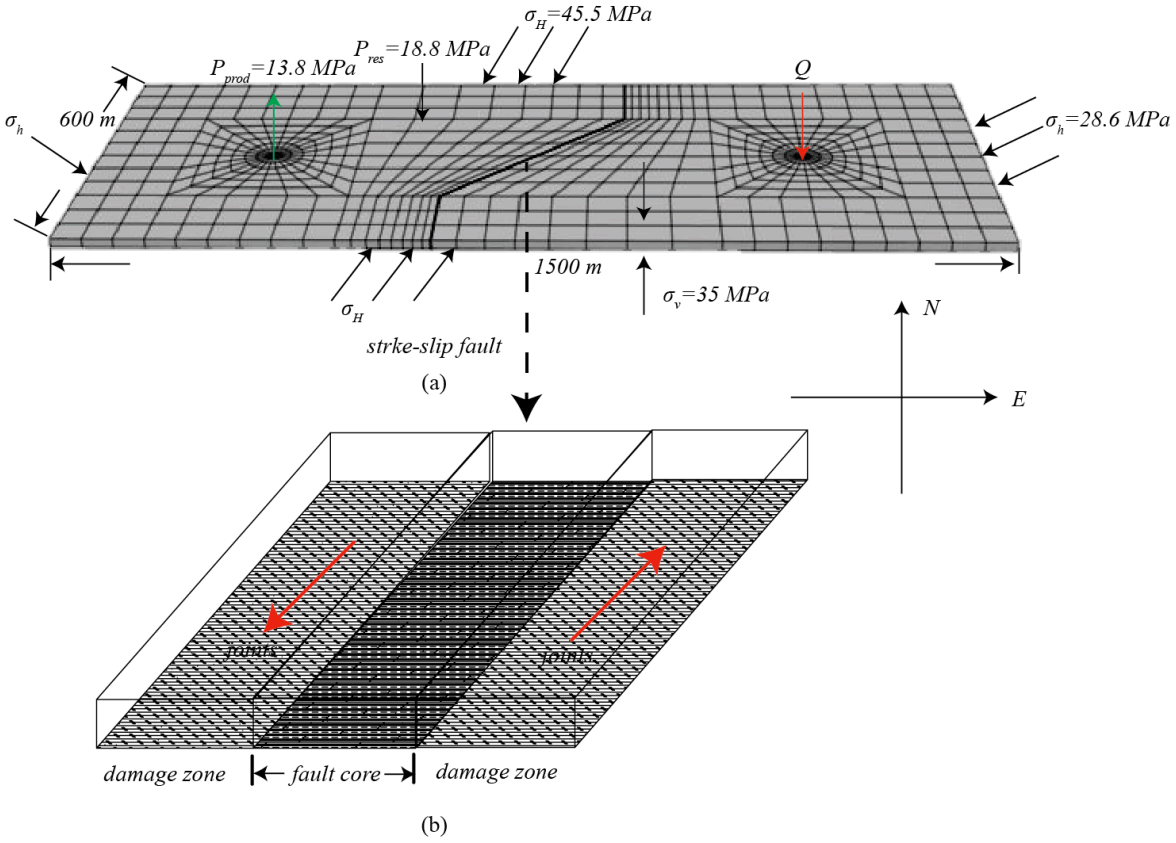

Figure 6 (a) Model geometry and applied stress boundary condition, initial condition, (b) strike-slip fault geometry in model.

Fluid and heat transport is accommodated by representing the reservoir as an equivalent dual permeability continuum. This dual porosity model accommodates the local thermal disequilibrium in heat exchange between rock matrix and fluid in fractures. The dual permeability continuum is represented by orthogonal fracture sets spaced equally in the three principal directions and with uniform initial aperture and with a functionally impermeable matrix.

Table 1 Material properties input in the model for host rock and fault [*Gan and Elsworth*, 2014].

Parameters	In-tact rock	Damage zone	Core zone
Young's modulus (GPa)	8	1.5	1.5
Shear modulus (GPa)	5.5	1	1
Permeability (m^2)	1×10^{-16}	5×10^{-13}	1×10^{-17}
Poisson's ratio	0.2	0.2	0.2
Friction angle	30	30	30
Fracture porosity	0.8	0.8	0.8
Fracture permeability (m^2)	1×10^{-13}	5×10^{-13}	1×10^{-17}
Cohesion (MPa)	8	0	0
Tensile strength (MPa)	10	0	0

6.4 Thermal drawdown behavior

Since the thermal stresses that are induced adjacent to the fault zone may cause seismic fault reactivation, we follow temperature change in the rock using the dimensionless parameters noted earlier. This analysis focuses on predicting the evolution of temperature in the rock (as opposed to fluid temperature as in many prior models [*Gringarten et al.*, 1975; *Elsworth*, 1990]), and captures the intrinsic relationship between the evolution of dimensionless fault rock temperature T_{Dr}, and dimensionless time t_D under various dimensionless flow rates Q_D. Moreover, complementary evaluations of water outflow temperature condition the utility of the reservoir for heat mining where magnitudes of flow rates, Q_D, are selected to minimize seismic risk.

The evolution of dimensionless fault rock temperature T_{Dr} versus dimensionless time t_D/Q_D is determined for different dimensionless flow rates Q_D as shown in Figure 2-3. This is for fracture network permeability of $1.0\times10^{-13}m^2$ but with different fracture spacing s to allow the full parameter space of Q_D to be explored. Apparent is that the thermal drawdown response of the rock is exclusively controlled by

the magnitude of Q_D. Table 2-2 presents the various Q_D values under different combinations of injection rate and fracture spacing, respectively. Here the main assumption for the expression of Q_D is that the direction of heat conduction in the matrix is orthogonal to the direction of the transverse fractures.

Figure 3 shows that the drawdown gradients of dimensionless temperature with time become infinite as represented by a steep (vertical) drawdown response around $t_D/Q_D \sim 1$, when the Q_D value decreases below 2.6×10^{-4}. Solutions are limited to this magnitude due to advection-dominant instabilities in TOUGH (Peclet Number > 2.6×10^{3}) with the dashed line in Figure 3 extrapolating this response. Furthermore, the drawdown response becomes asymptotic to $t_D/Q_D \sim 1$ as Q_D approaches 2.6×10^{-6} defining the lower bounding condition where a plug thermal front migrates through the reservoir and consequently yields the highest thermal gradients in space. Conversely, for high Q_D, the gradient of dimensionless temperature drawdown becomes progressively flatter as the flow rate is increased. When Q_D reaches 2.6×10^{4}, the curves become asymptotic to a horizontal line anchored at $T_D \sim 1$. This represents the case where water flow through the reservoir is sufficiently rapid that heat transfer from the rock to the fluid is small. This results in a uniform temperature distribution in the fluid and uniform thermal drawdown in the reservoir.

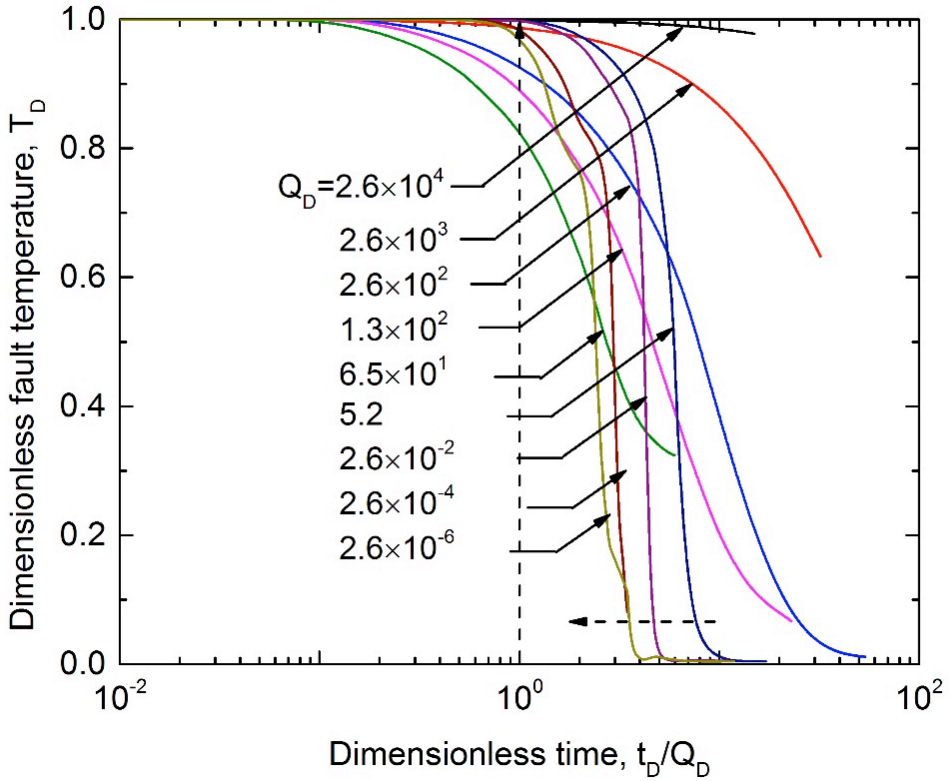

Figure 2 Dimensionless fault temperature T_D evolution vs dimensionless time t_D/Q_D under Q_D values varies respectively from 2.6×10^{-6} to 2.6×10^{4}.

Thus the bounding distributions of temperature in the reservoir and how they change with time are conditioned by this non-dimensional flow variable, Q_D. At high flow rates ($Q_D > 2.6\times10^{4}$) there is little heat transfer from the rock to the water, and the thermal drawdown in the reservoir is uniform as shown in Figure 5. Conversely, when the flow rate is low ($Q_D < 5.2$) then the chilled front in the rock propagates through the reservoir.

An alternate way to represent the transient response of the temperature at the fault within the reservoir by the dimensionless timing t_D alone. This dimensionless relationship $T_D - t_D$ returns a new response of the thermal drawdown in the rock (Figure 4). The individual drawdown curves are parallel for $Q_D < 5.2$. The factor Q_D has an impact in determining the sequence of the parallel curves with a steep decline in time. The curve with the lowest $Q_D = 2.6\times10^{-6}$ indicates the earliest drawdown in dimensionless time as $t_D = 10^{-5}$. For this Q_D -controlled thermal drawdown system, as the Q_D value grows one order of magnitude when $Q_D < 5.2$, the corresponding timing of drawdown is equivalently elevated by one order magnitude. When the $Q_D > 5.2$, the gradient of the rock temperature curves decrease gradually as the Q_D value grows, which represents the case of more significant heat transfer by heat advection. By means of this dimensionless type curve, the timing of thermal drawdown for reservoirs under different configurations may be rigorously explored.

Table 2 Q_D values for the fault under different reservoir configurations by variant injection rate and fracture spacing combinations.

Injection rate (kg/s)	**Fracture spacing (m)**	Q_D
100	1000	2.6×10^{4}
10	1000	2.6×10^{3}
100	100	2.6×10^{2}
50	100	1.3×10^{2}
25	100	6.5×10^{1}
200	10	5.2
100	1	2.6×10^{-2}
100	0.1	2.6×10^{-4}
100	0.01	2.6×10^{-6}

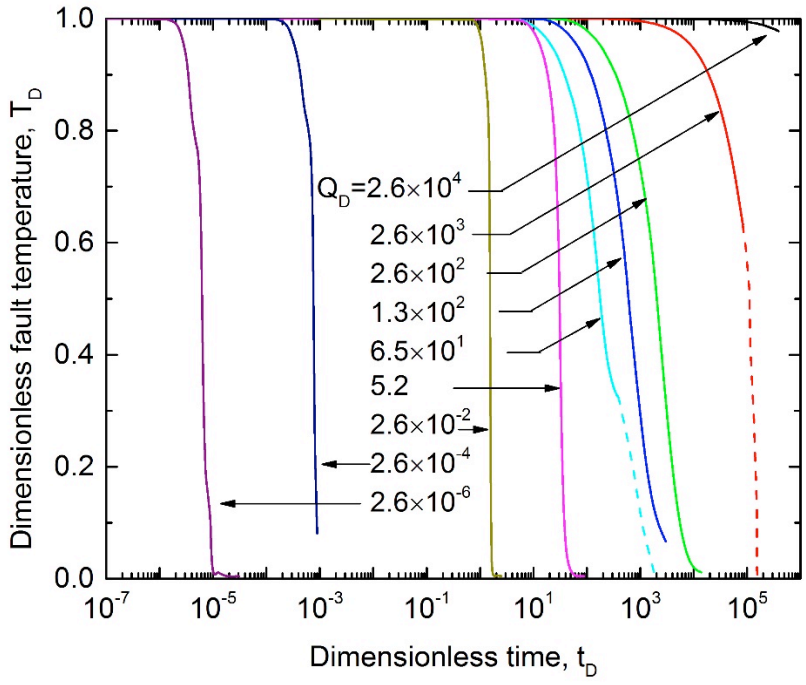

Figure 3 Dimensionless fault temperature T_D at the fault vs dimensionless time t_D under Q_D varies respectively from 2.6×10^{-6} to 2.6×10^{4}.

6.5 Thermal front propagation and induced seismicity

The migration of the thermal front within the reservoir depicts the efficiency of heat recovery from the surrounding geologic medium and controls the form of the thermal gradient at the front. Furthermore, the propagation of the thermal front under different non-dimensional flow rates Q_D alters the timing of its arrival and therefore the timing of any induced seismicity associated with that thermal stress. Importantly, two bounding behaviors are noted, based on the magnitude of the non-dimensional injection rate, Q_D. When Q_D is sufficiently large, the advective heat transfer within the fast flowing fluid is much more efficient than that due to conductive heat transfer to the fluid. In this instance the thermal front propagates from the injection well towards the production well without the presence of distinct uniform thermal front – indeed, in the limit, the water temperature is near uniform throughout the reservoir. Conversely, for small Q_D the short dimensionless conduction length in the blocks results in more efficient transfer by heat conduction and results in a distinct front but one that displaces at a slower rate v_T – a velocity $v_T = \frac{\rho_w c_w}{\rho_r c_r} v_w$, defined by the product of the ratio of the thermal capacities of water and rock and the fluid velocity v_w in the fracture.

Figure 5 shows the displacement of the thermal front within the rock as non-dimensional flow rates Q_D are varied. The injection well is to the left (x=0 m) with the production well to the right (x=900 m). The fault is intermediate (dashed arrow) between the injection and production wells. If the Q_D value is larger than 2.6×10^{2} (Figure 5c), the rock temperature across the entire reservoir declines uniformly. The flat and uniform drawdown curve corresponds to the larger magnitudes of Q_D (Figure 5a). Uniform longitudinal thermal drawdown of the rock results in the early breakthrough of cold water (Figure 5a). Conversely, when the Q_D values are smaller than 2.6×10^{-2}, the thermal front propagates as a thermal shock. Figure 5f with the smallest Q_D value of 2.6×10^{-6} shows the slowest rate of propagation of the thermal front which identifies the case for the most delayed breakthrough. This represents the case that is most desired in retaining outlet temperatures the highest although flow rates may not be sufficiently high to be economically viable as a geothermal reservoir.

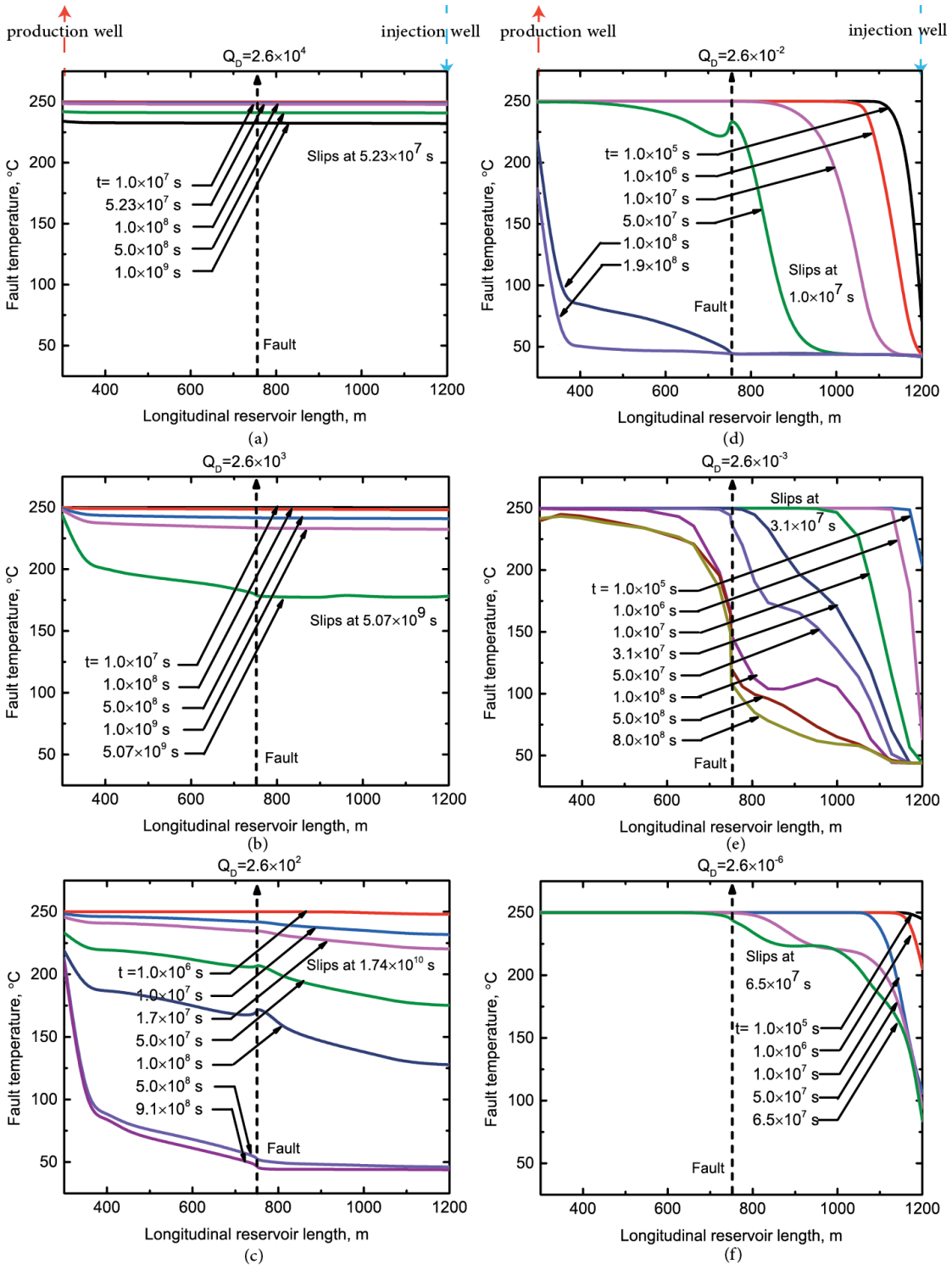

Figure 4 Thermal front propagation from the injection well (right axis) towards the production well (left axis) under different Q_D values, the figures from (a) to (f) respectively represent the Q_D values varied from 2.6×10^{-6} to 2.6×10^{4}.

The dimensionless form of timing of the onset of seismicity is linked to the arrival of this front at the location of the fault. This arrival time for the front, traveling a distance L^* at a propagation velocity v_T is

$$t_{analytical}^{seismic} = \frac{L^*}{v_T} = \frac{L^*}{\frac{\rho_w c_w}{\rho_m c_m} v_w} = \frac{L^*}{v_w} \frac{\rho_r c_r}{\rho_w c_w} \quad (14).$$

Since, the dimensionless time is defined as,

$$t_D = \frac{t}{K_r \rho_r c_r} \left(\frac{qsc_w}{HWL^*} \right)^2.$$

then substituting the dimensional time of equation (2) into equation (3) gives the timing of seismicity as $t_D \sim Q_D (\text{for } Q_D < 10^0)$. The relationship between the dimensionless timing for the onset of seismicity and the fluid velocity could be obtained by inserting $t_{analytical}^{seismic}$ into the equation of dimensionless time,

$$t_D^{seismic} = \frac{L^*}{v_w} \frac{\rho_r c_r}{\rho_w c_w} \frac{1}{K_r \rho_r c_r} \left(\frac{qsc_w}{HWL^*} \right)^2 = \frac{L^*}{v_w} \frac{K_r}{\rho_w c_w s^2} Q_D^2 \quad (15).$$

Therefore the term $t_D^{seismic} = \frac{L^*}{v_w} \frac{K_r}{\rho_w c_w s^2} Q_D^2$ in equation (15) could be used to capture the dimensionless timing of seismicity. Figure 6 shows that this timing relation is correct for $Q_D < 5.2$ where the injected fluid is able to completely deplete the heat from the reservoir adjacent to the injection well. When the value of Q_D is gradually increased above 5.2, then heat transfer by rapid advection dominates over conduction. In this condition there is no distinct thermal front to change the stress state of the fault and the error in the prediction of timing from this simple relationship $t_D \sim Q_D$ becomes more significant.

From the form of the rate of propagation of the cooling front within the reservoir it is apparent that the non-dimensional timing of arrival of the front scales with dimensionless flow rate (Figure 3). There is a linear relationship implied between Q_D and the corresponding timing of seismicity t_D (Figure 6). As the magnitude of Q_D increases from 2.6×10^{-6}, the dimensionless timing t_D for the thermally-driven induced seismicity increases approximately linearly – enabling timing to be defined in a quantitative manner.

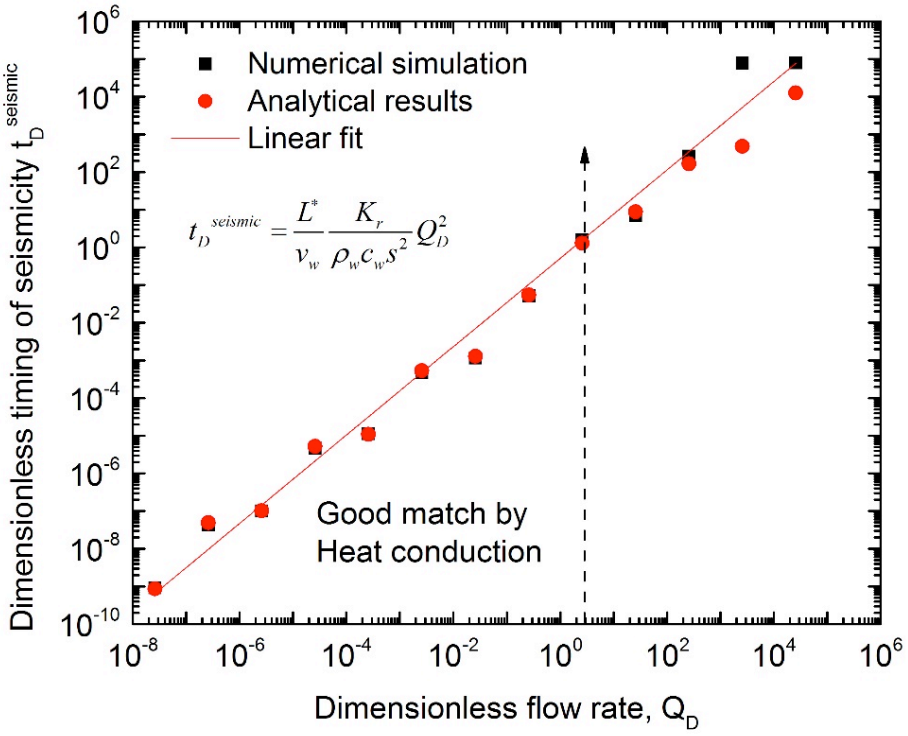

Figure 5 Validation of the dimensionless timing equation for the onset of seismicity between numerical simulation results and the analytical results under various Q_D values ($Q_D = 2.6\times10^{-8} \sim 2.6\times10^{2}$). Red circles represent the velocity results from the analytical equation, while the black squares represent the results from the simulations.

Figure 7 illustrates the thermal evolution of water temperature under the two bounding magnitudes of Q_D as 2.6×10^{4} and 2.6×10^{-6} respectively. At high dimensionless flow rate the cold front reaches the production well after $1.0\times10^{7} s$ (~120d). At low dimensionless flow rates ($Q_D = 2.6\times10^{-3}$) the outlet remains at the ambient temperature of the reservoir. This illustrates that geothermal production under large Q_D values may not be feasible as the advection dominated flow results in premature breakthrough, thus degrading the thermal output for the entire reservoir.

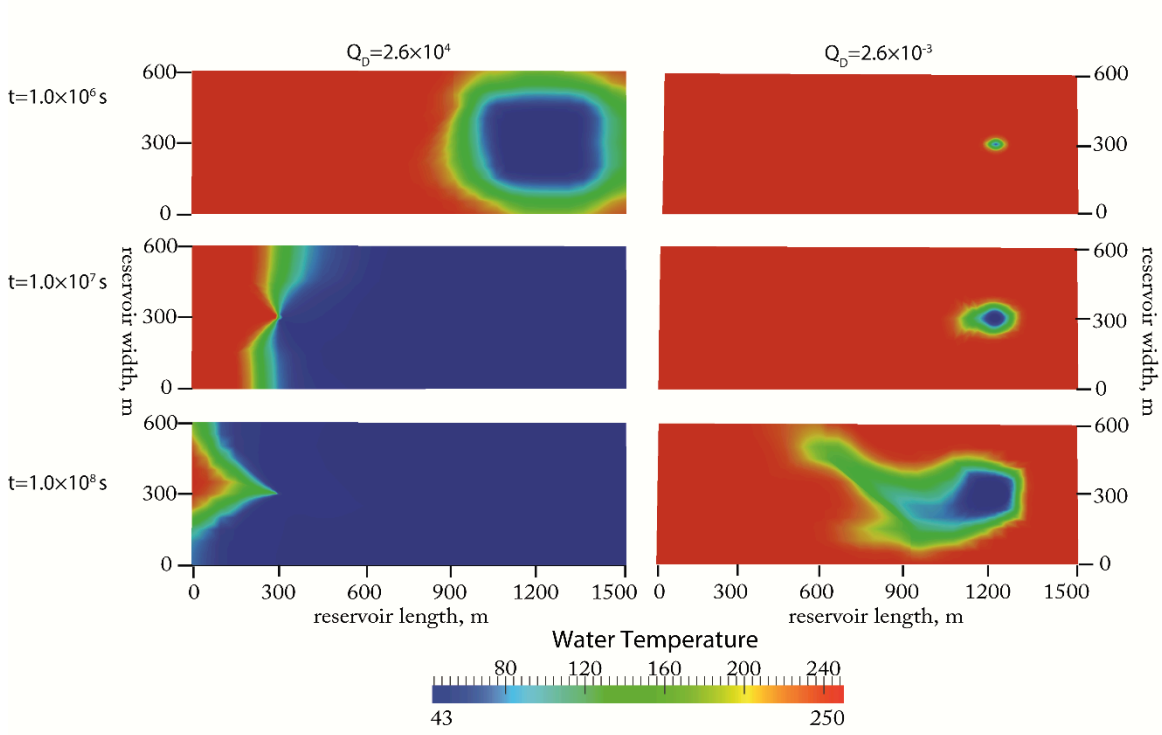

Figure 6 Comparison of water temperature evolution in the reservoir under two bounding Q_D values, the left side figures represent the condition of $Q_D = 2.6\times10^{4}$, the right side figures represent the condition of $Q_D = 2.6\times10^{-3}$.

The thermal front propagation under various magnitudes of Q_D substantially changes the evolution of the stress state around the fault. Figure 8 illustrates the thermal evolution of rock temperature under the two bounding magnitudes of Q_D as 2.6×10^{4} and 2.6×10^{-3}. This contrasts with Figure 7 for the evolution of water temperature distribution. For $Q_D = 2.6\times10^{-3}$, the rock and fluid are in thermal equilibrium with no significant temperature difference. A distinct thermal front develops to differentiate the cooled and hot region. Conversely, for $Q_D = 2.6\times10^{4}$ no distinct and observable thermal front develops. Also shown is the evolution of the Coulomb stress ratio (τ / σ_{neff}) in Figure 8(c). This shows that the stress state of the fault evolves significantly differently due to the bounding styles of thermal propagation in the reservoir at $Q_D > 2.6\times10^{4}$ and $Q_D < 2.6\times10^{-3}$. These induced thermal stresses may trigger fault reactivation when the fluid pressures alone are insufficient. We explore this in the following section.

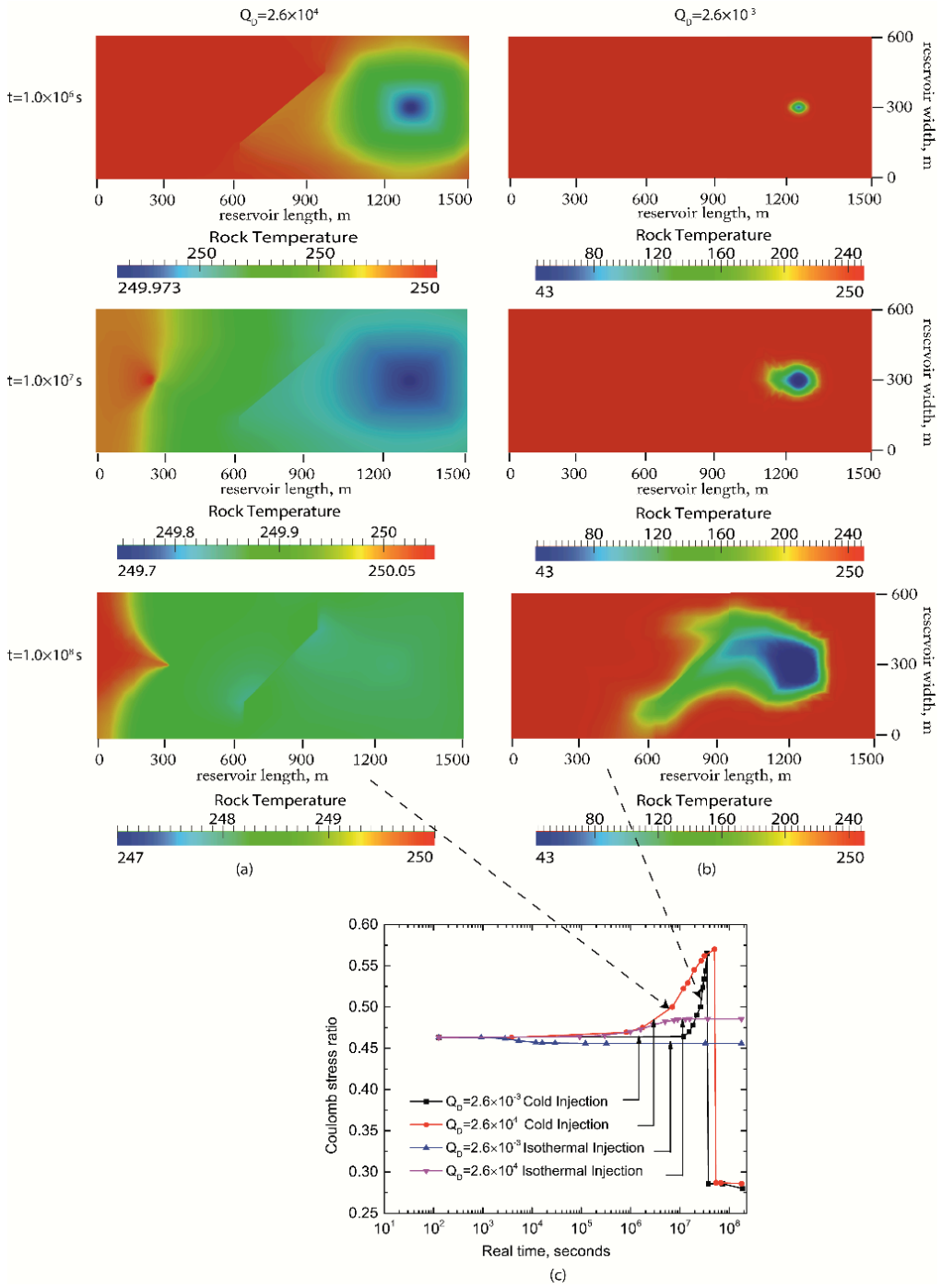

Figure 7 Contour of rock temperature distribution at $t = 1.0\times10^{6}s$, $1.0\times10^{7}s$, $1.0\times10^{8}s$ respectively for $Q_D = 2.6\times10^{4}$ (a) and $Q_D = 2.6\times10^{-3}$ (b). (c) represents the evolution of the coulomb stress ratio under $Q_D = 2.6\times10^{4}$ and $Q_D = 2.6\times10^{-3}$ with isothermal or non-isothermal injection conditions.

The propagation of the thermal front within the rock is therefore likely an important factor in defining the timing and magnitude of seismicity. When the dimensionless flow rate Q_D is smaller than 2.6×10^{-2}, the timing of seismicity is exclusively governed by the timing of the arrival of the thermal front at the fault (Figures 5-d, 5-e, and 5-f). In terms of the physical characteristics of the reservoir used here, these corresponding to real times of $t=1.0\times10^7 s(\sim 100d)$, $3.1\times10^7 s(\sim 300d)$, and $6.5\times10^7 s(\sim 752d)$ for $Q_D = 2.6\times10^{-2}$, 2.6×10^{-4}, 2.6×10^{-6} respectively. Conversely, for large Q_D, the cooling regime is spread more broadly across the reservoir and therefore may activate a larger patch at this changed stress. Thus, the arrival of the zone of high thermal gradient at the fault is the principal factor that controls the timing of thermally induced seismicity.

Moreover, the slip distance distributions for each patch along the fault reflect the magnitude of the seismic events (Figure 9(a)) that are associated with the different forms of the migrating thermal front. As the dimensionless injection rate Q_D increases, the corresponding magnitude of seismicity event also grows. The magnitude of these individual events may be evaluated from the slip distribution as

$$M_0 = \int_0^L \mu LW dD_c \qquad (16).$$

where M_0 is seismic moment, L is the fault length, W is the width of fault rupture, μ is the rigidity of fault (taken here as 1 GPa), and D_c is the slip distance along the fault patch. This seismic moment may be converted into a moment magnitude M_s, used to measure the strength of the seismic event. The M_s - M_0 relationship is defined as [*Kanamori and Abe*, 1979; *Purcaru and Berckhemer*, 1982],

$$\log M_0 = 1.5M_s + 16.1 \quad . \qquad (17)$$

The reservoir thickness is 15 m used in the model. In order to obtain moment magnitudes that are appropriate to the 3-D representation of the fault (fault area of 442m× 442 m), we use the results from the 2-D plane strain model and extrapolate these over the fault area. This switch between the 2-D slip model and the 3-D fault ignores the clamped boundaries (zero displacement) at the top and base of the fault and would slightly overestimate the moment magnitude—relative to the real case where the edges of the fault are clamped.

Figure 9b indicates that the magnitudes of induced events increase progressively with an increase in the dimensionless flow rate. For small Q_D (2.6×10^{-6}), the resulting event magnitude is 2.74 and this elevates to 2.86 as Q_D is increased (2.6×10^{3}).

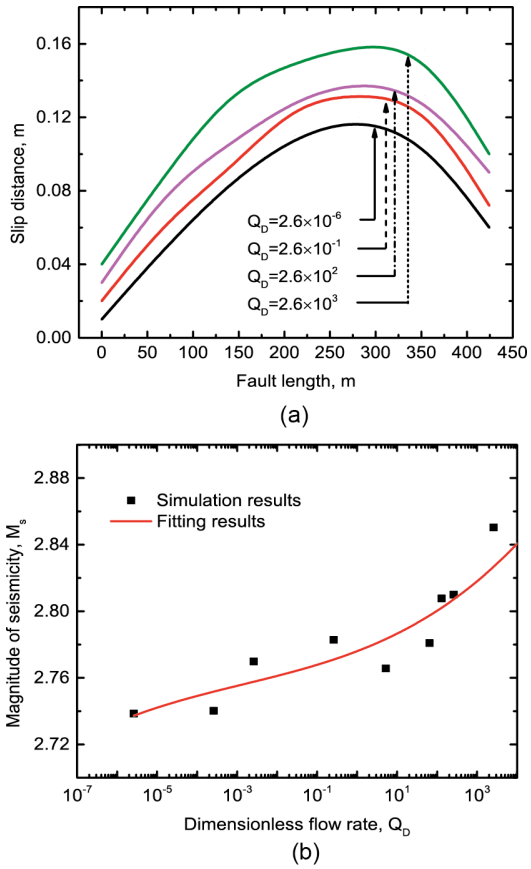

Figure 8 (a) the comparison of slip distance distributions in different patches along the fault under the different dimensionless flow rate Q_D , (b) the corresponding maximum magnitude of seismicity based on the slip distance results under different flow rate Q_D .

The outcome that the largest circulation rates give the largest events appears to contradict the suggestion that the largest events will result from the most non uniform thermal field – a thermal field that will occur for the lowest flow rates. A plausible mechanism for this observation is that the chilled area along the fault, which ultimately contributes to the destressing and then slips, correlates positively with Q_D. Thus the larger flow rates result in a larger cooled region on the fault and although the stress drops are smaller than for the abrupt thermal front, the resulting product of stress-drop and slipped area are larger. Figure 10(a) ($Q_D = 2.6\times10^{-8}$) shows that only a small portion of the fault is locally affected by the arrival of the thermal front for small non-dimensional flow rates ($t = 6.2\times10^{7}\,s$). In comparison, for a larger Q_D (2.6×10^{3}; Figure 10(b)), the cumulative thermal stress initiates a larger fault reactivation at later time ($t = 5.0\times10^{9}\,s$) since the entire fault is uniformly cooled. This explains the observations of Figure 9 where

event magnitude grows with Q_D. Thus both the dimensionless timing of seismicity t_D and the event magnitude M_s both increase with an increase in the dimensionless flow rate as shown in Figure 9 and 10.

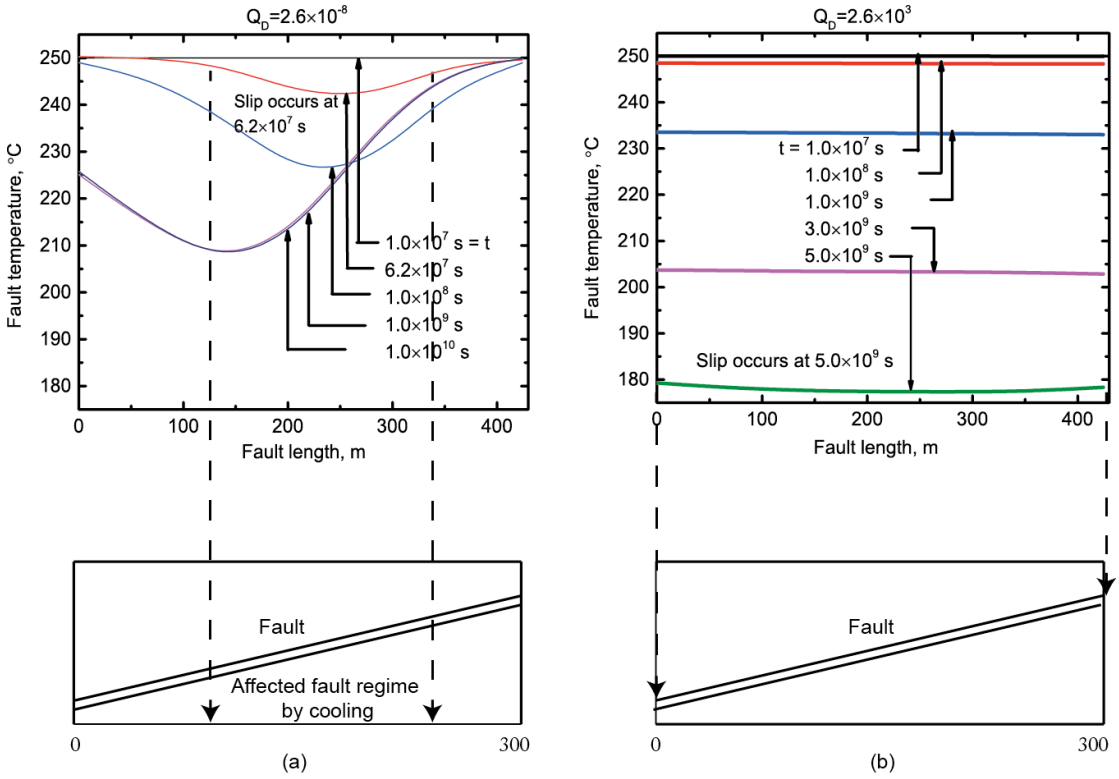

Figure 9 (a) The fault temperature evolution under $Q_D = 2.59\times10^{-8}$, the two dashed lines represent the area affected by the thermal stress acting on the fault when slip occurs at $6.2\times10^7 s$, (b) the fault temperature evolution under $Q_D = 2.59\times10^3$, the two dashed lines at the two tips of fault shows the fault regime affected by the thermal stress due to the cooling.

6.6 Output power optimization

Since the propagation of the thermal front at different dimensionless flow rates Q_D influences both the form and distribution of thermal drawdown within the reservoir, the overall thermal output of the reservoir should scale with Q_D. Thus the rate of thermal energy production (power) may be determined scaled with this parameter, together with its longevity. These two observations, together give the cumulative energy output.

Thermal power output, P_t, may be defined as,

$$P_t = Q\Delta H \qquad (18).$$

where Q is the mass flow rate (kg/s), and ΔH is the enthalpy difference between the outlet water enthalpy and the enthalpy of injection water.

Figure 11 compares the evolution of power generation rate for various Q_D. The curves share an identical initial generation rate of ~30 MW, but diverge after the transient production period $t = 1.0\times10^3 s$. The response for the two end-member magnitudes of Q_D (2.6×10^{-6} and 2.6×10^4) represent the two most unfavorable production scenarios. At large flow rates ($Q_D > 2.6\times10^4$) the reservoir is unable to transfer heat to the massive flux of cold water after the initial removal of heat from the fracture skin. As a consequence the outlet drops precipitously after $t = 1.0\times10^7 s (\sim 115 d)$. The converse is true at low flow rates ($Q_D = 2.6\times10^{-6}$) where the output is hot but the low mass flow rate limits power generation to ~15Mw. The sweetspot with the most favorable conditions for power generation are in the range of $Q_D = 2.6\times10^{-2} \sim 2.6\times10^2$. The curve with $Q_D = 2.6\times10^{-2}$ yields the maximum cumulative power generation within 1 year, while the red curve with $Q_D = 2.6\times10^2$ results in larger potential of late stage power generation. It could be explained that the large volume of injection reduced the effective stress by elevating the pore pressure of reservoir at a large extent, the permeability around the production well could be further improved by the occurrence of fracture shearing. Therefore the mass flow rate at the outlet increased significantly. According to Figure 11, it is desirable to produce the geothermal reservoir with flow rates in the range $Q_D = 2.6\times10^{-2} \sim 2.6\times10^2$ to maximize energy recovery.

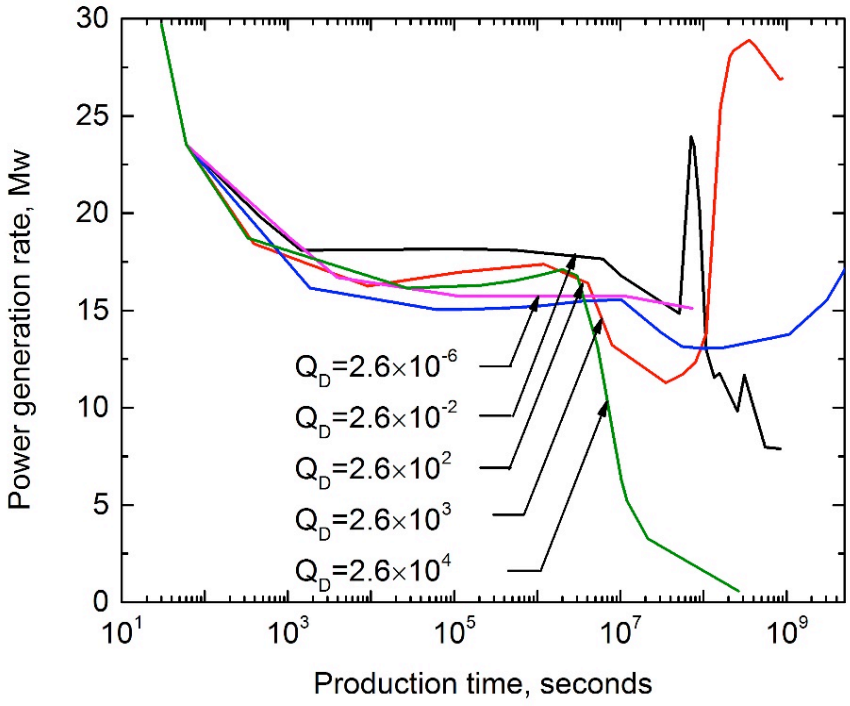

Figure 10 The results of power generation rate calculation under different Q_D values within 50 years injection, the magenta curve represents the smallest Q_D 2.6×10^{-6}, and the green curve represents the largest Q_D value equal to 2.59×10^{4}.

6.7 Conclusions

The foregoing defines the evolution of heat transfer in a fractured geothermal reservoir characterized by non-dimensional parameters. The evolution of water temperature and mean temperature in the rock is conditioned by dimensionless parameters representing the flow rate Q_D and time t_D. The dimensionless flow rate Q_D is conditioned by the in-situ fracture spacing, prescribed mass injection rate and reservoir geometry and influences the thermal drawdown response of the reservoir. The sensitivity tests have explored the effect of, fracture spacing, fault permeability and injection temperature [*Gan and Elsworth*, 2014], Based on this dimensionless model, this work captures the thermal drawdown response of the host hot rock at different reservoir scales and for different spacing and permeabilities of fracture networks. More importantly, the timing and magnitude of thermally-driven fault seismicity are rigorously investigated under the various scenarios of thermal front propagation in rocks.

The primary control parameter Q_D transforms dimensionless timing and temperature data into two bounding asymptotic behaviors. These two bounding asymptotic behaviors refer to the situations of heat transfer dominated by heat conduction where the drawdown gradients of dimensionless temperatures with time become asymptotically and infinitely steep (vertical) around $t_D/Q_D \sim 1$, when the Q_D value decreases below 2.6×10^{-4}. When Q_D reaches 2.6×10^{4}, the curves become asymptotic to a horizontal line anchored at $T_D \sim 1$. This represents the case where the velocity of fluid in the reservoir is sufficiently rapid that heat transfer from the rock to the fluid is conduction limited and small. This results in an early cold water breakthrough at the outlet and uniform thermal drawdown in the rock. The magnitude of Q_D has an impact in determining the sequence of the parallel steep curves (dimensionless t_D). When the Q_D value grows by one order of magnitude, the corresponding dimensionless timing t_D for thermal depletion of water or rock is approximately elevated by one order magnitude for $Q_D < 5.2$. The situation with a lower magnitude Q_D (< 5.2 in this model configuration) yields a uniform propagation of the thermal front, while the case with larger magnitude Q_D ($> 2.6\times10^{2}$) produces a more uniform thermal distribution across the whole reservoir without a distinct thermal front.

Under the condition of propagation of a uniform thermal front, the timing for fault reactivation is determined as the thermal front arrives at the fault. The spatial thermal gradient adjacent to the front (and

then arriving at the fault) is the principal factor defining the timing of triggered seismicity. As the dimensionless ratio Q_D increases, accordingly the dimensionless timing for the onset of thermal-driven seismicity is also linearly increased. Similarly, the magnitude of fault slip distance also grows with increments in Q_D, since the cooled area of fault area that exhibits thermal stress changes is proportionally increased with an increase in Q_D.

Finally, the Q_D magnitude plays an important role in determining the rate of power generation and the ultimate heat extraction efficiency of the reservoir. It reveals that the optimum water production condition is located at an intermediate magnitude of Q_D in the range of $2.6\times10^{-2} - 2.6\times10^{2}$. The two bounding magnitudes of Q_D represent unfavorable conditions where flow rates are either too small or outlet temperatures too small to yield significant power.

Acknowledgement

This work is a partial result of support from the US Department of Energy under project DOE-DE-343 EE0002761. This support is gratefully acknowledged. The authors would like to thank the anonymous reviewers for their valuable comments and suggestions to improve the quality of the paper.

6.8 References

Biot, M. A. (1941), General Theory of Three-Dimensional Consolidation, *Journal of Applied Physics*, 12(2), 155_164.

Bodvarsson, G. (1969), On the temperature of water flowing through fractures, *Journal of Geophysical Research*, 74(8), 1987-1992.

Bödvarsson, G. S., and C. F. Tsang (1982), Injection and Thermal Breakthrough in Fractured Geothermal Reservoirs, *Journal of Geophysical Research: Solid Earth*, 87(B2), 1031_1048.

Byerlee, J. (1978), Friction of rocks, *Pure Appl. Geophys*., 116(4-5), 615-626.

Elsworth, D. (1989a), Thermal recovery from a multiple stimulated HDR reservoir, *Geothermics*, 18(5–6), 761-774.

Elsworth, D. (1989b), Theory of thermal recovery from a spherically stimulated hot dry rock reservoir, *Journal of Geophysical Research: Solid Earth*, 94(B2), 1927-1934.

Elsworth, D. and Xiang, J. (1989). A reduced degree of freedom model for permeability enhancement in blocky rock. *Geothermics*, Vol. 18, No. 5/6, pp. 691-709.

Elsworth, D. (1990), A comparative evaluation of the parallel flow and spherical reservoir models of HDR geothermal systems, *Journal of Volcanology and Geothermal Research*, 44(3–4), 283-293.

Gan, Q., and D. Elsworth (2014), Analysis of Fluid Injection-Induced Fault Reactivation and Seismic Slip in Geothermal Reservoirs, *J. Geophys Res. Solid Earth* 119, 3340_3353, doi:10.1002/2013JB010679.

Ganguly, S., and M. S. Mohan Kumar (2014), Analytical solutions for transient temperature distribution in a geothermal reservoir due to cold water injection, *Hydrogeol J*, 22(2), 351-369.

Ghassemi, A., S. Tarasovs, and A. H.-D. Cheng (2003), An integral equation solution for three-dimensional heat extraction from planar fracture in hot dry rock, *Int. J. Num. Anal. Methods Geomech*, 27(12), 989_1004.

Gringarten, A. C., and P. A. Witherspoon (1973), Extraction of heat from multiple-fractured dry hot rock, *Geothermics*, 2(3–4), 119_122.

Gringarten, A. C., P. A. Witherspoon, and Y. Ohnishi (1975), Theory of heat extraction from fractured hot dry rock, *J. Geophy. Res*., 80(8), 1120_1124.

Holman, J. P. (2002), Heat Transfer - Si Units - Sie, McGraw-Hill Education (India) Pvt Limited.

Kanamori, H., and K. Abe (1979), Reevaluation of the turn-of-the-century seismicity peak, *Journal of Geophysical Research: Solid Earth*, 84(B11), 6131-6139.

Paul Segall, Shaun D. Fitzgerald, A note on induced stress changes in hydrocarbon and geothermal reservoirs, *Tectonophysics*, Volume 289, Issues 1–3, 15 April 1998, Pages 117-128, ISSN 0040-1951, http://dx.doi.org/10.1016/S0040-1951(97)00311-9.

Pruess, K. (1983), Heat transfer in fractured geothermal reservoirs with boiling, *Water Resources Research*, 19(1), 201-208.

Pruess, K., and Y.-S. Wu (1993), A New Semi-Analytical Method for Numerical Simulation of Fluid and Heat Flow in Fractured Reservoirs, SPE Advanced Technology Series, 1(02), 63 - 72.

Purcaru, G., and H. Berckhemer (1982), Quantitative relations of seismic source parameters and a classification of earthquakes, *Tectonophysics*, 84(1), 57-128.

Shaik, A. R., S. S. Rahman, N. H. Tran, and T. Tran (2011), Numerical simulation of Fluid-Rock coupling heat transfer in naturally fractured geothermal system, *Applied Thermal Engineering*, 31(10), 1600-1606.

Taron, J., and D. Elsworth (2009), Thermal–hydrologic–mechanical–chemical processes in the evolution of engineered geothermal reservoirs, *International Journal of Rock Mechanics and Mining Sciences*, 46(5), 855-864.

Taron, J., and D. Elsworth (2010), Coupled mechanical and chemical processes in engineered geothermal reservoirs with dynamic permeability, *Int. J. Rock Mech. Min. Sci*., 47(8), 1339_1348.

Williams, C. F., M. J. Reed, and M. and R.H. (2008), A Review of Methods Applied by the U.S. Geological Survey in the Assessment of Identified Geothermal ResourcesRep. Open-File Report 2008–1296, U.S. Department of the Interior, U.S. Geological Survey.

Xu, T., E. Sonnenthal, N. Spycher, and K. Pruess (2004), TOUGHREACT User's Guide: A Simulation Program for Non-isothermal Multiphase Reactive geochemical Transport in Variable Saturated Geologic Media, edited.

Xu, T., J. A. Apps, and K. Pruess (2003), Reactive geochemical transport simulation to study mineral trapping for CO2 disposal in deep arenaceous formations, *Journal of Geophysical Research: Solid Earth,* 108(B2), 2071.

Xu, T., E. Sonnenthal, N. Spycher, K. Pruess (2004), TOUGHREACT User's Guide: A Simulation Program for Non-isothermal Multiphase Reactive Geochemical Transport in Variably Saturated Geologic Media, Lawrence Berkeley National Laboratory Report LBNL-55460.

7 CHAPTER 7 MAPPING PERMEABILITY TENSORS IN FRACTURED GEOTHERMAL RESERVOIRS USING MEQ DATA

Abstract

In the stimulation of fractured geothermal reservoirs, injection wellhead pressure, flow rate and microearthquake (MEQ) data are crucial feedbacks recorded in order to characterize the evolution of subsurface fluid flow. However, one of the hurdles to successful EGS development and operation is the lack of reliable evaluation for the initial and evolving hydraulic properties of the fractured reservoir. Specific spatial conditions (e.g., location and direction) of fracture permeability in the field are vital in defining reservoir response during stimulation and then production. To constrain the evolving permeability, we propose a model that maps the in-situ permeability based onto the *Oda* crack tensor using the moment magnitude of individual MEQs, assuming that the induced seismicity is controlled by the Mohr-Coulomb shear criterion. The MEQ catalog of locations, fault plane solutions, and moment magnitudes are used to estimate fracture apertures of individual events/fractures that are a dynamic function of in-situ stress, fluid pressure, shear displacement and fracture size. The corresponding in-situ 2D permeability tensors are computed and mapped at various scales within the reservoir. Results suggest that the permeability magnitude largely depends on MEQ moment magnitude and fracture frictional properties while permeability direction is dominantly controlled by fracture orientation. However, uncertainty remains within the results, which need improvements in constraint from laboratory and in-situ fracture characterization, the quality of seismic monitoring and reliability of appropriate assumptions.

7.1 Introduction

Enhanced Geothermal Systems (EGS) are engineered reservoirs created to recover the geothermal resource from high temperature but low permeability rock formations. In general, the creation and operation of an EGS project comprises two phases. In the first phase, the reservoir is stimulated to generate sufficient permeability through hydroshearing of pre-existing fractures in the reservoir [1]. During stimulation, elevated fluid pressures induce microearthquakes (MEQs) by decreasing the effective normal stresses on the fracture planes. As microseismic events provide valuable feedback to the stimulation, microseismic monitoring is one of the most effective ways to characterize the underlying active processes and the evolution of permeability in the reservoir. This is accomplished through the use of moment tensors derived for the events [2]. Moment tensors, in turn, may be mathematically interpreted to estimate the geometry of the fracture zone, the orientation of fracture planes and the dynamics of fracture development. In the second phase, a production well is subsequently planned and optimally accommodated according to the monitored spatial distribution of MEQs in order to maximize thermal production. Although there is wide agreement that microseismicity may signal the enhancement of

permeability in EGS reservoirs (**Figure 1(a)**) and it has become a method to optimally locate a production well, the quantification of the assumed enhancement and the physical connections between MEQ data and spatial permeability distribution and evolution are not well constrained.

A number of approaches provide insight into connections between in-situ MEQ data and subsurface fluid activity and reservoir state. Permeability may be defined from the spatio-temporal distribution of the fluid-injection-induced seismicity [3]. This model establishes a relation between fluid diffusion distance and spatio-temporal distribution of MEQs from which an equivalent permeability of the entire reservoir is derived. However, a noticeable shortcoming of this approach is lack of sufficient consideration of regional geomechanical effects and variations in fracture permeability caused by hydroshearing. As a result, it has limitations in constraining the evolving permeability within a more detailed and specific region and plays a limited role in defining response at finer resolution. In addition, a viable approach estimating a linkage between fluid pressure and in-situ MEQ data is suggested to investigate the interactions between triggering fluid pressures and magnitudes of MEQs [4, 5]. This method integrates focal mechanisms, tomographic techniques and the Mohr-Coulomb failure criterion to indicate the fluid pressure along the fracture plane at the time of slip. Though this work provides good constraint of a 3D distribution of fluid pressures in the stimulated zone of the reservoir, it does not include the contribution of the fracture network in the evolution of hydraulic properties (i.e. permeability) that are of crucial interest for long-term EGS production.

To compensate for this inadequacy, a MEQ-permeability coupling model is proposed to estimate the in-situ reservoir permeability using monitored MEQ data [6]. This method assumes that induced seismicity is controlled by the Mohr-Coulomb shear criterion and applies the moment magnitude of MEQs to inversely calculate fracture shear slip. Assuming the veracity of the cubic law, permeability is approximately averaged on a suitable representative elementary volume of reservoir (REV). This method is particularly suitable for poorly characterized orientations of fracture sets. However, the hydraulic effect imposed by geometric contributions of fracture networks [7] is not fully considered in this approach. If fracture planes whose locations and orientations in the area of interest are well defined by the microseismic characterization, a discrete fracture models is assumed to be more appropriate for the evaluation of permeability.

A mathematical model-fabric tensor may be used to describe the geometric characteristics of cracked rock and to determine transport characteristics [7]. Based on previous work, in this study, we explore the use of an MEQ-DFN-permeability coupling model using Oda's crack tensor theory [7, 8]. This model transforms the MEQ data into information on the discrete fracture network and maps the hydraulic properties of the reservoir (**Figure 1(b)**). We first perform a synthetic model study that directly stresses

this feature of this method and indicates the most significant factors that dominate the resolution of the evaluated permeability. Finally, we apply this model to the in-situ MEQ data recorded for the October 2014 stimulation of the Newberry EGS project. The significance of this model lies in two aspects: (1) it allows abundant observations of MEQ to constrain the structure and distribution of in-situ permeability evolution; and (2) it reinforces the importance of determining high fidelity in-situ geomechanical parameters (e.g., fracture orientation, fracture stiffness, dilation and friction) and moment tensors, as crucial in successfully constraining permeability evolution.

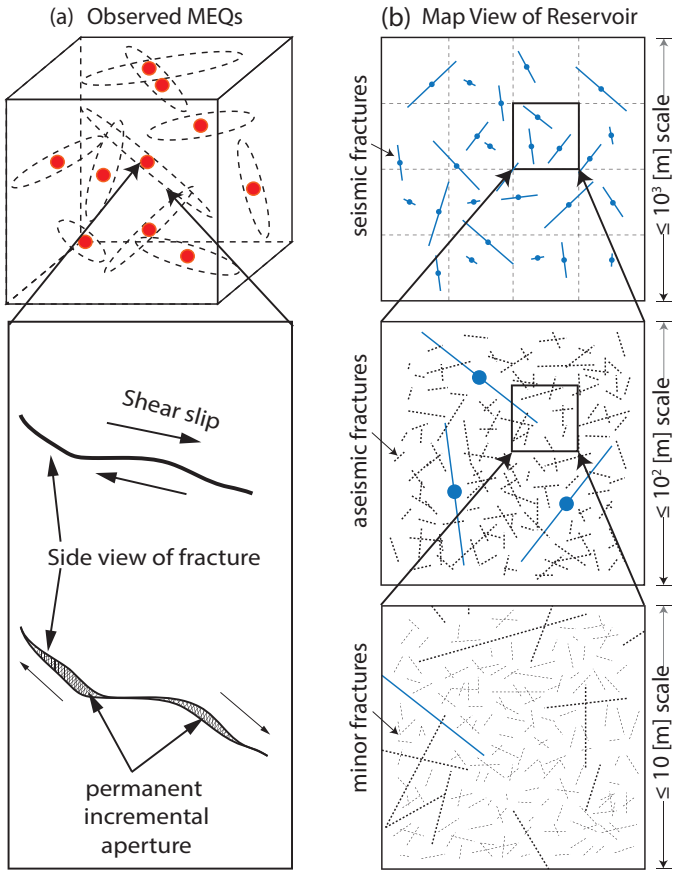

Figure. 1. (a) Schematic graph of observed MEQs and shear slip of fractures. (b) Schematic graph of distributed seismic fractures and aseismic fractures with scales from 10^3 to 10^1 m.

Mathematical formulations

In a representative elementary volume V, a fabric tensor considers position, density, shape, dimension and orientation of fractures and averages these features in each arbitrary direction [7, 8] as

$$F_{ij} = \rho_{frac} \frac{\pi}{4} \int_0^b \int_0^l \int_\Omega l^3 n_i n_j E(n,l,b) d\Omega dl db \tag{1}$$

where F_{ij} is the fabric tensor; ρ_{frac} is the density of centers of fracture planes in the controlled volume; $E(n,l,b)$ is a probability density function that describes the number of fractures with size (i.e., trace length) in the range $l \sim (l+dl)$ and with apertures in the range $b \sim (b+db)$; $\boldsymbol{n}$ is the unit vector to the fracture plane oriented within a small solid angle $d\Omega$. This concept has been extended [9] to represent a permeability tensor based on the assumption that 1) the rock matrix is impermeable and 2) the fluid is channeled in parallel fracture planes with volumetric flow rate proportional to b^3. Thus the permeability tensor k_{ij} is presented as,

$$k_{ij} = \lambda(P_{kk}\delta_{ij} - P_{ij}) = \begin{bmatrix} k_{xx} & k_{xy} & k_{xz} \\ k_{yx} & k_{yy} & k_{yz} \\ k_{zx} & k_{zy} & k_{zz} \end{bmatrix} \tag{2}$$

$$P_{ij} = \rho_{frac} \frac{\pi}{4} \int_0^b \int_0^l \int_\Omega l^2 b^3 n_i n_j E(n,l,b) d\Omega dl db \tag{3}$$

where $\lambda = \lambda(F_{ij})$ is a dimensionless constant associated with fracture interconnectivity and is restricted between 0 and 1/12; δ_{ij} is the Kronecker delta; i and j represent coordinate directions x, y, z. For a 2D problem, i and j are defined within x and y.

For the permeability tensor, the fracture aperture can further be expressed as a combination of nonlinear normal stress-dependent aperture b_n and shear stress-dependent aperture b_s [10] as,

$$b = b_n + b_r \tag{4}$$

$$b_n = b_r + (b_{\max} - b_r) \cdot \exp[-\alpha_s \cdot (\sigma_n - P_f)] \tag{5}$$

where b_r is the residual hydraulic aperture; $b_{\max}$ is the maximum opening; α_s [1/MPa] is the stiffness parameter determined from experiments; σ_n is the remote normal stress perpendicular to the fracture surface; and P_f is the internal fluid pressure in the fracture. In this work, we assume that shear failure of a pre-existing fracture occurs at the critical normal stress σ_n' and critical fluid pressure $P_f = P_{cf}$, expressed as,

$$\sigma_n = \frac{\sigma_1 + \sigma_3}{2} + \frac{\sigma_1 - \sigma_3}{2} \cos 2\theta \tag{6}$$

$$P_{cf} = \frac{\sigma_1 + \sigma_3}{2} - \frac{\sigma_1 - \sigma_3}{2} \frac{\sin 2\theta - \cos 2\theta \cdot \tan\phi}{\tan\phi} \tag{7}$$

$$\sigma_n^{'} = \sigma_n - P_f \tag{8}$$

$$P_{wf} = P_{cf} - P_0 \tag{9}$$

where σ_1 is the maximum principal stress; σ_3 is the minimum principal stress; θ is the fracture normal with respect to the maximum principal stress; ϕ is the friction angle; and P_{wf} is the minimum wellhead pressure needed to reactivate pre-existing fractures. When the increased fluid pressure triggers fracture slip, the shear aperture b_s will increase and its magnitude is controlled by the slip distance Δu and fracture dilation angle Ψ. This physical relation is described as,

$$b_s = \Delta u \cdot \tan\psi \tag{10}$$

The maximum opening of the fracture is predicted using a sublinear aperture-to-length scaling law, postulating that fractures of different lengths preserved in a homogenous body of rock are all in the same condition (i.e., constant stress intensity K_{IC}) [11]. The law is expressed as:

$$b_{\max} = \alpha_l \cdot l^e = \frac{K_{IC} \cdot (1 - v^2)}{E \cdot \sqrt{\pi / 8}} \tag{11}$$

where α_l is the pre-exponential constant defined by the constant stress intensity factor K_{IC} with units of m^{1-e}, Young's modulus E, and Poisson's ratio v; l refers to fracture radius; and e is the power-law scaling exponent. However, the shear aperture component b_s is only applicable when shear failure occurs during a seismic event. If fluid pressure is insufficient to induce shear failure on fractures, the permeability evolution is only dominated by the effective normal stress. When shear failure occurs, the seismic energy M_o, known as seismic moment, is released during shear slip. The seismic moment and moment magnitude are quantified as,

$$M_0 = G \cdot A \cdot \Delta u \tag{12}$$

$$M_w = \frac{2}{3}(\log M_0 - 16.1) \tag{13}$$

where G is the average shear modulus of the fracture embedded in the rock mass, A is the area of the fracture surface, and Δu is the average displacement over the entire fracture surface quantified [12] as,

$$\Delta\mu = \beta_s \cdot \Delta\mu_{\max} = \beta_s \cdot \frac{\Delta\tau}{K_s} \tag{14}$$

$$\Delta\tau = \sigma_n^{'} \cdot (\mu_s - \mu_d) \tag{15}$$

$$k_s = \frac{G \cdot \eta}{l} \tag{16}$$

where Δu_{max} is the maximum final dislocation for 100% stress drop $\Delta\tau$; K_s is the fracture stiffness; μ_s is the static frictional coefficient; and μ_d is the dynamic frictional coefficient. Assuming that fractures in the reservoir are penny-shaped, thus the geometric factor η has the value of $7\pi/24$ [13, 14].

For fractures with frictional weakening properties, if fracture diameter is smaller than the critical length L_c, then failure will occur stably and will be aseismic. L_c is expressed as follows,

$$L_c = \eta \cdot \frac{G}{K_c} \tag{17}$$

where K_c is the effective-rheologic stiffness K_c.

These prior physical relations (*i.e.*, **Eq. (1)** to **Eq. (17)**) are illustrated in **Figure 2** and indicate that the spatial distribution of MEQs can imply local stress magnitude of fractures within the reservoir if reservoir gradients are well constrained. The stress state as well as reservoir material properties control the fracture properties that can be quantitatively correlated to MEQ magnitudes by fracture size. As a result, the permeability enhancement by shear slip in an EGS stimulation can be estimated through such relations.

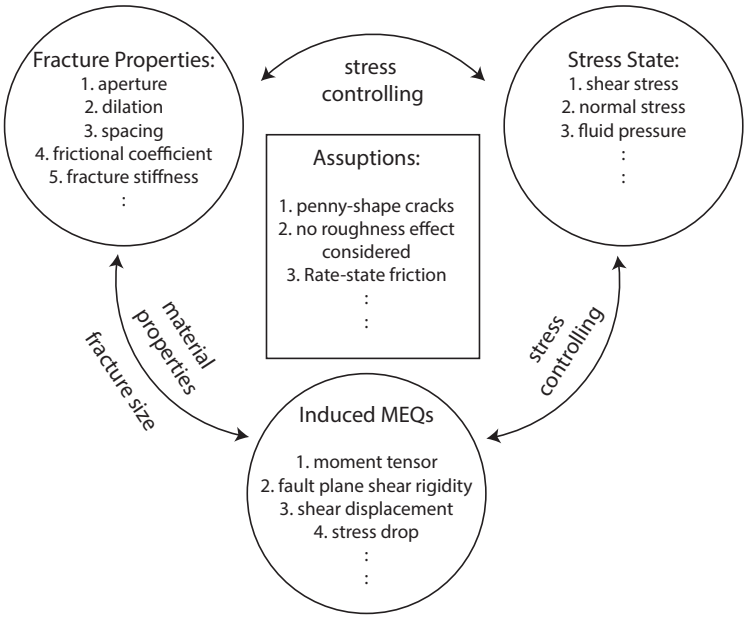

Figure. 2. Schematic diagram of relations among physical properties and variables that controlling MEQ-Permeability coupling.

7.2 Synthetic Model study

A parametric study of the physical relations described in Section 2 has been reported previously [6]. Among the large number of variables defined in the model, the results of the parametric analysis suggest that the two most important factors determining the reliability of the estimated permeability are: (1) geomechanical fracture properties (i.e., frictional drop and dilation angle) and (2) Precision of MEQ data (i.e., populations, locations and magnitudes, and focal mechanism solutions). In addition, the effects of the size of the representative element volume and discrete fracture network on the mapped permeability are important in defining an appropriate resolution of permeability map. Hence, to capture the features of the proposed method, we build a synthetic forward DFN-Microseismicity-Permeability (DFN-MEQ-*k*) model to provide an intuitive understanding of how to evaluate moment magnitude of induced seismicity from shear-slipping fractures and the resulting enhanced aperture. Further we indicate how mapped permeability varies with representative elementary volume of the fracture network domain.

7.2.1 Model Description

In the model, we set 200 randomly oriented fractures in a 2D domain with an edge dimension of 1500 m x 1500 m (**Figure 3**). The fracture lengths are randomly generated within the range from 1 to 800 m and are described as a frequency-length power law for the fractures [15] as follows,

$$n(L) = a \cdot L^{-\xi} \tag{18}$$

where $n(L)$ is the density distribution of the number of fractures present in the interval [L, $L+dL$]; a is a density constant and ξ is a exponent.

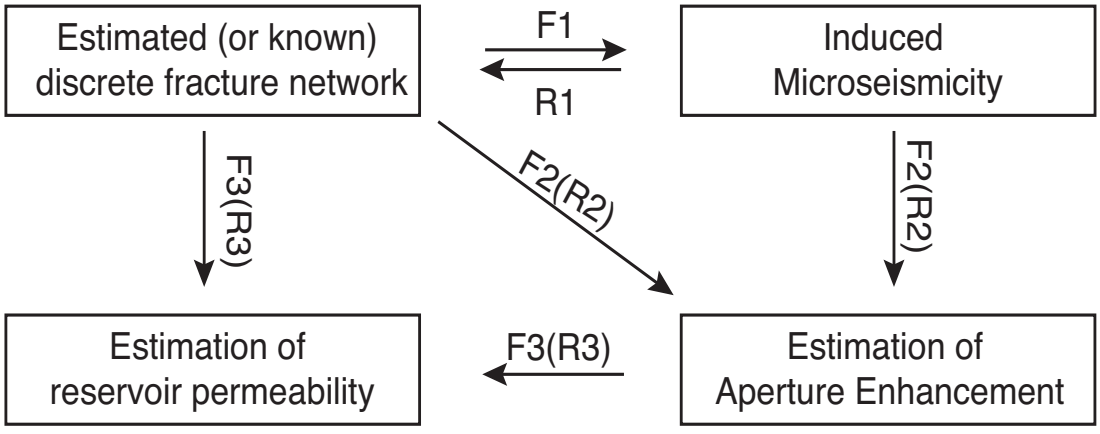

Figure. 3. Schematic flow chart of forward DFN-MEQ-*k* model. Route F1 to F3 refers to the forward sequence for the synthetic model while R1 to R3 refers to the inverse sequence for in-situ data analysis.

Maximum and minimum principal stresses are applied horizontally in x and y directions respectively. Eliminating the complexity of the stress interactions between each fracture, we assume that all fractures are mechanically independent. In addition, wellhead pressure is imposed on the entire domain rather than originating from a point source. **Figure 4** represents a reservoir with discrete fractures, in which a representative elementary volume with a certain size is taken to evaluate regional permeability. The geomechanical parameters are listed in Table 1.

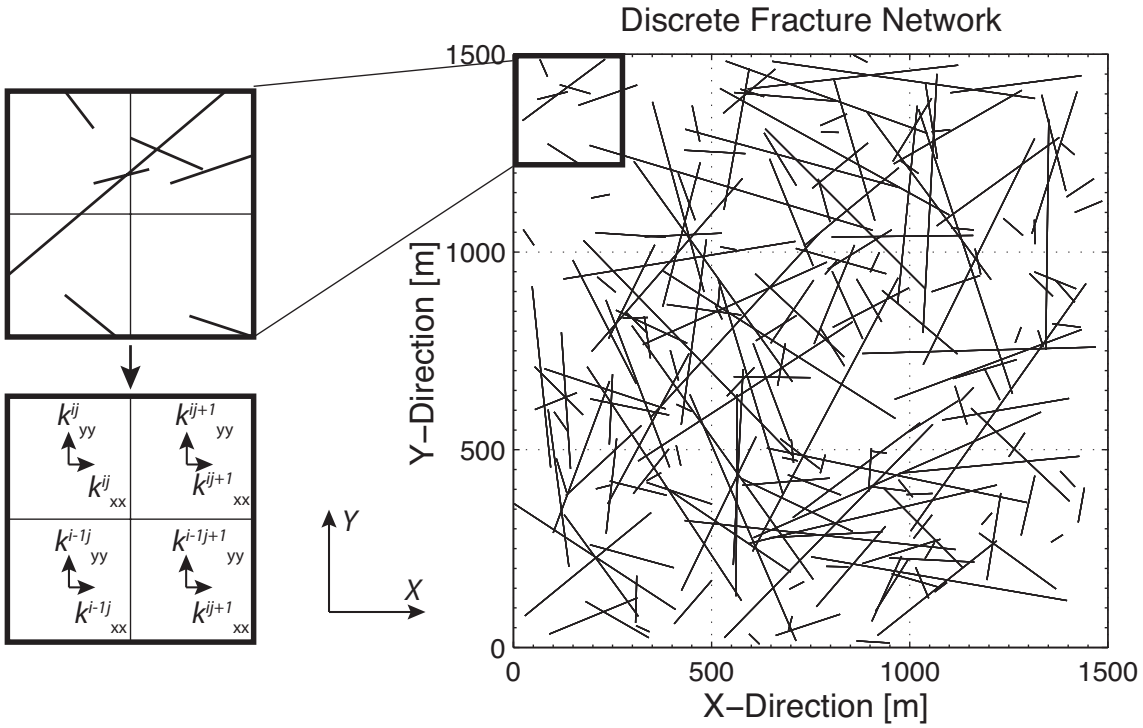

Figure 4. Generated discrete fracture network. A representative elementary volume of the reservoir is taken for the estimation of regional permeability.

Table 1. Parameters for synthetic DFN-MEQ-*k* model

Parameters	Value	Units
Fracture length: L	35.6~791.9	m
Static friction: μ_s	0.6	-
Dynamic friction: μ_d	0.5	-
Maximum principal stress: σ_1	72	MPa
Minimum principal stress: σ_3	45	MPa
Initial pore-pressure: P_0	29.4	MPa
Wellhead pressure: P_w	5, 10, 15	MPa
Fracture orientation: θ	2.4~358.6	°
Residual aperture: b_r	0.00005	m
Dilation angle: ψ	5	°
Bulk modulus: K	20	GPa
Poison ratio: v	0.25	-
Constant stress intensity factor: K_{IC}	10	$MPa.m^{1/2}$
Nonlinear fracture stiffness: α_s	0.3	1/MPa
Power law scaling exponent: e	0.5	$m^{1/2}$
Fracture density constant: a	0.4	-
Fracture distribution exponent: ξ	0.75	-
Representative volume size: S	30, 50, 100	m

7.2.2 Results and Interpretation

Figure 5 illustrates the evolution of slipped vs. un-slipped fractures, the resulting microseismic events, the corresponding moment magnitudes and shear-enhanced apertures of reactivated fractures. In **Figure 5 (a)** to **(c)**, favorably oriented fractures are prone to be reactivated under low fluid pressures. When increasing the wellhead pressure, unfavorably oriented fractures are gradually reactivated to slip and correspondingly increase the population of MEQs. The moment magnitude of these shear failures are shown in **Figure 5 (d)** to **(f)**, where the clustered slipped fractures result in denser zones of microseismicity. It is also noted that the failure of fractures with larger size would lead to higher moment magnitudes. Since aperture is enhanced during shear slip and higher moment magnitude will lead to larger slip, it can be observed that the higher moment magnitude in **Figure 5 (d)** to **(f)** has led to larger enhanced aperture in **Figure 5 (g)** to **(i)**.

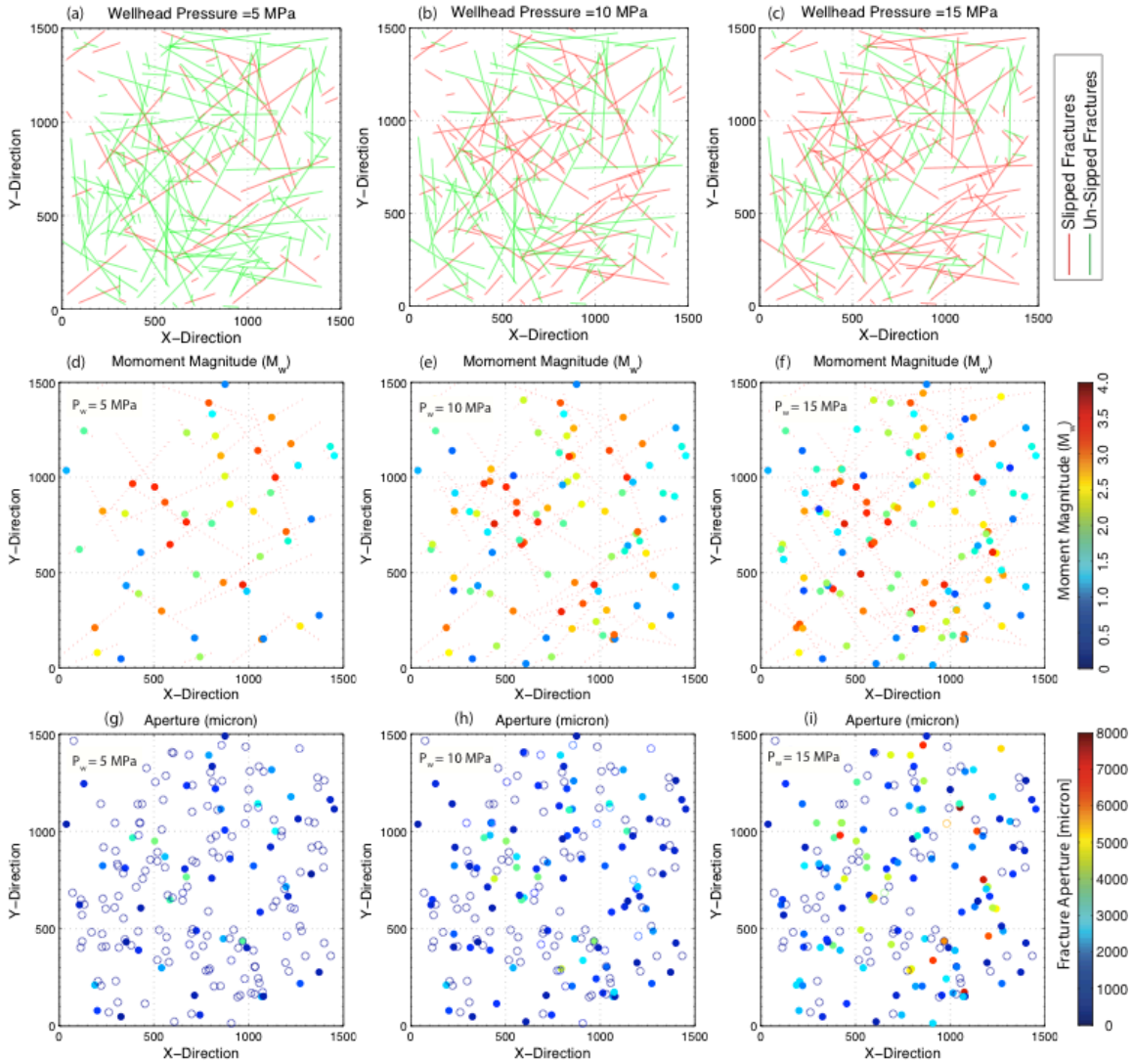

Figure 5. (a) to (c) Stimulated fractures vs. un-stimulated fractures under different wellhead pressures; (d) to (f) Moment magnitudes of corresponding slipped fractures; (g) to (i) Magnitude of apertures of corresponding slipped fractures (solid circle) vs. apertures of un-slipped fractures (empty circle).

Figure 6 shows the panel of the mean permeability map of the synthetic reservoir with different scales of the representative elementary volume. The flow properties obtained from the fracture models consider the total sum of the areas of the fractures contained in each representative volume. As fracture aperture is determined by injection pressure, fracture length, moment magnitude, and fracture orientation, the permeability tensor takes an average of all these attributes. Evidently, high injection pressure can enhance the reservoir permeability by inducing more MEQs. The resolution of the permeability map is dependent on the size of the selected representative elementary volume and can be adjusted based on known fracture sizes and the entire reservoir scale.

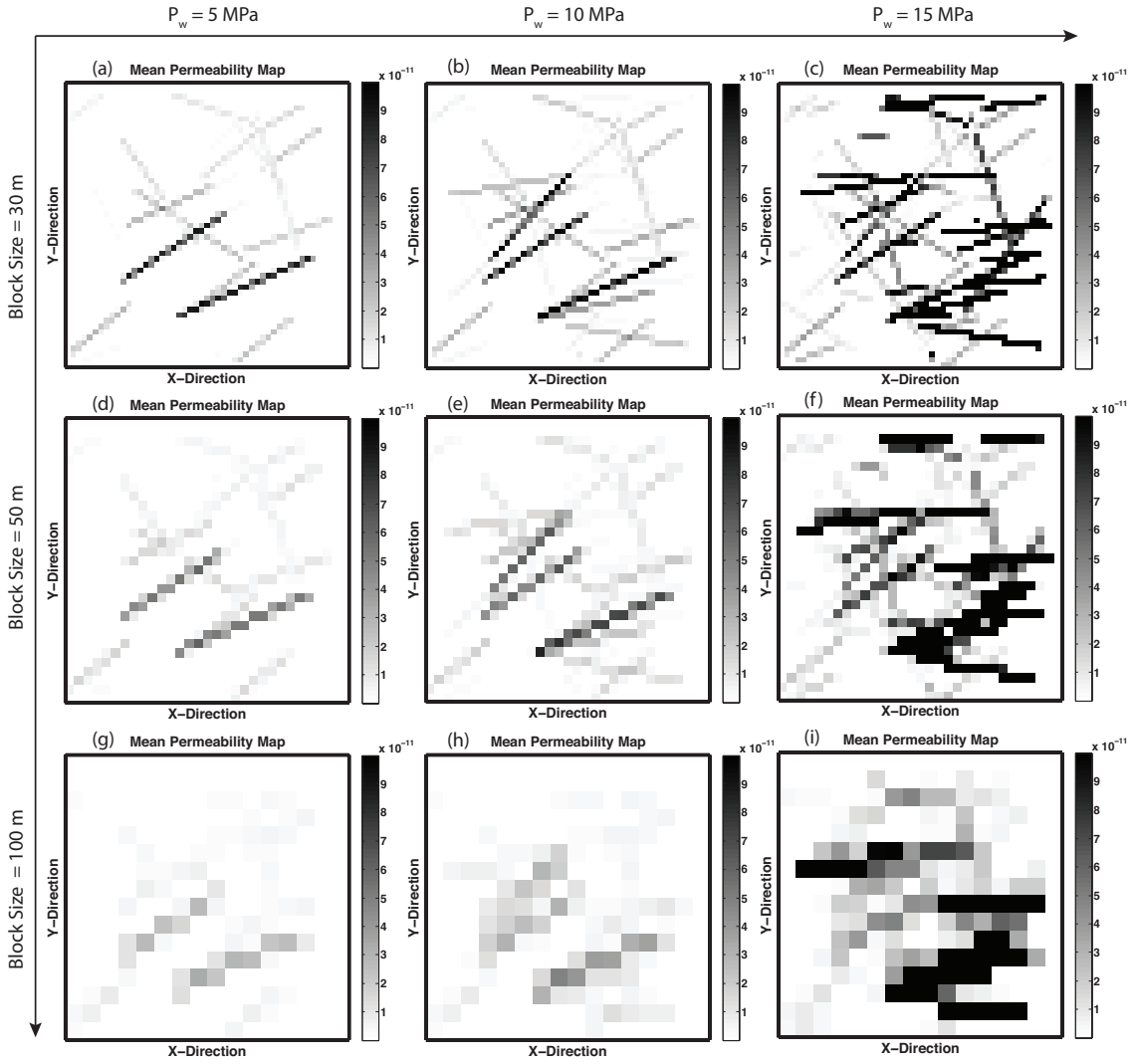

Figure 6. Mean permeability map of a synthetic reservoir with different size REVs. (a) to (c) Permeability map of a small REV (30 m) under wellhead pressure from 5 MPa to 15 MPa; (d) to (f) Permeability map of a mid-size REV (50 m) under wellhead pressure from 5 MPa to 15 MPa; (g) to (i) Permeability map of a large REV (100 m) under wellhead pressure from 5 MPa to 15 MPa.

7.2.3 Summary

The synthetic model maps the reservoir permeability based on the discrete fracture network and assumed Mohr-Coulomb shear failure criterion, providing an intuitive understanding of connection among discrete fracture networks, microseismicity and reservoir permeability. This model, if following an inverse modeling sequence as indicated in **Figure 3**, can be applied to in-situ data obtained from microseismic monitoring. However, this method may be subject to restrictions such as poorly estimated in-situ fracture orientation and in-situ stress due to the added complexity of a significantly heterogeneous subsurface system. In the following section, we perform an evaluation of in-situ MEQ data in the mapping of reservoir hydraulic properties.

7.3 in-situ meq data evaluation

Differing from the synthetic networks of **Section 3**, natural reservoir fracture networks are significantly more complex and more difficult to characterize. For in-situ characterization, statistical field measurement of the surface outcrop is essential and a useful method to reveal fracture structure of near-surface formations. However, microseismic monitoring is the only effective way to characterize fracture networks at depth. In this study, we perform a data analysis on in-situ MEQ data from the first two rounds of the 2014 Newberry EGS stimulation (first round from Sept 24th to Oct 15th and second round from Nov 11th to Nov 20th) that followed an earlier 2012 stimulation [2, 16].

7.3.1 MEQ Observations and Assumptions

In the 2014 stimulation, about 350 MEQs are located by a fifteen-station microseismic array (**Figure 7**) (data are provided from the webpage http: //fracture.lbl.gov /Newberry /location.txt). **Figure 8 (a)** indicates that all MEQs locate within the depth range ~2000 m to ~3300 m while more than 75% of these seismic events occurred within the range ~2500 m to ~3300 m. Among these 350 MEQs, moment tensors are available for the 99 events with the best quality [17] and identify the strikes and dip angles of corresponding fault planes.

To analyze all seismic events, we use these 99 focal mechanism solutions as a statistical reference and randomly assign the strike and dip angle values to non-MT seismic fractures based on a normal

distribution. In **Figure 8 (b)** and **(c)**, dip angles of the fractures from the John Day formation zone share similar ranges with those from the Intruded John Day formation. However, strikes in the shallower formation show a different orientation to the deeper formation. Accordingly, the strike orientations of non-MT events are statistically assigned based on the individual geologic formation.

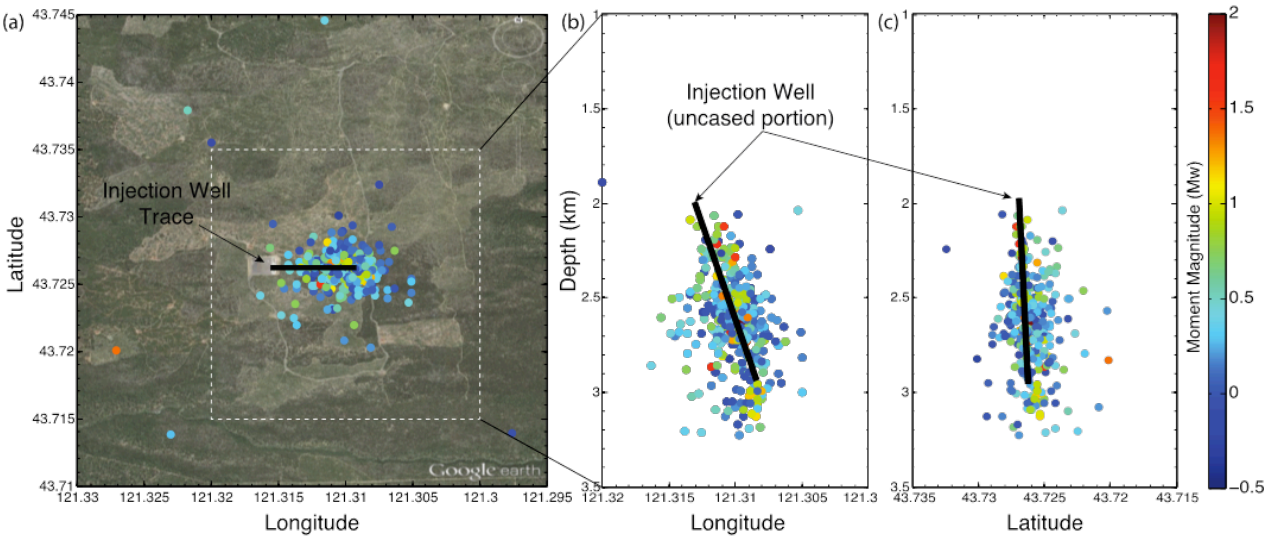

Figure 7. (a) Map view of distribution of 350 seismic events in Newberry EGS reservoir during 2014 stimulation. (b) Vertical view of MEQ distribution with Longitude. (c) Vertical view of MEQ distribution with Latitude.

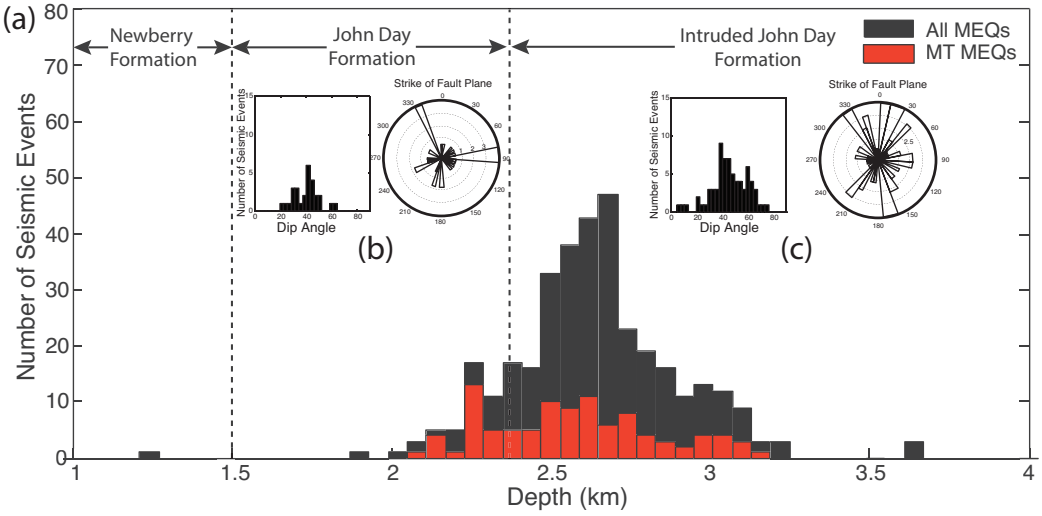

Figure 8. (a) Histogram of MEQ frequency with depth. Red bars represent the events for which moment tensors were derived. (b) Dip angle and strike distribution of MEQs in John Day formation. (c) Dip angle and strike distribution of MEQs in Intruded John Day formation.

The stress regime is a determining factor that defines the shear failure behavior of the fractures. For the Newberry EGS reservoir, we use the normal faulting regime according to World Stress Map. However, the observed focal mechanism solutions show combined double-couple (DC) and non-double-couple (non-DC) results, suggesting a possible strike-slip regime. Due to insufficient evidence to resolve this ambiguity, we use the stress regime aligned with the previous in-situ investigation and related THM simulations [16, 18, 19]. We constrain the vertical σ_v, maximum horizontal σ_H, and minimum horizontal σ_h, stresses to be zero at the surface and use gradients of 24.1, 23.5 (N-S) and 15.0 (E-W) MPa/km. For such a stress configuration, the dip angle of the fault plane is equal to the angle between the fracture normal relative to the maximum principal stress.

As all MT events indicate mixed failure modes, the non-DC portion suggests crack opening or closing in the stimulation [20, 21], which makes the estimation of fracture size more difficult. To establish the permeability connections between DC and non-DC events, we assume two end-member scenarios. The first is where the non-DC event results from the slip (DC event) where the moment is defined as

$$M_0 = A(G + K \cdot \tan\psi) \cdot \Delta u_s \tag{20}$$

and alternatively where the non-DC event occurs without slip as

$$M_0 = K \cdot A \cdot \Delta b_n \tag{21}$$

where G is the shear modulus; K is the bulk modulus; and A is the area of fault patch; Δu_s and Δb_n are shear slip distance and the change of normal aperture, respectively. In this work, we assume all events to be mixed-mode events where compactive or dilational displacements are assumed triggered by shear.

The observed moment magnitudes of MEQs are constrained between -0.28 to 2.0 with a b value close to unity [6], suggesting that the size of the seismic fractures in the Newberry EGS reservoir are expected to be between meters and one-hundred meters and cannot exceed a thousand meters. Because these observed MEQs do not overprint each other, this implies that shear slip only occurred once for each reactivated fracture. Thus each distinct seismic event is assumed to represent a pre-existing fracture in the reservoir. Hence we estimate the size of each fracture using **Eq. (12)** to **Eq. (16)** using the parameters in **Table 2**. The calculated fracture trace length ranges from ~20 m to ~ 300 m. The corresponding fracture trace length distribution is illustrated in **Figure 9 (a)**, agreeing with the widely observed power-law distribution of fracture sizes in natural reservoirs [22].

Table 2. Parameters for in-situ data analysis

Parameters	Value	Units
Frictional drop: $\Delta\mu$	0.010	-
Vertical stress gradient: γ_v	24.1	MPa/km
Min-horizontal stress gradient: γ_h	15.0	MPa/km
Pore-pressure gradient: γ_w	9.8	MPa/km
Residual aperture: b_r	5.0e-5	m
Dilation angle: ψ	10	°
Bulk modulus: K	17.0	GPa
Poison ratio: v	0.27	-
Nonlinear fracture stiffness: α_s	0.210	1/MPa
Power law scaling exponent: e	0.5	$m^{1/2}$
Constant stress intensity factor: K_{IC}	8.0	$MPa.m^{1/2}$
Porosity: Φ	0.3	-
Fluid viscosity: η_f	1.0e-3	Pa.s
Grain bulk modulus: K_g	50.0	GPa
Fluid bulk modulus: K_f	2.2	GPa
Grid size: S	50	m
Fracture density constant: a	7.5	-
Fracture distribution exponent: ξ	1.6	-

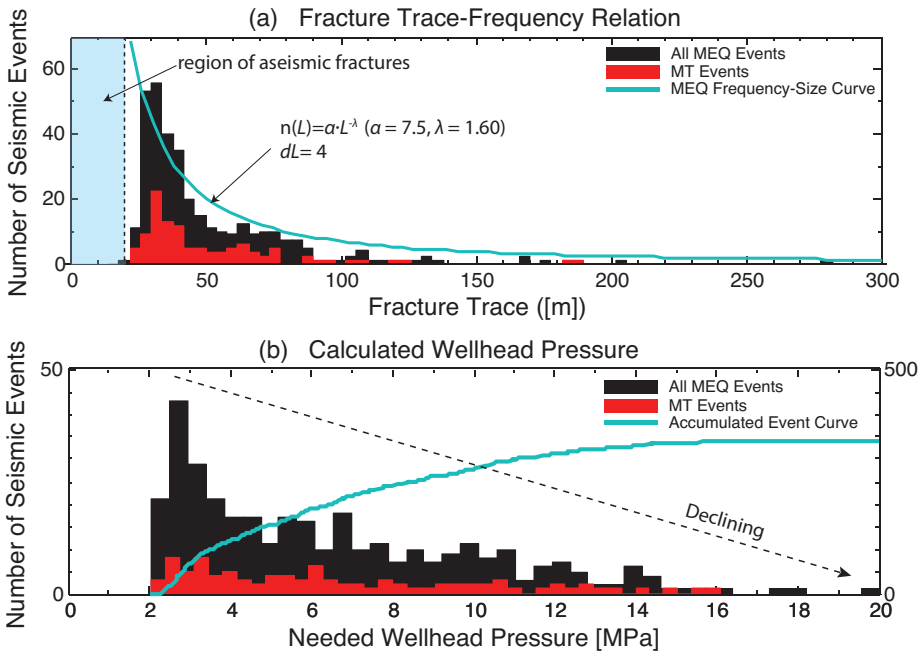

Figure 9. (a) Size distribution of in-situ fractures calculated from MEQ data. (b) Fracture frequency with corresponding required reactivating wellhead pressures (extra fluid pressure).

We assume that the fluid flow is essentially horizontal and in order to analyze spatial variations of permeability in the reservoir, we select a layer with the highest concentration of seismic events as an example where fracture traces are projected to a plane of zero-thickness [23]. The layer is constrained to between the depths of 2500 m to 2600 m and bounded by latitude 43.715° to 43.735° and longitude -121.32° to -121.30°. The lengths of the fracture traces of the corresponding seismic events are calculated and illustrated in **Figure 9 (a)**. Compared to the reservoir scale (~10^3 m), the lengths of fracture traces (10^1 m to 10^2 m) are approximately one to two orders of magnitude smaller, suggesting a poor interconnection of these fractures. Due to the low permeability of the rock matrix, there must be abundant pre-existing fractures within the reservoir as fluid conduits and connecting each observed seismic fracture (**Figure 1**). These particular small "infill" fractures remain aseismic [6]. In this study, the calculated critical fracture trace is ~ 20 m and this agrees with previous frictional experimental results showing the smallest possible seismic fracture trace to be ~ 14m which is of the same order of magnitude [24].

The number of these small size aseismic fractures can be estimated using the power law frequency-length of the fractures. Thus the total number of fractures n_{tot} can be described as follows:

$$n_{tot} = n_{aseis} + n_{seis} = n_{aseis} + n_f + n_{uf} \tag{21}$$

where n_{tot} is the total population of fractures in the reservoir; n_{aseis} is the population of aseismic fractures with fracture size less than critical length; n_{seis} is the number of seismic fractures including the population (n_f) of activated fractures with favorably oriented fractures and the population (n_{uf}) of unactivated fractures with relatively unfavorably oriented fractures. In this relation, it is noted that when wellhead pressure increases sufficiently, the unactivated fractures convert to "activated" fractures. In **Figure 9 (b)**, the number of unactivated fractures decreases with elevated wellhead pressures and declines to zero at P_{wf} = ~20 MPa that is the same as the maximum operating wellhead pressure in the field. Over the period of the two rounds of the stimulation, we assume that n_f within the stimulated area has reached a maximum while n_{uf} approaches zero. Thus we set the known number of n_f to be the same as the number of observed MEQs and use the identified power-law distribution to invert for the approximate number of small fractures (aseismic fractures below the seismic size limit for slip) within the reservoir.

However, the orientation and locations of the sub-seismic fractures are poorly characterized in the Newberry EGS reservoir. As a result, we use a homogeneous Poisson process to define the coordinates of the fracture centers that are uniformly but randomly distributed within the domain as illustrated in **Figure 10**. Thus the total reservoir permeability can be regarded as a superposition of seismic fracture permeability, aseismic fracture permeability and matrix permeability as:

$$k_{tot} = k_{aseis} + k_{seis} + k_m \tag{22}$$

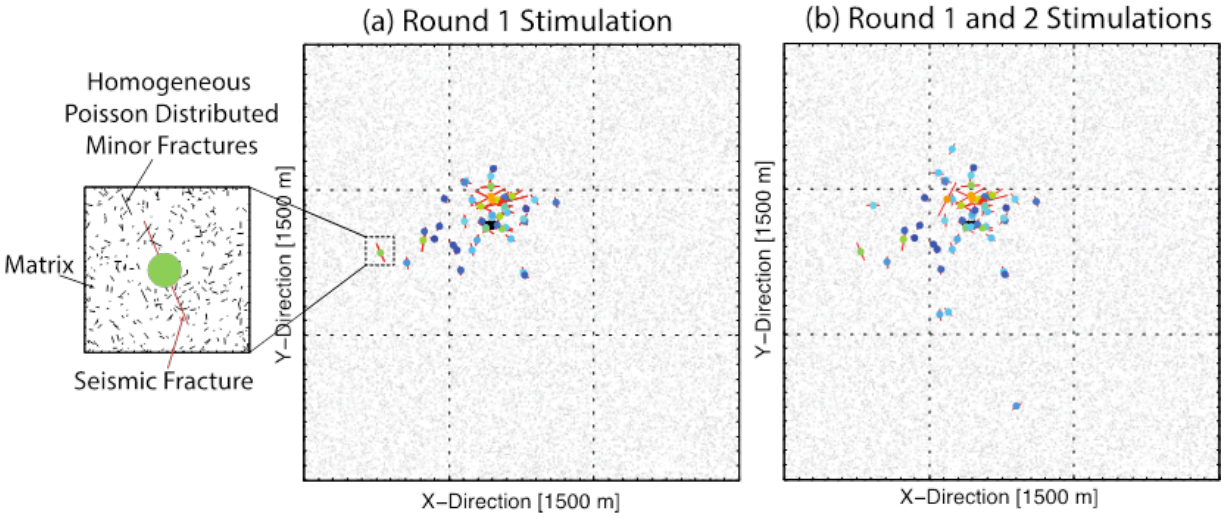

Fig. 10. Map view of created DFN from microseismic events and corresponding strike orientations at a depth of 2500 m to 2600 m (projected to a zero-thickness plane. (a) MEQs and fracture trace map during the first stimulation (b) MEQs and fracture traces ma during the accumulated period of both the first and second round stimulations.

7.3.2 Results and Interpretation

The relation between slip distances of seismic fractures and fracture size is presented in **Figure 11 (a)**, showing that slip increases linearly (from ~0.15 mm to ~2.22 mm) with growing fracture trace length (~ 20 m to ~ 282 m). The shearing enhanced apertures of fractures are plotted in **Figure 11(b)**, increasing with slip distance (as well as fracture size). **Figure 12** presents the stimulated permeability map of the resulting DFN in **Figure 10**, illustrating that the most permeable zone is created adjacent to the injection well in the first round stimulation (northwestern quadrant). After the second stimulation, the permeability is enhanced around the injection well, and develops preferentially towards the north and the south. The estimated equivalent mean permeability of the selected seismic layer following both rounds of the stimulation are ~1.64×10^{-15} m^2 and ~1.68×10^{-15} m^2, respectively. Confirmatory and independent estimates of the equivalent mean permeability may be recovered at reservoir scale (~10^3 m x 10^3 m x 10^3 m) using pore-pressure diffusion lengths [3] and the 99 MT events. The diffusion-length versus time curves are shown in **Figure 13**, suggesting that the reservoir permeability evolved from k= ~0.7×10^{-15} m^2 to k= ~1.3×10^{-15} m^2. This is smaller than the model results from MEQ-DFN-*k* but within less than a half order of magnitude. This difference is mainly conditioned by the MEQ-DFN-*k* model deriving permeability for the most seismically-dense zone while the pore-pressure diffusion method averages permeability over the entire reservoir.

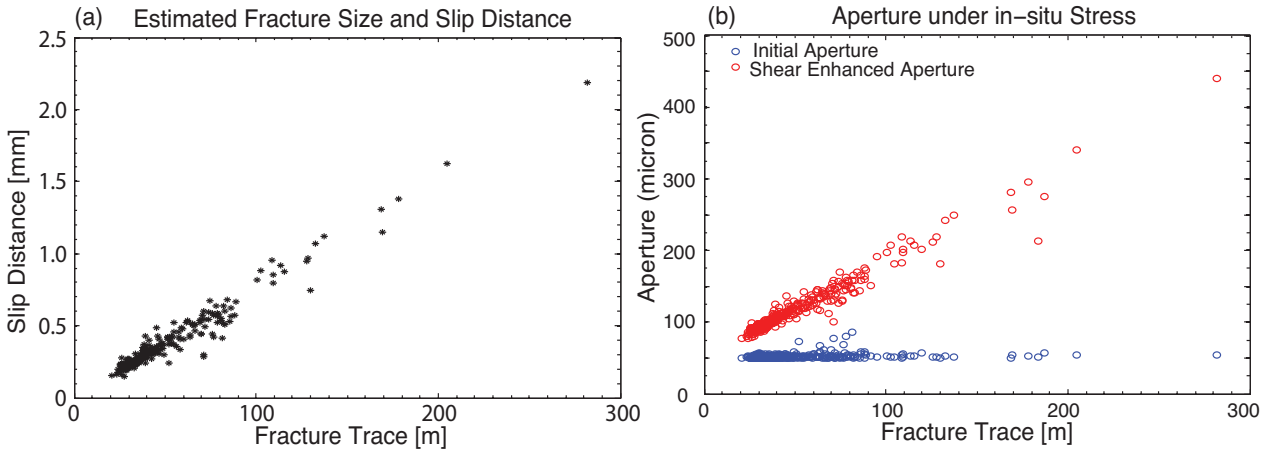

Figure 11. (a) Calculated slip distance of fractures in the Newberry EGS reservoir. (b) Initial apertures of fractures and shear slip enhanced aperture of fractures.

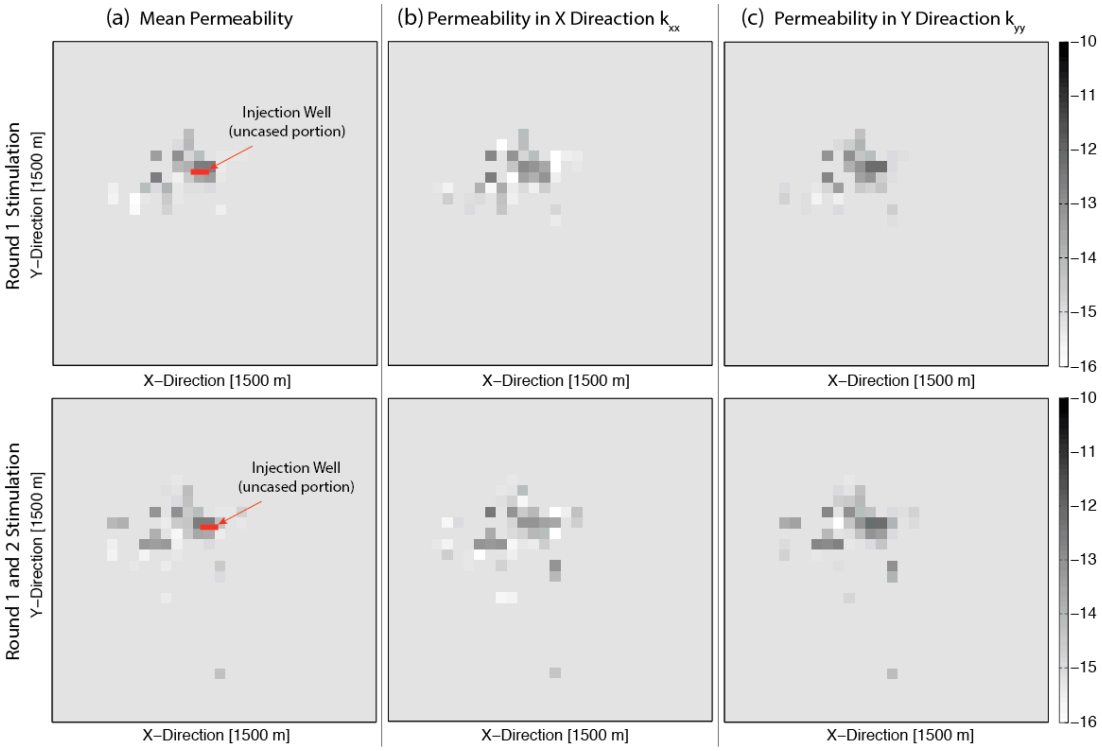

Figure 12. Cellular grid of stimulated permeability created using the DFN. (a) Scenario of mean permeability. (b) Scenario of permeability in X (East-West) direction. (c) Scenario of permeability in Y (North-South) direction. The magnitude of permeability is color-coded. Deep colors indicate high permeability and dense zone of microseismicity correspond to highest permeability.

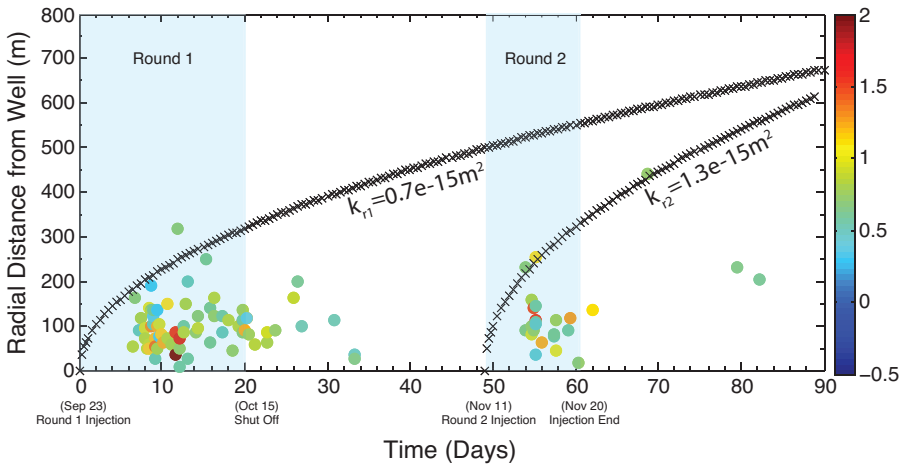

Figure 13. Spatio-temporal distribution of fluid-injection-induced seismicity during the 2014 Newberry EGS stimulation. Diffusion-length versus time curve labeled for equivalent permeabilities at reservoir scale.

7.4 Conclusions and discussion

In this work we present a simple but reliable M_w-DFN-k model that tightly links observed MEQ data to a statistically based DFN model where in-situ permeability tensors are derived. We first conduct a study using synthetic data, which suggests that the moment magnitudes and lengths of fracture traces are proportionally correlated with the effects of geomechanical conditions and properties of fractures. The resolution of permeability is largely determined by the cellular grid size and the fracture size. In the analysis of in-situ data, based on high-quality moment tensors, geostatistical approaches are employed to generate fracture properties in the reservoir scale range. The results appropriately define the permeable zones within the Newberry EGS reservoir where dense zone of microseismicity correspond to the highest permeability.

This model has established a solid physical coupling between the fracture properties, hydroshearing-induced seismicity, and fracture permeability. It has a promising potential for mapping evolving permeability using in-situ MEQ data in unconventional reservoirs at various scales. Higher accuracy and reliability of the results can be achieved through improving the accuracy of the parameters that are used in the model. Particularly in practical operations, the quality of the observed moment tensors recovered through microseismic monitoring is key in determining the accuracy of the properties of the in-situ fractures and the recovered permeability tensors of the EGS reservoir. Thus this study using both synthetic and in-situ MEQ data has highlighted three aspects that must be surmounted in the successful in-situ characterization of subsurface reservoirs: (i) conducting precise laboratory and in-situ characterization of intrinsic fracture properties and stress regime; (ii) obtaining high quality microseismic monitoring data; and (iii) defining reliable assumptions and simplifications for uncertainties for heterogeneous reservoirs.

Acknowledgement

This work is a partial result of support provided by DOE Grant DE-EE002761. This support is gratefully acknowledged.

7.5 References

1. Cladouhos, T.T., S. Petty, B. Larson, J. Iovenitti, B. Livesay, and R. Baria. 2009. Toward More Efficient Heat Mining: A Planned Enhanced Geothermal System Demonstration Project, Geothermal Resources Council Transactions, 33, 2009.
2. Cladouhos, T.T., M.W. Swyer, M. Uddenberg, and S. Petty. 2015. Results from Newberry Volcano EGS Demonstration. In Proceedings of 40th Workshop on Geothermal Reservoir Engineering Stanford University, Stanford, CA, 25 - 29 January 2015.

3. Shapiro, S.A., E. Hugenges, and G. Borm, G. 1997. Estimating the Crust Permeability from Fluid-Injection-Induced Seismic Emission at the KTB site, Geophys. J. Int. 131: F15-F18.

4. Terakawa, T., A. Zoporowski, B. Galvan, and S.A. Miller. 2010. High-pressure fluid at hypo-central depths in the L'Aquila region inferred from earthquake focal mechanisms. Geology. 38: 11, 995-998.

5. Terakawa, T., S.A. Miller, and N. Deichmann. 2012. High fluid pressure and triggered earthquakes in the enhanced geothermal system in Basel, Switzerland, J. Geophys. Res. 117: B7, B07305.

6. Fang, Y., D. Elsworth, and T.T. Cladouhos. 2015. Estimating In-Situ Permeability of Stimulated EGS Reservoirs Using MEQ Moment Magnitude: an Analysis of Newberry MEQ Data. In Proceedings of 40th Workshop on Geothermal Reservoir Engineering Stanford University, Stanford, CA, 25 - 29 January 2015.

7. Oda, M. 1982. Fabric tensor for discontinuous geological materials. Soils. Found. 22: 4, 96-108.

8. Oda, M. 1984. Similarity rule of crack geometry in statistically homogeneous rock masses. Mech. Mater. 3: 2, 119-129.

9. Oda, M. 1985. Permeability tensor for discontinuous rock masses. Géotechnique. 35: 483-495.

10. Rutqvist, J., C.F. Tsang, and Y. Tsang. 2004. Analysis of Stress and Moisture Induced Changes in Fractured Rock Permeability at the Yucca Mountain Drift Scale Test. In Elsevier Geo-Engineering Book Series, 2: 161-166.

11. Olson, J.E. 2003. Sublinear Scaling of Fracture Aperture versus Length: An Exception or the Rule? J. Geophys. Res. 108: B9, 2413.

12. Brune, J.N. 1970. Tectonic Stress and the Spectra of Seismic Shear Waves from Earthquakes, J. Geophys. Res. 75: 4997-5009.

13. Dieterich, J.H. 1986. A model for the nucleation of earthquake slip, Earthquake Source Mechanics. 37: 37-47.

14. Dieterich, J.H. 1992. Earthquake nucleation on faults with Rate-and State-Dependent Strength. Tectonophysics. 211: 14, 115-134.

15. Davy, P. 1993. On the frequency - length distribution of the San Andreas fault system. J. Geophys. Res. 98: B7, 12141-2152.

16. Fang, Y., D. Elsworth, and T. Cladouhos. 2014. Bimodal depth distribution of MEQs in the Newberry geothermal reservoir. In Proceedings of 48th US Rock Mechanics/Geomechanics Symposium. Minneapolis, MN, June 1-4, 2014.

17. Julian, B.R. and G.R. Foulger. 2004. Microearthquake focal mechanisms – A tool for monitoring geothermal systems. Geotherm. Res. Council Bull. 33: 166-171.

18. Davatzes, N.C. and S. H. Hickman. 2011. Preliminary analysis of stress in the Newberry EGS well NWG 55-29. Geothermal Resources Council Transactions, 35: 1, 323-332.

19. Sonnenthal, E.L., J.T. Smith, T.T. Cladouhos, J. Kim and L. Yang. 2015. Thermal-Hydrological-Mechanical-Chemical modeling of the 2014 EGS stimulation experiment at Newberry Vocano, Oregon. In Proceedings of 40th Workshop on Geothermal Reservoir Engineering Stanford University, Stanford, CA, 25 - 29 January 2015.

20. Julian, B.R. 1998. Non-double-couple earthquakes 1. Theory. J. Rev. Geophys. 36: 4, 525-549.

21. Miller, A.D., G.R. Foulger and B.R. Julian. Non-double-couple earthquakes 2. Observations. J. Rev. Geophys. 36: 4, 551-568.

22. Bonnet, E., O. Bour, N.E. Odling, P. Davy, I. Main, P. Cowie and B. Berkowitz. 2001. Scaling of fracture systems in geological media. J. Rev. Geophys. 39: 347-383.

23. Bundschuh, J., and M.C. Suarez Arriaga. 2010. Introduction to the Numerical Modeling of Groundwater and Geothermal systems. 1st ed. London: Taylor & Francis Group.

24. Fang, Y., S.A.M. den Hartog, D. Elsworth, C. Marone and T.T. Cladouhos, T.T. 2015. Anomalous Distribution of Microearthquakes in the Newberry Geothermal Reservoir: Mechanisms and Implications, Geothermics. (Submitted).

8 CHAPTER 8 A CONTINUUM MODEL FOR COUPLED STRESS AND FLUID FLOW IN DISCRETE FRACTURE NETWORKS

Abstract

We present a model coupling stress and fluid flow in a discontinuous fractured mass represented as a continuum by coupling the continuum simulator TF_FLAC^{3D} with cell-by-cell discontinuum laws for deformation and flow. Both equivalent medium crack stiffness and permeability tensor approaches are employed to characterize pre-existing discrete fractures. The advantage of this approach is that it allows the creation of fracture networks within the reservoir without any dependence on fracture geometry or gridding. The model is validated against thermal depletion around a single stressed fracture embedded within an infinite porous medium that cuts multiple grid blocks. Comparison of the evolution of aperture against the results from other simulators confirms the veracity of the incorporated constitutive model, accommodating stress-dependent aperture under different stress states, including normal closure, shear dilation, and for fracture walls out of contact under tensile loading. An induced thermal unloading effect is apparent under cold injection that yields a larger aperture and permeability than during conditions of isothermal injection. The model is applied to a discrete fracture network to follow the evolution of fracture permeability due to the influence of stress state (mean and deviatoric) and fracture orientation. Normal closure of the fracture system is the dominant mechanism where the mean stress is augmented at constant stress obliquity ratio of 0.65 – resulting in a reduction in permeability. Conversely, for varied stress obliquity (0.65 – 2) shear deformation is the principal mechanism resulting in an increase in permeability. Fractures aligned sub-parallel to the major principal stress are near-critically stressed and have the greatest propensity to slip, dilate and increase permeability. Those normal to direction of the principal stress are compacted and reduce the permeability. These mechanisms increase the anisotropy of permeability in the rock mass. Furthermore, as the network becomes progressively more sparse, the loss of connectivity results in a reduction in permeability with zones of elevated pressure locked close to the injector – with the potential for elevated pressures and elevated levels of induced seismicity.

8.1 Introduction

Geothermal energy is a potentially viable form of renewable energy although the development of EGS as a ubiquitous source has considerable difficulties in developing an effective reservoir with sustained thermal output. One key solution in generating an effective reservoir is to stimulate using low-pressure hydraulic-shearing or elevated-pressure hydraulic-fracturing. In either case, the stimulation relies on changes in effective stresses driven by the effects of fluid pressures, thermal quenching and chemical effects, each with their characteristic times-scales. Thus incorporating the effects of coupled multi-physical processes (Thermal-Hydraulic-Mechanical-Chemical) exerts an important control on the

outcome [*Taron and Elsworth*, 2010]. Therefore an improved understanding of coupled fluid flow and geomechanical process offers the potential to engineer permeability enhancement and its longevity – and thus develop such reservoirs at-will, regardless of the geological setting [*Gan and Elsworth*, 2014a; b]. This is a crucial goal in the development of EGS resources.

The constitutive relationships linking fluid flow and deformation are more complex when the subsurface fluids flow through geological discontinuities like faults, joints and fractures. To better represent the discontinuities in the simulation of fractured masses, past efforts have focused on discretizing individual fractures or averaging fracture properties into the effective properties of each grid block [*Goodman*, 1968; *Noorishad et al.*, 1982; *Elsworth*, 1986; *Heuze et al*, 1990; *Kolditz and Clauser*, 1998], and investigating the coupled hydraulic–mechanical–thermal influence within the deformable fractured medium [*Rutqvist and Stephansson*, 2003; *Kohl, et al.*, 1995]. Currently available models for fracture simulations are primarily divided into equivalent continuum and discontinuum approaches. Discontinuum models include boundary element methods [*Ghassemi and Zhang*, 2006; *McClure and Horne*, 2013], and distinct element methods [*Fu et al.*, 2013; *Min and Jing*, 2003; *Pine and Cundall*, 1985]. The discontinuum approach for fractured masses assumes that the rock is assembled from individual blocks delimited by fractures. The fractures can be represented by either explicit fracture elements along fractures, or by interfaces [*Zhang and Sanderson*, 1994]. Given that rocks and fractures are explicitly characterized, the discontinuum approach is able to investigate the small-scale behavior of fractured rock masses, which may be more realistic in replicating in-situ behavior. However, discontinuum models applied in large reservoir simulations and for long term predictions demand greater computational efficiency and time.

Conversely, the major assumption for the equivalent continuum approach is that the macroscopic behavior of fractured rock masses, and their constitutive relations, can be characterized by the laws of continuum mechanics. The equivalent continuum approach has the advantage of representing the fractured masses at large scale, with the potential to recover simulation results of long-term response. The behaviors of fractures are implicitly included in the equivalent constitutive model and via effective parameters for modulus and permeability. One central concept in developing equivalent continuum approaches is that of crack tensor theory [*Oda*, 1986]. This includes a set of governing equations for solving the coupled stress and fluid flow problem with geological discontinuities, which contains the fracture size, fracture orientation, fracture volume, and fracture aperture. The rock mass is treated as an equivalent anisotropic porous elastic medium with the corresponding elastic compliance and permeability tensors.

We adapt the continuum simulator TFREACT [*Taron et al.*, 2009], which couples analysis of mass and energy transport in porous fractured media (TOUGH) and combines this with mechanical deformation

(FLAC3D, [*Itasca,* 2005]) with extra constitutive models including permeability evolution and dual-porosity poroelastic response. The purpose in this work is to extend the analysis of fracture flow and fracture deformation to randomly and discretely fractured rocks, and to provide a tractable solution to optimize for fluid flow and thermal production in spatially large and complex fracture networks. To better represent the permeability evolution due to the influence of stress, the constitutive model for stress-dependent permeability evolution is extended to include the scenario of fractures opening in extension – specifically where large fractures traverse individual computational cells. For this, crack tensor theory is employed to determine the equivalent mechanical properties of the fractured rock mass in tensor form, differentiating the responses of the fluid flow and stress from both the intact rock and the fractured rock mass. The constitutive model for the evolution of stress-dependent permeability accommodates three different stress states, including normal closure, shear dilation, and the potential for fracture walls to lose contact under extensional loading. The accuracy of the simulator is assessed by validation against the interaction of fracture opening and sliding deformation in response to fluid injection inside a single long fracture embedded in a poroelastic medium. By assessing the simulation results against the results of other discontinuum simulators, the feasibility of the approach is confirmed in simulating the coupled thermal-hydro-mechanical behavior in discretely fractured rock masses. A series of parametric tests are conducted with different mean stress conditions and stress obliquity conditions and fracture network configurations. These provide insights into fluid transport and the evolution of fracture aperture characteristics and permeability including the evolution of permeability anisotropy and flow channeling.

8.2 Constitutive model development

To implement an equivalent continuum model accommodating the fractured mass, four constitutive relations require to be incorporated. These are the relations for a crack tensor, a permeability tensor, a model for porosity representing the fracture volume, and a model for stress-dependent fracture aperture.

8.2.1 Crack tensor

To represent the heterogeneous distribution of components of fractured rock in the simulation, the mechanical properties of fractures are characterized in tensor form based on the crack tensor theory proposed by Oda [*Oda*, 1986]. The theory is based on two basic assumptions: (1) individual cracks are characterized as tiny flaws in an elastic continuum; and (2) the cracks are represented as twin parallel fracture walls, connected by springs in both shear and normal deformation. By predefining the fracture properties, such as position, length, orientation, aperture, and stiffness, we implement crack tensor theory as a collection of disc-shaped fractures in a 3D system, and modify the distribution of modulus corresponding to the fractured rock and intact rock in each intersected element. Here the intact rock is

assumed to be isotropic, the conventional elastic compliance tensor M_{ijkl} for intact rock is formulated as a function of Poisson ratio, ν, and the Young's modulus of the intact rock, E, as

$$M_{ijkl} = \frac{(1+\nu)\delta_{ik}\delta_{jl} - \nu\delta_{ij}\delta_{kl}}{E} \quad (1)$$

The compliance tensor C_{ijkl} for the fractures is defined as a function of fracture normal stiffness K_{nf}, fracture shear stiffness K_{sf}, fracture diameter D, and components of crack tensors F_{ij}, F_{ijkl} respectively .

$$C_{ijkl} = \sum^{fracnum} \left[\left(\frac{1}{K_{nf}D} - \frac{1}{K_{sf}D} \right) F_{ijkl} + \frac{1}{4K_{sf}D} \left(\delta_{ik}F_{jl} + \delta_{jk}F_{il} + \delta_{il}F_{jk} + \delta_{jl}F_{ik} \right) \right] \quad (2)$$

where *fracnum* is the number of fractures truncated in an element block, δ_{ik} is the Kronecker's delta. The related basic components of crack tensor for each crack intersecting an element are defined F_{ij} as below [*Rutqvist et al.*, 2013],

$$F_{ij} = \frac{1}{V_e}\frac{\pi}{4}D^3 n_i n_j \quad (3)$$

$$F_{ijkl} = \frac{1}{V_e}\frac{\pi}{4}D^3 n_i n_j n_k n_l \quad (4)$$

$$P_{ij} = \frac{1}{V_e}\frac{\pi}{4}D^2 b^3 n_i n_j \quad (5)$$

where F_{ij}, F_{ijkl}, P_{ij} are the basic crack tensors, b is the aperture of the crack, V_e is the element volume and n is the unit normal to each fracture. Therefore the formula for the total elastic compliance tensor T_{ijkl} of the fractured rock can be expressed as,

$$T_{ijkl} = C_{ijkl} + M_{ijkl} \quad (6)$$

Combining equation 3-5 into equation 2, the equivalent fracture Young's modulus E^f and Poisson ratio ν^f can be obtained as,

$$E^f = \frac{1}{\frac{1}{E} + (\frac{1}{K_{nf}} - \frac{1}{K_{sf}})\frac{1}{V_e}\frac{\pi}{4}D^2 n_1^4 + \frac{1}{K_{sf}}\frac{1}{V_e}\frac{\pi}{4}D^2 n_1^4} \quad (7)$$

$$\nu^f = \frac{\nu}{E}E^f - (\frac{1}{K_{nf}} - \frac{1}{K_{sf}})\frac{E^f}{V_e}\frac{\pi}{4}D^2 n_1^2 n_2^2 \quad (8)$$

Given the assumption that the properties of modulus are anisotropic, the equivalent bulk modulus K and shear modulus G for the fractured rock mass are formulated as below,

$$K = \frac{1}{\frac{1}{K_{\text{int}\,act}} + \sum^{nf} \frac{V_{ratio}}{b}\left[(\frac{1}{K_{nf}} - \frac{1}{K_{sf}})\left(1 - n_2^4\right) + \frac{1}{K_{sf}} n_1^2\right]} \quad 9$$

$$G = \frac{1}{\frac{1}{G_{\text{int}\,act}} + \sum^{nf} \frac{2V_{ratio}}{b}\left[(\frac{1}{K_{nf}} - \frac{1}{K_{sf}})\left(n_1^4 - n_1^2 n_2^2\right) + \frac{1}{K_{sf}} n_1^2\right]} \quad 10$$

where $K_{\text{int}\,act}$ is the bulk modulus of the intact rock, $G_{\text{int}\,act}$ is the shear modulus of the intact rock and V_{ratio} is the volumetric ratio of the truncated fracture over the element volume. The stress-dependent evolution of fracture aperture will in turn update the equivalent modulus of the fractured rock masses.

8.2.2 Permeability tensor and aperture evolution

Considering that the randomly distributed fractures may be intersected by multiple elements in the reservoir gridding, the directional fracture permeability is defined as a permeability tensor k_{ij}, which is able to represent the orientation of fractures and the explicit fracture volume intersecting any element block.

$$k_{ij} = \sum^{nf} \frac{1}{12}(P_{kk}\delta_{ij} - P_{ij}) = \sum^{nf} \frac{1}{12}(\frac{V_{ratio}}{b_{ini}} b^3 n_k^2 \delta_{ij} - \frac{V_{ratio}}{b_{ini}} b^3 n_i n_j)$$

where b_{ini} is the initial aperture of the fracture.

The effect of stress has a direct impact in changing the evolution of the fracture aperture, which will in turn change the compliance tensor in the simulation loop. Prior models for stress permeability coupling include hyperbolic models of aperture evolution [*Bandis et al.*, 1983; *Barton and Choubey*, 1977], which can describe the response of fracture aperture in normal closure under the influence of in-situ stress. The functionality of the hyperbolic model is mediated by the parameters of initial fracture normal stiffness K_{nf}^0, maximum closure of the fracture aperture $d_{n\max}$, initial aperture of the fracture, b_{ini}, and the effective normal stress of the fracture $\sigma_n^{'}$, which is formulated as,

$$\Delta d_n = \frac{d_{n\max}}{1 + \frac{K_{nf}^0 d_{n\max}}{\sigma_n^{'}}} \quad 11$$

A simplified Barton-Bandis hyperbolic model [*Baghbanan and Jing, 2007*] is adopted to model aperture evolution by introducing a new parameter – the critical normal stress σ_{nc}, which means that the normal compliance C_n is reduced significantly when the aperture closure approaches the maximum closure. In order to simplify the hyperbolic solution it is assumed that the ratio of maximum normal closure $d_{n\max}$ relative to initial fracture aperture b_{ini} is constant at 0.9. Given this assumption, the hyperbolic normal closure equation is transformed as,

$$\sigma_n^{'} = \frac{\sigma_{nc}\Delta d_n}{10(0.9b_{ini} - \Delta d_n)} \qquad 12$$

and the normal stiffness is determined by the normal stress as,

$$K_{nf} = \frac{(10\sigma_n^{'} + \sigma_{nc})^2}{9\sigma_{nc}b_{ini}} \qquad 13$$

where $\sigma_{nc}(MPa) = 0.487b_{ini}(\mu m) + 2.51$. Figure 1 shows the hyperbolic relationship between the normal stress and the aperture corresponding to different predefined apertures. This shows that the larger the initial aperture, the larger drawdown gradient of normal stress.

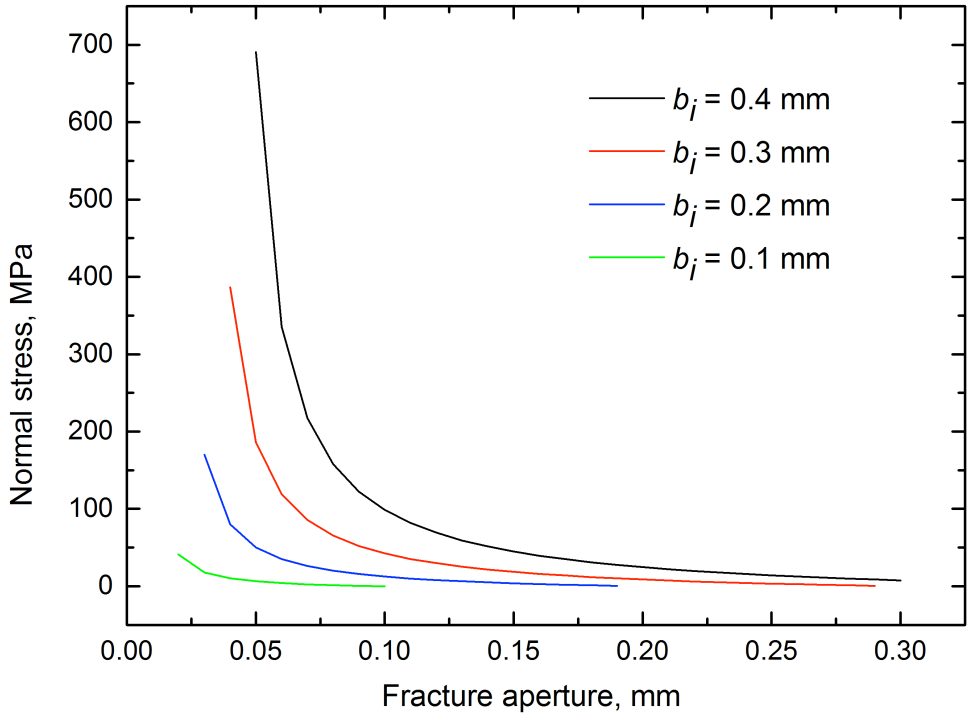

Figure 1 The impact of initial aperture in the relationship between normal stress and fracture aperture.

Fracture shear slip and related dilation are included in the simulator by lumping the influence into the response of the matrix rock being sheared. When the Coulomb failure criterion is reached, the shear displacement u_s will generate shear dilation b_{dila} in the normal direction according to the equation (Figure 2),

$$b_{dila} = u_s \tan\phi_d \qquad 14$$

where ϕ_d is the dilation angle. Figure 2 identifies the relationship between the shear stress and displacement due to normal dilation. When the shear stress reaches the critical magnitude τ_{sc}, which is determined by the Coulomb failure criterion, shear failure triggers normal dilation (red line) to increase the fracture aperture as the shear displacement increases. To incorporate the weakening response for the onset of shear failure in fractured rock masses, the reduction of a linear slope gradient (black line) represents the significant reduction of fracture shear stiffness from K_{s1} to K_{s2} due to shear failure. The magnitude of the aperture increment added by shear dilation can be calculated as,

$$b_{dila} = \frac{\tau - \tau_{sc}}{K_s} \tan\phi_d \qquad 15$$

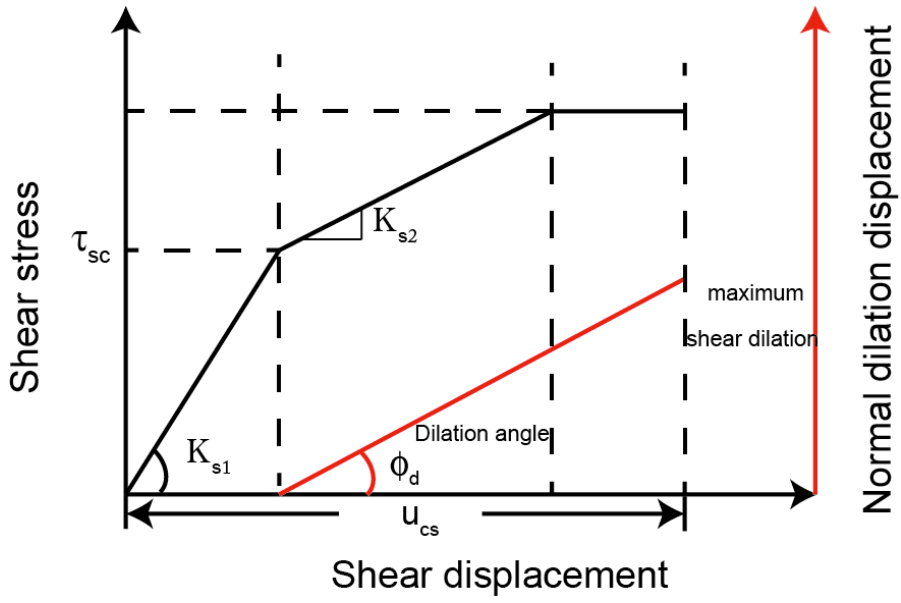

Figure 2 Fracture normal dilation displacement evolution induced from the shear slip in fracture.

When the fluid pressure in the fracture exceeds the normal stress across the fracture, the two walls of the fracture are separated and the effective normal stress is zero [*Crouch and Starfield*, 1991] since $P_f = \sigma_n$.

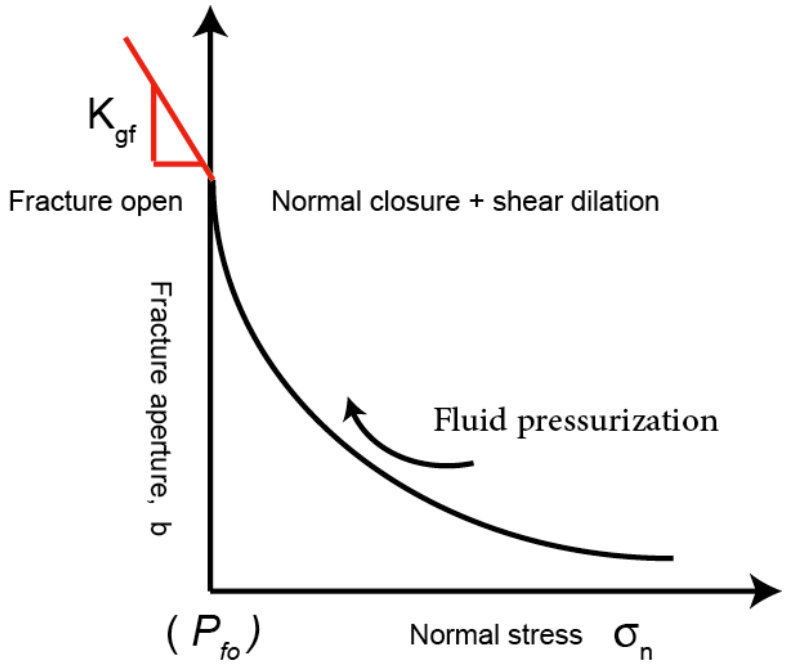

Figure 8 Fracture aperture evolution under different normal stress state.

Figure 3 represents the constitutive relation for fracture aperture evolution applied in this model. The curve to the right is the regime under normal closure and shear dilation. However, as soon as the fluid pressure reaches the critical magnitude P_{fo} where effective stress is zero (left side in Figure 3), a geometrical stiffness K_{gf} for a penny-shaped fracture is employed to calculate the induced normal opening displacement when the two walls are under tension. The normal opening displacement is linear with an increment of fluid pressure ($P_f - P_{f0}$). This geometrical stiffness K_s^{rock} [*Dieterich*, 1992], although small, is much larger than that of the fracture in shear and is defined as,

$$K_s^{rock} = \eta \frac{2G}{D} = \frac{7\pi}{12} \frac{G}{D} \qquad 16$$

where G is the shear modulus of the intact rock, D is the fracture half length, and η is a geometrical factor which depends on the crack geometry and assumptions related to slip on the patch [*Dieterich*, 1992]. In

this study, η is defined to represent a circular crack and is given as $\frac{7\pi}{24}$. Therefore the equation for the fracture opening displacement b_{open} is formulated as below,

$$b_{open} = \frac{P_f - P_{f0}}{K_{gf}} = \frac{P_f - P_{f0}}{10K_s^{rock}} = \frac{(P_f - P_{f0})}{10 \times \frac{7\pi}{12}\frac{G}{D}} \quad 17$$

To summarize, equations 11, 15, and 17, represent the relations for considering stress-dependent aperture change including normal closure, shear dilation, and fracture opening is obtained as,

$$b = b_{ini} - \frac{9b_{ini}\sigma_n^{'}}{\sigma_{nc} + 10\sigma_n^{'}} + \frac{\tau - \tau_{sc}}{K_s}\tan\phi_d + \frac{(P_f - P_{f0})}{10 \times \frac{7\pi}{24}\frac{G}{r}} \quad 18$$

To summarize, equations 11, 15, and 17 represent the relations for considering stress-dependent aperture change including normal closure, shear dilation, and fracture opening is obtained as,

$$\begin{aligned} b &= b_{ini} - b_{normal} + b_{dila} + b_{open} \\ &= b_{ini} - \frac{9b_{ini}\sigma_n^{'}}{\sigma_{nc} + 10\sigma_n^{'}} + \frac{\tau - \tau_{sc}}{K_s}\tan\phi_d + \frac{(P_f - P_{f0})}{10 \times \frac{7\pi}{12}\frac{G}{D}} \end{aligned} \quad 18$$

where b_{ini} is the initial aperture of the fracture, b_{normal} is the reduction of aperture due to the normal closure, $\sigma_n^{'}$ is the effective normal stress of the fracture, σ_{nc} is the critical normal stress, τ_{sc} is the critical shear stress where shear failure happens.

8.3 Porosity model

Considering that deformations occur independently within the two different media of fracture and matrix, it is important to accommodate the evolution of the dual porosity system with the induced strain, since the porosity is iteratively coupled in the hydro-mechanical simulations. Hence in this study, there are two different equations to represent the evolution of porosity in fracture and matrix. In terms of the matrix, the volumetric strain is employed to update the matrix porosity as [*Chin et al.*, 2000],

$$\phi_{n+1}^m = 1 - (1 - \phi_n^m)e^{-\Delta\varepsilon_v^s} \quad 19$$

where $\Delta\varepsilon_v^s$ is the change in matrix volumetric strain, ϕ_{n+1}^m and ϕ_n^m are the matrix porosity at time t_{n+1} and t_n respectively. The fracture porosity is calculated as below,

$$\Delta\varepsilon_v^f = \frac{\Delta b}{b_{ini}} \quad (20)$$

$$\phi_{n+1}^f = 1-(1-\phi_n^f)e^{-\Delta\varepsilon_v^f} \quad (21)$$

where Δb is the aperture change, $\Delta\varepsilon_v^f$ is the change of fracture volumetric strain. The assumption is made that only the aperture evolution Δb in the normal direction is considered in calculating the fracture volumetric strain $\Delta\varepsilon_v^f$.

8.3.1 Numerical simulation workflow

Based on the constitutive model described above, the workflow for the equivalent continuum model is presented in Figure 4. The simulation initiates with the equilibration of temperature (*T*) and pore pressure (P_f) in TOUGH. Subsequently, initial data describing the fracture network, including fracture orientation, trace length, aperture, and modulus are input into a FORTRAN executable. The compliance tensor transfers the composite fracture modulus with the equilibrium pore pressure distribution into FLAC3D to perform the stress-strain simulation. The revised undrained pore pressure field is then redistributed, based on principles of dual porosity poromechanics, and applied to both fracture and matrix. The stress-dependent fracture aperture is calculated and updated based upon the failure state of the fracture. Since the fracture permeability and composite modulus of the fractured medium are both mediated by the magnitude of fracture aperture, the fracture aperture is iteratively adjusted in the simulation loop to define the revised fracture permeability and to alter the compliance tensor of the composite fractured mass.

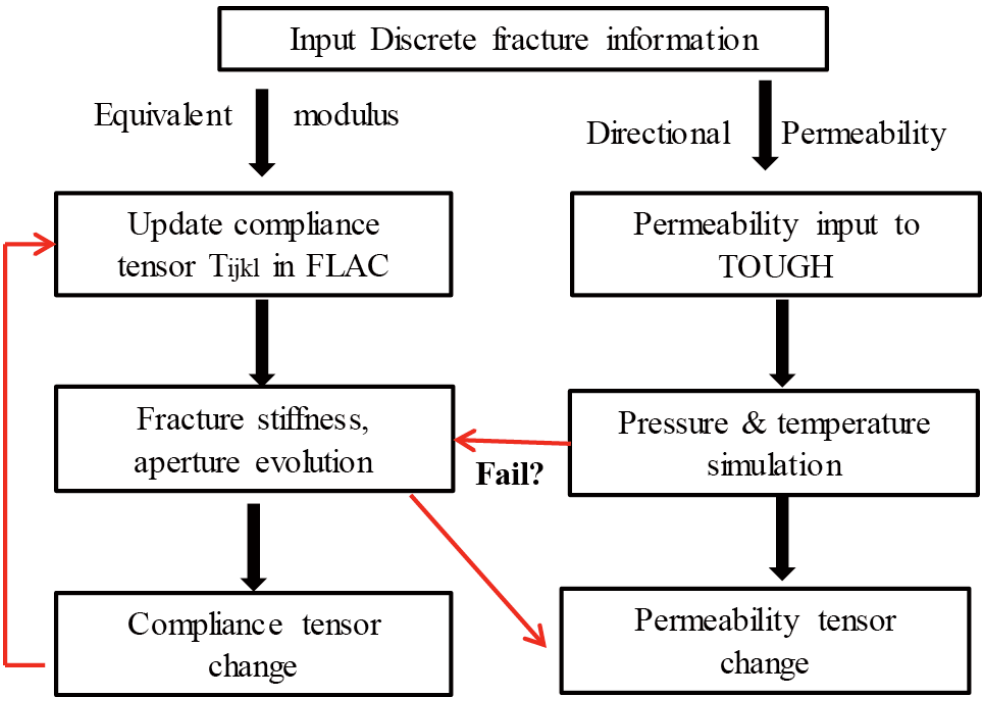

Figure 3 Equivalent continuum simulation workflow implementation in TF_FLAC^{3D}.

8.4 Model verification

In this section, the discrete fracture network (DFN) model is verified by comparing the results against other discrete fracture network models. The model in this study [*Kelkar et al.*, 2015] is an injection well intersecting a single fracture that dilates and slips in response to fluid injection .

8.4.1 Model setup

Figure 5 shows the reservoir geometry applied in this study. The single fracture is oriented at 45 degrees to the principal stresses and embedded within an infinite medium. The fracture has a length of 39 m with an initial width of 1 mm and does not propagate. The injection well is centrally located along the fracture with constant injection at $6.0\times10^{-8} m^3/s$. The maximum principal stress is 20 MPa (y-direction) and the minimum principal stress is 13 MPa (x-direction). Initial pore pressure and reservoir temperature are each uniform at 10 MPa and 420 K. The initial reservoir properties used in this model are listed in Table 1. The pre-stressed fracture is in equilibrium with the prescribed stress and pore pressure to yield the desired initial aperture of 1 mm.

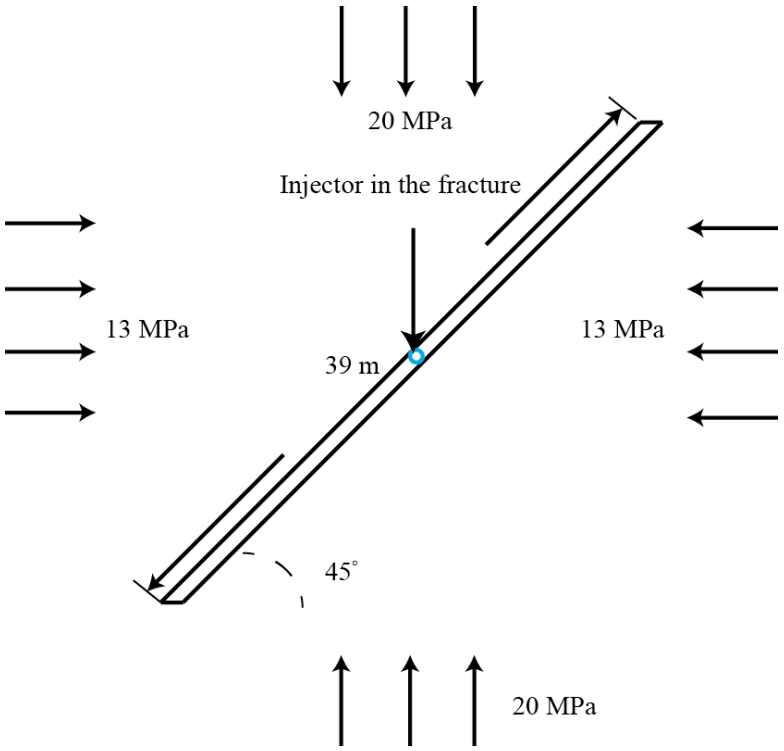

Figure 4 Reservoir configuration for injection inside a 39 m long fracture within an infinite medium.

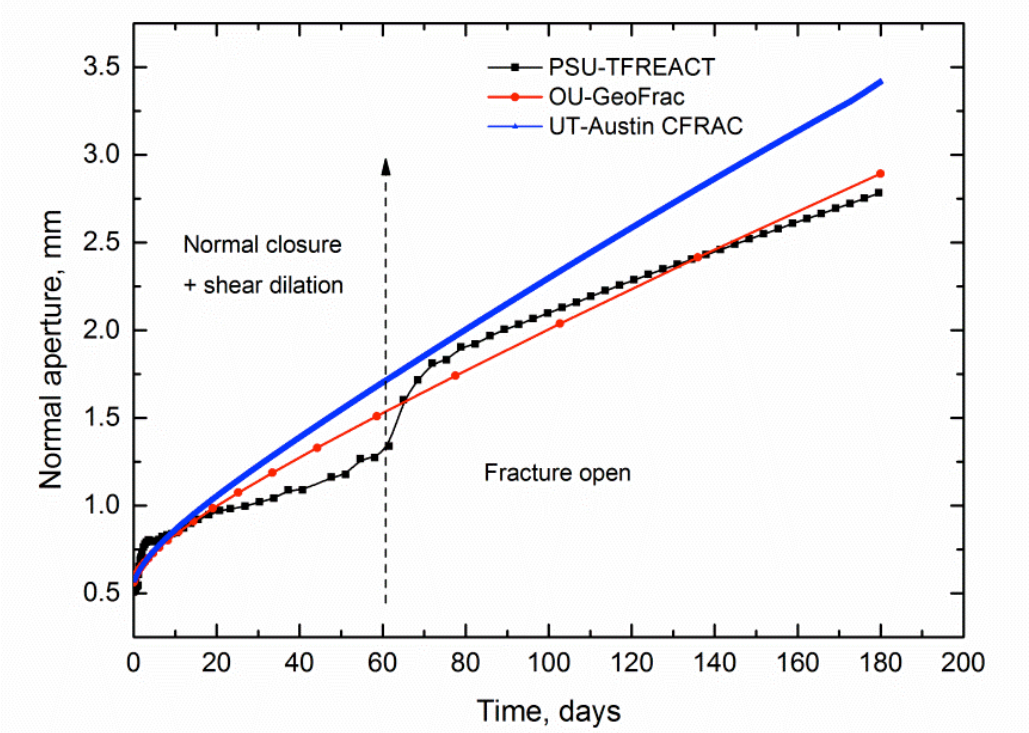

Figure 5 Fracture aperture evolution comparisons against other discontinuum models.

Table 1 Data used in the simulation [*McTigue*, 1990].

Parameter (unit)	Magnitude
Shear modulus, G (GPa)	15
Poisson's ratio, ν	0.25
Undrained Poisson's ratio	0.33
Matrix permeability, k_m, (m^2)	4.0×10^{-19}
Matrix porosity, ϕ_m	0.01
Biot's coefficient, α	0.44
Water viscosity, μ, (Pa.s)	3.547×10^{-4}
Fluid compressibility, (MPa^{-1})	4.2×10^{-4}
Thermal expansion coefficient of solid, α_s (K^{-1})	2.4×10^{-5}
Thermal diffusivity of intact porous rock, c^T (m^2/s)	1.1×10^{-6}
Fluid density, ρ_w (Kg/m^3)	1000
Heat capacity of fluid, c_w ($Jkg^{-1}K^{-1}$)	4200
Initial reservoir temperature (*K*)	420
Injection water temperature (*K*)	400
Initial joint normal stiffness, k_n, (GPa/m)	0.5
Initial joint shear stiffness, k_s, (GPa/m)	50
Fracture aperture initial, b_{ini} (mm)	1
In-situ stress (*MPa*) – y direction	20
In-situ stress (*MPa*) – x direction	13
Initial reservoir pore pressure (*MPa*)	10
Injection rate (m^3/s) /m thickness of reservoir	6.0×10^{-8}
Friction angle, dilation angle	30°, 2.5°
Fracture cohesion, *C*, *MPa*	0

8.4.2 Results discussion

In this section, the results are compared between the contrasting conditions of isothermal injection and non-isothermal injection. To isolate the impact of the induced thermal stress effect in the aperture

evolution, the liquid viscosity is set as constant for both the isothermal and non-isothermal injection conditions.

Figure 3-6 presents the results of fracture aperture evolution under isothermal injection conditions for the first 180 days. By comparing the results from our equivalent continuum approach against other those for discrete fracture models, including GeoFrac [*Ghassemi and Zhang*, 2006] and CFRAC [*McClure and Horne*, 2013] we verify that the equivalent continuum model TF_FLAC^{3D} is able to match results for the evolution of fracture aperture.

Figure 7 presents the evolution of injection pressure in the fracture among the three different simulators for the condition of isothermal injection. There is a good agreement between the injection pressures recovered from TF_FLAC^{3D} and the other discrete fracture models. In this response, the normal aperture grows slowly under initial pressurization and most rapidly as the walls lose contact and the full geometric stiffness of the fracture is mobilized as the fracture walls lose contact. The walls of the fracture are out of contact after ~60 days of injection. Due to permeability enhancement in the fracture, the injection pressure gradient in the fracture decreases after the fracture opens.

Figure 8 presents a comparison of injection pressures between isothermal and non-isothermal injection. In this, water is injected at 400 K for a system originally in thermal equilibrium at 420 K. The injection pressure results for these two conditions are similar. However, there is a notable difference in the growth in fracture aperture between the two injection scenarios (Figure 9). The major difference occurs when the fracture walls lose contact. Prior to fracture separation, the fracture aperture for non-isothermal injection is slightly larger than that for isothermal injection. This can be explained by following the evolution of the normal stress acting across the fracture, as noted in Figure 3-10 – and is a consequence of thermal unloading by the quenching fluid. The thermal unloading effect is more pronounced when the fracture is in extension (open).

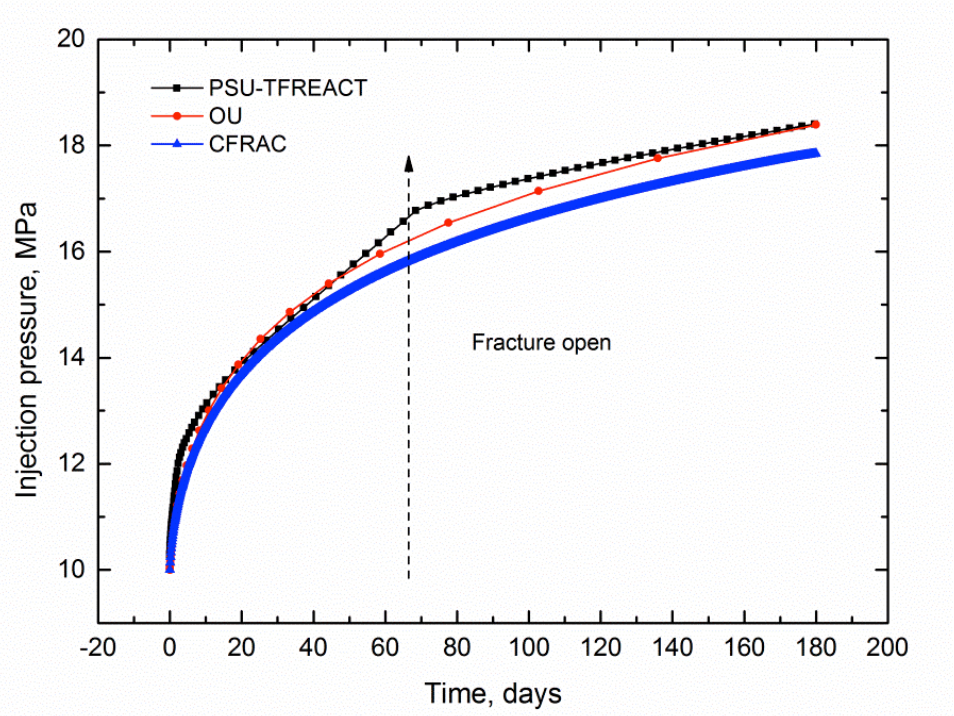

Figure 6 Evolution of fracture injection pressures evaluated by various models.

Figure 11 shows the distribution of aperture along the fracture at 72 days and 180 days for both the isothermal injection and non-isothermal injection cases. There is no significant difference in the distribution of fracture aperture for isothermal and non-isothermal cases at 72 days, although the results diverge by 180 days. By 180 days, the influence of the quenching fluid in reducing the fracture-local normal stress has become sufficiently significant to increase the aperture by ~3% for a permeability increase of the order of 1.03^3~10%.

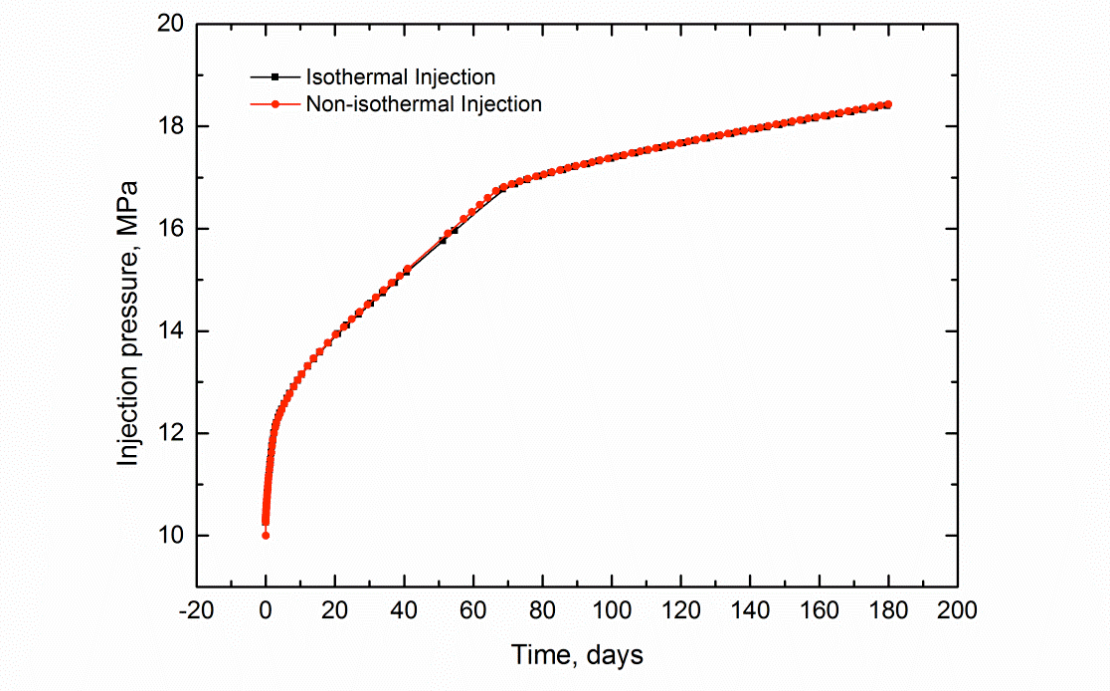

Figure 7 Evolution of injection pressure for isothermal injection (black line) and non-isothermal injection (red line).

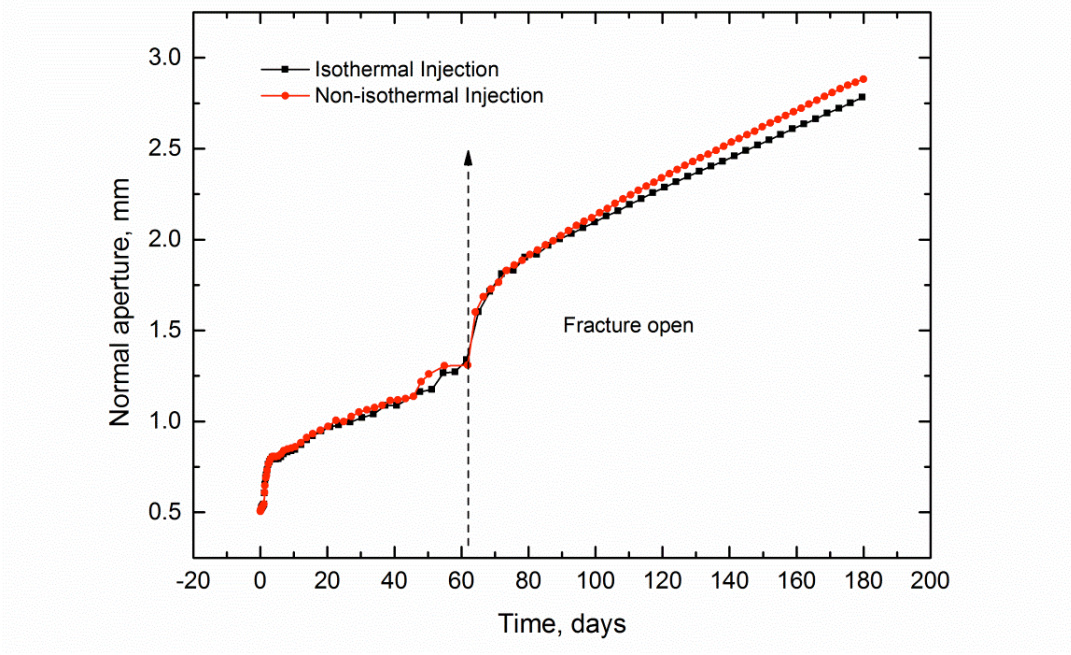

Figure 8 Evolution of fracture normal aperture for isothermal injection (black line) and non-isothermal injection (red line), respectively.

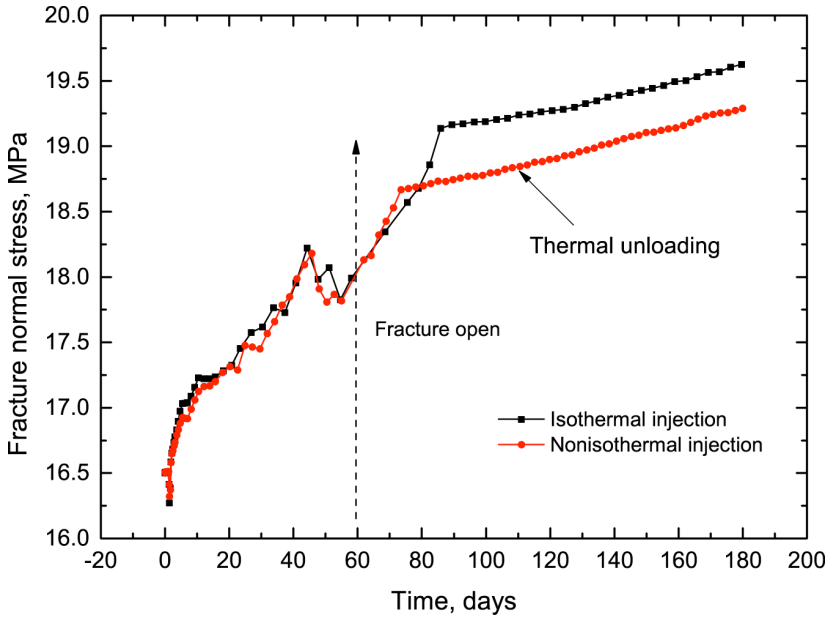

Figure 9 Evolution of fracture normal stress under isothermal injection (black line) and non-isothermal injection (red line).

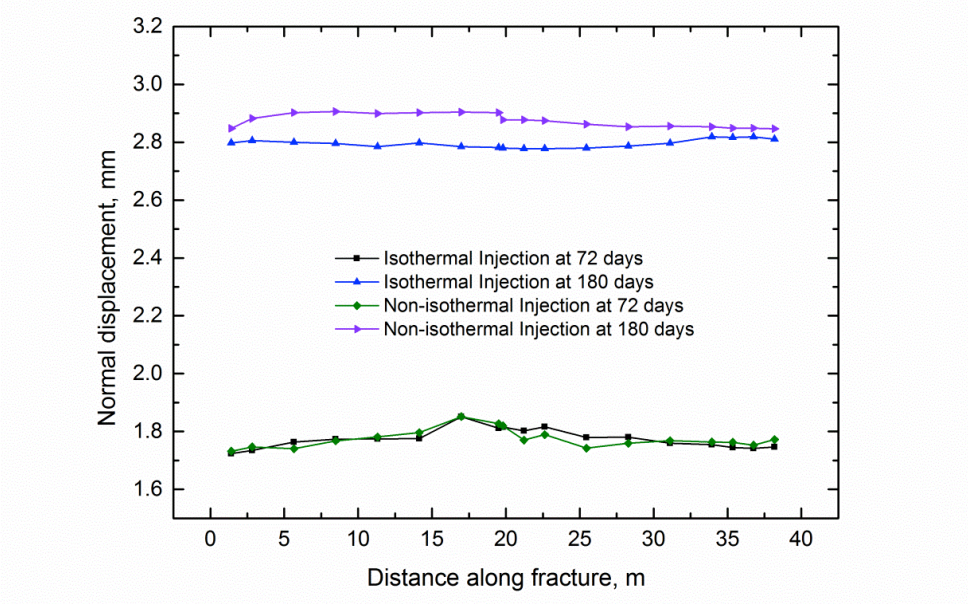

Figure 10 Aperture distribution along the fracture at 72 days and 180 days under conditions of both isothermal injection and non-isothermal injection.

8.4.3 Multi-fracture validation

The previous TFREACT simulator is able to simulate the response of fracture aperture and pore-elasticity in the framework of orthogonal fracture sets. In this section, the simulation of multi-fracture intersection was completed between the equivalent continuum model TF_FLAC^{3D} and the original TFREACT (Figure 13), which aims at validating the correctness of the developed equivalent continuum model in simulating the interaction of multi-fractures. In Figure 12, there are two sets of orthogonal fractures (red and green lines) ubiquitously distributed in a $200m \times 200m \times 10m$ reservoir. The fractures are separated at a constant spacing 4m. The injector is centrally located in the reservoir with a constant injection rate of 0.01 m^3/s. The reservoir properties are described in Table 1.

In the model of continuum TFREACT, the evolution of fracture permeability is represented by a hyperbolic function as,

$$b = b_r + (b_m - b_r) \times \exp(\sigma_N \times a) \qquad 21$$

Where b_r is the residual aperture, b_m is the maximum aperture, σ_N is the effective normal stress of the fracture (MPa), a is the non-linear fracture stiffness (1/MPa), which is defined as 1.4 MPa^{-1} in this model. Figure 13 shows the evolution of fracture aperture over time. There is good agreement in the magnitude of fracture aperture between the continuum TFREACT and the equivalent continuum TF_FLAC^{3D}. The injection pressure results are either validated in Figure 14. When the fracture pressure increases, the decreased effective normal stress prompts the enhancement of fracture aperture.

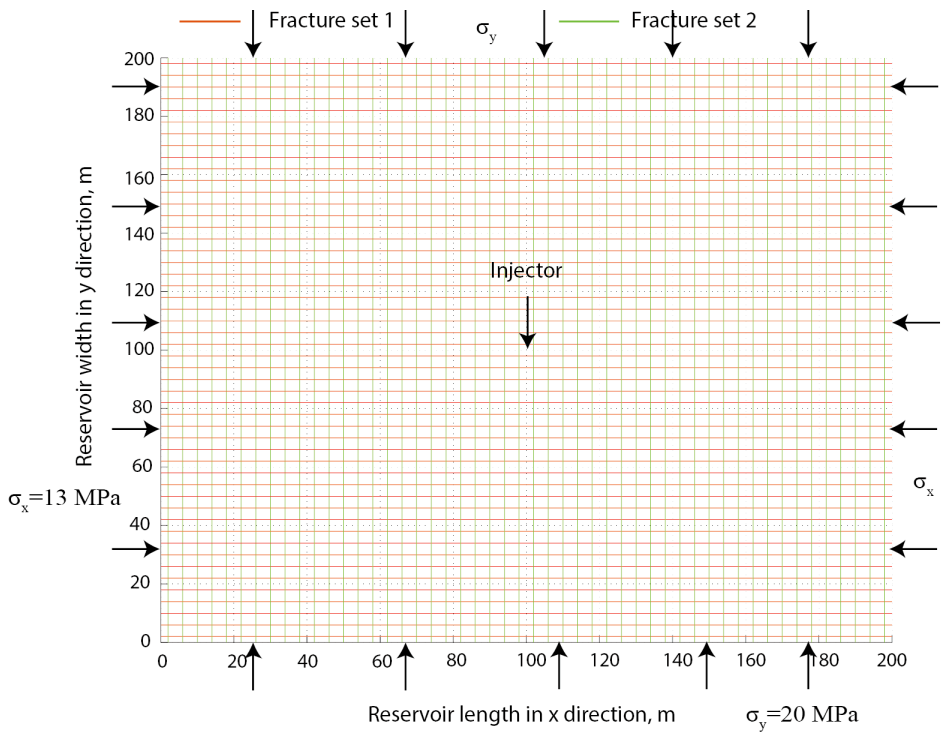

Figure 11 Schematic of two sets of orthogonal fracture ubiquitously distributed in a 200m × 200m × 10m reservoir.

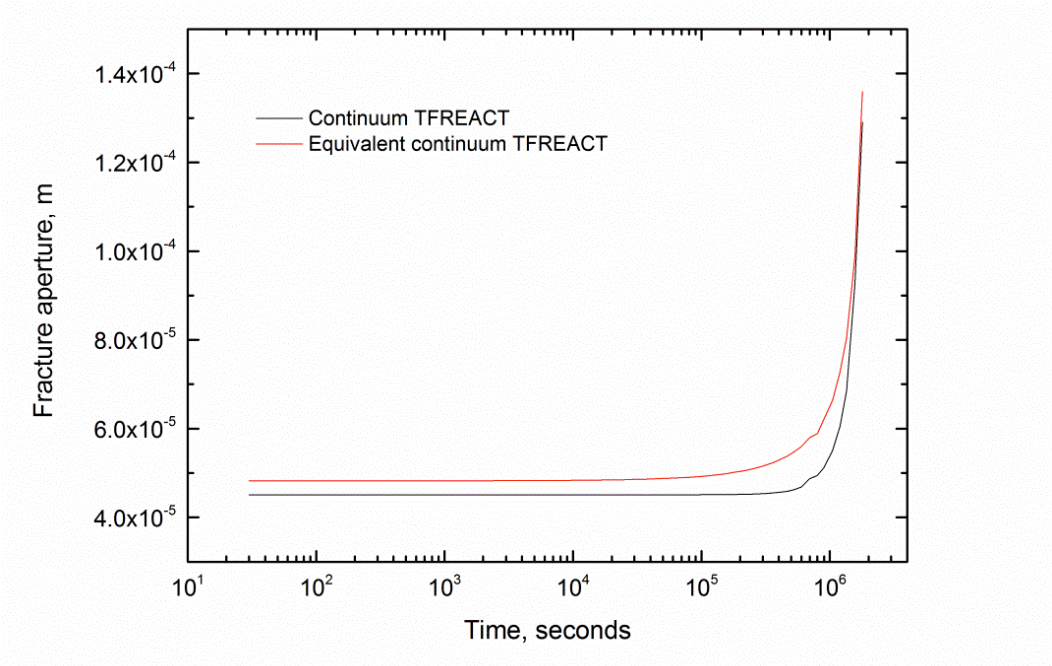

Figure 12 Validation of fracture aperture at the injection well between the developed equivalent continuum TF_FLAC^{3D} and the original continuum TFREACT [*Taron et al.*, 2009].

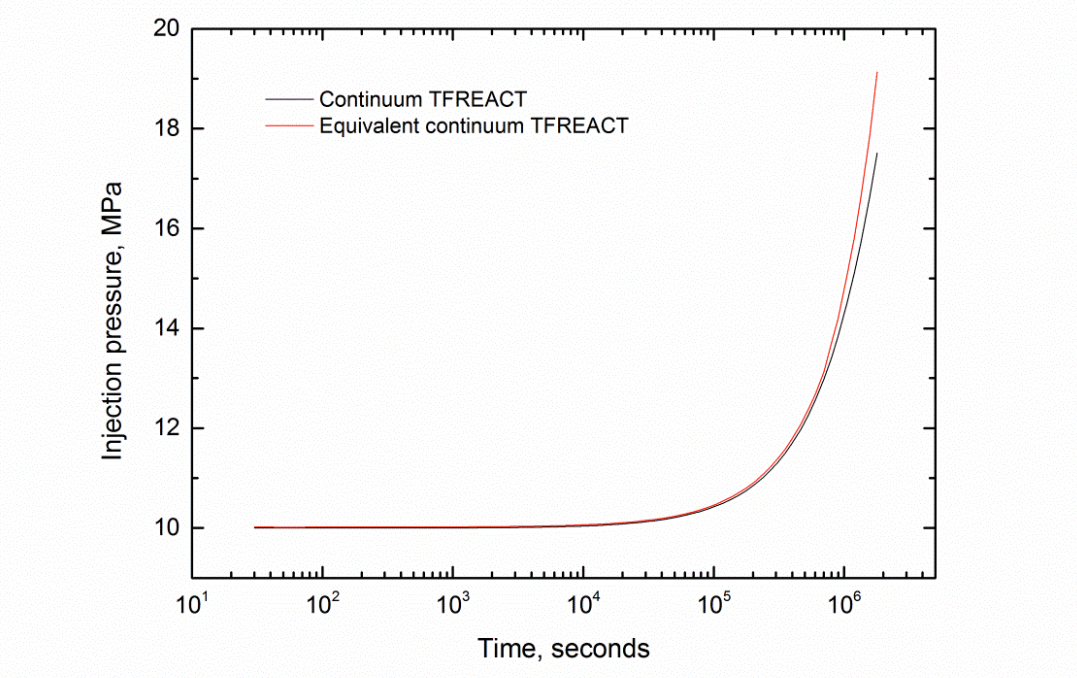

Figure 13 Validation of injection pressure between the developed equivalent continuum TF_FLAC^{3D} and the original continuum TFREACT.

8.5 DFN application

In realistic reservoir, fractures networks usually are non-uniformly distributed. Complex fracture pattern yields heterogeneous fluid flow and heat thermal drawdown [*Bear*, 1993; *Tsang and Neretnieks*, 1998], and the development of anisotropic fracture permeability, which could induce flow channeling in the major fractures [*Chen et al.*, 1999; *Min et al.*, 2004]. In this section, a reservoir model with two discrete fracture networks sets is constructed to address the evolution of fracture permeability, due to the influence of stress state and fracture orientation.

8.5.1 Fracture network generation

To create the discrete fracture network in the simulation, various factors including fracture location, orientation, length, and aperture are necessarily considered. In this work, the two fracture networks are oriented at azimuths (from the North) of 020 degrees and 135 degrees in a $200m \times 200m \times 10m$ reservoir (Figure 15c). The injector is located at coordinate (20,140). The geometry of each individual fracture is defined by prescribing the starting and ending point according to the fracture length and orientation (Figure 15a). Each set of fractures comprises 50 individual fractures of various lengths distributed within the reservoir. There are several major fractures which allow the fluid to diffuse into the majority of

reservoir. The length of fractures in the reservoir follows the traditional lognormal distribution (Figure 15b) [*de Dreuzy et al.*, 2001; *Muralidharan et al.*]. The fracture length is constrained in the range of 1m to 60m. The initial aperture for each fracture is determined by a power law function (equation 22) [*Olson*, 2003], which implies that longer fractures of trace length l have greater initial aperture b_i.

$$b_i = 1.25\times10^{-5} * l^{0.8} \qquad 22$$

Figure 16 indicates that the initial fracture aperture in this model varies from $5.0\times10^{-5} m$ to $2.5\times10^{-4} m$, corresponding to the predefined range of fracture length.

The reservoir properties in the DFN model are the same and are defined in Table 1. In the base case, the maximum principal stress is 20 MPa (N-S direction) and the minimum principal stress is 13 MPa (E-W direction). The initial reservoir pressure is uniform at 10 MPa. The water is injected at a constant rate of $5.0\times10^{-6}\ m^3/s$.

Figure 17(a) shows the resulting fracture pressure distribution at 180 days for the base case. The fracture permeability distribution in Figure 17(b) corresponds to the shear stress drop along both fracture sets in Figure 17(c) and 17(d). The shear stress around the injector drops ~3 MPa for the fracture set oriented at 045 degrees. Furthermore, the path of shear stress drop also follows with the path of major fractures, which increases the permeability of fractures.

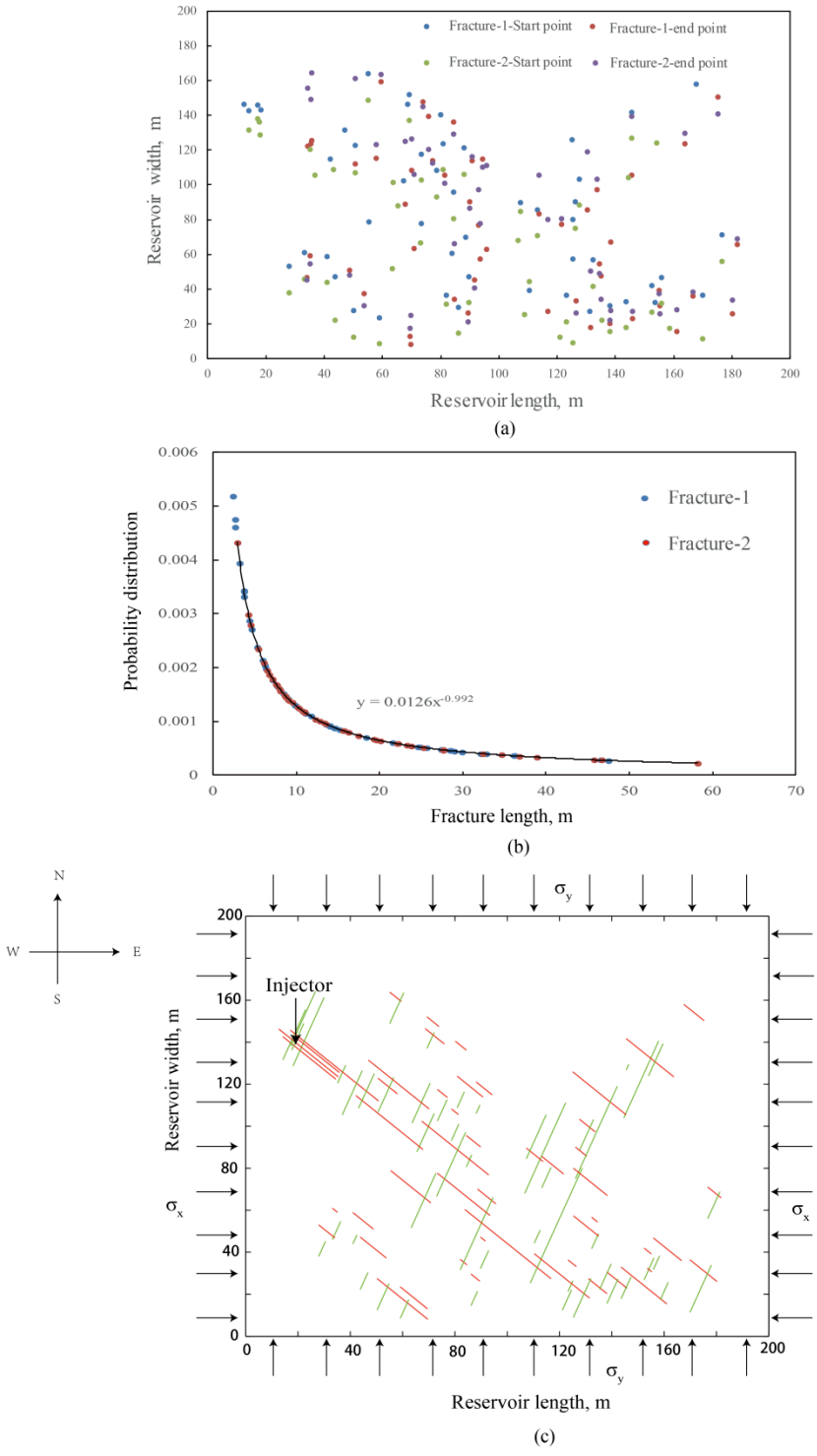

Figure 14 (a) Locations of starting points and ending points for the two sets of fractures in the reservoir, (b) lognormal probability distribution for the length of fractures, (c) distribution of fracture networks in a 200 m × 200m× 10m reservoir, fractures in red are oriented at 135 degrees, and those in green are oriented at 020 degrees (with respect to the North).

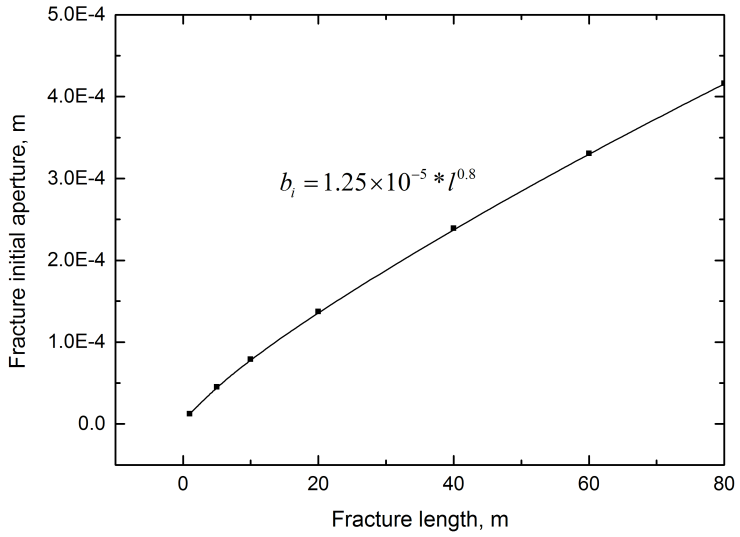

Figure 15 Power law relationships between the fracture length and initial fracture aperture.

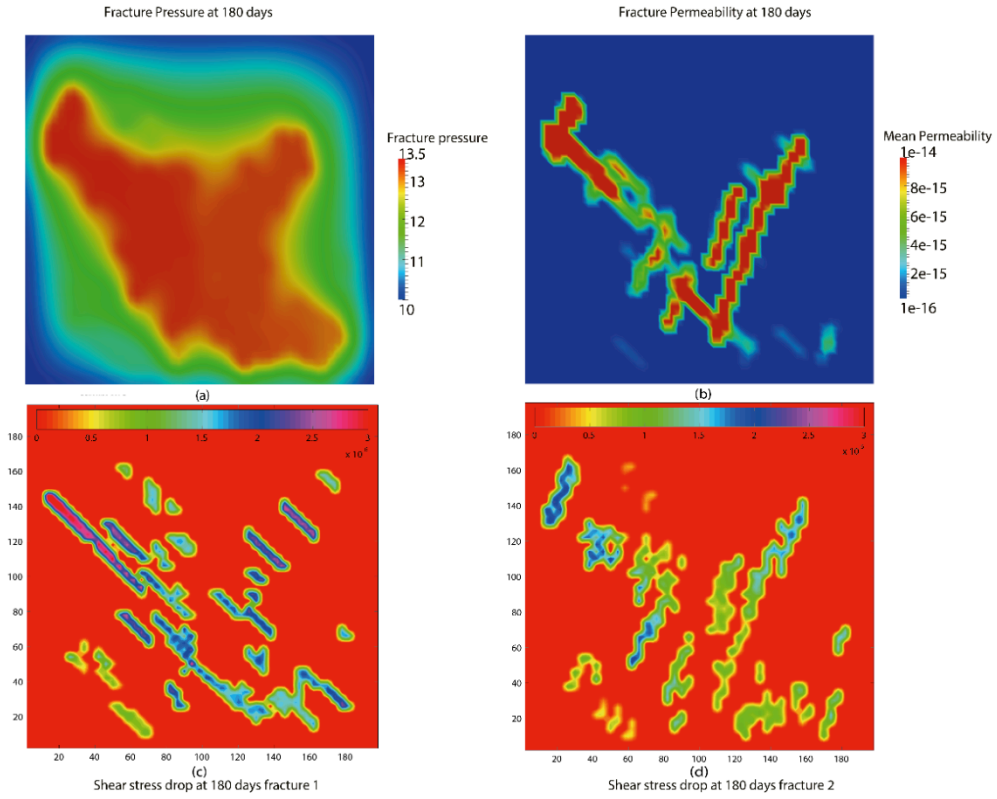

Figure 16 (a) Fracture pressure distribution for the base case at 180 days, (b) contour of fracture mean permeability, (c) shear stress drop along the first fracture set, (d) shear stress drop along the second set of fractures.

8.5.2 Effect of applied stress

Applied boundary stress has a direct impact in determining the potential of fracture shear failure and the resulting permeability evolution. Therefore it is desirable to investigate the various ratios of boundary stress conditions influencing the evolution of fracture permeability. To evaluate the effect of stress state, two scenarios of the ratio of boundary stresses are proposed. Table 2 illustrates the composition of the sensitivity tests for these applied boundary stresses. The initial reservoir pressure and injection rate are kept constant for all the cases.

Table 2 Sensitivity tests of applied stress boundaries in the fracture aperture evolution.

Test category	σ_x, MPa	σ_y, MPa	σ_x / σ_y
Stress ratio	13	20	0.65
	19.5	30	0.65
	26	40	0.65
	39	60	0.65
Stress difference	20	20	1
	30	20	1.5
	40	20	2

The first test category in Table 2 indicates the schedule for the constant stress ratio. The applied boundary stresses are increasing proportionally, such that the stress ratio of σ_x / σ_y is kept constant at 0.65. Figure 18 shows the fracture aperture distribution at 180 days for the two sets of fractures with increasing stress σ_x from 13 MPa to 40 MPa. When the applied stresses are proportionally increasing, the initial apertures for the both fracture sets decrease uniformly, the response of normal closure is the dominant behavior by decreasing the initial aperture, resulting from the increased fracture normal stress.

Figure 19 illustrates the evolution of fracture permeability close to injector under the fixed stress ratio. As the applied boundary stresses are augmenting proportionally, the failure potential declines. Fracture closure is the dominating response due to the increased normal stress, resulting in reduction of fracture permeability.

Conversely, the deviatoric stress is elevated in the second set of cases by increasing the boundary stress σ_x, while holding the applied boundary stress σ_y constant at 20 MPa. In Figure 20, the fracture

permeability close to the injection well was selected to illustrate the development of permeability anisotropy when the stress difference is increasing. When the boundary stress σ_x is increasing from 13 MPa to 40 MPa, the anisotropy of fracture permeability emerges. Figure 3-21 points out the fracture aperture evolutions for the two sets of fractures with an increasing deviatoric stress. As the applied boundary stress in the major principal stress direction (E-W direction) increases, the fractures normal to the major principal stress direction (fracture set 2) close, while the fractures aligned sub-parallel to the major principal stress (fracture set 1) are nearly critically stressed and have the greatest propensity to slip, dilate. Therefore the apertures in set 1 fractures are larger than those in set 2 fractures.

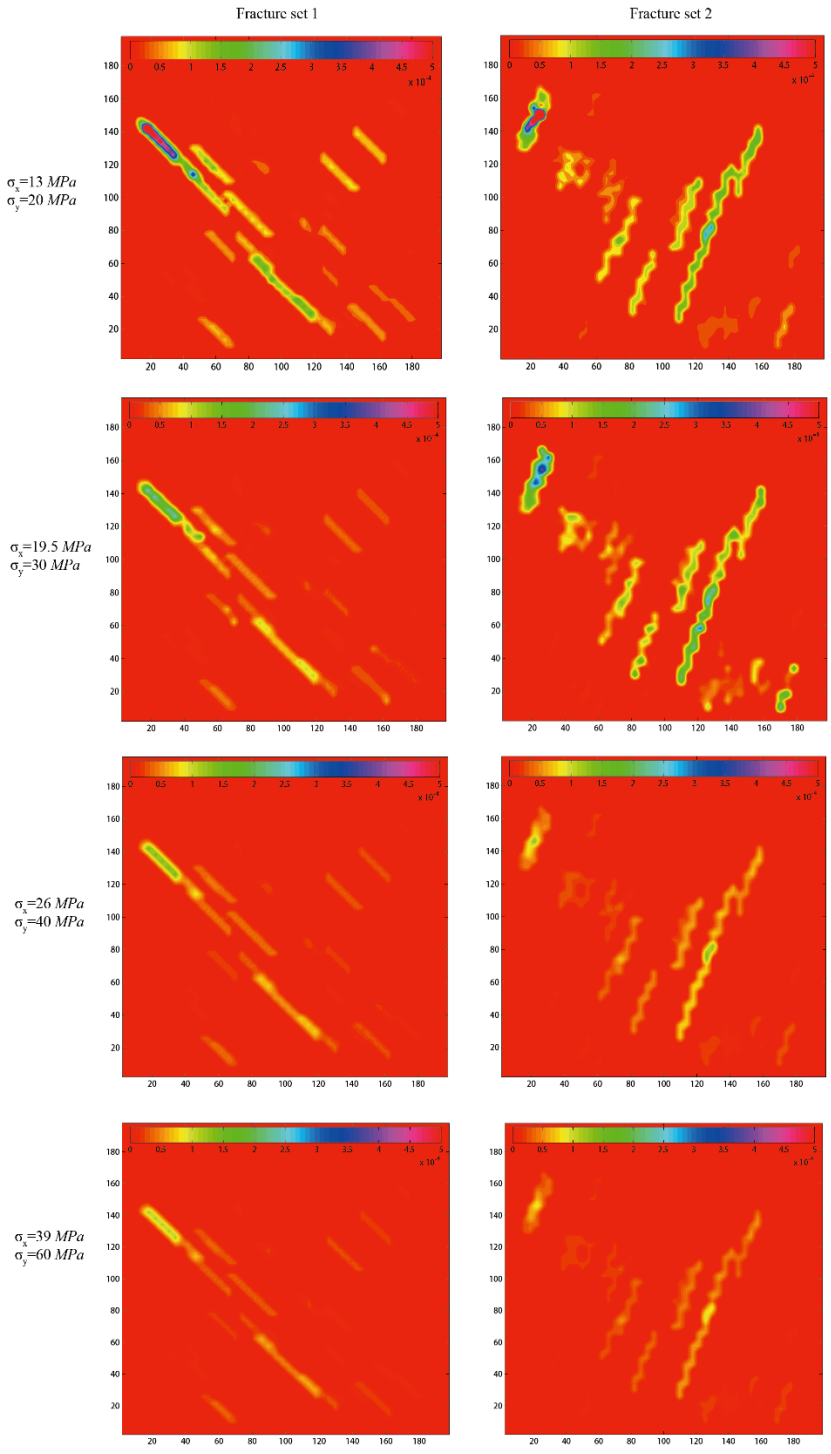

Figure 17 Fracture aperture distributions for the two sets of fractures under constant stress ratio at 180 days respectively.

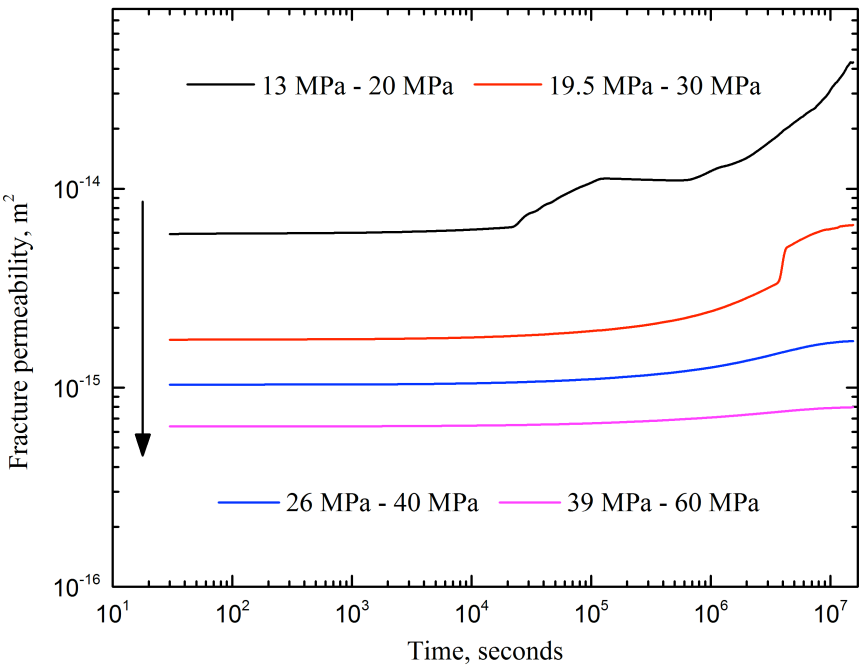

Figure 18 Evolutions of fracture permeability around the injector under the fixed stress ratio within 180 days.

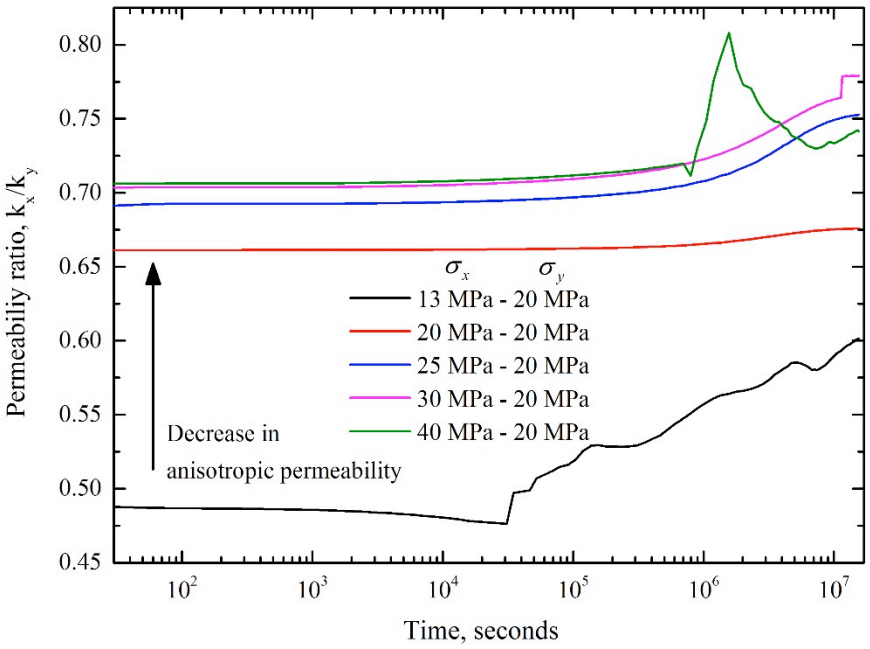

Figure 19 Evolution of fracture permeability ratio k_x over k_y under different stress difference.

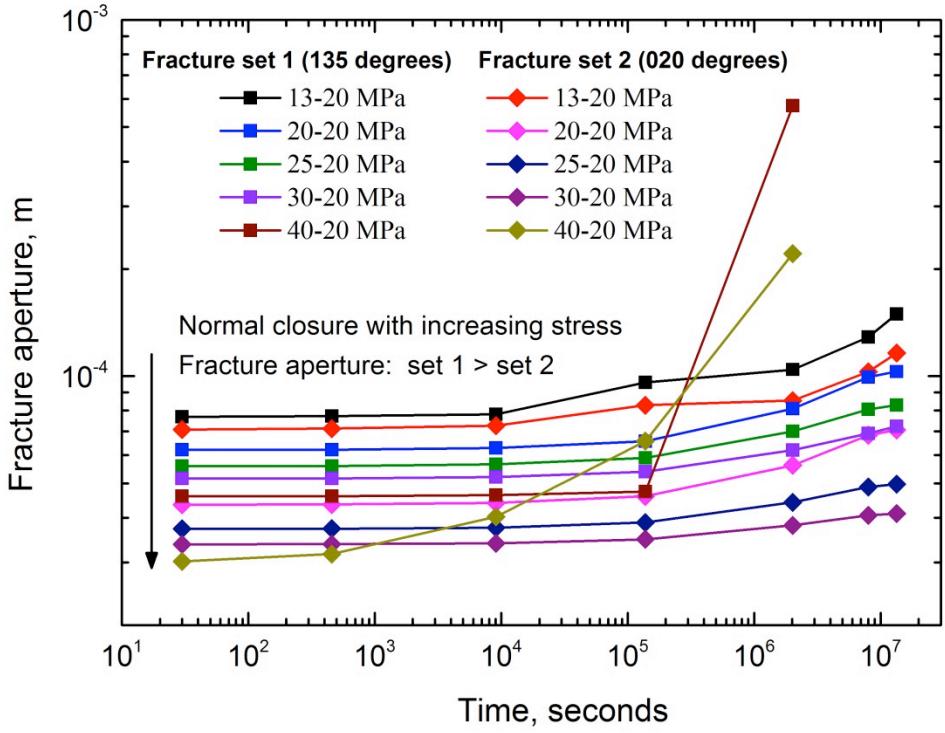

Figure 20 Evolution of fracture aperture for the two sets of fracture with increasing stress difference. Normal closure is the dominating response as deviatoric stress increased. Fracture aperture in set 1 is larger than the set 2.

8.5.3 Effect of fracture orientation

Fracture orientation plays an important role in determining the stress state around the fracture, which will influence the potential of fracture failure and permeability enhancement. In this study, the impact of fracture orientation is assessed by comparing the evolution of fracture permeability between the critically-stressed and non-critically stressed situations. Figure 22 shows the designated fracture network geometries striking at azimuths of 020-135 degrees (Figure 22a), 060-120 degrees (Figure 22b), and 015-165 degrees (Figure 22c) (with respect to the North direction). The trace length for each fracture in the three cases is maintained the same magnitude, but at different azimuths. The network is not well connected when the set of fractures are oriented sub-parallel to the N-S direction (Figure 22c). Figure 3-23 shows the distributions of fracture aperture at 180 days for different fracture orientations. Since the major principal stress is imposed in the N-S direction, the acting normal stress on the fractures aligned sub-parallel to the N-S direction (Figure 23c) is smaller than the fractures oriented normal to the N-S direction (Figure 3-23b), therefore it can be seen that the fracture aperture around the injector with 015-165 degrees (Figure 3-23c) are larger than the aperture in the case with 060-120 degrees (Figure 3-23b). However, since the fractures are not well connected in the third case with 015-165 degrees orientation, the

permeability enhancement is only focused around the injector zone, the fracture pressure build-up is high enough to trigger the local shear failure around the injection well.

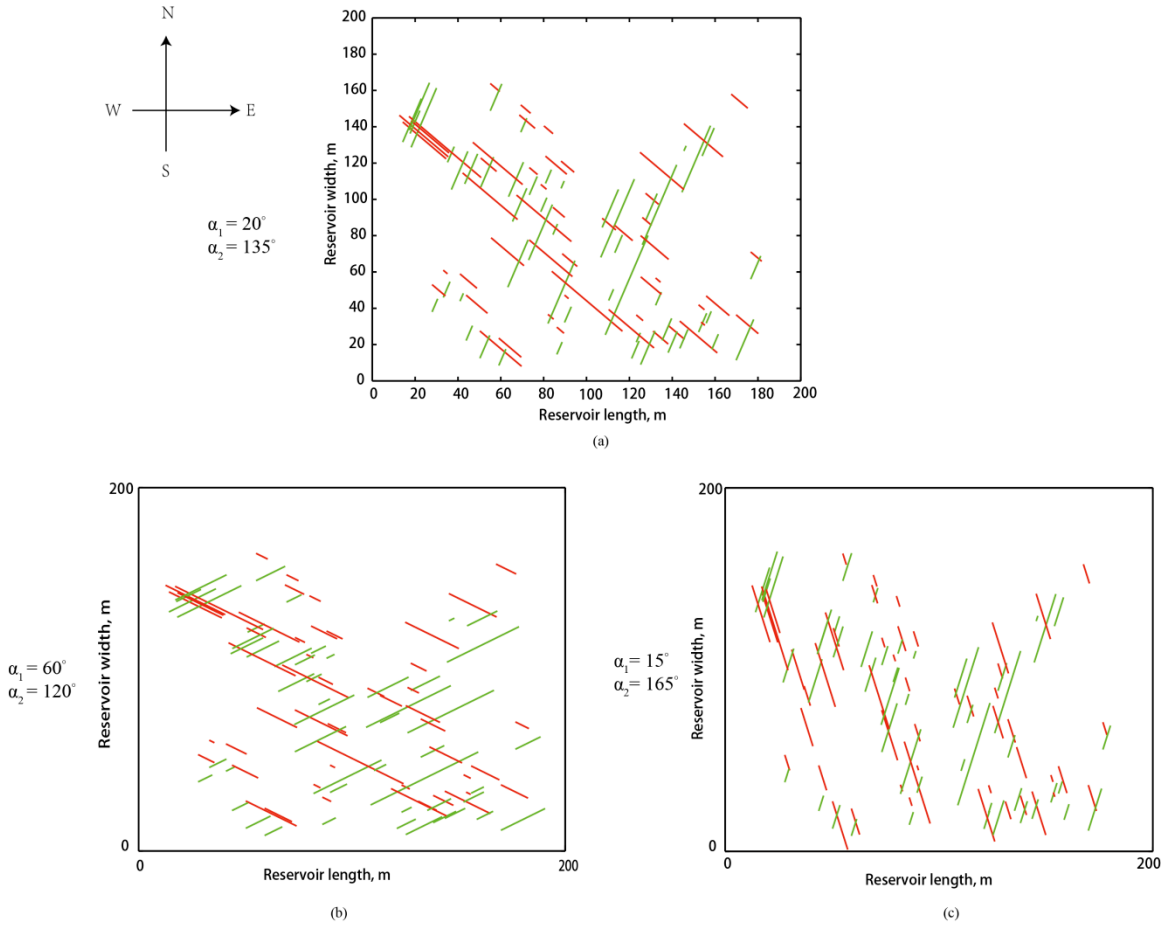

Figure 21 Contour of fracture networks under different orientations representing the fractures oriented at 020-135 degrees, 060-120 degrees, and 015-165 degrees with respect to the North separately.

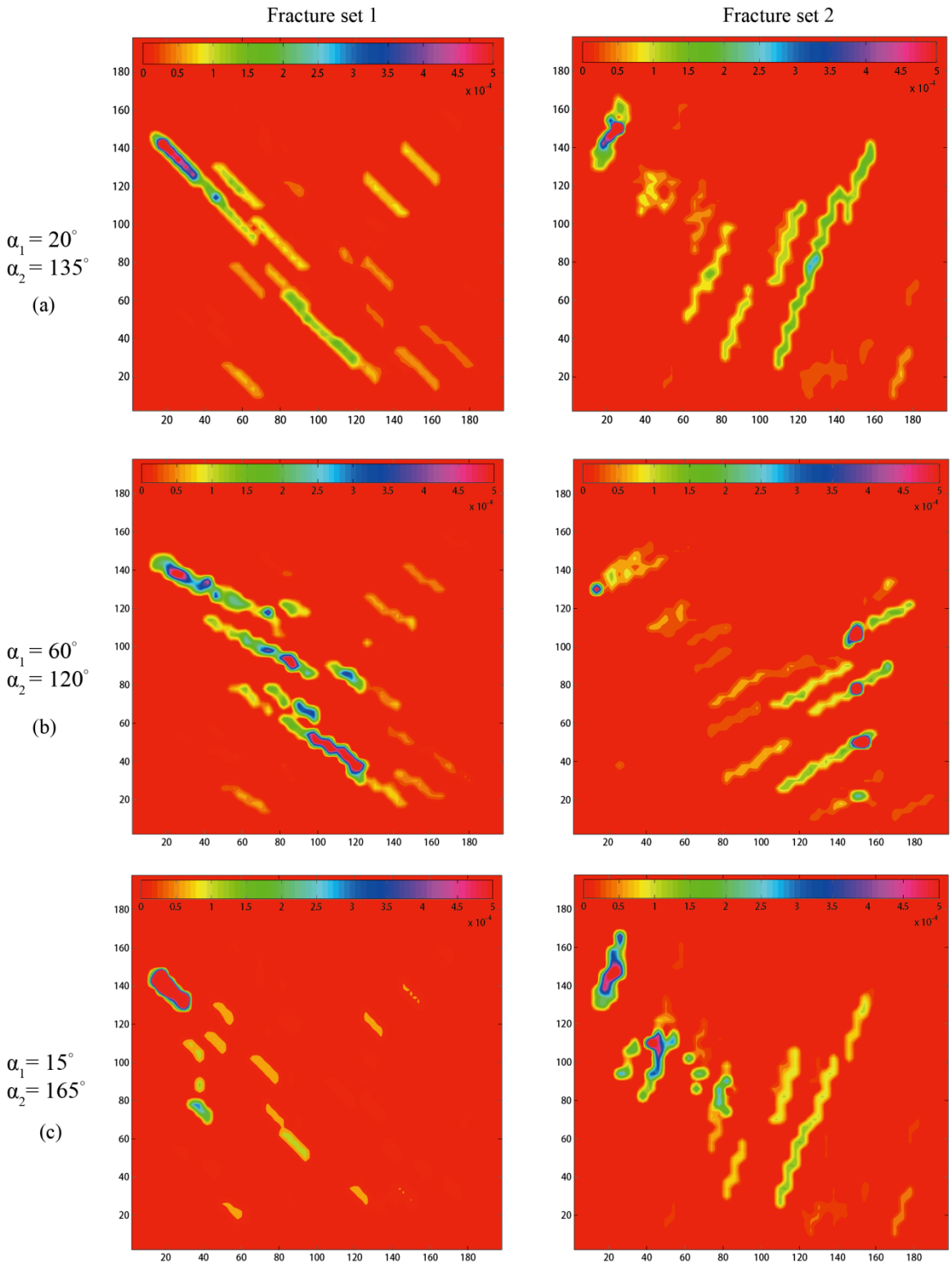

Figure 22 Fracture aperture comparisons at 180 days between different fracture orientations at 020-135 degrees, 060-120 degrees, and 015-165 degrees with respect to North.

8.6 Conclusion

This work presents the development of an equivalent continuum model to represent randomly distributed fractured masses, and investigating the evolution of stress-dependent permeability of fractured rock masses. The model incorporates both mechanical crack tensor and permeability tensor approaches to characterize the pre-existing fractures, accommodating the orientation and trace length of fractures. Compared to other discrete fracture models, the advantages of this model are primarily represented in simulating the large scale reservoir including the long term coupled thermal-hydraulic-mechanical response, and also without any dependence in the fracture geometry and gridding. The accuracy of simulator has been evaluated against other discrete fracture models by examining the evolution of fracture aperture and injection pressure during injection. The simulator is shown capable of predicting the evolution of the fracture normal aperture, including the state of fracture normal closure, shear dilation, and out of contact displacements under tensile loading.

The influence of stress state (mean and deviatoric) and fracture orientation on the evolution of fracture permeability are assessed by applying the model to a discrete fracture network. Normal closure of the fracture system is the dominant mechanism in reducing fracture permeability, where the mean stress is augmented at a constant stress obliquity ratio of 0.65. Conversely, for varied stress obliquity (0.65 – 2) shear deformation is the principal mechanism resulting in an increase in permeability. Fractures aligned sub-parallel to the major principal stress are near critically-stressed and have the greatest propensity to slip, dilate and increase permeability. Those fractures normal to direction of the principal stress are subjected to the increasing normal stress, and reduce the permeability. These mechanisms increase the anisotropy of permeability in the rock mass. Furthermore, as the network becomes progressively more sparse, the loss of connectivity results in a reduction in permeability with zones of elevated pressure locked close to the injector – with the potential for elevated levels of induced seismicity.

Acknowledgement

This work is a partial result of support from the US Department of Energy under project DOE-DE-343 EE0002761. This support is gratefully acknowledged.

8.7 References

Baghbanan, A., and L. Jing (2007), Hydraulic properties of fractured rock masses with correlated fracture length and aperture, *International Journal of Rock Mechanics and Mining Sciences*, *44*(5), 704-719, doi:http://dx.doi.org/10.1016/j.ijrmms.2006.11.001.

Bandis, S. C., A. C. Lumsden, and N. R. Barton (1983), Fundamentals of rock joint deformation, *International Journal of Rock Mechanics and Mining Sciences & Geomechanics Abstracts*, *20*(6), 249-268, doi:http://dx.doi.org/10.1016/0148-9062(83)90595-8.

Barton, N., and V. Choubey (1977), The shear strength of rock joints in theory and practice, *Rock Mechanics*, *10*(1-2), 1-54, doi:10.1007/BF01261801.

Bear, J. (1993), 1 - Modeling Flow and Contaminant Transport in Fractured Rocks, in *Flow and Contaminant Transport in Fractured Rock*, edited by J. B.-F. T. d. Marsily, pp. 1-37, Academic Press, Oxford, doi:http://dx.doi.org/10.1016/B978-0-12-083980-3.50005-X.

Chen, M., M. Bai, and J. C. Roegiers (1999), Permeability Tensors of Anisotropic Fracture Networks, *Mathematical Geology*, *31*(4), 335-373, doi:10.1023/A:1007534523363.

Chin, L. Y., Raghavan, R., & Thomas, L. K. (2000). Fully Coupled Geomechanics and Fluid-Flow Analysis of Wells With Stress-Dependent Permeability. Society of Petroleum Engineers. doi:10.2118/58968-PA

Crouch, S. L., and A. M. Starfield (1991), *Bound Elem Solid Mechanics*, Taylor & Francis.

de Dreuzy, J.-R., P. Davy, and O. Bour (2001), Hydraulic properties of two-dimensional random fracture networks following a power law length distribution: 2. Permeability of networks based on lognormal distribution of apertures, *Water Resources Research*, *37*(8), 2079-2095, doi:10.1029/2001WR900010.

Dieterich, J. H. (1992), Earthquake nucleation on faults with rate-and state-dependent strength, *Tectonophysics*, *211*(1–4), 115-134, doi:http://dx.doi.org/10.1016/0040-1951(92)90055-B.

Elsworth, D. (1986), A hybrid boundary element-finite element analysis procedure for fluid flow simulation in fractured rock masses, *International Journal for Numerical and Analytical Methods in Geomechanics*, *10*(6), 569-584, doi:10.1002/nag.1610100603.

Fu, P., S. M. Johnson, and C. R. Carrigan (2013), An explicitly coupled hydro-geomechanical model for simulating hydraulic fracturing in arbitrary discrete fracture networks, *International Journal for Numerical and Analytical Methods in Geomechanics*, *37*(14), 2278-2300, doi:10.1002/nag.2135.

Gan, Q., and D. Elsworth (2014a), Analysis of fluid injection-induced fault reactivation and seismic slip in geothermal reservoirs, *Journal of Geophysical Research: Solid Earth*, *119*(4), 2013JB010679, doi:10.1002/2013JB010679.

Gan, Q., and D. Elsworth (2014b), Thermal drawdown and late-stage seismic-slip fault reactivation in enhanced geothermal reservoirs, *Journal of Geophysical Research: Solid Earth*, *119*(12), 2014JB011323, doi:10.1002/2014JB011323.

Ghassemi, A., and Q. Zhang (2006), Porothermoelastic Analysis of the Response of a Stationary Crack Using the Displacement Discontinuity Method, *Journal of Engineering Mechanics*, *132*(1), 26-33, doi:doi:10.1061/(ASCE)0733-9399(2006)132:1(26).

Goodman, R.E., R.L. Taylor, and T.L. Brekke (1968), A model for the mechanics of jointed rock *J. Soil Mech. Fdns Div. Am. Soc. civ. Engrs*, 94 (1968), pp. 637–660.

Heuze, F. E., Shaffer, R. J., Ingraffea, A. R., & Nilson, R. H. (1990). Propagation of fluid-driven fractures in jointed rock. Part 1—development and validation of methods of analysis. In *International Journal of Rock Mechanics and Mining Sciences & Geomechanics Abstracts* (Vol. 27, No. 4, pp. 243-254). Pergamon.

Itasca Consulting Group, Inc. (2000) *FLAC3D – Fast Lagrangian Analysis of Continua in Three-Dimensions, Ver. 5.0*. Minneapolis: Itasca.

Izadi, G., Elsworth, D. (2014), Reservoir stimulation and induced seismicity: roles of fluid pressure and thermal transients on reactivated fractured networks. *Geothermics* 51, 368–379.

Kelkar, S., M. McClure, and A. Ghassemi (2015), Influence of Fracture Shearing on Fluid Flow and Thermal Behavior of an EGS Reservoir - Geothermal Code Comparison Study, paper presented at

Fourtieth Workshop on Geothermal Reservoir Engineering, Stanford University, Stanford, California, Jauary 26-28, 2015.

Kolditz, O., & Clauser, C. (1998). Numerical simulation of flow and heat transfer in fractured crystalline rocks: application to the hot dry rock site in Rosemanowes (UK). *Geothermics*, *27*(1), 1-23.

Kohl, T., Evansi, K. F., Hopkirk, R. J., & Rybach, L. (1995). Coupled hydraulic, thermal and mechanical considerations for the simulation of hot dry rock reservoirs. *Geothermics*, *24*(3), 345-359.

McClure, M., and R. N. Horne (2013), *Discrete fracture network modeling of hydraulic stimulation: Coupling flow and geomechanics*, Springer Science & Business Media.

McTigue, D. F. (1990), Flow to a heated borehole in porous, thermoelastic rock: Analysis, *Water Resources Research*, *26*(8), 1763-1774, doi:10.1029/WR026i008p01763.

Min, K.-B., and L. Jing (2003), Numerical determination of the equivalent elastic compliance tensor for fractured rock masses using the distinct element method, *International Journal of Rock Mechanics and Mining Sciences*, *40*(6), 795-816, doi:http://dx.doi.org/10.1016/S1365-1609(03)00038-8.

Min, K.-B., J. Rutqvist, C.-F. Tsang, and L. Jing (2004), Stress-dependent permeability of fractured rock masses: a numerical study, *International Journal of Rock Mechanics and Mining Sciences*, *41*(7), 1191-1210, doi:http://dx.doi.org/10.1016/j.ijrmms.2004.05.005.

Muralidharan, V., D. Chakravarthy, E. Putra, and D. S. Schechter Investigating Fracture Aperture Distributions Under Various Stress Conditions Using X-Ray CT Scanner, edited, Petroleum Society of Canada, doi:10.2118/2004-230.

Noorishad, J., M. S. Ayatollahi, and P. A. Witherspoon (1982), A finite-element method for coupled stress and fluid flow analysis in fractured rock masses, *International Journal of Rock Mechanics and Mining Sciences & Geomechanics Abstracts*, *19*(4), 185-193, doi:http://dx.doi.org/10.1016/0148-9062(82)90888-9.

Oda, M. (1986), An equivalent continuum model for coupled stress and fluid flow analysis in jointed rock masses, *Water Resources Research*, *22*(13), 1845-1856, doi:10.1029/WR022i013p01845.

Olson, J. E. (2003), Sublinear scaling of fracture aperture versus length: An exception or the rule?, *Journal of Geophysical Research: Solid Earth*, *108*(B9), 2413, doi:10.1029/2001JB000419.

Pine, R. J., & Cundall, P. A. (1985). Applications of the fluid-rock interaction program (FRIP) to the modelling of hot dry rock geothermal energy systems. In *Proc. Int. Symp. on Fundamentals of Rock Joints* (pp. 293-302). Centek.

Rutqvist, J., C. Leung, A. Hoch, Y. Wang, and Z. Wang (2013), Linked multicontinuum and crack tensor approach for modeling of coupled geomechanics, fluid flow and transport in fractured rock, *Journal of Rock Mechanics and Geotechnical Engineering*, *5*(1), 18-31, doi:http://dx.doi.org/10.1016/j.jrmge.2012.08.001.

Rutqvist, J., & Stephansson, O. (2003). The role of hydromechanical coupling in fractured rock engineering. *Hydrogeology Journal*, *11*(1), 7-40.

Taron, J., and D. Elsworth (2010), Coupled mechanical and chemical processes in engineered geothermal reservoirs with dynamic permeability, *International Journal of Rock Mechanics and Mining Sciences*, *47*(8), 1339-1348, doi:http://dx.doi.org/10.1016/j.ijrmms.2010.08.021.

Taron, J., D. Elsworth, and K.-B. Min (2009), Numerical simulation of thermal-hydrologic-mechanical-chemical processes in deformable, fractured porous media, *International Journal of Rock Mechanics and Mining Sciences*, *46*(5), 842-854, doi:http://dx.doi.org/10.1016/j.ijrmms.2009.01.008.

Tsang, C.-F., and I. Neretnieks (1998), Flow channeling in heterogeneous fractured rocks, *Reviews of Geophysics*, *36*(2), 275-298, doi:10.1029/97RG03319.

Zhang, X., and D. Sanderson (1994), Fractal Structure and Deformation of Fractured Rock Masses, in *Fractals and Dynamic Systems in Geoscience*, edited by J. Kruhl, pp. 37-52, Springer Berlin Heidelberg, doi:10.1007/978-3-662-07304-9_3.

9 CHAPTER 9: PRODUCTION OPTIMIZATION IN FRACTURED GEOTHERMAL RESERVOIR BY COUPLED DISCRETE FRACTURE NETWORK MODELING

Abstract

In this work, a stimulation then heat production optimization strategy is presented for prototypical EGS geothermal reservoirs by comparing conventional stimulation-then-production scenarios against revised stimulation schedules. A generic reservoir is selected with an initial permeability in the range of 10^{-17} to 10^{-16} m^2, fracture density of ~0.09 m^{-1} and fractures oriented such that either none, one, or both sets of fractures are critically stressed. For a given reservoir with a pre-existing fracture network, two parallel manifolds are stimulated that are analogous to horizontal wells that allow a uniform sweep of fluids between the zones. The enhanced connectivity that develops between the injection zone and the production zone significantly enhances the heat sweep efficiency, while simultaneously increasing the fluid flux rate at the production well. For a 10m deep section of reservoir the resulting electric power production reaches a maximum of 14.5 MWe and is maintained over 10 years yielding cumulative energy recoveries that are a factor of 1.9 higher than for standard stimulation. Sensitivity analyses for varied fracture orientations and stimulation directions reveal that the direction of such manifolds used in the stimulation should be aligned closely with the orientation of the major principal stress, in order to create the maximum connectivity. When the fractures are less prone to fail, the output electric power is reduced by a decrease in the fluid flux rate to the production well. The short circuiting response during heat extraction is significant for the low fracture density condition, which can result early thermal breakthrough in the production well.

9.1 Introduction

Enhanced geothermal reservoirs (EGS) have been shown to be a viable resource for the recovery of thermal energy. However, due to their intrinsic characteristic of low permeability and porosity they have proved intractable in developing sufficient fluid throughput by stimulation. The principal challenge has been in developing adequate permeability in the reservoir that also retains sufficient heat transfer area [*Tester et al.*, 2006].

Numerical simulation is a reliable approach to investigate coupled multi-physics processes (Thermal-Hydraulic-Mechanical) and to better understand the fundamental mechanisms and feedbacks that occur in geothermal reservoirs. This is particularly important due to the intense pressure-sensitivity of fractures in the coupling of permeability and heat transfer area [*Taron and Elsworth*, 2009]. From previous studies, thermal quenching and resulting contractile strains may substantially unload the reservoir and increase both fracture aperture and permeability via creep or by induced seismicity and fault reactivation [*Gan and*

Elsworth, 2014a; b; *Segall and Fitzgerald*, 1998]. This may occur close-in to the wellbore at early times and at later times in the far-field when larger features and faults may be affected [*Elsworth et al.*, 2010; *Taron and Elsworth*, 2010a]. For discretely fractured rock masses, there are two major approaches to simulate the influence of randomly distributed fractures. One approach is as an equivalent continuum [*Taron and Elsworth*, 2010b] where the aggregate response is represented and an alternative is a discontinuum approach [*Ghassemi and Zhang*, 2006; *McClure and Horne*, 2013; *Min and Jing*, 2003; *Pine and Cundall*, 1985] where individual fractures are discretized and their individual response followed. Continuum methods have the advantage of effectively simulating behavior at large (field) scale and for the long-term due to the lower computational requirements. The behavior of fractures is implicitly included in the equivalent constitutive models for both deformation and transport. The central effort in developing the equivalent continuum approach is the incorporation of crack tensor theory [*Oda*, 1986]. This is different in behavior from the application of discrete fracture network models (DFNs) where the behavior of individual fractures is explicitly represented in the macroscopic response. In previous work [*Gan and Elsworth*, 2015], an equivalent continuum T-H-M coupled simulator TF_FLAC^{3D} has been developed to investigate the evolution of stress-dependent fracture permeability in equivalent DFNs. The benefits of this continuum simulator are in mechanically representing the fractured mass by adopting a crack tensor, but also in simulating the heat and mass transport by advection and in the long term, albeit for continuum problems.

Strategies for optimizing production (high flowrate, high temperature and long duration) in geothermal reservoirs have been explored [*Marcou*, 1985; *Akin et al.*, 2010; *Pham*, 2010] by identifying the impact of various parameters on thermal extraction, and in proposing strategies to enhance thermal power generation. The rate of heat energy production is defined by the effluent water temperature and flow rate from the production well. The ideal condition is to maintain both a high flux rate and high temperature for as long as possible, while simultaneously delaying thermal breakthrough to the production well. The reservoir volume (and temperature) is the key parameter that determines the cumulative magnitude of energy production over the entire reservoir life [*Sanyal et al.*, 2005]. This reservoir volume is in turn influenced by the well separation distance as the reservoir volume scales with the cube of this separation for a typical doublet injection-recovery system [*Vörös et al.*, 2007]. In addition to reservoir volume and geometry, the characteristics of the injected fluid also exert some influence. Water density changes little in non-boiling systems but water viscosity may change by a factor of two or three with a change in temperature of 100-200 C and may therefore exert a direct impact on thermal production [*Watanabe et al.*, 2000]. In addition to the ultimate recovery of thermal energy from the system, the rate of recovery is also important.

Dimensionless solutions are useful in defining the rate limiting processes and dependent properties for energy recovery. These simplified models capture the essence of the conductive heat supply to the convecting heat transfer fluid and define this process as the rate limiting step [*Elsworth*, 1989; 1990; *Gringarten and Witherspoon*, 1973; *Gringarten et al.*, 1975; *Pruess and Wu*, 1993; *Shaik et al.*, 2011]. The dimensionless parameter controlling the effectiveness of thermal recovery scales with the product of mass flow rate and fracture spacing to the second power [*Gan and Elsworth*, 2014] thus defining the principal desire for small spacing between fractures in draining the heat from the fracture-bounded matrix blocks.

This principal objective to circulate fluids at low rate per unit volume of the reservoir but to access small spacing between fractures is the principal requirement of a successful EGS system. However, fracture spacing, if activating and accessing pre-existing fracture networks is not a controllable parameter. The one controlling measure in production is to establish a uniform fluid-, and thereby thermal-sweep, of the reservoir. The divergent flow field close to the point-source injectors in doublet systems is not effective in providing a uniform sweep, but flow from parallel wells or from stimulated parallel wells offers a better prospect of establishing a uniform flow field. In the oil and gas industry, the drilling and stimulation of parallel, and typically horizontal, wells has been developed to considerable success for unconventional reservoirs, over the past decade. In this work, a new stimulation strategy is explored that comprises the development of two parallel and high permeability manifolds each as a separate injection zone and production zone. It is anticipated that this stimulation schedule will generate analogous results to the drilling of two horizontal wells and therefore in increasing the flow sweep efficiency from the injection zone towards the production zone.

9.2 Model setup

We explore various stimulation strategies to determine their effect on both the magnitude and longevity of thermal recovery rates for a given reservoir with a defined pre-existing fracture network. For these reservoirs, the fracture permeability of the network evolves subject to the influence of the change in stress state, including normal closure, shear dilation, and the potential for fracture walls to lose contact. Coupled thermal effects exert a strong effect in changing the fracture normal stress with a concomitant influence on both fracture-normal dilation and on shear-slip-induced dilation and in ultimately modifying permeability. This work includes both the influence of an initial stimulation followed by a production phase – throughout which permeability evolves in response to the evolving effective stress regime. In particular, we explore the potential that the stimulation may develop hydraulically-interconnected manifolds along the axis of a supposed horizontal well (E-W direction) that in turn may be used to develop a uniform flow field across the reservoir (in the N-S direction) – to a second parallel manifold

also aligned in the E-W direction. Another stimulation strategy is to develop permeable manifolds in the N-S direction by connecting the drilling wells in N-S direction. These two behaviors will be different due to the directional characteristics of both the stress regime and the topology of the fracture network that is overprinted on the well pattern. The influence of fracture stimulation direction is illustrated through a comparison of the different development scenarios.

9.2.1 Reservoir Model

A reservoir containing a discrete fracture network is created using an updated discrete fracture network model using the equivalent continuum simulator TF_FLAC^{3D}. Figure 4-1a shows one scenario of the resulting fracture network in a reservoir $1500m \times 1500m \times 10m$. The initial pressure distribution is uniform at 10 MPa, and the initial homogenous rock temperature is 250 C. The minor principal stress is imposed at 19.5 MPa in the N-S direction, while the major principal stress is 30 MPa in the E-W direction. The fractures comprising the network are sub-vertical and are oriented (strike) at 45 degrees and 120 degrees with respect to the North direction, respectively. There are 1000 fractures for each set. The length of fractures follows a lognormal distribution with a mean length of 80 m (Figure 4-2) [*de Dreuzy et al.*, 2001]. A power law is implemented to correlate fracture trace length l with the fracture aperture b_i [*Olson*, 2003] as,

$$b_i = 1.25\times10^{-5} * l^{0.8} \qquad 1$$

The fracture density ρ_f $(1/m)$ is expressed as the ratio of fracture surface area to the volume of matrix rock, as,

$$\rho_f = \frac{\sum A_f^i}{V_{rock}}$$

where A_f^i is the surface area of the i_{th} fracture, and V_{rock} is the total rock volume. The fracture density in this particular case is equal to 0.09 m^{-1}.

The geometries of the pre-existing discrete fracture networks are presented in Figure 1. It is assumed that the DFN consists of two fracture sets. The initial permeability of the fracture network is of the order of 10^{-17} to 10^{-16} m^2. The fractures in each fracture set are each oriented at a uniform angle. Two fracture geometries are chosen. The first is where both sets of fractures are favorably oriented for slip and strike 045° and 120° clockwise from the North (Figure 1a) [*Odling, et al*, 1999; *Riahi and Damjanac*, 2013]. The second geometry is where one set is less favorably aligned for slip where the fractures strike 020° and 135° with respect to the North direction (Figure 1b). The impact of fracture orientations on thermal

transport and heat recovery is assessed through the comparison between these two fracture geometries. The distributions of fracture lengths for both scenarios are the same, leaving fracture orientation relative to the stress field as the only significant variable.

Table 4-1 Rock and fracture properties used in the simulation.

Parameter (unit)	Magnitude
Shear modulus, G (*GPa*)	15
Poisson's ratio, ν	0.25
Undrained Poisson's ratio, $\nu_{undrain}$	0.33
Matrix permeability, k_m (m^2)	1.0×10^{-18}
Fracture permeability, k_f (m^2)	$10^{-17}\sim10^{-16}$
Matrix porosity, ϕ_m	0.01
Fracture porosity, ϕ_f	0.1
Biot coefficient, α	0.88
Water viscosity, μ, (*Pa.s*)	3.547×10^{-4}
Fluid compressibility, (MPa^{-1})	4.2×10^{-4}
Thermal expansion coefficient of solid, α_s, (K^{-1})	2.4×10^{-5}
Thermal diffusivity of intact porous rock, c^T, (m^2/s)	1.1×10^{-6}
Heat capacity of fluid, c_w ($Jkg^{-1}K^{-1}$)	4200
Initial reservoir temperature, T_0, (*K*)	523
Injection water temperature, T_{inj}, (*K*)	323
Initial joint normal stiffness, k_n, (*GPa/m*)	0.5
Initial joint shear stiffness, k_s, (*GPa/m*)	50
In-situ stress (*MPa*) – E-W direction	30

In-situ stress (MPa) – N-S direction	19.5
Initial reservoir pore pressure, p_0, (MPa)	10
Injection pressure, p_{inj}, (MPa)	15
Fracture friction angle, (degrees)	35°
Fracture dilation angle, (degrees)	3°
Fracture cohesion, C, (MPa)	0
Production pressure, p_{pro}, (MPa)	7

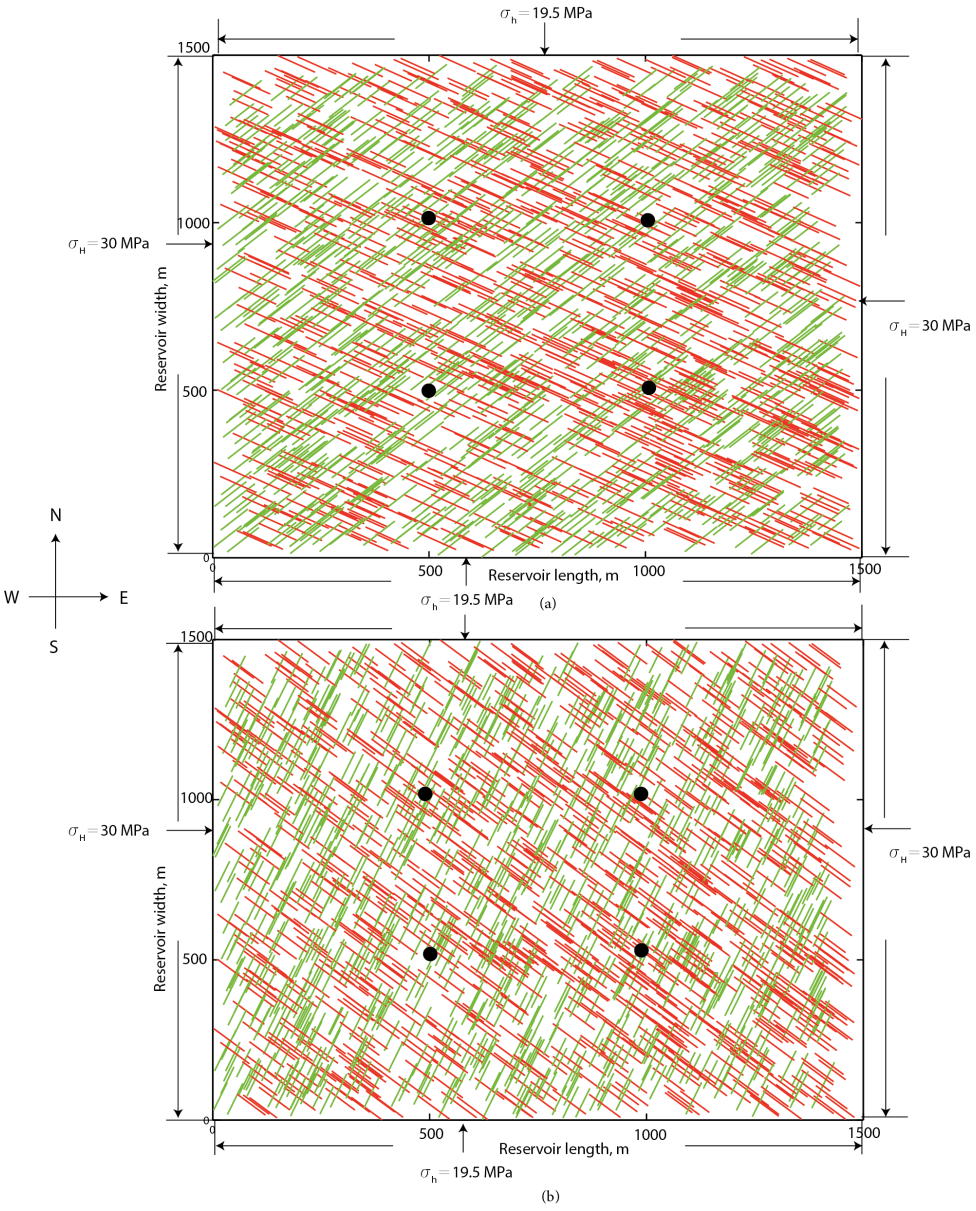

Figure 1 (a) Discrete fracture network distribution with orientations striking 045 and 120 degrees with respect to the North, (b) and a second discrete fracture network distribution with orientations at 020 and 135 degrees with respect to the North. These two orientations are chosen to evaluate the impact of fracture network geometry on fluid flow and heat transport.

9.2.2 Stimulation – production case

The influence of stimulation strategy is investigated by stimulating the reservoir in multiple different modalities. Figure 2 schematically shows the two predefined stimulation scenarios: the first produces two parallel manifolds in the E-W direction (Figure 2a), while a second alternative is to develop two parallel manifolds in the N-S direction (Figure 2b) respectively. These parallel manifolds (Figure 2a) are then

used to promote a uniform flow regime across the reservoir. In this there are four potential well sites at points A (500, 1000), B (1000, 1000), C (500, 500), D (1000, 500). In terms of stimulation in the E-W direction, only the two injection wells at A and B are initially stimulated at 20 kg/s for 10 hours [*Darnet et al.* 2006]. Then the other two wells at C and D are stimulated, again at 20 kg/s for 10 hours, while the injection wells at A and B are shut-in. The developed manifolds result in enhancing the fracture permeability horizontally between A-and-B and C-and-D, separately. Similarly, the N-S stimulation scenario is designed to first develop a manifold between injection wells at B-D with the same constant injection rate of 20 kg/s for 10 hours, and then to switch to inject at same rate into A and C for 10 hours (Figure 2b). Then the eventual production scenario is designed to place two injectors at wells C and D at a constant pressure of 15 MPa, while the producers are located at A and B points at a constant pressure of 7 MPa (Figure 2c). In either instance, the pressure drop across the reservoir is 8 MPa.

Table 2 Case studies designed in the study for different stimulation – production scenarios

Case No.	Stimulation Scenario	Fracture Orientation, degree	Fracture Friction Angle, degree
1	Stimulation (E-W)	020 - 135	35 - 35
2	No Stimulation	020 - 135	35 - 35
3	Stimulation (E-W)	045 - 120	35 - 35
4	Stimulation (E-W)	045 - 120	35 - 75

Table 2 indicates the separate cases explored in this study. The fracture properties in Case 2 are identical with those in Case 1, however there is no initial stimulation performed. The influence of stimulation is revealed by comparing Case 2 against Case 1. The results in Case 3 with a different fracture orientation of 045 –and- 120 degrees illustrates the impact of fracture orientation on heat recovery, as the fracture aperture is stress sensitive due to the variation of fracture orientation. Case 4 is implemented to examine the influence of fracture failure potential in the production of heat from the reservoir. In this, a 75 degree friction angle is set for the secondary set of fractures in Case 4 to evaluate the influence where one set of fractures has less potential to slip.

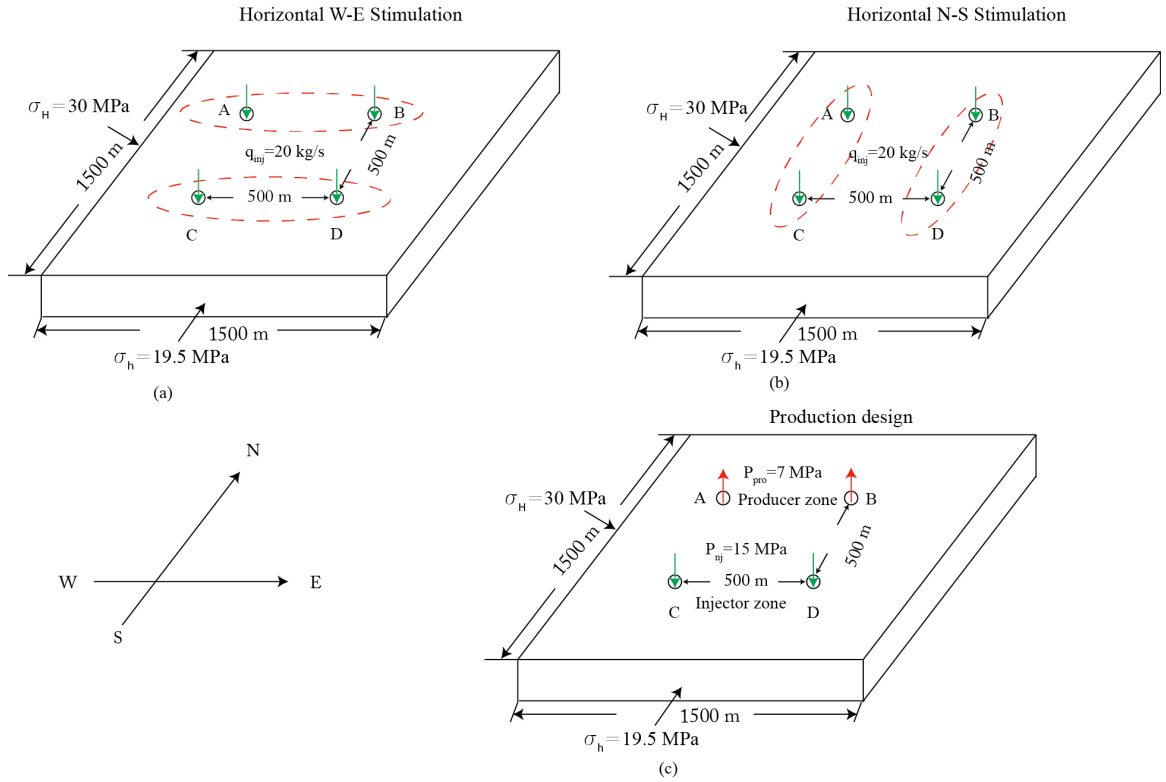

Figure 2 Schematic of injection and production design, (a) stimulate the producer zone and injector zone separately at 20 kg/s in W-E direction, (b) stimulate the reservoir in N-S direction at 20 kg/s, (c) the eventual production design including two injection well at C and D points at constant pressure 15 MPa, and two production wells at A and B points at constant pressure 7 MPa.

9.3 Results Discussion

The magnitude of permeability evolution and the resulting influence on heat energy extraction are the primary variables in this study. The potential optimization strategy is explored by investigating the relationship between the permeability enhancement and the resulting efficiency of heat recovery. The stimulation prior to the production phase develops parallel hydraulically interconnected manifolds along the horizontal axis of the injection wells in the E-W direction. This, in turn, will ultimately return a uniform flow sweep across the reservoir during the production stage, from the injector zone to the second parallel manifold in the producer zone in the N-S.

Figure 4-3 shows a comparison of the evolution in fracture permeability for the various fracture properties and stimulation scenarios. Figures 3(a) and 3(b) represent the initial fracture permeability distribution for the fractures oriented at 045 – 120 degrees and 020 – 135 degrees with respect to the North direction. The initial equivalent permeability of the fracture network is in the range of 10^{-17} to 10^{-16} m^2. The directional

fracture permeability is defined as a permeability tensor k_{ij} accommodating the orientation of the fractures and the explicit fracture volume intersecting an element block as,

$$k_{ij} = \sum^{nf} \frac{1}{12} \left(\frac{V_{ratio}}{b_{ini}} b^3 n_k^2 \delta_{ij} - \frac{V_{ratio}}{b_{ini}} b^3 n_i n_j \right)$$

where b_{ini} is the initial aperture of fracture, n is the unit normal to each fracture, V_{ratio} is the volumetric ratio of the truncated fracture over the element volume.

The fracture permeability distribution following the initial E-W stimulation for the fractures oriented at 045 – 120 degrees is presented in Figure 3(c). The two black dashed circles show the development of two permeable horizontal manifolds created in the northern and southern portions of the reservoir. The fracture permeability is significantly improved by ~3 orders magnitude following the stimulation, due to an effective increase in fracture aperture of the order of 10 times during the extensile loading. Since the fractures are oriented close to the E-W direction, the fracture permeability along this direction of stimulation is significantly enhanced (E-W direction).

The dashed black circle in Figure 3(d) shows the principal area where the fracture permeability is enhanced following stimulation for fracture orientations at 020 – 135 degrees. The red area representing the permeability-enhanced regime is oriented at an azimuth of ~060 degree. Moreover, the area of permeability enhancement is smaller than that in Figure 3(d), in this case since the fractures (020 – 135 degrees) are not favorably oriented along the stimulation direction (E-W).

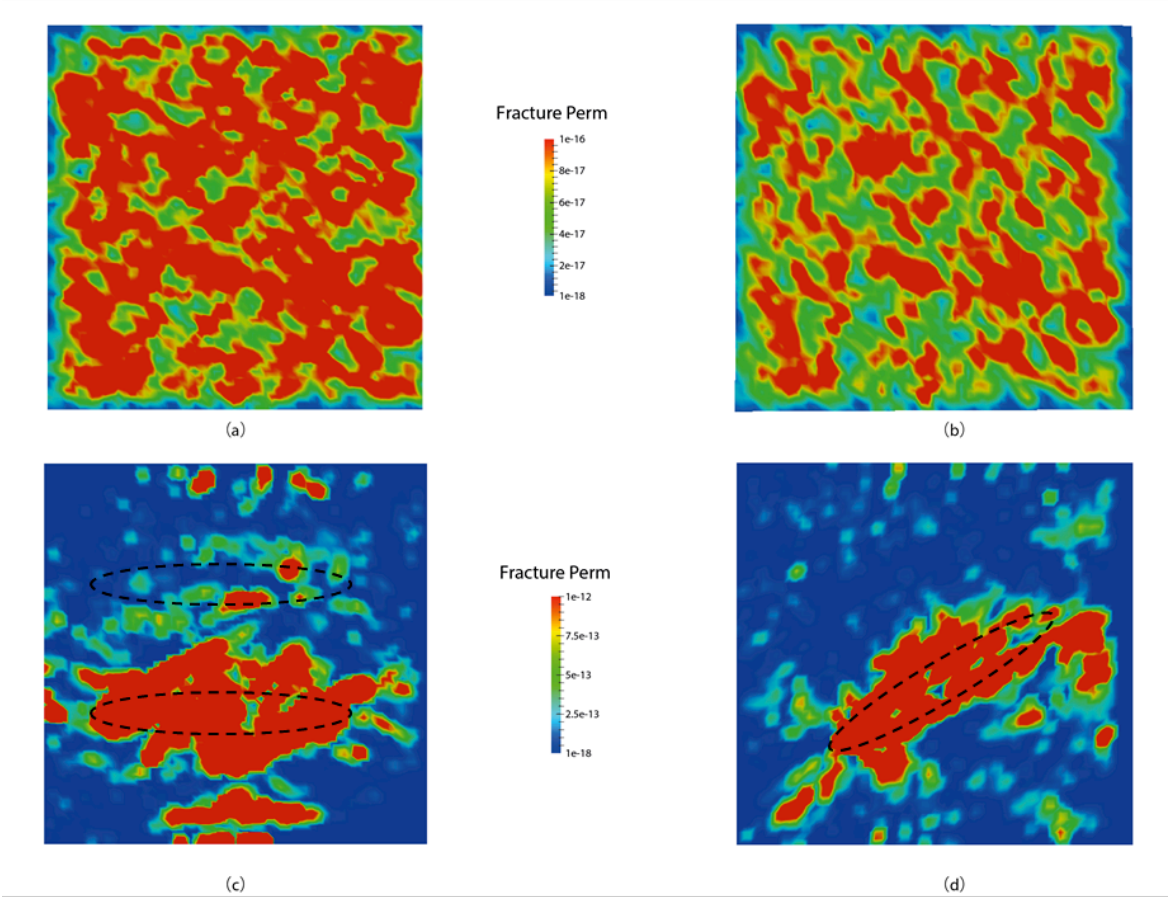

Figure 3 Contour plots of equivalent rock mass permeability evolution, (a) initial fracture permeability distribution for fractures oriented 045 – 120, (b) initial fracture permeability distribution for the scenario of fractures oriented 020 – 135, (c) development of two interconnected manifolds after the E-W stimulation for fractures oriented 045 – 120, (d) fracture permeability distribution after the E-W stimulation for fractures oriented 020 – 135 degrees.

The corresponding cases for the generation of power from the various stimulations are presented in Figure 4. The magnitude of instantaneous electric power generation W_h is calculated as a product of flow rate and the enthalpy of the water as [*Pruess*, 2006],

$$W_h = \sum_{i=1}^{i=2} \alpha q_{pro}^{i} (h_{pro} - h_{inj}) \qquad 2$$

where α is the heat utilization efficiency, assumed to be 0.45 in this calculation [*Sanyal and Butler*, 2005]. h_{pro} is the water enthalpy at the production well with the highest enthalpy in this work equals to

$1.08\times10^{6}\ j/kg$ (250 C), h_{inj} is the enthalpy of the injected cold water, which is equal to $2.0\times10^{5}\ j/kg$ and q^{i}_{pro} is the flow rate in the i_{th} production well (kg/s).

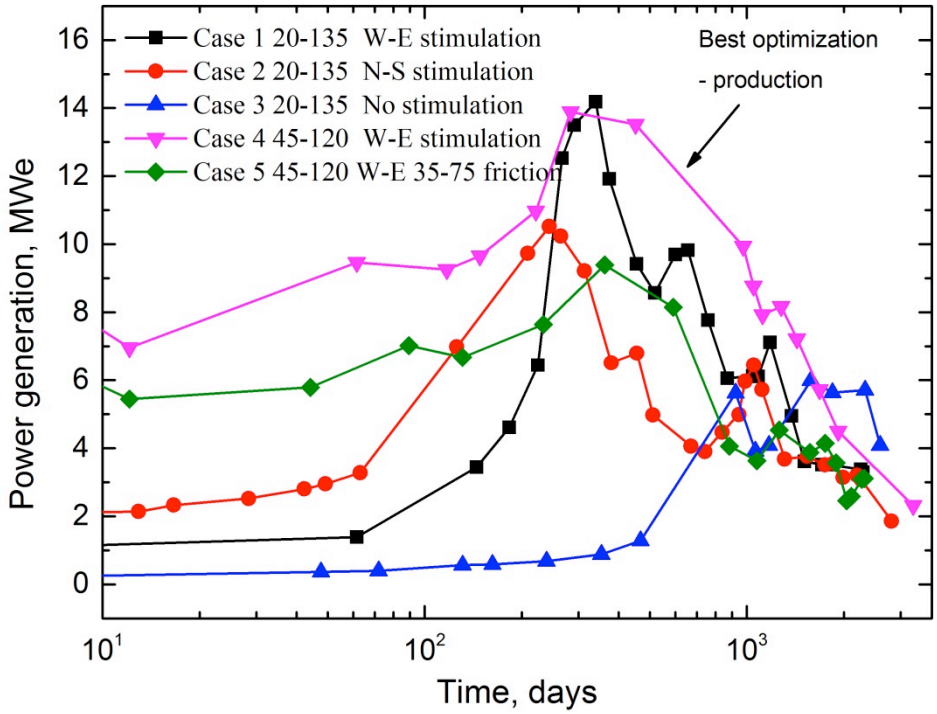

Figure 4 Comparison of total electric power generation from two production wells between all five cases. The magenta curve (Case 4) is for fractures oriented 045 – 120 degrees with E-W stimulation and this returns the highest electric power generation. Case 3 shown by the blue curve for fractures oriented 020 – 135 degrees but without stimulation indicates the lowest power generation.

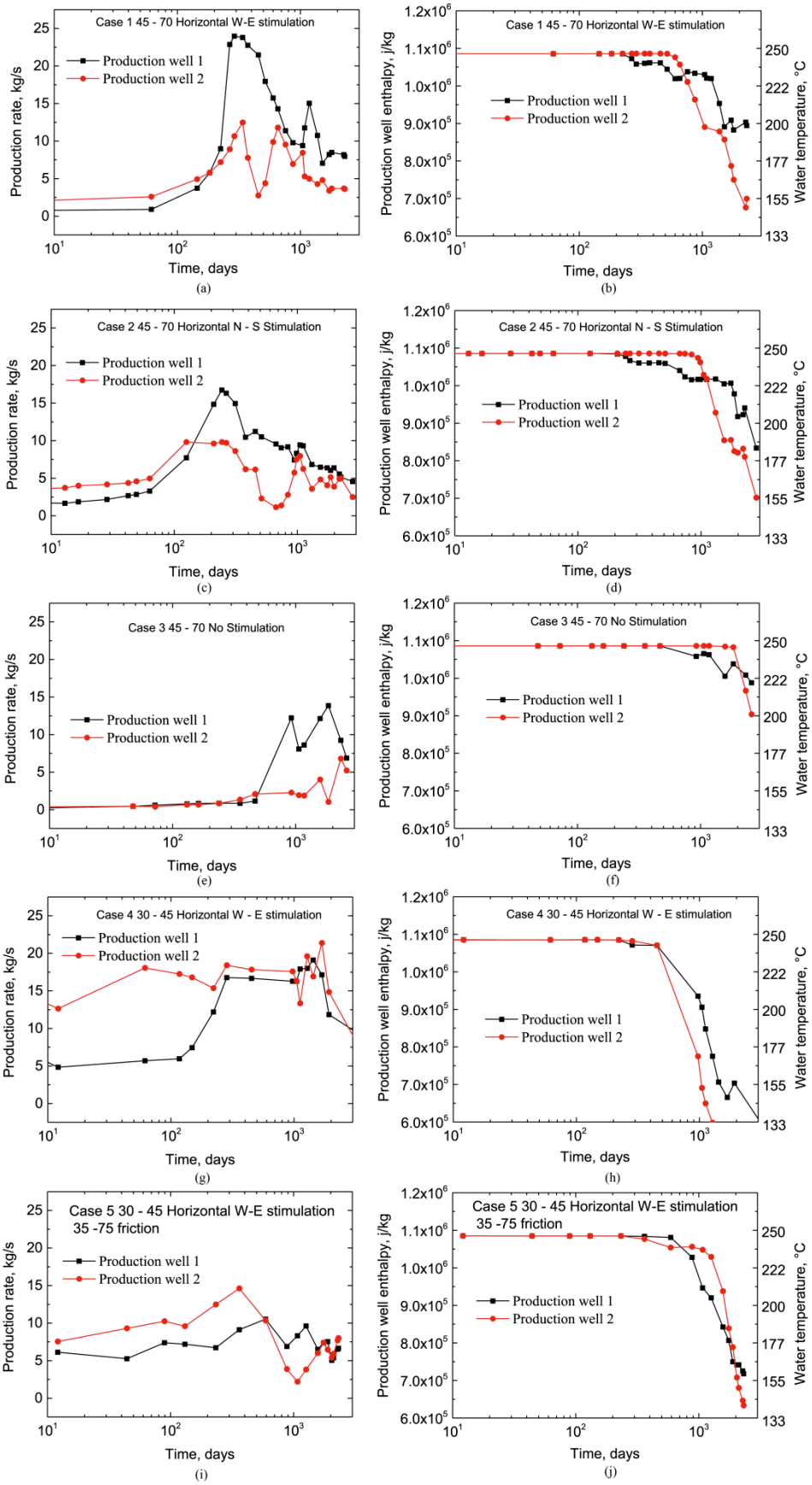
Case 1 45 - 70 Horizontal W-E stimulation
Production well 1
Production well 2
Production rate, kg/s
Time, days
(a)
Case 1 45 - 70 Horizontal W-E stimulation
Production well 1
Production well 2
Production well enthalpy, j/kg
Water temperature, °C
Time, days
(b)
Case 2 45 - 70 Horizontal N - S Stimulation
Production well 1
Production well 2
Production rate, kg/s
Time, days
(c)
Case 2 45 - 70 Horizontal N - S Stimulation
Production well 1
Production well 2
Production well enthalpy, j/kg
Water temperature, °C
Time, days
(d)
Case 3 45 - 70 No Stimulation
Production well 1
Production well 2
Production rate, kg/s
Time, days
(e)
Case 3 45 - 70 No Stimulation
Production well 1
Production well 2
Production well enthalpy, j/kg
Water temperature, °C
Time, days
(f)
Case 4 30 - 45 Horizontal W - E stimulation
Production well 1
Production well 2
Production rate, kg/s
Time, days
(g)
Case 4 30 - 45 Horizontal W - E stimulation
Production well 1
Production well 2
Production well enthalpy, j/kg
Water temperature, °C
Time, days
(h)
Case 5 30 - 45 Horizontal W-E stimulation
35 -75 friction
Production well 1
Production well 2
Production rate, kg/s
Time, days
(i)
Case 5 30 - 45 Horizontal W-E stimulation
35 -75 friction
Production well 1
Production well 2
Production well enthalpy, j/kg
Water temperature, °C
Time, days
(j)

Figure 5 Evolution of flow rate and water temperature (enthalpy) in the two production wells. Plots in the left column (a, c, e, g, i) represent the flow rate evolution in the two production wells for the five cases (1-5), plots in the right column (b, d, f, h, j) represent the evolution of water temperature in the two production wells respectively.

The results indicate that Case 4 (fractures oriented at 045 – 120 degrees) returns the highest power output, sustaining the highest power generation within 10 years. The peak magnitude of generated power from the two production wells is maintained around 14 MWe. The evolution of the flow rate and corresponding water temperature from Case 4 suggests that the horizontal E-W stimulation is the most effective in maintaining both a high production flow rate and elevated temperature of outflow water at the highest level (Figure 5 (g) and (h)).

The predefined high friction angle of 75 degrees for the second fracture network in Case 5 is intended to lock this fracture set as resistant to failure. The corresponding results for power generation indicate the reduced potential of shear failure that impairs the magnitude of power generation by decreasing the fracture permeability.

The lowest intensity of power generation (Figure 4) represents Case 5 (no stimulation performed). Even though the temperature at the production well is maintained with the least thermal drawdown (Figure 5f), the flow rate in the production wells are small and uneconomical for power generation. Therefore this indicates that horizontal permeable manifolds are potentially both efficient and necessary for economical heat extraction from these geothermal reservoirs.

The distributions of rock temperature are presented in Figure 6 for the previous five cases at the same elapsed time of $t = 6.34\ years$. Examining the temperature distribution in the reservoir yields some impression of the best performance of heat production with the best heat sweep efficiency. Figures 6 (a) and (b) show the distributions of rock temperature for fractures orientated 020 – 135 degrees with stimulation along in the E-W and then the N-S directions, separately. The cooled volume in Figure 6(b) is slightly smaller than that in Figure 6(a). The distribution of rock temperature in Figure 6(a) and (b) indicate a sharper thermal front propagating from injector to producer. The cooling regime for the case without stimulation (Figure 6(c)) is the smallest among all the cases studied. The thermal extraction is limited to around the injection wells due to the low reservoir permeability. Figure 6(d) shows the case with the most complete heat energy depletion in the reservoir for Case 4. The reservoir between the injection wells and the production wells has been cooled both significantly and uniformly - the rock temperature has been cooled to the temperature of injected water. This cooling response reinforces the

results for the largest heat generation from Case 4. If one set of fractures is less able to slip, then the cooling path would follow the major conductive fractures as shown in Figure 6(e).

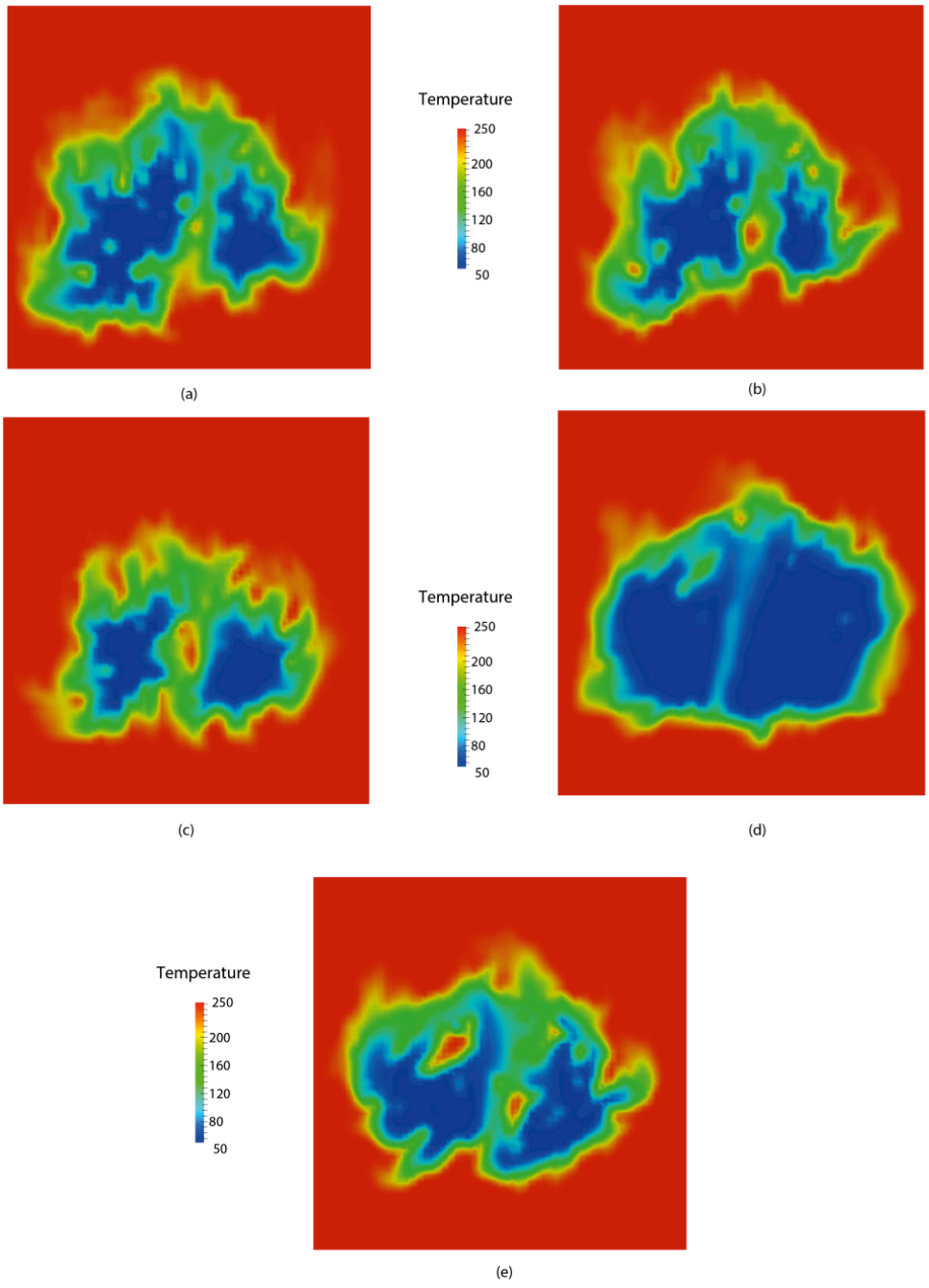

Figure 6 Contour of rock temperature distribution at $t = 6.34\ years$. (a) Case 1 fracture orientations 020 – 135 degrees after E-W stimulation, (b) Case 2 fracture orientations 020 – 135 degrees after N-S stimulation, (c) Case 3 without stimulation, (d) Case 4 fracture orientations 045 – 120 degrees after E-W

stimulation, (e) Case 5 fracture orientations 045 – 120 degrees with friction angle 035 – 75 degrees after E-W stimulation.

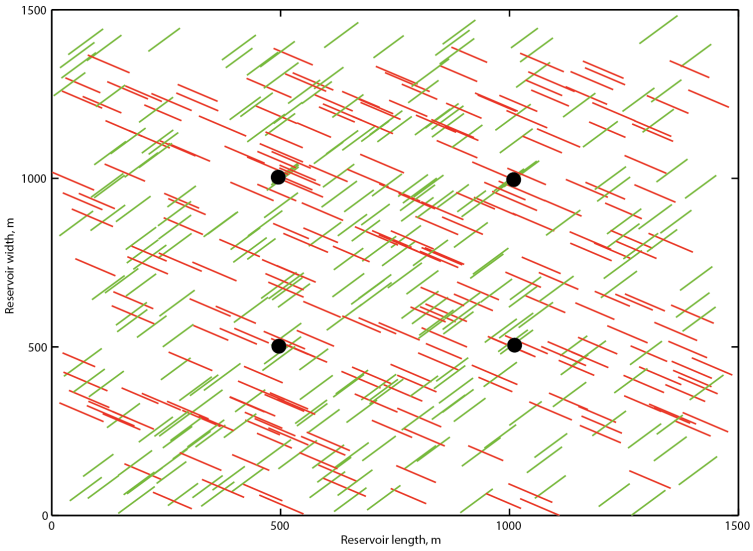

(a)

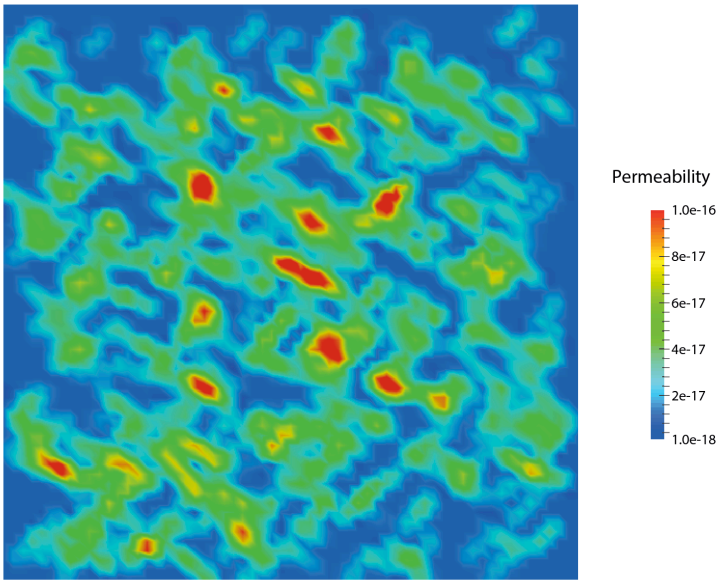

(b)

Figure 7 (a) Distribution of fracture networks in the reservoir oriented at 045 and 120 degrees respect to the North with 250 Fractures $\rho_f = 0.0223\, m^{-1}$ in each set, (b) contour of initial fracture permeability before stimulation.

Fracture density is a crucial factor in influencing the extraction of heat energy. In this section, another reservoir geometry with fewer fractures is developed to examine the impact of fracture density on power generation. Figure 7(a) shows the distribution of fractures in the reservoir. Two sets of fractures oriented at 045 – 120 degrees are arranged with 250 fractures in each set. The corresponding fracture density ρ_f is equal to 0.0223 m^{-1}, which is only one-quarter of the previous reservoir conditions with 1000 fractures. Figure 7(b) represents the distribution of initial fracture permeability. The stimulation and subsequent production schedules are identical for both cases.

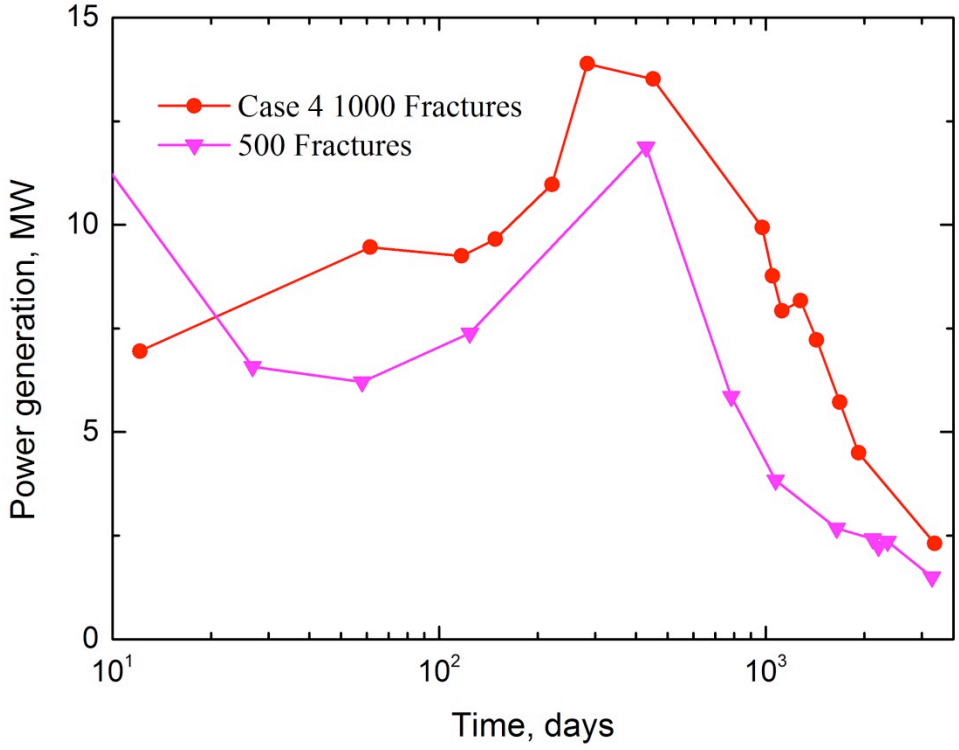

Figure 8 Power generation evolution comparisons between the Case 4 with 1000 fractures $\rho_f = 0.089\ m^{-1}$ and the case with 500 fractures $\rho_f = 0.0223\ m^{-1}$.

The evolution of instantaneous electric power generation for the low fracture density case is presented in Figure 8. The comparison between the different fracture densities reveals that an increased fracture density can significantly enhance the generated power. The more permeable reservoir with a larger fracture density has the advantages in collecting higher flow rates, and avoiding short circuit during the heat extraction. The total power generation in the higher fracture density condition yields a peak

magnitude around 14.5 MWe, while the peak power generation in the smaller fracture density condition reaches only 11.5 MWe.

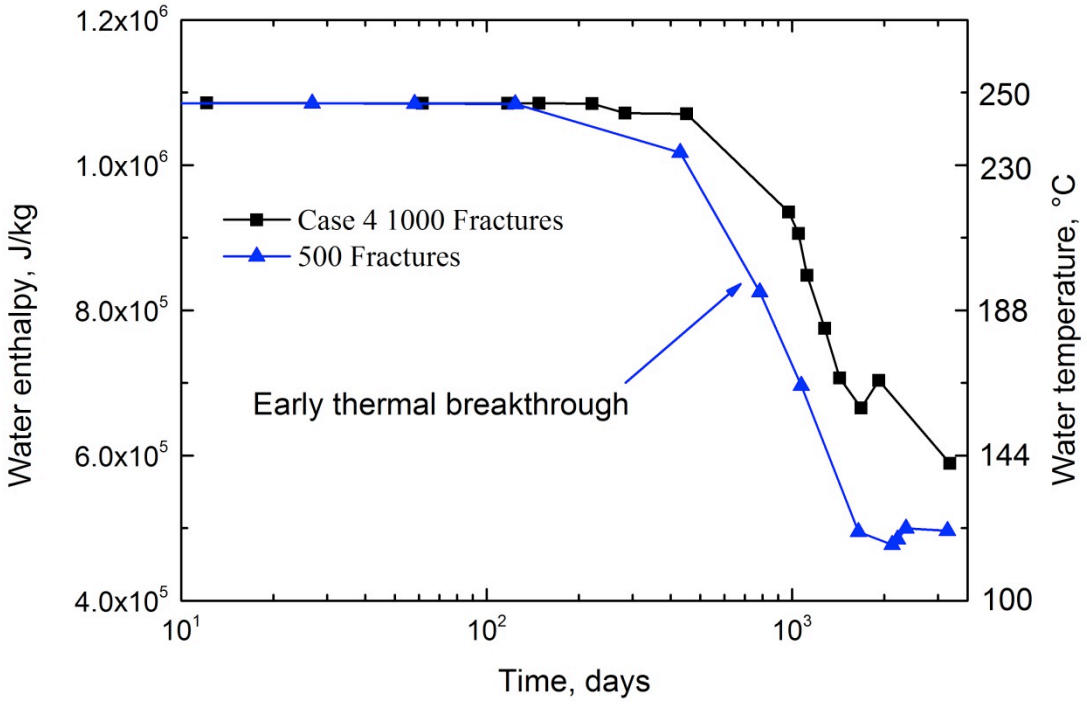

Figure 9 Evolution of water enthalpy at the production well between Case 4 with high fracture density $\rho_f = 0.089\ m^{-1}$ and the lower fracture density Case $\rho_f = 0.0223\ m^{-1}$.

Moreover, the resulting lower power generation in the small fracture density end-member case is not only due to the low flow rates in the production wells, but also the response to the early thermal breakthrough in the production wells. The temperature evolution of produced water for both cases is presented in Figure 9. The black line shows the water enthalpy and temperature for the produced water in Case 4 for the reservoir with a high fracture density, while the blue line depicts the evolution of produced water enthalpy and temperature in the low fracture density condition (Case 6). It is obvious that the thermal drawdown response in the production well for the high fracture density case started significantly earlier than that for the low fracture density case. The sparse distribution of the fracture network prevents the cold water from picking up sufficient heat energy from the surrounding (and more distant) rock. The early thermal breakthrough due to the induced short circuit is not a favorable scenario for geothermal energy production, either.

The rock temperature distribution at $t = 6.34\ years$ in Figure 10 further reinforces the response of the short circuit in the reservoir with lower fracture density. The narrow cooling path from the bottom injectors to the top producers indicates a response of preferred fracture channeling during heat transport. It can be concluded that the fracture density has a strong impact on the heat energy transport in geothermal reservoirs. Larger fracture density increases the flow rate in the production well, and also increases the heat circuit length to substantially improve sweep efficiency.

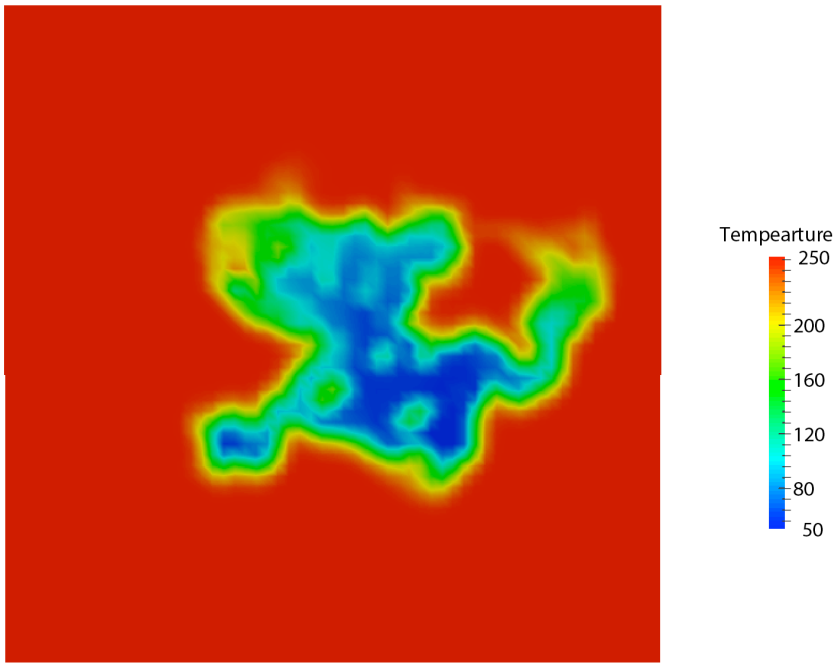

Figure 10 Contour of rock temperature at $t = 2.0\times10^{8} s$ for the lower fracture density case $\rho_f = 0.0223\ m^{-1}$.

9.4 Conclusions

The previous case studies focus on examining the impact of fracture orientation, stimulation strategy, and the fracture density in enhancing the permeability and heat energy extraction from geothermal reservoirs. The best production optimization strategy is obtained from a series of simulations aimed to enhance both the magnitude and longevity of thermal recovery rates.

Reservoir stimulation is demonstrated to be efficient in significantly enhancing the generated power, compared against the results without stimulation. In this study, the eventual production schedule is designed to generate a fluid sweep path in the direction of the minor principal stress (N-S direction). The

best optimization that results in the highest power generation is to create two parallel permeable manifolds along the major principal stress direction – in the example here, in the E-W direction. The parallel manifolds become hydraulically interconnected along the axis of the horizontal injection wells in the E-W direction, which are analogous to horizontal wells that allow a uniform sweep of fluids between the zones. The long term production results verify that the manifolds return an improved heat sweep efficiency. Furthermore, the fracture orientation is either very important in influencing the stimulation result. Fractures oriented at 045–120 degrees result in the greatest fracture permeability enhancement along the stimulation direction. Therefore, the developed manifolds with fractures oriented at 045–120 degrees are more permeable and conductive, compared to the case with fractures oriented at 020-135 degrees. Additionally, the fracture density either has direct impact in the heat extraction. The larger fracture density (small fracture spacing) has significant advantages for the heat production by increasing the flow rate in the production wells. The evolution of water temperature in the production well illustrates that the early thermal breakthrough tends to occur in the reservoir with lower fracture density.

Acknowledgement

This work is a partial result of support from the US Department of Energy under project DOE-DE-343 EE0002761. This support is gratefully acknowledged.

9.5 Reference

Akın, S., Kok, M. V., & Uraz, I. (2010). Optimization of well placement geothermal reservoirs using artificial intelligence. *Computers & Geosciences*,*36*(6), 776-785.

de Dreuzy, J.-R., P. Davy, and O. Bour (2001), Hydraulic properties of two-dimensional random fracture networks following a power law length distribution: 2. Permeability of networks based on lognormal distribution of apertures, *Water Resources Research*, *37*, 2079-2095.

Darnet, M., Marquis, G., & Sailhac, P. (2006). Hydraulic stimulation of geothermal reservoirs: fluid flow, electric potential and microseismicity relationships. *Geophysical Journal International*, *166*(1), 438-444.

Elsworth, D. (1989), Thermal recovery from a multiple stimulated HDR reservoir, *Geothermics*, *18*(5), 761-774.

Elsworth, D. (1990), A comparative evaluation of the parallel flow and spherical reservoir models of HDR geothermal systems, *Journal of Volcanology and Geothermal Research*, *44*(3), 283-293.

Elsworth, D., J. Taron, I. Faoro, D.-S. Lee, J. Liu, A. Niemeijer, and H. Yasuhara (2010), Evolution of Deformability and Transport Properties of Fractured Rocks Under the Action of Stress and Chemistry, paper presented at EGU General Assembly Conference Abstracts.

Gan, Q., and D. Elsworth (2014a), Analysis of fluid injection‐induced fault reactivation and seismic slip in geothermal reservoirs, *Journal of Geophysical Research: Solid Earth*, *119*(4), 3340-3353.

Gan, Q., and D. Elsworth (2014b), Thermal drawdown and late‐stage seismic‐slip fault reactivation in enhanced geothermal reservoirs, *Journal of Geophysical Research: Solid Earth*.

Ghassemi, A., and Q. Zhang (2006), Porothermoelastic analysis of the response of a stationary crack using the displacement discontinuity method, *Journal of engineering mechanics*, *132*(1), 26-33.

Gringarten, A., and P. Witherspoon (1973), Extraction of heat from multiple-fractured dry hot rock, *Geothermics*, *2*(3), 119-122.

Gringarten, A., P. Witherspoon, and Y. Ohnishi (1975), Theory of heat extraction from fractured hot dry rock, *Journal of Geophysical Research*, *80*(8), 1120-1124.

Marcou, J. A. (1985). Optimizing development strategy for liquid dominated geothermal reservoirs (Doctoral dissertation, Stanford University).

McClure, M., and R. N. Horne (2013), *Discrete fracture network modeling of hydraulic stimulation: Coupling flow and geomechanics*, Springer Science & Business Media.

Min, K.-B., and L. Jing (2003), Numerical determination of the equivalent elastic compliance tensor for fractured rock masses using the distinct element method, *International Journal of Rock Mechanics and Mining Sciences*, *40*(6), 795-816.

Oda, M. (1986), An equivalent continuum model for coupled stress and fluid flow analysis in jointed rock masses, *Water Resources Research*, *22*(13), 1845-1856, doi:10.1029/WR022i013p01845.

Odling, N. E., Gillespie, P., Bourgine, B., Castaing, C., Chiles, J. P., Christensen, N. P., & Watterson, J. (1999). Variations in fracture system geometry and their implications for fluid flow in fractured hydrocarbon reservoirs. *Petroleum Geoscience*, *5*(4), 373-384.

Olson, J. E. (2003), Sublinear scaling of fracture aperture versus length: an exception or the rule?, *Journal of Geophysical Research: Solid Earth (1978–2012)*, *108*(B9).

Pham, M., Ponte, C. K. C., Cabeças, R., Martins, R., & Rangel, G. (2010). Production/Injection Optimization Using Numerical Modeling at Ribeira Grande, São Miguel, Azores, Portugal. In *Proc. World Geothermal Congress 2010*.

Pine, R. J., & Cundall, P. A. (1985). Applications of the fluid-rock interaction program (FRIP) to the modelling of hot dry rock geothermal energy systems. In *Proc. Int. Symp. on Fundamentals of Rock Joints* (pp. 293-302). Centek.

Pruess, K. (2006), Enhanced geothermal systems (EGS) using CO 2 as working fluid—a novel approach for generating renewable energy with simultaneous sequestration of carbon, *Geothermics*, *35*(4), 351-367.

Pruess, K., and Y.-S. Wu (1993), A new semi-analytical method for numerical simulation of fluid and heat flow in fractured reservoirs, *SPE Advanced Technology Series*, *1*(2), 63-72.

Riahi, A., & Damjanac, B. (2013, February). Numerical study of hydro-shearing in geothermal reservoirs with a pre-existing discrete fracture network. In*Proceedings of the 38th Workshop on Geothermal Reservoir Engineering, Stanford, CA* (pp. 11-13).

Sanyal, S. K., and S. J. Butler (2005), An analysis of power generation prospects from enhanced geothermal systems, *Geothermal Resources Council Transactions*, *29*.

Sanyal, S. K., E. E. Granados, S. J. Butler, and R. N. Horne (2005), An alternative and modular approach to enhanced geothermal systems, paper presented at World Geothermal Congress.

Segall, P., and S. D. Fitzgerald (1998), A note on induced stress changes in hydrocarbon and geothermal reservoirs, *Tectonophysics*, *289*(1–3), 117-128, doi:http://dx.doi.org/10.1016/S0040-1951(97)00311-9.

Shaik, A. R., S. S. Rahman, N. H. Tran, and T. Tran (2011), Numerical simulation of fluid-rock coupling heat transfer in naturally fractured geothermal system, *Applied thermal engineering*, *31*(10), 1600-1606.

Taron, J., and D. Elsworth (2009), Thermal–hydrologic–mechanical–chemical processes in the evolution of engineered geothermal reservoirs, *International Journal of Rock Mechanics and Mining Sciences*, *46*(5), 855-864.

Taron, J., and D. Elsworth (2010a), Constraints on compaction rate and equilibrium in the pressure solution creep of quartz aggregates and fractures: Controls of aqueous concentration, *Journal of Geophysical Research: Solid Earth (1978–2012)*, *115*(B7).

Taron, J., and D. Elsworth (2010b), Coupled mechanical and chemical processes in engineered geothermal reservoirs with dynamic permeability, *International Journal of Rock Mechanics and Mining Sciences*, *47*(8), 1339-1348.

Tester, J. W., B. Anderson, A. Batchelor, D. Blackwell, R. DiPippo, E. Drake, J. Garnish, B. Livesay, M. C. Moore, and K. Nichols (2006), The future of geothermal energy: Impact of enhanced geothermal systems (EGS) on the United States in the 21st century, *Massachusetts Institute of Technology*, *209*.

Vörös, R., R. Weidler, L. de Graaf, and D. Wyborn (2007), Thermal modelling of long term circulation of multi-well development at the Cooper Basin hot fractured rock (HFR) project and current proposed scale-up program, paper presented at Proceedings of the Thirty-Second Workshop on Geothermal Reservoir Engineering, Stanford, CA, USA.

Watanabe, K., Y. Niibori, and T. Hashida (2000), Numerical study on heat extraction from supercritical geothermal reservoir, paper presented at Proceedings World Geothermal Congress.

10 PUBLICATIONS AND PRESENTATIONS

Journal Articles

1. Gan, Q. and Elsworth, D. (2015) Production optimization in geothermal reservoirs using a coupled discrete fracture network model. In preparation.
2. Gan, Q. and Elsworth, D. (2015) An equivalent continuum model for coupled stress and fluid flow in discrete fractures in geothermal reservoirs. In preparation.
3. Izadi, G., Elsworth, D. (2015) The influence of thermal-hydraulic-mechanical-and chemical effects on the evolution of permeability, seismicity and heat production in geothermal reservoirs. Geothermics. Vol 53. pp. 385-395. http://dx.doi.org/10.1016/j.geothermics.2014.08.005
4. Gan, Q. and Elsworth, D. (2014) Thermal drawdown and late-stage seismic-slip fault-reactivation in enhanced geothermal reservoirs. J. Geophys. Res. Vol. 119, pp. 8936-8949. http://dx.doi.org/10.1002/2014JB011323
5. Husain, T., Elsworth, D., Voight, B., Mattioli, G., Jansma, P. (2014) Influence of infusion rate and magma rheology on the growth of lava domes.. J. Volc. Geotherm. Res. Vol. 285, pp. 100-117. http://dx.doi.org/10.1016/j.jvolgeores.2014.08.013
6. Gan, Q., Elsworth, D. (2014) Analysis of fluid injection-induced fault reactivation and seismic slip in geothermal reservoirs. J. Geophys. Res. Vol. 119, No. 4, pp. 3340-3353. http://dx.doi.org/10.1002/2013JB010679.
7. Izadi, G., Elsworth, D. (2014) Reservoir stimulation and induced seismicity: role of fluid pressure and thermal transients on reactivated fracture networks. Geothermics. Vol. 51. pp. 368-379. http://dx.doi.org/10.1016/j.geothermics.2014.01.014
8. Izadi, G., Elsworth, D. (2013) The effects of thermal stress and fluid pressures on induced seismicity during stimulation to production within fractured reservoirs. Terra Nova. Vol. 25. pp. 774-380. http://dx.doi.org/10.1111/ter.12046
9. Zheng, B., and Elsworth, D. (2013) Strength evolution in heterogeneous granular aggregates during chemo-mechanical compaction. Int. J. R. Mechs. Vol. 60. pp. 217-226. http://dx.doi.org/10.1016/j.ijrmms.2012.12.031
10. Zheng, B., and Elsworth, D. (2012) Evolution of permeability in heterogeneous granular aggregates during chemical compaction: granular mechanics models. J. Geophys. Res. Vol. 117, No. B3, B03206. http://dx.doi.org/10.1029/2011JB008573

Papers in Conference Proceedings

1. Fang, Y., Elsworth, D., Cladouhos, T. (2015) Mapping permeability tensors in fractured reservoirs using MEQ data. Proc. 49th US Symposium on Rock Mechanics and Geomechanics. San Francisco. June 29-July 1.
2. Elsworth, D., Gan, Q., Fang, Y., Pogacnik, J., Taron, J., Izadi, G., Guglielmi, Y., Im, K.J., Ishibashi, T. (2015) Control of permeability and seismicity – keys to the successful development of EGS reservoirs. Proc. 10th Anniversary Int. Symp. of the Center of Environmental Science and Disaster Mitigation for Advanced Research, Muroran, Japan, March 13-14. pp. K1-K4.
3. Fang, Y., Elsworth, D., Cladouhos, T. (2015) Estimating in-situ permeability of stimulated EGS reservoirs using MEQ moment magnitude: an analysis of Newberry MEQ data. Proc. 40th Workshop on Geothermal Reservoir Engineering, Stanford, California Jan 26-28. SGP-TR-204.
4. Gan, Q. and Elsworth, D. (2015) Fault reactivation due to thermal drawdown in enhanced geothermal reservoirs. Proc. 40th Workshop on Geothermal Reservoir Engineering, Stanford, California Jan 26-28. SGP-TR-204.
5. Im, K.J., Elsworth, D., Fang, Y. (2015) Asymptotic analysis of thermal stimulation of geothermal reservoirs. Proc. 40th Workshop on Geothermal Reservoir Engineering, Stanford, California Jan 26-28. SGP-TR-204.

6. Pogacnik, J., Elsworth, D., O'Sullivan, M., O'Sullivan, J. (2014) A damage mechancis approach to the simulation of hydroshearing around an injectin well. Proc. Symp. On Recent Adv. In Numerical Simulation of Hydraulic Fracture, Rzeszow, Poland. July.

7. Elsworth, D., Gan, Q., Marone, C., Connolly, P., Alpern, J., Culp, B., Im, K.J. (2014) Key coupled processes related to gas-fracturing in unconventional reservoirs. 8th Aisian Rock Mechanics Symposium (ARMS8). Sapporo, Japan. October. pp. 43-50.

8. Fang, Y., Elsworth, D., Cladouhos (2014) Bimodal depth distribution of MEQs in the Newberry Geothermal Reservoir. Proc. 48th US Symposium on Rock Mechanics and Geomechanics. Minneapolis, Minnesota. June 2-4. ARMA 14-7722.

9. Mohan, A.R., Turaga, U., Shembekar, V., Viswanathan, S., Elsworth, D., Pisupati, S.V. (2013) Technical feasibility of polygeneration: a case study of combining CO2-EG with IGCC. Proc. Int. Conf. Coal Science and Technology. Oct. University Park, PA.

10. Mohan, A.R., Turaga, U., Shembekar, V., Viswanathan, S., Elsworth, D., Pisupati, S.V. (2013) Simultaneous sequestration and extraction of geothermal energy using CO_2 from an IGCC Plant as a Heat Transfer fluid for power generation from EGS. Proc. 30th Int. Pittsburgh Coal Conf. September 16-19.

11. Izadi, G., and Elsworth, D. 2013. The influence of thermal- hydraulic-mechanical- and chemical effects on the evolution of permeability, seismicity and heat production in geothermal reservoirs. Proc. 47th US Symposium on Rock Mechanics and Geomechanics. San Francisco. June 23-26. ARMA 13-436.

12. Benato, S., Reeves, D.M., Parashar, R., Davatzes, N., Hickman, S., Elsworth, D., Spielman, P., Taron, J. (2013) Computational investigation of hydro-mechanical effects on transmissivity evolution during the initial injection phases as the desert peak EGS project, European Geothermal Congress.

13. Benato, S., Reeves, D.M., Parashar, R., Davatzes, N., Hickman, S., Elsworth, D., Spielman, P., Taron, J. (2013) Computational investigation of hydro-mechanical effects on transmissivity evolution during the initial injection phases as the desert peak EGS project, NV. Proc. 38th Workshop on Geothermal Reservoir Engineering. Stanford University. February.

14. Mohan, A.R., Turaga, U., Shembekar, V., Viswanathan, S., Elsworth, D, Pisupati, S. 2013. Using CO_2 from an IGCC plant as a heat transfer fluid for the extraction of geothermal energy for power generation from EGS. Proc. 38th Workshop on Geothermal Reservoir Engineering. Stanford University. February.

15. Izadi, G., Elsworth, D. 2012. Evolution of induced seismicity due to interactions between thermal, hydraulic, mechanical and chemical processes in EGS reservoirs. Proc. 46th US Symposium on Rock Mechanics and Geomechanics. Chicago. June 24-27.

16. Taron, J., Wang, W., Elsworth, D., Kolditz, O. 2011. EGS reservoir (THMC) modeling techniques and the influence of bulk chemistry on mechanical stress. Proc. GeoProc2011. Perth, Western Australia. July 6-9.

17. Izadi, G., Zheng, B., Taron, J., Elsworth, D. 2011. Evolution of permeability and triggered seismicity: fluid pressure, thermal and chemical effects in enhanced geothermal systems. Proc. GeoProc2011. Perth, Western Australia. July 6-9.

18. Izadi, G., Elsworth, D. (2011) Influence of energy release in fracture networks on reservoir evolution and triggered seismicity in EGS reservoirs. Proc. 45th US-Canada Symp. on R. Mechs, San Francisco, June.

19. Zheng, B., Elsworth, D. (2011) Permeability evolution in mechanically and chemically-perturbed granular mechanics models of EGS reservoirs. Proc. 45th US-Canada Symp. on R. Mechs, San Francisco, June.

Selected Invited Presentations

1. Elsworth, D., Marone, C., Taron, J., Izadi, G., Gan, Q., Zhong, Z., Fang, Y., Candela, T. 2015. Roles of URLs in probing controls on induced seismicity and related permeability evolution. URL Networking Commission Workshop. 14th International ISRM Congress on Rock Mechanics. Montreal, Canada. May10. [Invited]

2. Elsworth, D., Gan, Q., Fang, Y., Pogacnik, J., Taron, J., Izadi, G., Guglielmi, Y., Im, K.J., Ishibashi, T. (2015) Control of permeability and seismicity – keys to successful development of EGS geothermal

reservoirs. 10th Anniversary Int. Symp. Center of Environmental Science and Disaster Mitigation for Advanced Research (CEDAR). Muroran, Japan. March 13-14. [Keynote]

3. Elsworth, D. (2014) Roles of URLs in Probing controls on induced seismicity and permeability evolution. AGU Fall Meeting, San Francisco, Abstract T33A-4639. [Invited]

4. Elsworth, D. 2014. Unconventional energy resources – the key to climate security? Masterclass, Chinese Academy of Sciences, Wuhan. November 27, 2014. [Invited]

5. Elsworth, D. 2014. Permeability evolution on reactivated fracture networks and induced seismicity – stimulation of reservoirs for EGS and gas shale. ETH, Zurich. May. [Invited]

6. Elsworth, D. 2013. Resolving key uncertainties in subsurface energy recovery: one role of in situ URLs. AGU Fall Meeting, San Francisco, Abstract H31G-1270. [Invited]

7. Elsworth, D. and Taron, J. 2013. Effects of solid-state and pore-fluid chemistry and stress on permeability evolution. GSA Penrose Conference on Predicting and Detecting Natural Flow Paths for Geothermal Fluids in Deep Sedmentary Basins. Park City, UT. October. [Keynote]

8. Elsworth, D. 2013. Computational methods in enhanced geothermal systems. JASON study on Enhanced Geothermal Systems. La Jolla, California, June 20-21. [Invited]

9. Izadi G., Elsworth D. 2013. Permeability evolution on reactivated fracture networks and induced seismicity during EGS reservoir stimulation. SPE/AAPG Western Regional Meeting. April 19-25. Monterey, CA. [Invited].

10. Elsworth, D. 2013. Energy from unconventional reservoirs: contemporary challenges and opportunities. School of Civil Engineering. University of Queensland, St. Lucia. January 16. [Invited]

11. Elsworth, D. 2012. DUSEL Interdisciplinary science studies: biology, geoscience and geoengineering@DUSEL. ASPERA Workshop on Underground Synergies with Astro-Particle Physics: Multi-Disciplinary Studies in the World's Deep Underground Science Facilities. Durham, UK. December 17-19. [Invited]

12. Elsworth, D., Izadi, G., Zheng, B., Gan, Q., Taron, J. 2012. Evolution of induced seismicity in response to injection into fractured reservoirs. EOS Trans. AGU Fall Meeting, San Francisco, Abstract H13L-01. [Invited]

13. Elsworth, D. 2012. Reactive flow and permeability dynamics. GRC Workshop on Reservoir Stimulation: Current Understanding and Practice and the Way Forward. Reno, NV. September 28-29. [Invited]

14. Chandra, D., Hall, D., Elsworth, D. 2012. Challenges and opportunities in the recovery of deep geothermal energy as a reliable baseload supply. EnergyPath 2012 Conference. Allentown, June. [Invited]

15. Izadi, G., Zheng, B., Taron, J., Elsworth, D. 2012. Evolution of permeability and triggered seismicity: fluid pressure, thermal and chemical effects in enhanced geothermal systems. United States – New Zealand Joint Geothermal Workshop, Rotorua, April. [Invited]

16. Izadi, G., Zheng, B., Taron, J., Elsworth, D. 2012. Roles of fluid pressure, thermal and echmical effects in conditioning permeability and induced seismicity in enhanced geothermal systems. (9th Int. Workshop on Water Dynamics, Tohoku University, Sendai, Japan. March. [Invited]

17. Elsworth, D., Izadi, G., Zheng, B., Taron, J. 2011. Fluid pressure, thermal and chemical effects in conditioning permeability and triggered seismicity in enhanced geothermal systems. EOS Trans. AGU, 91(53) Fall Meeting Suppl., Abstract H31L-01. [Invited]

18. Elsworth, D. 2011. Roles of URLs in exploring complex process feedbacks related to energy recovery and the sequestration of energy wastes. Workshop on URL Networking. ISRM Congress, Oct 17. Beijing. [Invited]

19. Elsworth, D. 2011. Complex process couplings related to deep geologic sequestration and energy recovery. Penn State University. Department of Mathematics.

20. Elsworth, D. 2011. The Energy New Deal: contributions and challenges for our comprehension of complex coupled behaviors. Proc. GeoProc2011. Perth, Western Australia. July 6-9. [Keynote]

21. Taron, J., Elsworth, D., Izadi, G., Zheng, B. 2011. Modeling the complex evolution of fractured geothermal reservoirs. SIAM Conference on Mathematical and Computational Issues in the Geosciences. March 21-24. Long Beach, California. [Invited]

22. Taron, J., Izadi, G., Zheng, B., Elsworth, D. 2011. Influence of THMC couplings on thermal recovery from EGS systems. SIAM Conference on Mathematical and Computational Issues in the Geosciences. March 21-24. Long Beach, California. [Invited]

23. Elsworth, D., Zheng, B., Izadi, G., Taron, J. 2011. Modeling complex coupled processes involved in the evolution of EGS reservoirs: stimulation through production then decline. AAPG/SPE/SEG Hedberg Conference on Enhanced Geothermal Systems. Napa. March 14-17. Napa, California. [Invited]

24. Elsworth, D. (2011) Complex process couplings in systems pushed far-from-equilibrium: Application to deep geologic sequestration and energy recovery. Workshop on CO_2 Storage in Carboniferous Formations and Abandoned Mines. China University of Mining and Technology. Beijing. January 8-9. [Plenary]

25. Elsworth, D., Murdoch, L., Onstott, T., et al. 2011. Geoscience and Geoengineering@DUSEL.

    a. China University of Mining and Technology, Beijing. January.

    b. Northeastern University, Shenyang. January.

    c. Tsinghua University, Beijing. January.

26. Elsworth, D., Murdoch, L., Onstott, T., et al. 2010. Geoscience and Geoengineering@DUSEL. Committee to Assess the Deep Underground Science and Engineering Laboratory (DUSEL). National Research Council. Washington, DC., December 14-15.

27. Elsworth, D., Faoro, I., Marone, C., Taron, J., Samuelson, J., Yasuhara, H., Polak, A. 2010. Permeability evolution in fractured media – short- and long-term effects. Conf. on Dynamically Determined and Controlled Permeability. DOE BES. San Francisco, December 11-12.

28. Elsworth, D. 2010. The US deep underground science and engineering laboratory (DUSEL): Opportuniites for discovery in energy recovery and the sequestration of energy-related wastes. University of Oklahoma, Norman. November 19.

29. Elsworth, D. 2010. The energy new deal: contributions and challenges of carbon sequestration, geothermal energy and low carbon fuels. Masterclass. University of Western Australia. October 7.

30. Elsworth, D. 2010. Subsurface engineering – band-aid or enduring solution to the looming prospects of peak oil and climate change. Public Lecture. University of Western Australia. October 6.

31. Elsworth, D., Onstott, T.C. and Murdoch, L. 2010. Science@DUSEL: Biology, Geoscience and Engineering. First Annual DURA Meeting and PDR Rollout. Fermilab, Chicago. September.

32. Elsworth, D. 2010. Complex process couplings related to deep geologic sequestration and energy recovery.

    a. Department of Urban Management. Kyoto University. July.

    b. Advanced Institute for Science and Technology, Geological Survey of Japan, Tsukuba City. July.

    c. Japanese Society for Civil Engineers, Rock Mechanics Committee. Tokyo. July.

    d. Japanese Atomic Energy Agency. Mizunami. July.

Graduate Theses

1. Izadi, Ghazal. Evolution of Permeability and Induced Seismicity within Fractured Reservoirs. Ph.D. Thesis. 205 pp. Energy and Geo-Environmental Engineering, The Pennsylvania State University, University Park, Pennsylvania (2012).

2. Gan, Quan. Analysis of induced seismicity and heat transfer in geothermal reservoir by coupled simulation. Ph.D. Thesis. 180 pp. Energy and Geo-Environmental Engineering, The Pennsylvania State University, University Park, Pennsylvania (2015).